UNIVERSITY OF CALIFORNIA, SAN DIEGO

Eddy fluxes in baroclinic turbulence

A dissertation submitted in partial satisfaction of the
requirements for the degree Doctor of Philosophy
in
Oceanography

by

Andrew F. Thompson

Committee in charge:

William R. Young, Chair
Paola Cessi
Sarah T. Gille
Paul F. Linden
Jennifer A. MacKinnon
Richard Salmon
Janet Sprintall

2006

The dissertation of Andrew F. Thompson is approved, and it is acceptable in quality and form for publication on microfilm:

Chair

University of California, San Diego

2006

And is not human life in many parts of the earth governed to this day less by time than by weather, and thus by an unquantifiable dimension which disregards linear regularity, does not progress constantly forward but moves in eddies, is marked by episodes of congestion and irruption, recurs in ever-changing form, and evolves in no one knows what direction?

W. G. Sebald

TABLE OF CONTENTS

LIST OF FIGURES

LIST OF TABLES

ACKNOWLEDGMENTS

The successful completion of this thesis was dependent on the support and guidance of a number of people.

I am most indebted to my advisor, Bill Young. Among many things, Bill has introduced me to the magic of integration by parts and instructed me in the judicious use of adverbs. Most importantly, though, Bill has taught me to be more careful and precise with my research. I am a better scientist for having worked with him.

The other members of my committee have assisted me in many ways. I would specifically like to thank Rick Salmon for his steadfast encouragement in the face of slow progress; Paola Cessi for our copy room conversations, which although impromptu, unfailingly helped to organize my thoughts; Sarah Gille for her considerate advice about decisions involving science, career and family; Janet Sprintall for the opportunity to set foot in Antarctica, surely one of the most memorable experiences of my life, as well as a friendly smile every time I knocked on her door; Paul Linden for giving me *carte blanche* in the lab and for welcoming me at his group meetings; Jen MacKinnon for her enthusiastic assistance with any questions or requests I threw at her—she has provided me with a great role model as a young scientist. I would also like to ackowledge helpful conversations with Larry Armi, Glenn Ierley and Stefan Llewellyn-Smith at various points while I was at Scripps.

Phil Moses and Dana Dahlbo have had the answers to all my questions, which has enabled me to fully focus on my research. The graduate department staff, especially Alice Zheng, Dawn Huffman and Denise Darling have also smoothed a number of bumps along the road to a Ph.D.

I will miss the conversations, science-related and otherwise, I have shared with my friends at Scripps. I especially thank Dan Birch and John Taylor, who have been good friends and sounding boards since day one, and Nicolas LeDantec,

who has spent too much time in the office with me over the last three years.

I am blessed to have the support of my family in everything I do. I thank my parents and the Jules for always taking an interest in my studies and travels. I thank Juanita for sharing with me an engagement, two weddings, the arrival of our baby girl and all the love that goes with it during the course of this Ph.D. These are the events I am most proud of and I look forward to watching our love grow with our new family. Finally, I thank Sophia for providing perspective over the last six weeks.

The text of Chapter II, in full, is a reprint with minor modifications of the paper "Scaling baroclinic eddy fluxes: vortices and energy balance," *Journal of Physical Oceanography*, **36**, 720-738 (2006) (Copyright of the American Meteorological Society 2006). The dissertation author was the primary researcher and author of this paper. W. R. Young directed and supervised the research, which forms the basis of this chapter.

The text of Chapter III, in full, is a reprint with minor modifications of the paper "Assessment of a theory for eddy heat fluxes," submitted for publication to the *Journal of Atmospheric Sciences*. The dissertation author was the primary researcher and author of this paper. W. R. Young directed and supervised the research, which forms the basis of this chapter.

The text of Chapter V, in full, is a reprint with minor modifications of the paper "Spatial and temporal patterns of small-scale mixing in Drake Passage," accepted for publication in the *Journal of Physical Oceanography*. The dissertation author was the primary researcher and author of this paper. S. T. Gille, J. Sprintall and J. A. McKinnon directed and supervised the research, which forms the basis of this chapter; J. Sprintall supplied the XCTD data.

VITA

2000	B.A., Engineering Sciences, Dartmouth College, Hanover, NH
2001	Certificate of Advanced Study in Mathematics, University of Cambridge, U.K.
2002	Master of Philosophy in Fluid Flow, University of Cambridge, U.K.
2002–2006	Research Assistant Scripps Institution of Oceanography, University of California, San Diego
2006	Ph.D., Physical Oceanography Scripps Institution of Oceanography, University of California, San Diego.

PUBLICATIONS

A. F. Thompson, M. G. Worster and H. E. Huppert, 2003. A global conservation model for diffusion-controlled solidification of a ternary alloy. *Journal of Fluid Mechanics*, **483**, 191-197.

A. F. Thompson, M. G. Worster, H. E. Huppert and A. Aitta, 2003. Solidification and compositional convection of a ternary alloy. *Journal of Fluid Mechanics*, **497**, 167-199.

A. F. Thompson and G. Veronis, 2005. Diffusively-driven overturning of a stable density gradient. *Journal of Marine Research*, **63**, 291-313.

A. F. Thompson and W. R. Young, 2006. Scaling baroclinic eddy fluxes: vortices and energy balance. *Journal of Physical Oceanography*, **36**, 720-738.

A. F. Thompson, S. T. Gille, J. A. MacKinnon and J. Sprintall, 2006. Spatial and temporal patterns of small-scale mixing in Drake Passage. Accepted for publication in the *Journal of Physical Oceanography*.

A. F. Thompson and W. R. Young, 2006. Baroclinic eddy heat fluxes: zonal flows and energy balance. Submitted to the *Journal of Atmospheric Sciences*.

PRESENTATIONS

A. F. Thompson, S. T. Gille, J. A. MacKinnon and J. Sprintall, 2006. "Spatial and temporal patterns of small-scale mixing in Drake Passage," *American Geophysical Union, Ocean Sciences Meeting*, Honolulu, HI.

W. R. Young and A. F. Thompson, 2006. "Beta plane jets and equilibration of baroclinic eddies," *American Geophysical Union, Ocean Sciences Meeting*, Honlulu, HI.

A. F. Thompson and P. F. Linden, 2005. "Stratification of a closed region containing two buoyancy sources," *58th Annual Meeting of the Division of Fluid Dynamics, American Physical Society*, Chicago, IL.

A. F. Thompson and W. R. Young, 2005. "Scaling baroclinic eddy fluxes: vortices and energy balance," *15th Conference on Atmospheric and Oceanic Fluid Dynamics, American Meteorological Society*, Cambridge, MA.

A. F. Thompson and W. R. Young, 2004. "Scaling baroclinic eddy fluxes," *Global Circulation and the Atmosphere*, Pasadena, CA.

FIELDS OF STUDY

Major Field: Oceanography
Studies in Physical Oceanography
Professors Myrl C. Hendershott, Paul E. Robbins and Lynne D. Talley,

Studies in Fluid Mechanics
Professors Laurence Armi, Paola Cessi, Stefan G. Llewellyn-Smith, Richard Salmon and Clinton Winant

Studies in Applied Mathematics
Professors Stefan G. Llewellyn-Smith, Forman Williams and William R. Young

Studies in Waves
Professors Robert T. Guza, Myrl C. Hendershott and W. Kendall Melville

Studies in Data Analysis
Professors Sarah T. Gille and Robert Pinkel

Studies in Numerical Methods
Professor Thomas R. Bewley

ABSTRACT OF THE DISSERTATION

Eddy fluxes in baroclinic turbulence

by

Andrew F. Thompson
Doctor of Philosophy in Oceanography
University of California, San Diego, 2006
Professor William R. Young, Chair

The eddy heat flux generated by the statistically equilibrated baroclinic instability of a uniform, horizontal temperature gradient is studied using a two-mode quasigeostrophic model. An overview of the dependence of the eddy diffusivity of heat D_τ on the planetary potential vorticity gradient β, the bottom friction κ, the deformation radius λ, the vertical shear of the large-scale flow $2U$ and the domain size L is provided at 70 numerical simulations with $\beta = 0$ (f-plane) and 110 simulations with $\beta \neq 0$ (β-plane).

Strong, axisymmetric, well-separated baroclinic vortices dominate the equilibrated barotropic vorticity and temperature fields of f-plane turbulence. The heat flux arises from a systematic northward (southward) migration of anti-cyclonic (cyclonic) eddies with warm (cold) fluid trapped in the cores. Zonal jets form spontaneously on the β-plane, and stationary, isotropic, jet-scale eddies align within the strong eastward-flowing regions of the jets. In both studies, the vortices and jets give rise to a strong anti-correlation between the barotropic vorticity ζ and the temperature field τ. The baroclinic mode is also an important contributor to dissipation by bottom friction and energizes the barotropic mode at scales larger than λ. This in part explains why previous parameterizations for the eddy heat flux based on Kolmogorovian cascade theories are found to be unreliable.

In a separate study, temperature and salinity profiles obtained with expendable conductivity, temperature and depth (XCTD) probes within Drake Passage, Southern Ocean are used to analyze the turbulent diapycnal eddy diffusivity κ_ρ to a depth of 1000 meters. The Polar Front separates two dynamically different regions with strong, surface-intensified mixing north of the Front. South of the Polar Front mixing is weaker and peaks at a depth of approximately 500 m, near the local temperature maximum. Peak values of κ_ρ are found to exceed 10^{-3} m^2 s^{-1}. Wind-driven near-inertial waves, mesoscale eddies and thermohaline intrusions are discussed as possible factors contributing to observed mixing patterns.

I

Introduction

The large-scale circulation of the atmosphere and ocean is characterized by flows with scales of hundreds to thousands of kilometers, which vary on time scales of days to years. Yet circulation patterns remain influenced by smaller-scale processes, such as internal waves, mesoscale eddies, atmospheric storms, etc. The difficulty in representing dynamics that connect vastly different scales is a fundamental problem of large-scale geophysical flows. This dissertation considers two rather different examples of small/mesoscale processes that are essential for understanding global heat, energy and momentum budgets. Chapters II through IV consider the effects of coherent vortices and zonal (along latitude) jets on meridional (along longitude) heat transport in a simple, baroclinically unstable system. Chapter V presents an observational study of the distribution of small-scale vertical mixing across Drake Passage, Southern Ocean.

I.1 Baroclinic instability and eddy fluxes

In the atmosphere and ocean, a poleward heat flux arises to balance heating at the equator and cooling at the poles. In a broad sense, this differential heating generates large overturning cells, for example the meridional overturning

circulation in the ocean (Wunsch & Ferrari 2004) and the Hadley cell in the tropical atmosphere (Gill 1982), which transport warm (cold) fluid poleward (equatorward) in the upper (lower) portion of the cell. However, the atmosphere and ocean are dominated by rotation and stratification, which add important complications to geophysical transport. The meridional temperature gradient and its associated sloping isopycnals give rise to a zonal flow through the thermal wind balance. The zonal flow is unable to relax the meridional gradient, but potential energy stored in the sloping isopycnals is released through baroclinic instability. Baroclinic instability leads to the formation of mesoscale eddies and atmospheric storms on scales comparable to the deformation radius of the respective environments (roughly 50 km in the ocean and 1000 km in the atmosphere). Heat transport by these coherent structures, the eddy heat flux, makes an important contribution to relaxing the temperature gradient, which is ultimately maintained by solar heating. Figure I.1 summarizes these processes.

The first part of this thesis focuses on understanding the poleward eddy heat flux that arises from a large-scale, uniform, unstable temperature gradient. Inclusion of the eddy heat flux in general circulation models, or GCMs, is essential for producing accurate representations of the global climate. Decadal (or longer) simulations using GCMs are currently too coarse to resolve ocean eddies, and may only weakly resolve atmospheric storms. Improvements in numerical models may mean that climate simulations will compute eddy fluxes directly in the future, however, an understanding of how environmental parameters, such as the large-scale temperature gradient, influence eddy fluxes is still desirable. Thus, the goal is to survey the eddy heat flux in a simple baroclinic model and to determine a physically-motivated relationship between the flux and control parameters.

We study the eddy heat flux with a two-mode (or two-layer), doubly-periodic quasi-geostropic (QG) model. The equations of motion are described in detail in Appendix A. The model is forced with a fixed temperature gradient (or equivalently a fixed velocity jump between the upper and lower layers) that is

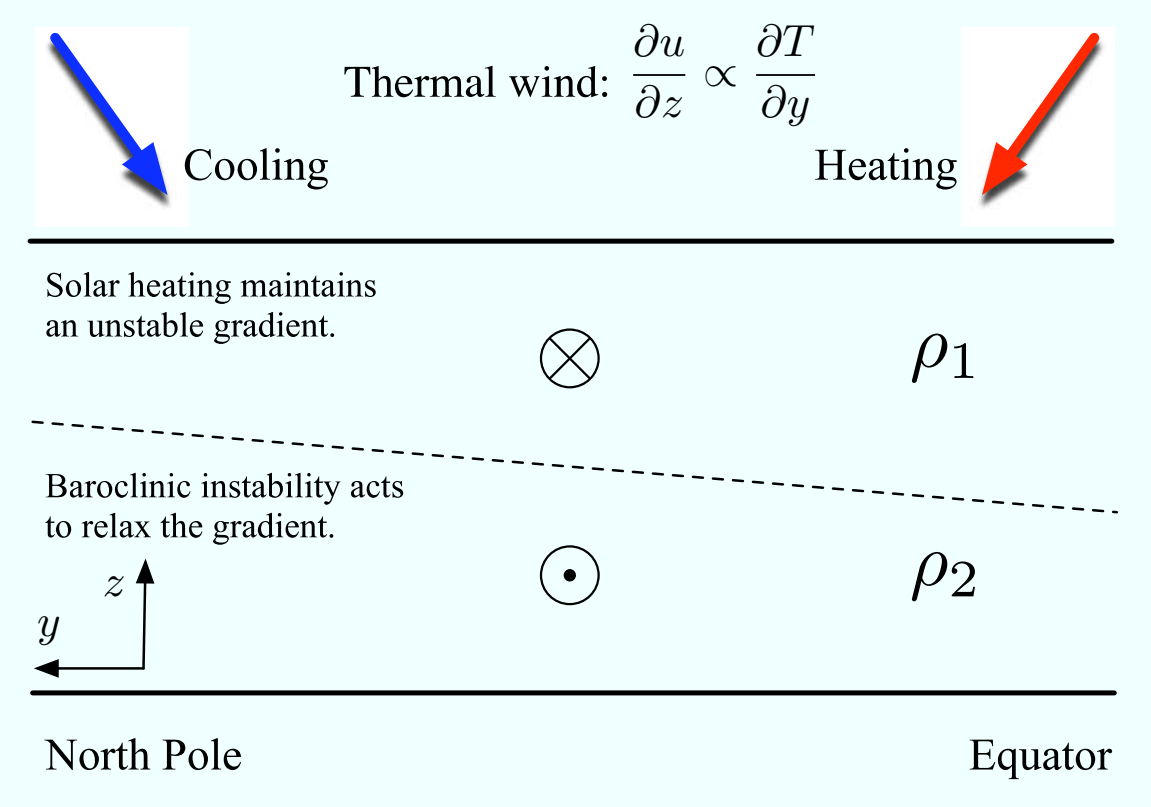

Figure I.1: Schematic of a baroclinically unstable flow. Differential heating in the meridional direction leads to sloping isopycnals and a vertically sheared zonal flow through the thermal wind relationship. Potential energy stored in the sloping isopycnals is released through baroclinic instability, which generates eddies comparable in size to the deformation radius.

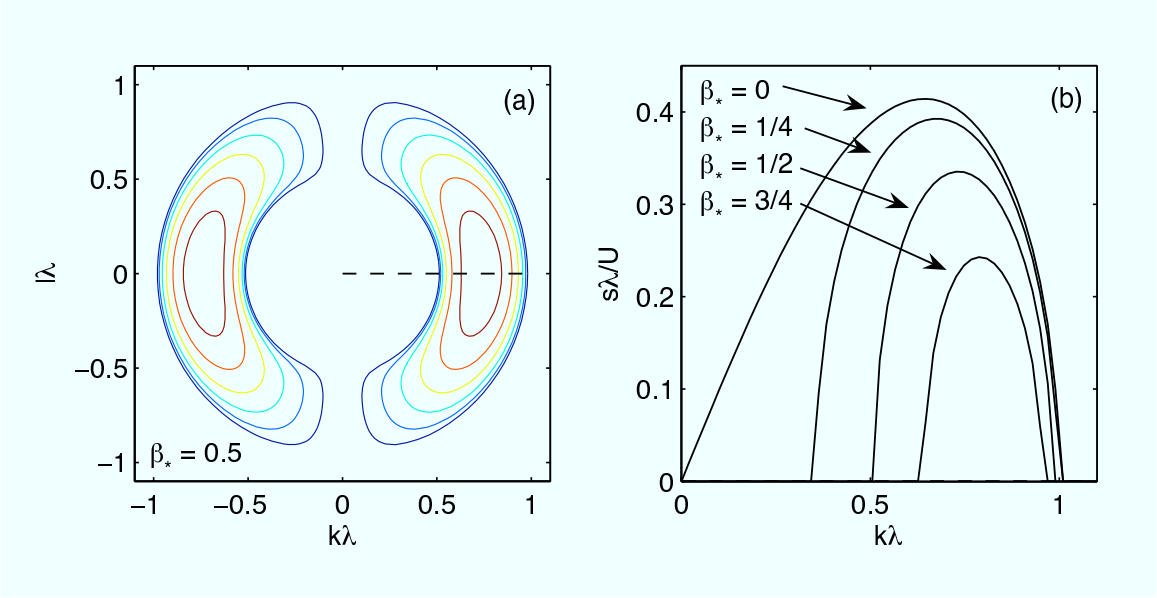

Figure I.2: (a) Contours of the linear baroclinic instability growth rate $s\lambda/U$ as a function of zonal $k\lambda$ and meridional $l\lambda$ wavenumbers with $\beta_* = \beta\lambda^2/U = 1/2$. Here λ is the deformation radius and $2U$ is the vertical shear between upper and lower layers. The fastest growing mode occurs along $l\lambda = 0$ (meridional bands). Panel (b) shows the growth rate along the line $l\lambda = 0$ for four different values of β_*. In the absence of friction, the critical value for instability is $\beta_* = 1$.

baroclinically unstable. The linear baroclinic instability problem was characterized by Eady (1949), who showed that a rotating fluid with a constant vertical shear is unstable at all wavenumbers up to a large wavenumber cutoff. Charney (1947) presented a more realistic model of baroclinic instability by including the planetary vorticity gradient, or the β effect, in his calculations. Charney found that β has a stabilizing influence at low wavenumbers, such that instability only occurs if a critical vertical shear $U_c = 2\beta\lambda^2$ is exceeded, where λ is the deformation radius. The linear instability is summarized in Figure I.2.

Growth of the instability is eventually saturated through frictional processes. In the numerical model, this is accomplished through a linear Ekman drag acting on the lower layer. The resulting statistically steady state is turbulent and eddy statistics are calculated by averaging over both space and time to remove turbulent fluctuations. Besides saturating the instability, bottom friction may also

act to destabilize the baroclinic system at values of β that would otherwise be stable (Holopainen 1961). Thus, we find that bottom friction plays a crucial role in the equilibrated heat flux.

I.2 Eddy flux theories

Because of the strong effects of rotation and stratification, geophysical flows behave similarly to two-dimensional flows, including the characteristic turbulent cascade of energy to large scales. Rhines (1977) and Salmon (1980) characterize the energy transfers in baroclinic turbulence as a direct transfer of energy in the baroclinic mode with a simultaneous inverse cascade of the barotropic mode. This scenario, referred to here as the "dual cascade," is summarized in Figure I.3. Energy enters at large scales in the baroclinic mode through solar heating and undergoes a direct cascade to the deformation radius. Deformation-scale eddies generated through baroclinic instability energize the barotropic mode (Larichev & Held 1995), and initiate an inverse cascade that is ultimately halted by bottom friction. The β effect may also modify the isotropic view of the inverse cascade shown in Figure I.3.

The dual cascade scenario has been used as a framework to derive parameterizations for the meridional eddy heat flux in baroclinic systems (Larichev & Held 1995, Held & Larichev 1996, Lapeyre & Held 2003). These models rely on the assumption that energy supplied by large-scale differential heating makes its way to small scales in the barotropic mode before undergoing an inverse cascade. Thus the inverse cascade rate is equivalent to the dissipation, similar to the purely barotropic model of Smith *et al.* (2002). The theory is closed by identifying a wavenumber that represents the halting scale of the inverse cascade (k_0 in Figure I.3). This wavenumber may depend on bottom friction (Larichev & Held 1995), β (Held & Larichev 1996, Lapeyre & Held 2003) or both (Danilov & Gurarie 2002).

We test recent eddy flux parameterizations with results from our numer-

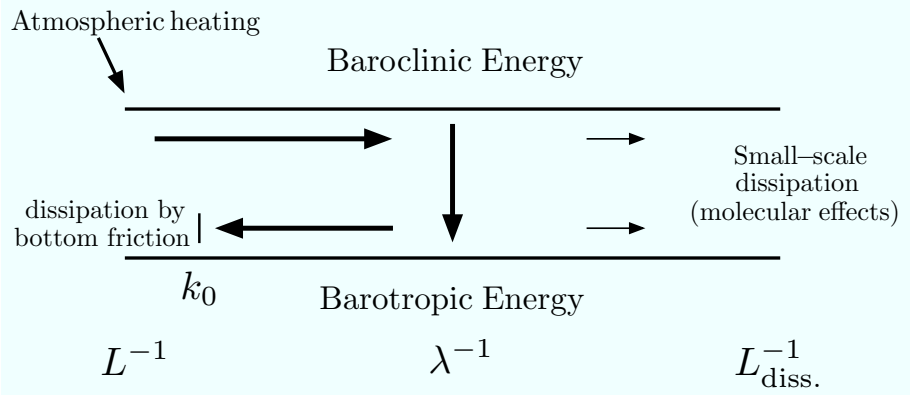

Figure I.3: Schematic of the "dual cascade" view of energy transfers in baroclinic turbulence (Rhines 1977, Salmon 1980). Energy enters in the form of potential energy in the baroclinic mode due to differential solar heating. There is a direct cascade of energy in the baroclinic mode. Transfer to the barotropic mode occurs near the deformation radius through baroclinic instability. Energy then undergoes an inverse cascade in the barotropic mode until it is removed through large scale dissipation, such as Ekman drag. The β effect may also alter this isotropic view of the barotropic inverse cascade at large scales.

ical simulations in Chapters II and III. We find that parameterizations based on Kolmogorovian spectral cascades are inaccurate over a broad region of parameter space.

Eddy flux theories dependent on energy cascade arguments make little contact with the physical reality that QG turbulence is dominated by coherent structures. Simulations with $\beta = 0$ and sufficiently large bottom friction contain many coherent vortices (see Figure II.3(d))[1]. These structures have opposite signed potential vorticity in the upper and lower layers, which is the defining feature of a heton (Hogg & Stommel 1985). Because of bottom drag, however, the lower layer vortex is always weaker than its upper layer counterpart. These vortex pairs are not strongly self-propelled, but rather the pair is advected by the far-field velocity of other hetons.

These observations motivate a description of the fluid as a "gas" con-

[1]For simulations with very weak bottom friction, there is nothing to halt the inverse cascade and eddies grow to the domain size. In these simulations, there are only one or two large eddies in the domain and eddy statistics are not meaningful.

taining many baroclinic vortices (similar to the model of Carnevale *et al.* 1991). Through this model we relate vortex-core values of important descriptors such as the temperature and the vorticity to domain-averaged values. These scalings are combined with relationships derived from statistically steady invariants of the system, namely the energy balance and the cross-invariant (a special case of the enstrophy balance), to form the basis of a vortex-centric theory for the eddy heat flux. The vortex gas scalings are discussed in Chapter II and are verified with a vortex census algorithm described in Appendix B. A semi-empirical formula for the eddy heat flux is given solely in terms of external parameters of the system and is shown to be an improvement over earlier predictions in the literature.

I.3 β and zonal jets

Variations in the Coriolis parameter with latitude caused by planetary curvature, or the β-effect, affect geophysical flows by introducing an anisotropy that results in the spontaneous generation of zonal jets. Zonal jets are a persistent feature on many of the large planetary atmospheres, especially Jupiter and Saturn (Vasavada and Showman 2005). Figure I.4 shows a photograph of at least eight stable jets in Jupiter's atmosphere taken from the Cassini satellite on a recent flyby. Because of the Earth's smaller radius, the terrestrial atmosphere is limited to a single meandering jet stream in each hemisphere. There is, however, increasing evidence that zonal jets are abundant in the ocean basins. These oceanic jets have been identified in numerical simulations (Richards *et al.* 2006) as well as in sea surface height anomalies from satellite altimetry (Maximenko *et al.* 2005). Since the deformation radius is at least an order of magnitude smaller in the ocean than in the atmosphere, oceanic jets have meridional scales as small as three degrees of latitude allowing many jets within a single ocean basin.

Zonal jets are characterized by an asymmetry between eastward (narrow and fast) and westward (broad and slow) regions (Panetta 1993). In the baroclinic

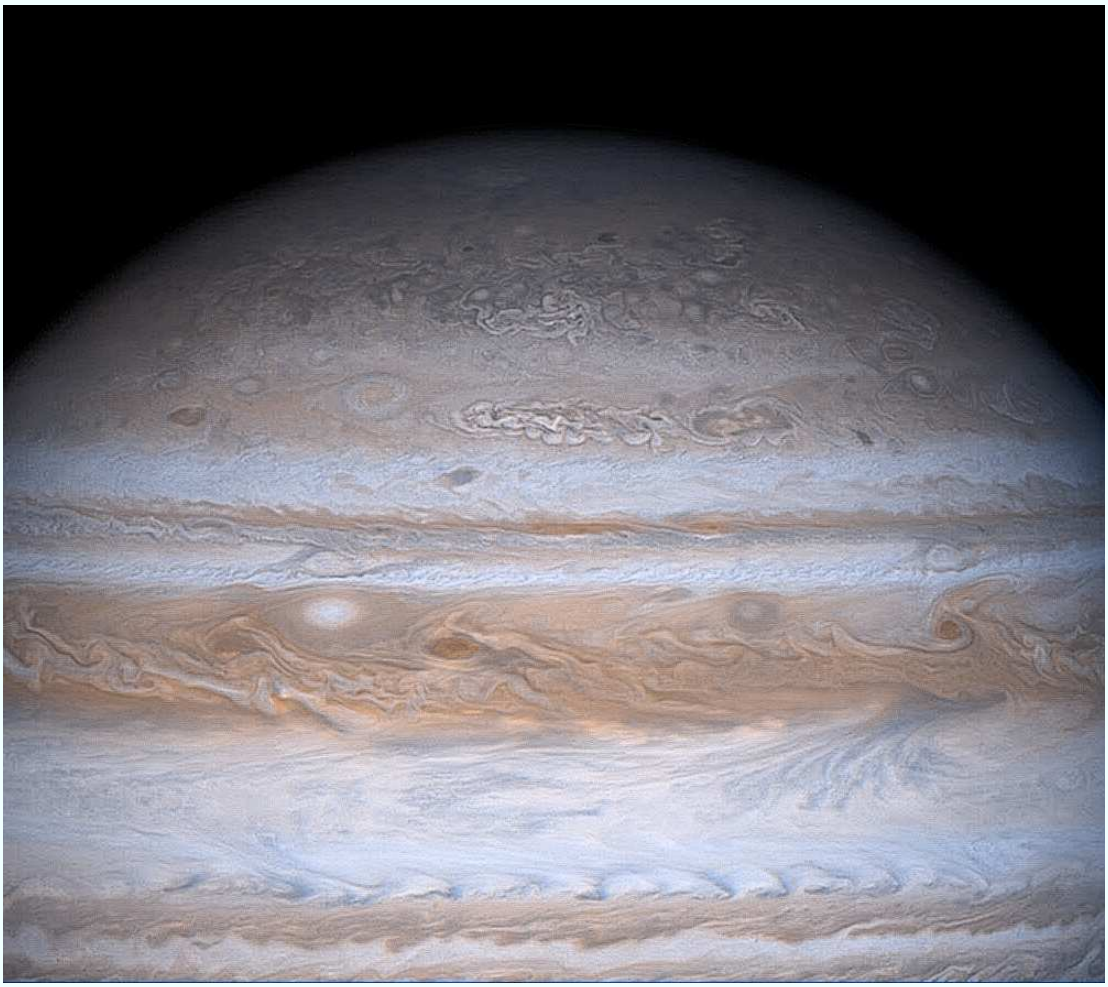

Figure I.4: Photograph of zonal jets on Jupiter as taken by the Cassini satellite. The banded structure marks regions of intense jet streams that reach speeds of nearly 500 kilometers per hour. Vortex-like atmospheric storms embedded within the jets are sheared apart as they move out towards the jet edges. This photo was obtained from NASA's Jet Propulsion Laboratory website: www.jpl.nasa.gov/jupiterflyby.

system, the vertical shear is largest within the rapid eastward flowing regions and therefore baroclinically unstable eddies grow fastest here. The growth of these eddies is the same process produces atmospheric storms (strong baroclinic eddies) within in the Earth's jet stream. In this way, zonal jets in the numerical simulations act like "storm tracks" as described by Chang *et al.* (2002).

Robinson (2006) has shown that baroclinic eddies are primarily responsible for the remarkable persistence of midlatitude jets in the Earth's atmosphere. Robinson's work follows other recent studies (Huang & Robinson 1998, Manfroi & Young 1999, Dritschel *et al.* 2006) that explain the "self-maintanence" of zonal jets in terms of a negative viscosity (Starr 1968, McIntyre 1970) that forces the zonal mean flow. Eddies generated during baroclinic instability meander onto the flanks of the jets where the zonal flow shears the eddies. This gives rise to non-zero Reynolds stresses that transfer energy from the eddy component into the zonal mean flow[2]. This process is described in detail in Chapter IV. The system may reach equilibrium, i.e. the negative viscosity effects are saturated, if damping is introduced, typically in the form of large-scale bottom drag.

The introduction of β also modifies the dual cascade scenario as shown in Figure I.3. β-plane flows are subject to both wavelike and turbulent motions (Rhines 1975), with the transition between regimes occurring at the Rhines scale ℓ_R, where

$$\ell_R \sim \sqrt{\frac{\mathcal{U}}{\beta}}\,. \tag{I.1}$$

Here, ℓ_R is a natural length scale arising from β and a velocity scale $\mathcal{U}$, where Rhines (1975) takes $\mathcal{U}$ to be the total RMS velocity, including both zonal and eddy components of the flow. Rhines further suggests that β halts the barotropic inverse cascade at wavenumber $k_\beta^{\mathrm{Rh}} = \ell_R^{-1}$. Vallis and Maltrud (1993) pursued this idea and make the important observation that at small wavenumbers, where

[2]In our two-layer simulations we find that the Reynolds stresses are only significant in the upper layer. Transfer between upper and lower layers occurs primarily through a form drag interaction.

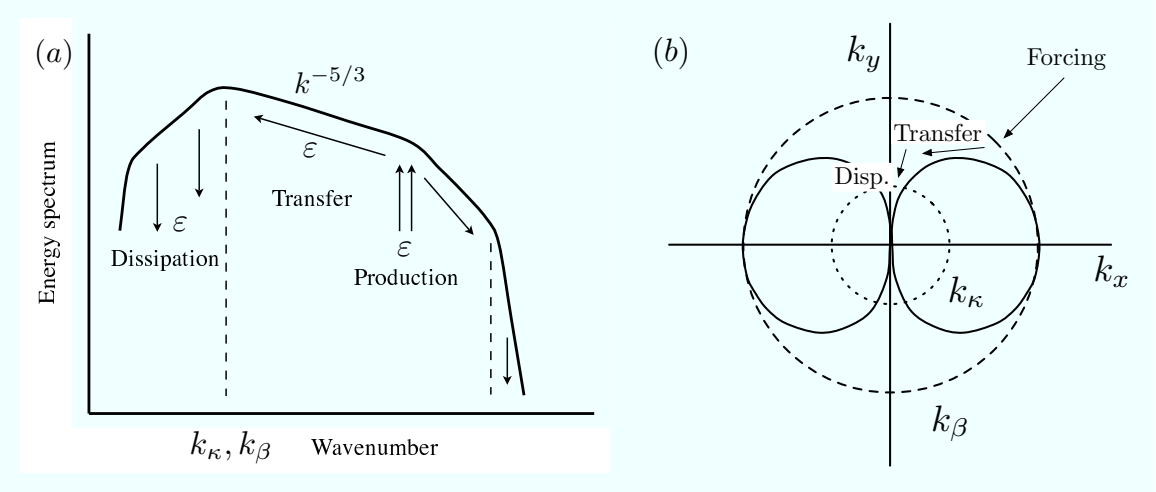

Figure I.5: (a) Sketch of an idealized isotropic inverse cascade. The spectrum is forced at large wavenumbers and is transferred upscale with a characteristic slope of $k^{-5/3}$. Energy is eventually removed by bottom friction at scales $k < k_\kappa$ or anisotropy develops at $k = k_\beta$. (b) A sketch of the anisotropic inverse cascade as described by Vallis & Maltrud (1993). At high wavenumbers the cascade is isotropic. At k_β, marked by the dashed curve, energy is preferentially channelled into zonal modes and is eventually dissipated at scales $k < k_\kappa$, marked by the dotted curve. For cases where $k_\kappa > k_\beta$, the inverse cascade is halted before strong zonal jets can develop. There is a dumbbell-shaped region (solid curves) within which there is little energy (see also Figure IV.10).

the β-effect is important, the inverse energy cascade can no longer be represented by an isotropic spectrum (Figure I.5(a)). Instead, Vallis & Maltrud (1993) argue that two-dimensional spectra will exhibit a dumbbell-shaped region centered along the x-axis that is devoid of energy. This occurs because at a certain transition wavenumber k_β, the formation of Rossby waves slows the inverse cascade and energy is channelled into zonal modes perpendicular to the restoring force of β. Figure I.5(b) shows a sketch of the energy transfers in the anisotropic case.

The exact value of k_β has been a source of controversy and confusion for the past 20 years. Besides the wavenumber associated with the Rhines scale, k_β^{Rh}, Vallis and Maltrud (1993) suggest that k_β is determined by the length scale derived from the energy cascade rate ε and β, or $k_\beta^{\mathrm{VM}} = (\beta^3\varepsilon)^{1/5}$. Holloway and Hendershott (1977) offer a third possibility for k_β, where now the balance is

between β and the RMS barotropic vorticity, $k_\beta^{\mathrm{HH}} = \beta/\sqrt{\langle\zeta^2\rangle}$, where $\langle\rangle$ indicates both a spatial and temporal average. These three length scales are all distinct, and further ambiguity arises as to whether the velocity $\mathcal{U}$ and vorticity ζ scales should be comprised of eddy components, zonal components or both.[3]

Regardless of the exact definition of k_β, this wavenumber still represents a terminus for the *isotropic* inverse cascade of the barotropic mode, and is typically a crucial part of eddy flux parameterizations. Still, while β clearly affects the inverse cascade, β does not dissipate energy and thus cannot halt the inverse cascade alone. Bottom drag dissipates energy in zonal and eddy components and is ultimately responsible for halting the inverse cascade.

Although bottom friction is crucial for obtaining an equilibrated steady state, few studies have considered the combined effect of β and bottom friction on the eddy heat flux of β-plane turbulence. Danilov & Gurarie (2002) propose frictional, $k_\kappa^{\mathrm{DG}} \sim \kappa^{3/2}\varepsilon^{-1/2}$, and β wavenumbers, $k_\beta^{\mathrm{DG}} \sim \beta^{1/2}\kappa^{1/4}\varepsilon^{-1/4}$, where κ is the coefficient of bottom friction, which they use to determine the transition between friction-dominated and β-dominated flow. Smith *et al.* (2002) provide a scaling for the turbulent eddy diffusivity[4] in terms of both β and κ for a barotropic system, however, the different method of forcing used in this study makes it difficult to adapt this model to the baroclinic system (see discussion in Chapter III). Finally, Held & Larichev (1996) and Lapeyre & Held (2003) propose that the baroclinic eddy heat flux is independent of bottom friction when β is strong.

Chapter III presents a suite of 110 statistically equilibrated simulations of baroclinic turbulence, which indicates that over most of parameter space bottom

[3]The transition wavenumber k_β (usually in the guise of the Rhines scale k_β^{Rh}) has also been touted as being equivalent to the inverse of the jet spacing. While there are no numerical simulations that clearly support the Rhines scale as defined in (IV.3) as the jet spacing (Vallis 2006, personal communication), a recent prediction by Dritschel *et al.* (2006) propose jet spacing $\sim$ max.$\left(\ell_R, \ell_R^2/\lambda\right)$. In the baroclinic system, the most thorough study to date has been conducted by Panetta (1993), who showed that the Rhines scale does indeed predict the jet length *if* the velocity scale is taken to be twice the square root of the total eddy kinetic energy. In Chapter IV we verify Panetta's (1993) prediction with our suite of numerical simulations.

[4]The turbulent eddy diffusivity is defined to be the eddy flux divided by minus the large-scale gradient.

friction does influence both the eddy heat flux and the structure of the zonal jets. The results of Chapter III suggest that the importance of the baroclinic mode in the total dissipation by bottom drag and in the transfer of energy between the eddy and zonal mean flow is not properly captured by energy cascade arguments.

Another failing of previous cascade theories is that they do not explicitly account for the zonal flows which are characteristic of β-plane turbulence. Chapter IV is primarily a descriptive account of both the zonal jets and the large-scale stationary eddies in the baroclinic simulations. A "phenomenological" model of baroclinic turbulence that incorporates these structures is the focus of ongoing work.

I.4 Diapycnal mixing and the Southern Ocean

Eddy fluxes arising from baroclinic instability are an integral part of horizontal transports in the atmosphere and ocean. An understanding of *vertical* transport processes is equally important in developing accurate circulation models. In the ocean, diapycnal (cross-density surface) mixing is an essential element of the thermohaline circulation. The thermohaline circulation results from downwelling at a few isolated locations in the Nordic, Labrador and Weddell Seas and upwelling throughout the rest of the ocean basins. Upwelling occurs through mixing events, such as internal wave breaking, which happen over temporal and spatial scales that are too small to be resolved directly by numerical simulations. GCMs thus rely on parameterizations to incorporate the effects of small-scale diapycnal mixing. Improving these parameterizations remains an active area of research.

Munk (1966) first suggested that wide-spread small-scale diapycnal mixing could close the thermohaline circulation. Assuming spatially-uniform mixing, Munk employed a one-dimensional advection-diffusion model to conclude that a turbulent diapycnal diffusivity $\kappa_\rho = 10^{-4}$ m^2 s^{-1} was necessary to balance downwelling at high latitudes. The first indirect estimates of ocean mixing by Osborn

& Cox (1972) and Osborn (1980), however, reported diffusivities an order of magnitude smaller than Munk's prediction. Eventually direct tracer release studies (Toole *et al.* 1994) confirmed open ocean diffusivities of 10^{-5} m^2 s^{-1}. Many studies have since shown that mixing is not uniform (Munk & Wunsch 1998, Wunsch & Ferrari 2004); instead, enhanced mixing occurs in regions close to sharp topographical features such as islands and ocean ridges (Polzin *et al.* 1997, Klymak *et al.* 2006). It remains uncertain whether these localized mixing "hot spots" are sufficient to close the thermohaline circulation. Limited sampling in polar regions due to harsh weather conditions continues to contribute to this uncertainty.

Characterization of diapycnal mixing in the Southern Ocean is of further interest because of the region's unique properties. Isopycnals outcrop in the Southern Ocean making deep and intermediate waters susceptible to wind and buoyancy forcing at the surface. Outcropping isopycnals have been identified as potential sites of large atmospheric uptake, implying that the Southern Ocean provides one of the first signals of rapid and anthropogenically-forced climate change (Banks *et al.* 2000, Gille 2002). Vertical mixing also helps regulate the conversion of Deep Water into Sub-Antarctic Mode Water[5] (Speer *et al.* 2000), which is then exported to the three major ocean basins. Thus, the Southern Ocean has a large influence on the transport of heat and other tracers throughout the globe and its inclusion in GCMs is essential.

While the Antarctic Circumpolar Current (ACC) is primarily characterized by a strong zonal flow, the ACC's "residual" meridional circulation is an important means of transporting heat and other tracers across lines of latitude. The residual circulation is thought to be driven by near-surface Ekman flow and mesoscale eddies generated by baroclinic instability (Karsten & Marshall, 2002). The role of diapycnal mixing in this circulation, however, is still poorly understood

[5]Toggweiler & Samuels (1995, 1998) argue that the conversion of North Atlantic Deep Water, through diapycnal mixing in the Southern Ocean, reduces the magnitude of the globally-averaged diapycnal diffusivity needed to close the thermohaline circulation. This would explain the small magnitude of mixing rates in the open ocean and eliminate the "missing mixing" problem.

(Figure I.6).

Numerical and theoretical models by Karsten *et al.* (2002) and Bryden & Cunningham (2003) assume that mixing in the Southern Ocean occurs primarily along isopycnals, and diapycnal exchanges are limited to surface processes. A recent numerical study by Cessi & Fantini (2005), though, suggests that diapycnal mixing plays a prominent role in determining the depth of the thermocline and the deep stratification of the Southern Ocean. An improved understanding of the interaction between diapycnal mixing and meridional eddy fluxes is needed and provides a natural connection between the two topics covered in this disseration.

While direct measurements of diapycnal mixing in the Southern Ocean obtained from microstructure profilers are just now becoming available, recent studies (Kunze 2003, Naveira Garabato *et al.* 2004, Sloyan 2005, see discussion in section V.2) infer diapycnal mixing rates from "outer turbulence" scales, or finescale structure, $O(1$ m). Chapter V also presents a study of turbulent mixing rates inferred from finescale data. Measurements are made in the upper 1000 m throughout Drake Passage, which is an important choke point of the ACC and a region subject to intensified mixing over sharp topographical features (Naveira Garabato *et al.* 2004).

Since 2002, temperature and salinity profiles from XCTD (expendable conductivity, temperature and depth) probes have been collected by the U.S. Antarctic Supply Vessels travelling between Punta Arenas, Chile and Palmer Station, Antarctica as part of SIO's High Resolution XBT/XCTD Network. The purpose of the sampling, which occurs between four and six times per year, is to monitor seasonal and interannual change in upper ocean properties across Drake Passage. The XCTD data set is unique in that it provides one of the few studies where mixing measurements have been made in the same location over a long period of time. A full discussion of the sampling characteristics of the XCTD appears in Chapter V.

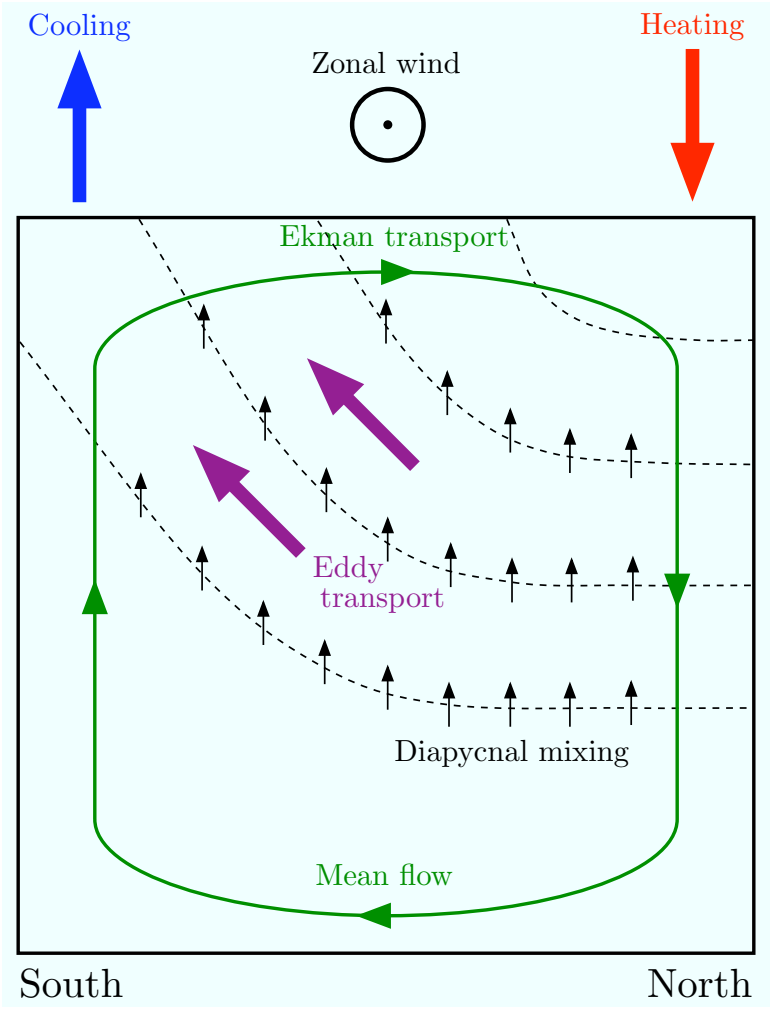

Figure I.6: Schematic of the meridional circulation in the Antarctic Circumpolar Current (ACC), based on Karsten *et al.*'s (2002) Figure 1. The strong eastward zonal wind drives a northward Ekman transport (green curve). Differential heating across the ACC also generates sloping isopycnals and mesoscale eddies through baroclinic instability (see also Figure I.1). Transport by these eddies balances the Ekman transport to a large extent; the resulting residual circulation is discussed by Karsten & Marshall (2002). Most models of the ACC's residual circulation neglect sub-surface diapycnal exchanges. However Cessi & Fantini (2005) find that sub-surface mixing may have an important influence on meridional transport in the ACC.

I.5 Mixing parameterizations

In Chapter V we use two independent methods of estimating diapycnal mixing from outer turbulence scales, (1) Thorpe scales and (2) vertical strain spectra. These two methods are discussed in some detail in section V.3, and therefore will be sketched only briefly here.

The Ozmidov scale L_O is defined as

$$L_O = \varepsilon^{1/2} N^{-3/2} , \tag{I.2}$$

where ε is the dissipation rate of turbulent kinetic energy and N is the buoyancy frequency. L_O is the scale at which inertial and buoyancy effects are comparable. Unfortunately ε is expensive to measure directly because it requires cm-scale resolution. The Thorpe scale L_T (Thorpe 1977), on the other hand, is a related length scale that indicates the size of density inversions in a stratified fluid. Figure I.7 summarizes the calculation of L_T. Dillon (1982) and others have shown that L_O is linearly proportional to L_T, although the constant of proportionality may vary depending on the mixing environment. Thus, turbulent dissipation can be calculated with an estimate L_T, which only requires finescale measurements.

An alternative method for inferrring mixing rates comes from evidence that ocean mixing is related to the energy density of the internal gravity wave field. Nonlinear wave-wave interactions transfer energy and momentum to increasingly smaller-scale waves, which are more likely to break down into turbulence. The hypothesis, then, is that tractable formulas exist that relate differences between observed energy spectra and the energy spectrum of a canonical internal wave field (Garrett & Munk 1975) to the mixing rate of the sampled region (Henyey *et al.* 1986). The spectral method is based on larger scales than the Thorpe scale method and thus does not require as fine resolution. It also provides an estimate of mixing rates independent of the Thorpe scale estimate.

While the turbulent dissipation of kinetic energy ε in the ocean is the ac-

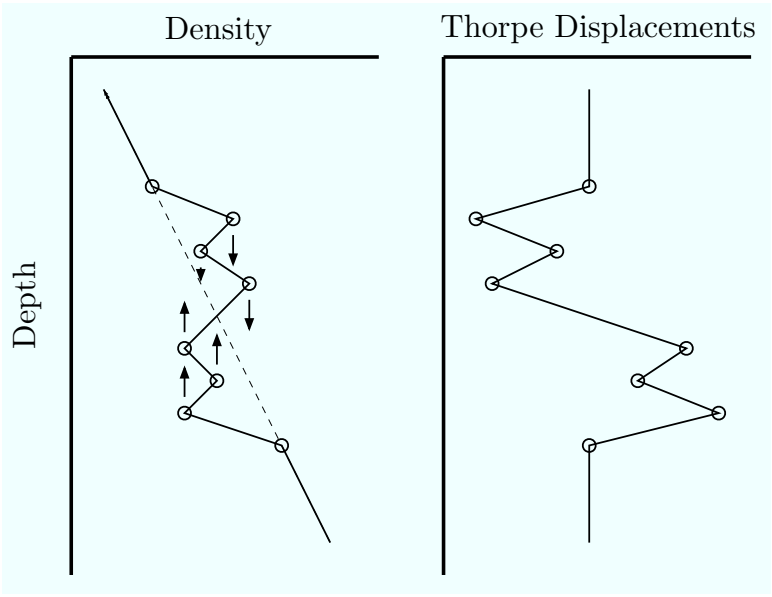

Figure I.7: Schematic of the Thorpe scale L_T derived from a density inversion in an otherwise stable potential density profile. Observations within an inversion are rearranged vertically to achieve a stable, monotonic profile. A sample moved from a depth z_n to a depth of z_m has a Thorpe displacement $d'_n = z_m - z_n$. The Thorpe scale L_T is the RMS value of the Thorpe displacements $L_T = \left\langle d'^2 \right\rangle^{1/2}$, where $\langle\rangle$ represents an average over a single overturn.

tual quantity of interest, ε is often converted to a diapycnal eddy diffusivity κ_ρ as a parameterization of small-scale mixing in numerical simulations. A thorough discussion of how to calculate κ_ρ from turbulent dissipation appears in Moum (1990) and is summarized in Ferron *et al.* (1998). Briefly, the extraction of turbulent kinetic energy from the mean kinetic energy P is balanced by the conversion of turbulent kinetic energy to potential energy B and dissipation of turbulent kinetic energy ε such that

$$P = B + \varepsilon \,. \tag{I.3}$$

The turbulent diffusivity κ_ρ arises from the assumption that a diffusive parameterization can be used to approximate the vertical density flux $w'\rho'$,

$$B = \frac{g}{\rho_0} \langle w'\rho' \rangle = N^2 \kappa_\rho \,, \tag{I.4}$$

where primes denote eddy quantities, N is the buoyancy frequency and $\langle\rangle$ represents an average over turbulent fluctuations. Using (I.3) and (I.4) and introducing the Richardson flux number $R_f = BP^{-1}$, yields

$$\kappa_\rho = \Gamma \varepsilon N^{-2} \,, \tag{I.5}$$

as proposed by Osborn (1980). Here $\Gamma = R_f/(1 - R_f)$, which is typically taken to be a constant equal to 0.2. A discussion of the proper estimate of N from the data is given in Chapter V.

II

Scaling baroclinic eddy fluxes: vortices and energy balance

II.1 Abstract

The eddy heat flux generated by the statistically equilibrated baroclinic instability of a uniform, horizontal temperature gradient is studied using a two-mode f-plane quasigeostrophic model. An overview of the dependence of the eddy diffusivity, D, on the bottom friction κ, the deformation radius λ, the vertical variation of the large-scale flow U and the domain size L is provided by numerical simulations at 70 different values of the two non-dimensional control parameters $\kappa\lambda/U$ and L/λ.

Strong, axisymmetric, well-separated baroclinic vortices dominate both the barotropic vorticity and the temperature fields. The core radius of a single vortex is significantly larger than λ, but smaller than the eddy mixing length $\ell_{\rm mix}$. On the other hand, the typical vortex separation is comparable to $\ell_{\rm mix}$. Anti-cyclonic vortices are hot, and cyclonic vortices are cold. The motion of a single vortex is due to barotropic advection by other distant vortices, and the eddy heat flux is due to the systematic migration of hot anti-cyclones northward and cold cyclones southwards. These features can be explained by scaling arguments and an analysis of the statistically steady energy balance. These arguments result in a relation between D and $\ell_{\rm mix}$. Earlier scaling theories based on coupled Kolmogoro-

vian cascades do not account for these coherent structures and are shown to be unreliable.

All the major properties of this dilute vortex gas are exponentially sensitive to the strength of the bottom drag. As the bottom drag decreases both the vortex cores and the vortex separation become larger. Provided that $\ell_{\rm mix}$ remains significantly smaller than the domain size, then local mixing length arguments are applicable, and our main empirical result is $\ell_{\rm mix} \approx 4\lambda \exp(0.3U/\kappa\lambda)$.

II.2 Introduction

Eddy heat and potential vorticity fluxes are part of a dynamical balance in which potential energy created by differential heating is released through baroclinic instability. Many theoretical and numerical studies have attempted to find physically plausible parameterizations of these eddy fluxes so that turbulent transport can be included in coarsely resolved climate models. Pioneering attempts used linear theory to describe the eddy structure and energy arguments to constrain the eddy amplitude (Green 1970, Stone 1972). More recently, though, fully non-linear numerical realizations of homogeneous quasi-geostrophic turbulence have been used to diagnose eddy fluxes in a statistical steady state maintained by imposing a uniform temperature gradient (Haidvogel & Held 1980; Hua & Haidvogel 1986; Larichev & Held 1995; Held & Larichev 1996; Smith and Vallis 2002; Lapeyre & Held 2003). The grail is a physically motivated relation between the eddy heat flux and control parameters, such as the imposed large-scale thermal gradient. Provided that there is scale separation between the mean and the eddies, the resulting flux-gradient relation might apply approximately to a spatially inhomogeneous flow. In other words, the hypothesis is that baroclinic eddy fluxes can be parameterized by a turbulent diffusivity, D, which might, however, depend nonlinearly on the large-scale temperature gradient (e.g., Pavan & Held 1996).

Our first goal in this work is largely descriptive: we characterize the de-

pendence of D on external parameters such as the domain size L, the bottom drag coefficient κ, the Rossby deformation radius λ, and the imposed velocity jump $2U$. Our notation is introduced systematically in Appendix A and is largely the same as that of Larichev & Held (1995, hereafter LH95): $\tau(x, y, t)$ and $\psi(x, y, t)$ are the disturbance streamfunctions of the baroclinic and barotropic modes respectively. A precise definition of the eddy diffusivity, D, is then

$$D \equiv U^{-1} \langle \psi_x \tau \rangle \ . \tag{II.1}$$

Here $\langle\rangle$ denotes both a horizontal average over the square $2\pi L \times 2\pi L$ domain, and an additional time average to remove residual turbulent pulsations.

$\langle \psi_x \tau \rangle$ in (II.1) is the product of the barotropic meridional velocity, ψ_x, and the thermal field τ i.e., the meridional heat flux is proportional to $\langle \psi_x \tau \rangle$. Moreover, the mechanical energy balance in a statistically steady state (see Appendix A) is

$$U\lambda^{-2} \langle \psi_x \tau \rangle = \kappa \left\langle |\nabla\psi - \sqrt{2}\nabla\tau|^2 \right\rangle + hyp\nu \,, \tag{II.2}$$

where "$hyp\nu$" indicates the hyperviscous dissipation of energy. The first term on the right hand side of (III.2) is the mechanical energy dissipation (Watts per kilogram) by bottom drag, κ. The left hand side of (III.2) is the energy extracted from the unstable horizontal temperature gradient by baroclinic instability. Enstrophy budgets also identify $\langle \psi_x \tau \rangle$ as the large-scale source balancing the hyperviscous enstrophy sink at high wavenumbers. Thus a single quantity, conveniently defined as D in (II.1), summarizes all of the important quadratic power integrals and fluxes in homogeneous baroclinic turbulence.

Dimensional considerations (Haidvogel & Held 1980) show that

$$D = U\lambda \times D_* \left(\frac{\lambda}{L}, \frac{\kappa\lambda}{U}, \frac{\nu}{UL^7} \right) \ , \tag{II.3}$$

where D_* is a dimensionless function. The final argument of D_*, involving the hyperviscosity ν, is small (see section II.8). For brevity we suppress reference to this hyperviscous parameter. In Figure II.1 we summarize a panoramic set of

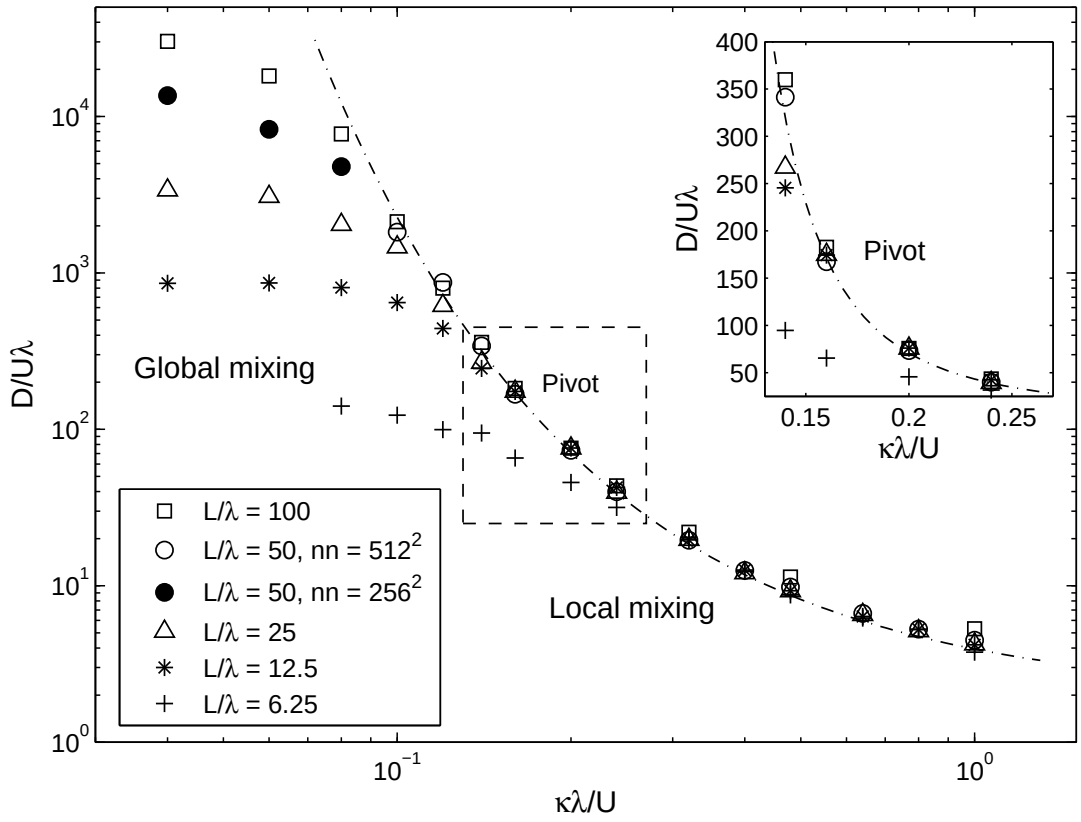

Figure II.1: A summary of eddy diffusivity, $D/U\lambda$, for 70 simulations. The smooth curve is $D_{\rm EB}^{\rm loc}$ in (II.31). At the pivot, simulations with L/λ varying by a factor of 8 have nearly the same value of $D/U\lambda$. As summarized in Table II.1, the resolution was held constant for each series of simulations, except for the series with $L/\lambda = 50$. In that series limited computer resources forced us to reduce the resolution from $\circ = 512^2$ to $\bullet = 256^2$ (see section II.8 for details).

numerical simulations revealing the main features of the function $D_*(\lambda/L, \kappa\lambda/U)$. D_* varies by over a factor of one thousand in response to much smaller changes in $\kappa\lambda/U$ and L/λ: there is plenty of scope for relatively crude scaling arguments to collapse this data. Finding this scaling is not entirely straightforward because there is not a convincing straight line anywhere in the loglog plot of Figure II.1. This is the first indication that the function D_* is not adequately characterized as a power law.

Classical theories of baroclinic turbulence (Rhines 1977; Salmon 1978,

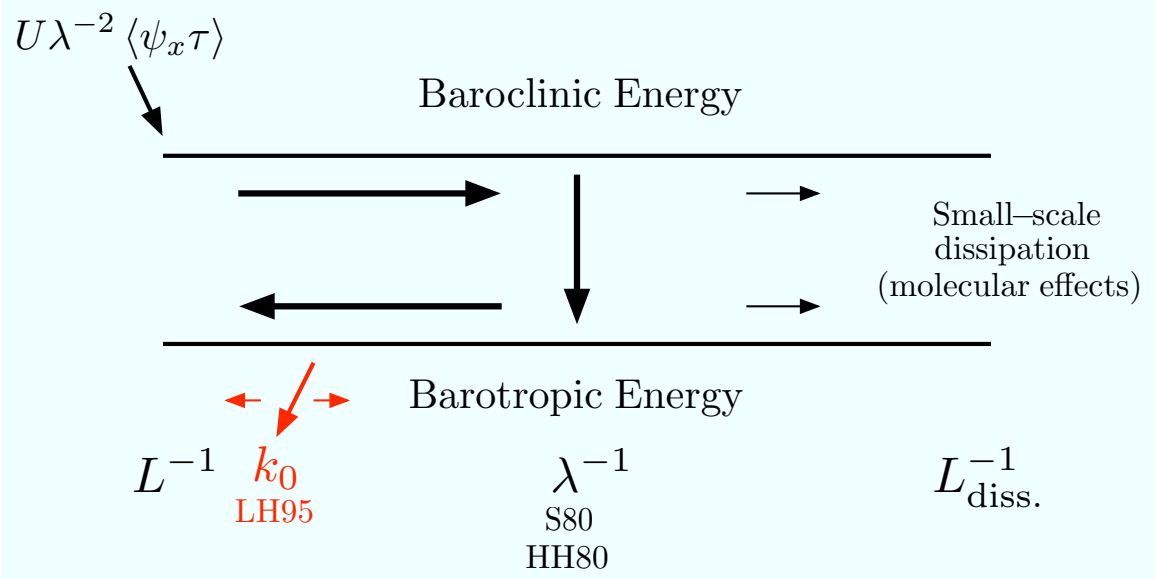

Figure II.2: Diagrammatic summary of the dual-cascade scenario (adapted from Salmon 1980). Baroclinic energy enters the system at scales comparable to the domain size, L, via differential heating. Baroclinic energy is then transfered to higher wavenumbers in a direct cascade. In the classical view (S80 and HH80), energy transfers from the baroclinic to the barotropic mode at the deformation wavenumber, $k \sim \lambda^{-1}$, and barotropic energy then cascades back to larger scales and is ultimately removed by bottom drag. LH95 revised this picture by showing that the wavenumber where energy is removed is correlated with energy production and the associated potential vorticity fluxes. LH95 identified this length scale k_0^{-1} as that of the energy-containing eddies and suggested that its location in the spectrum varied strongly with bottom drag.

1980; Haidvogel & Held 1980) argue that energy is created at large scales by differential heating and then cascades downscale to the Rossby deformation radius. Baroclinic energy is then converted to barotropic near the deformation radius, and the barotropic mode undergoes an inverse cascade until energy is removed by bottom drag. The dual-cascade scenario, summarized in Figure II.2, supposes that $L \gg \lambda$ so that there is spectral room for the cascades to operate. This regime, with the domain scale greatly exceeding the Rossby deformation radius, is also oceanographically relevant.

Early studies of baroclinic turbulence assumed that the mixing-length of baroclinic eddies was comparable to λ. In these circumstances, Haidvogel & Held (1980, hereafter HH80) argued that eddy statistics should be independent of the domain scale L. Varying the parameter L/λ between 7 and 15, HH80 provided evidence in support of this hypothesis. The data in Figure II.1 spans a significantly larger range of L/λ than does HH80, and further supports their conclusion that D is independent of L *provided* that $\kappa\lambda/U$ is not too small.

The proviso is necessary because Figure II.1 clearly shows an important distinction between two regimes: local mixing and global mixing. The local regime is exemplified by the point marked "pivot" in Figure II.1 (where $\kappa\lambda/U = 0.16$). At the pivot, four simulations with L/λ varying by a factor 8 have nearly the same D. The four pivot solutions exemplify the "local-mixing regime" of HH80, within which D is independent of L. But as $\kappa\lambda/U$ is reduced to very small values, eddy length scales grow. Once the eddy mixing length is comparable to the domain scale L, the system leaves the local-mixing regime and enters the global-mixing regime, also indicated in Figure II.1.

The notion of a diffusive parameterization, applicable to a slowly varying mean flow (Pavan and Held 1996), is valid only in the local mixing regime. Thus, our main focus in the remainder of this paper is characterization of the local regime.

Figure II.3 further illustrates how modest variations of bottom drag, κ, greatly change the nature of the flow. HH80 and LH95 previously noted this extreme sensitivity to κ, and rationalized it by arguing that bottom drag is the only mechanism preventing barotropic eddies from cascading upwards, all the way to the domain scale L. Pedlosky (1983) considered the linear instability problem with bottom friction and Riviere & Klein (1997) studied a weakly nonlinear system. But it is really the fully nonlinear studies that indicate the key role of bottom drag in equilibrated baroclinic turbulence. Smith & Vallis (2002) and Riviere et al. (2004) considered a relatively small range of κ, and showed that the eddy length scale decreases with increasing bottom drag. Arbic & Flierl (2004a) presented

similar results and also explored the regime $\kappa\lambda/U > 1$, where the lower layer velocities are small. We will not consider $\kappa\lambda/U > 1$ in this paper. Arbic & Flierl (2004a) also provide evidence from current meter data that mid-ocean eddies lie somewhere in the region $\kappa\lambda/U \approx 1$, which corresponds to the regime considered in this study.

A striking feature of the simulations is the formation and persistence of axisymmetric vortices. Figure II.3 shows that the size and density of these vortices are influenced by bottom friction. The global mixing solution in panel (c) of Figure II.3 is dominated by just a few vortices: the volatility of the corresponding time-series in panel (b) is due to the extreme fluctuations produced by two or three jostling vortices. It seems there is little hope of constructing a statistical theory of the few-vortex global mixing regime. The more important local regime is simpler in the sense that there are many interacting vortices: the corresponding time series in panel (b) is stable because of the many-vortex self-averaging. Thus simple statistical scaling theories may have some force in the local mixing regime. Specifically, the barotropic vorticity in panel (d) of Figure II.3 is best characterized as a "dilute gas" of vortices (Carnevale et al. 1991). This observation, combined with some deductions based on the statistically steady energy balance in (III.2), provides an analytic entry exploited in sections II.4 and II.5.

Within the vortex cores there is a strong anti-correlation between the barotropic vorticity, $\zeta \equiv \nabla^2\psi$, and temperature, τ: a cyclonic barotropic vortex traps cold fluid in its core while an anti-cyclonic barotropic vortex traps warm fluid in its core. Figure II.4 shows expanded views of (a) barotropic vorticity and (b) temperature corresponding to the the boxed region in Figure II.3(d). Panel (c) of Figure II.4 shows a scatter plot of temperature and barotropic vorticity from each point in Figure II.3(d). The scatter plot has a number of branches corresponding to individual vortices such as those in panels (a) and (b) (indicated by the gray points), therefore most of the temperature anomaly is in the vortices. The mutual advection of these vortices is the main mechanism by which heat is transported

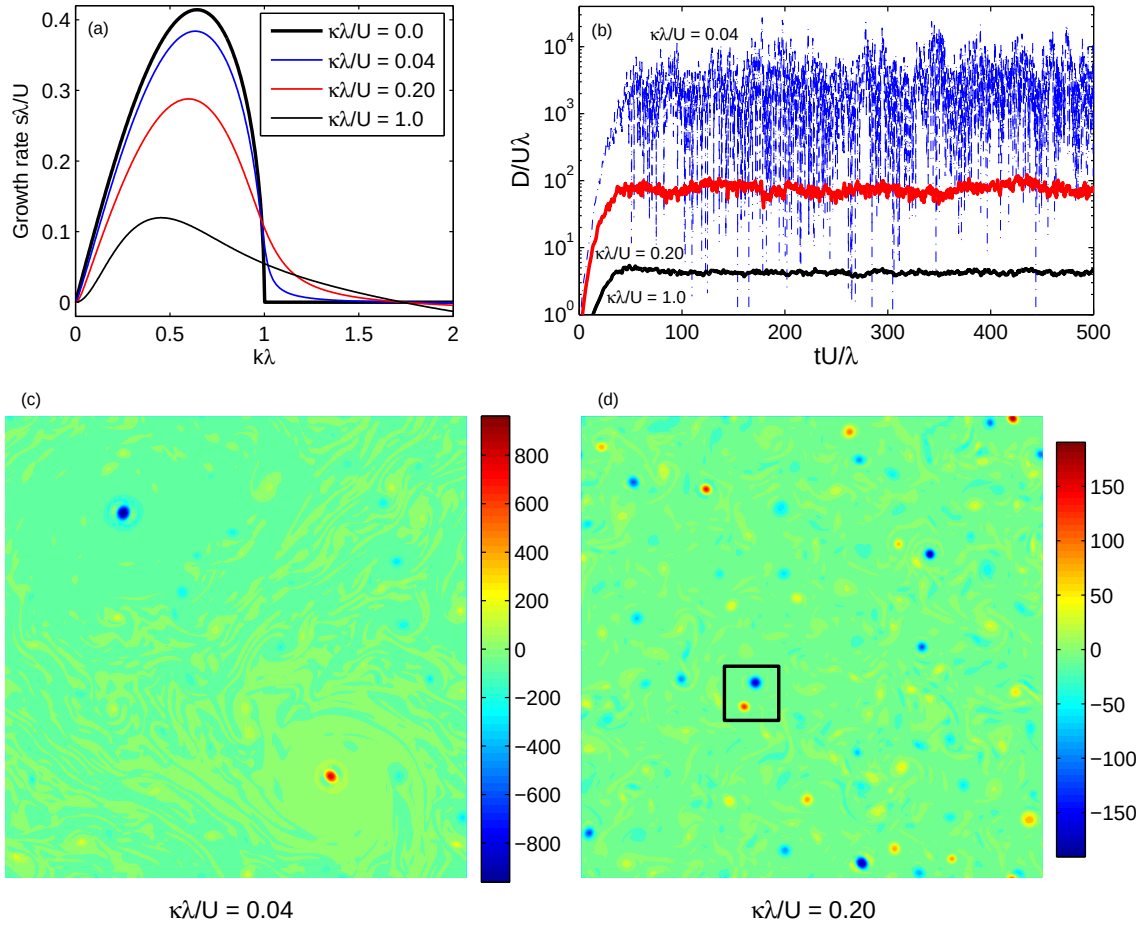

Figure II.3: (a) Growth rates of the linear baroclinic instability problem for different values of the bottom drag parameter. (b) Time series of eddy diffusivity for different values $\kappa\lambda/U$. The "instantaneous diffusivity" shown in these time series is defined by taking $\langle\rangle$ in (II.1) only as an (x, y)-average. Panels (c) and (d) show snapshots of the vorticity of the barotropic mode, $\nabla^2\psi\lambda/U$. In panels (b), (c) and (d), $L/\lambda = 25$. The box appearing in panel (d) is expanded in Figure II.4.

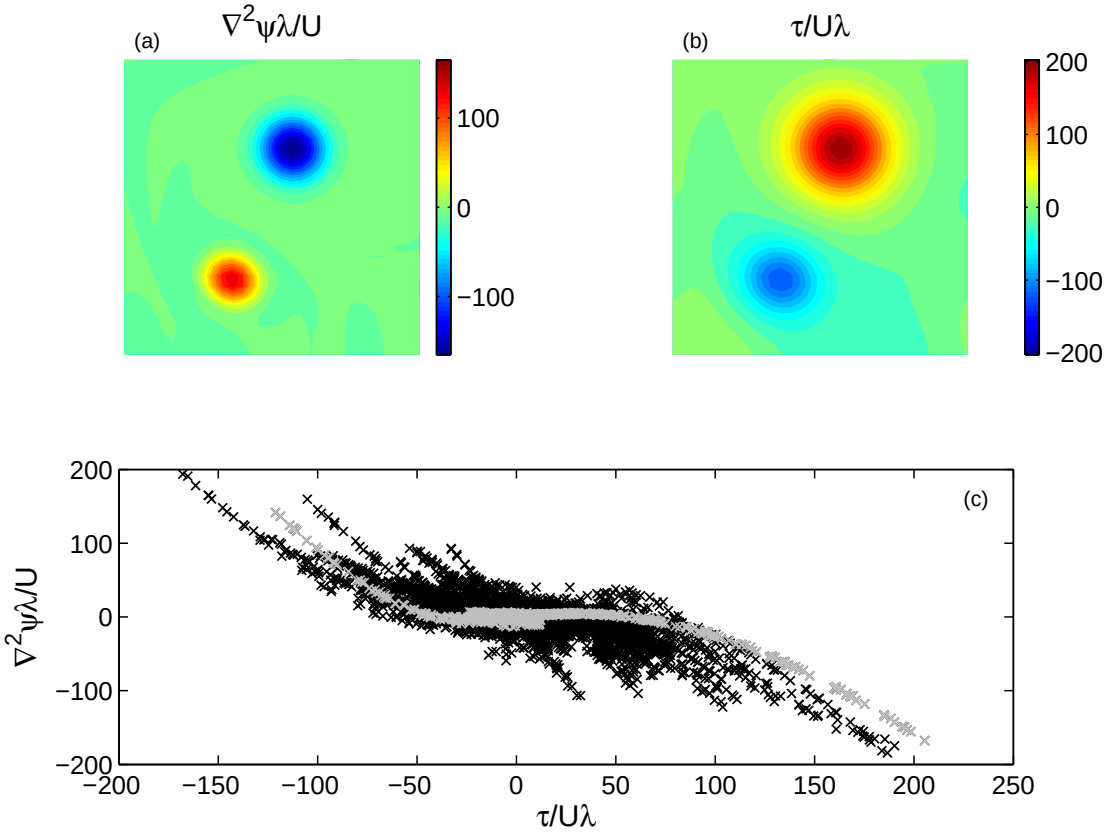

Figure II.4: Non-dimensional (a) barotropic vorticity and (b) temperature from the boxed region in Figure II.3(d). Panel (c) shows a scatter plot of temperature and barotropic vorticity data for the snapshot in Figure II.3(d). The gray points show the data that lie within the boxed region (panels (a) and (b) above). The branches of the scatter plot represent individual vortices and illustrate the strong correlation between temperature and barotropic vorticity in the vortex cores.

meridionally in this system.

LH95 showed that the potential vorticity flux and the meridional heat flux (both of which are proportional to D) are dominated by the largest length scales excited by the inverse cascade. LH95 associated the length $k_0^{-1} \gg \lambda$ with both the mixing length and the peak of the barotropic energy spectrum. LH95 then used the dual-cascade model as a framework to derive a scaling for the diffusive parameterization of the eddy fluxes (for more detail see section II.3).

However if the bottom drag is strong enough to limit the inverse cascade

to scales less than L, then arguments based on an inertial energy-conserving spectral fluxes are invalid. And if bottom drag is sufficiently small to allow a relatively undamped inverse cascade, then barotropic energy accumulates at the domain size, which is just the global mixing regime in Figure II.1. In Held & Larichev (1996) and Lapeyre & Held (2003), this concern is ameliorated because a planetary potential vorticity gradient β halts the inverse cascade without damping, so that the dual-cascade scenario is more plausible. But in the case studied here, with $\beta = 0$, the dual-cascade scenario is implausible. Compounding these difficulties, the dual-cascade scenario of Figure II.2 takes no explicit account of the vortices which dominate the thermal field.

For the reasons above, we reject the dual-cascade scenario, and we support this position by showing in sections II.3 and II.4 that the main scaling relations of the dual-cascade scenario are inaccurate. We instead argue that eddy fluxes result from the interaction of coherent baroclinic vortices. In the local mixing regime the self-averaging of these vortices allows the properties of a single "typical" vortex to be representative of domain-averaged quantities such as the turbulent diffusivity D. Therefore in section II.4 we will consider the properties of a typical vortex core. Relationships between vortex-core properties and domain-averaged values are then applied to the energy balance in section II.5, which results in a scaling for D in both global and local mixing regimes. In section II.6 we discuss the large-scale limit of the equations of motion and we show that there is a new conserved quantity, the cross-invariant, which characterizes the anti-correlation between τ and ζ. In section II.7 we present an empirical formula that collapses the results of the simulations. Section II.8 discusses the sensitivity of the numerical results to hyperviscosity and resolution, and section II.9 is the discussion and conclusion. Appendix A summarizes our notation and the two-mode quasigeostrophic equations, and in Appendix B we describe an automated vortex census algorithm used to verify our vortex-scaling assumptions.

II.3 Large eddies and dual-cascade scaling

LH95 performed large-domain simulations with $L/\lambda = 50$, which for the first time allowed the inverse cascade in the barotropic mode to be observed. Analyzing spectral representations of baroclinic and barotropic energy levels, LH95 found that energy production is localized at length scales much larger than the Rossby deformation radius λ. On the other hand, energy transfer from the baroclinic to the barotropic mode near λ plays the passive, but important, role of energizing the inverse cascade. LH95 then proposed a revision to the theory of HH80 and Salmon (1980) by arguing that the appropriate mixing length should be k_0^{-1}, not λ. LH95 identified k_0 as the wavenumber corresponding to the peak in the barotropic energy spectrum i.e., k_0 is both the wavenumber of the energy-containing eddies and the inverse of the mixing length. This modification of the dual-cascade scenario is indicated in Figure II.2 by the arrow labeled LH95. Figure II.2 also indicates that the exact location of k_0 along the barotropic spectrum can vary dramatically due to a strong dependence on bottom friction.

LH95 then proceeded to estimate the eddy diffusivity as

$$D = \text{characteristic barotropic velocity, } V \times \text{mixing length}\,. \tag{II.4}$$

Retaining the dual-cascade scenario as an interpretative framework, and taking k_0^{-1} as the mixing length, LH95 argue that $V \sim U/k_0\lambda$. Thus, once the dust settles, the final result is the dual-cascade scaling

$$D \sim U/k_0^2\lambda\,. \tag{II.5}$$

The strong dependence of D on bottom drag κ is implicit in k_0, but no relationship between k_0 and κ was proposed by LH95.

In Figure II.5 we test the scaling (II.5) using the data in Figure II.1 and the definition

$$k_0 \equiv \sqrt{\langle|\nabla\psi|^2\rangle \,/\, \langle\psi^2\rangle}\,. \tag{II.6}$$

Figure II.5(b) shows that k_0 defined in (II.6) corresponds well to the peak in the barotropic energy spectrum in both the local and global mixing regimes. We also find that k_0 defined in (II.6) is insensitive to changes in the hyperviscosity and numerical resolution.

If the scaling in (II.5) is valid, then the non-dimensional ratio $D\lambda k_0^2/U$ in Figure II.5(a) should be a constant, independent of both $\kappa\lambda/U$ and L/λ. Instead $D\lambda k_0^2/U$ varies by a factor of 10. Our conclusion is that (II.5) has little value as a correlation between eddy diffusivity D and the peak wavenumber of the barotropic energy spectrum, k_0. It is perhaps not surprising that a length scale associated with the barotropic energy spectrum gives poor quantitative agreement in a flow dominated by baroclinic vortices.

One reason behind the failure of (II.5) is the assumption that k_0^{-1} is equivalent to the mixing length. A more precise definition of the mixing length is

$$\ell_{\rm mix} \equiv U^{-1}\sqrt{\langle \tau^2 \rangle}\,. \tag{II.7}$$

According to this definition, $\ell_{\rm mix}$ times the basic state τ-gradient, U, is equal to the root mean square fluctuation, $\sqrt{\langle \tau^2 \rangle}$. This definition of the mixing length is consistent with the large-scale limit of the governing equations in which the baroclinic evolution equation reduces to advection of the quasi-passive scalar τ by the barotropic flow (see section II.6).

Figure II.6(a) shows that the non-dimensional number $k_0\ell_{\rm mix}$ varies by over a factor of two. Moreover, $k_0\ell_{\rm mix}$ has a maximum value as a function of $\kappa\lambda/U$. This peak in $k_0\ell_{\rm mix}$ is the clearest demarcation between the local and global mixing regimes in our simulations[1]. This peak arises because $\ell_{\rm mix}$ reaches the domain size (and saturates) at a smaller value of $\kappa\lambda/U$ then does the energy-containing length scale, k_0^{-1}. Further discussion of these two length scales appears in section II.9. Figure II.6(b) shows $\ell_{\rm mix}/\lambda$ as a function of $\kappa\lambda/U$. The dashed

[1]Both Figure II.1 and Figure II.6(a) show that the value of $\kappa\lambda/U$ at which the local to global transition occurs depends on L/λ. At $L/\lambda = 50$ the peak in $k_0\ell_{\rm mix}$ is roughly $\kappa\lambda/U = 0.1$ At $L/\lambda = 25$ the peak is at 0.16.

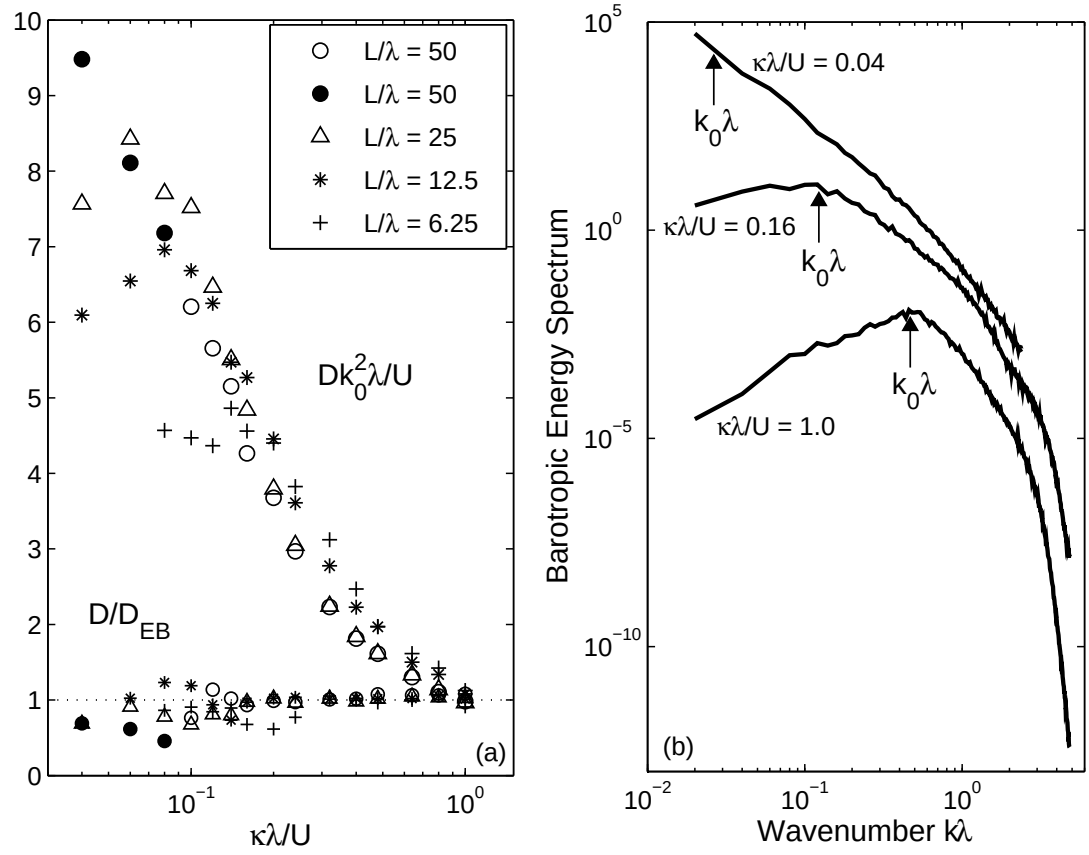

Figure II.5: (a) A comparison of the dual-cascade prediction, $D \sim U/k_0^2\lambda$, to the simulated D's. Also shown is the ratio of the simulated D to $D_{\rm EB}$ defined in (II.31) for the local mixing regime. Points within the global mixing regime use (II.29) with $\ell_{\rm mix} = \pi L$. (b) A comparison of the length scale k_0^{-1}, defined in (II.6), to the LH95 definition of the energy containing length, which is identified with the largest energy-containing wavenumber of the barotropic mode. The LH95 definition and our definition are in good agreement.

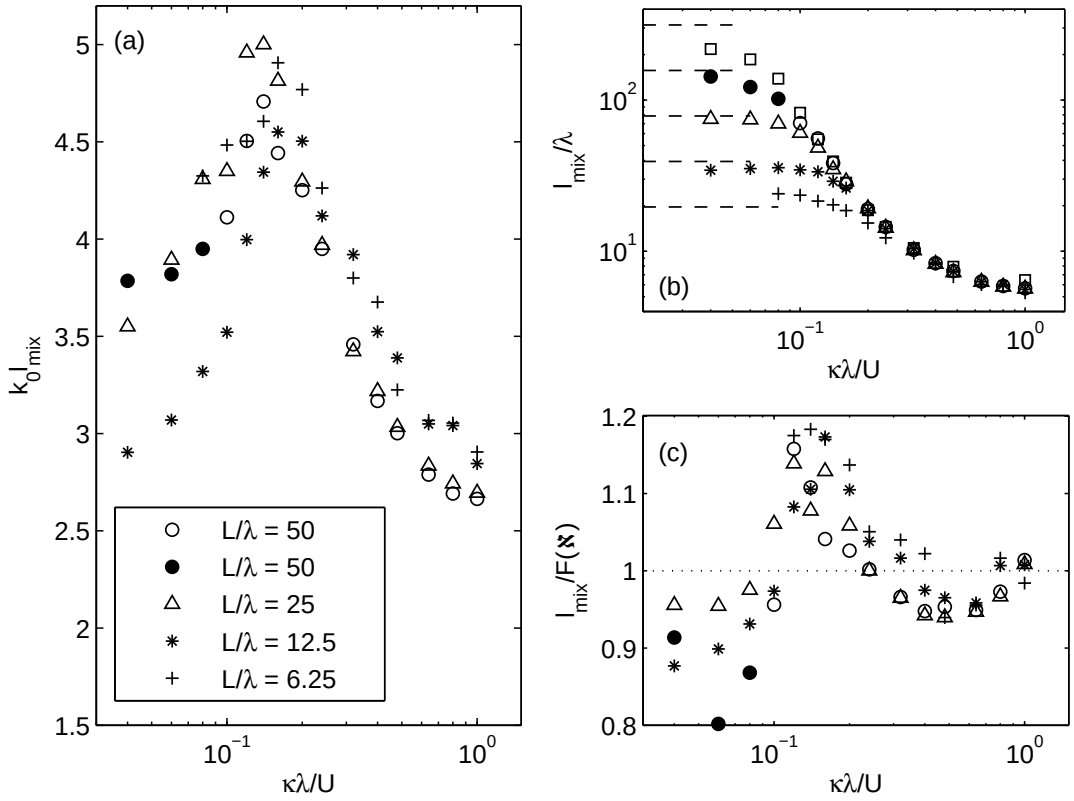

Figure II.6: (a) A comparison of k_0^{-1}, the LH95 length scale associated with the largest energy containing eddies, and $\ell_{\rm mix}$ our mixing length defined in (II.7). (b) A survey of $\ell_{\rm mix}/\lambda$ values showing the statistical independence of domain size at moderate values of $\kappa\lambda/U$. (c) A comparison of the observed mixing length to the empirical fit proposed in (II.37).

lines at the left are $\pi L/\lambda$ and indicate that $\ell_{\rm mix}$ saturates at about πL, or half the domain size, as $\kappa\lambda/U \to 0$. In the local mixing regime, the eddy diffusivity D is independent of domain size L, and Figure II.6(b) shows that the ratio $\ell_{\rm mix}/\lambda$ shares this independence.

Following the expression for D in (II.4) we also write the diffusivity in terms of the eddy mixing length and the meridional barotropic velocity V. We define

$$V \equiv \sqrt{\langle \psi_x^2 \rangle}, \tag{II.8}$$

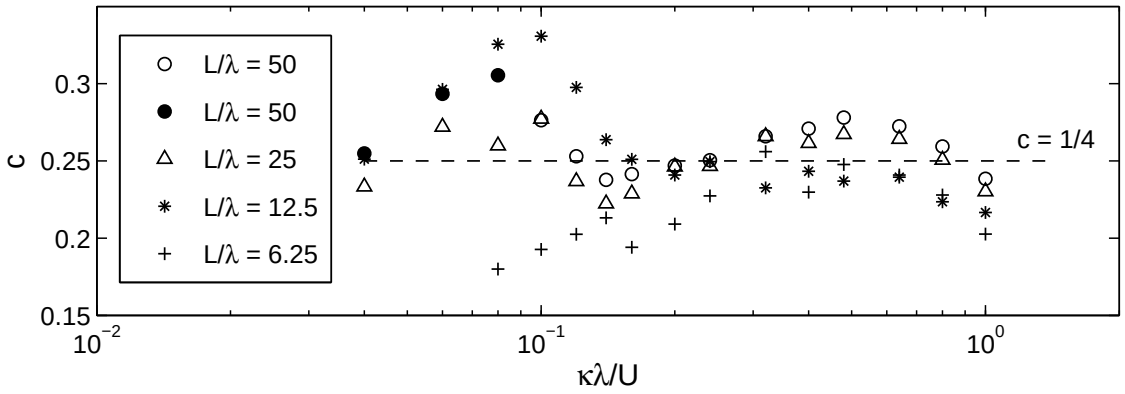

Figure II.7: A survey of the correlation coefficient c as defined in (II.9). Within the local mixing regime c is approximately equal to 1/4.

and we introduce the correlation coefficient

$$c \equiv \frac{\langle \psi_x \tau \rangle}{\sqrt{\langle \psi_x^2 \rangle \, \langle \tau^2 \rangle}} \,, \tag{II.9}$$

so that $D = cV\ell_{\rm mix}$. To examine this relationship we show the correlation c in Figure II.7. In the local regime c has a weak dependence on $\kappa\lambda/U$: the dashed line in Figure II.7 indicates that $c \approx 1/4$. Taking c to be constant, then, throughout the local mixing regime, an important scaling relation[2] is

$$D \sim V\ell_{\rm mix} \,. \tag{II.10}$$

II.4 Vortex properties in the local mixing regime

To this point we have introduced three diagnostics characterizing the domain-averaged flow, namely D, $\ell_{\rm mix}$ and V. We now consider the vortices themselves and relate vortex-core properties to D, $\ell_{\rm mix}$ and V. We employ three important scaling assumptions which are valid in the local mixing regime:

1. Temperature, τ, and barotropic vorticity, ζ, are dominated by the vortex cores. $\tau_{\rm core}$ and $\zeta_{\rm core}$ denote typical core values.

[2] $A \sim B$ ("A scales with B") means that the ratio A/B is approximately constant as the control parameters $\kappa\lambda/U$ and L/λ vary. In practical terms "approximately constant" means that A/B varies by $\pm 20\%$ e.g., (II.10) is true in the local mixing regime since $D = (0.25 \pm 0.05)V\ell_{\rm mix}$.

2. A typical core radius, $r_{\rm core}$, is significantly greater than λ, and core barotropic potential vorticity scales with the core baroclinic potential vorticity i.e., $\zeta_{\rm core} \sim \lambda^{-2}\tau_{\rm core}$.

3. $\ell_{\rm mix}$ scales with the typical spacing between vortices, and the total number of vortices $\sim (L/\ell_{\rm mix})^2$.

The three assumptions are supported by diagnosis of the simulations. Assumption 2 is a result of total potential vorticity conservation; assumption 2 is also supported by the scatter plot in Figure II.4 (c).

We consider the flow to be a dilute vortex gas. Since the temperature field is dominated by the vortex cores, the squared temperature fluctuation, $\langle\tau^2\rangle$, should scale with τ^2 integrated over a single vortex core, that is $\tau_{\rm core}^2 r_{\rm core}^2$, multiplied by the number of vortices in the domain, $L^2/\ell_{\rm mix}^2$, and finally divided by L^2 to form the average. Using the definition of $\ell_{\rm mix}$ in (II.7) we can thus write $\tau_{\rm core}$ in terms of the two length scales $\ell_{\rm mix}$ and $r_{\rm core}$ as:

$$\tau_{\rm core} \sim \frac{U\ell_{\rm mix}^2}{r_{\rm core}}\,. \tag{II.11}$$

We turn now to the second assumption, $\zeta_{\rm core} \sim \tau_{\rm core}/\lambda^2$, and eliminate $\tau_{\rm core}$ using (II.11). This gives:

$$\zeta_{\rm core} \sim \frac{U\ell_{\rm mix}^2}{\lambda^2 r_{\rm core}}\,. \tag{II.12}$$

Next, following Carnevale et al. (1991), and using the estimate in their equation (3), we relate the barotropic velocity V to the core vorticity by $V \sim \zeta_{\rm core} r_{\rm core}^2/\ell_{\rm mix}$. Eliminating $\zeta_{\rm core}$ with (II.12) one has:

$$V \sim \frac{U\ell_{\rm mix} r_{\rm core}}{\lambda^2}\,. \tag{II.13}$$

From (II.10) one now obtains the eddy diffusivity in terms of $r_{\rm core}$ and $\ell_{\rm mix}$:

$$D \sim \frac{U\ell_{\rm mix}^2 r_{\rm core}}{\lambda^2}\,. \tag{II.14}$$

It is amusing that the scaling relations above imply that $D \sim \zeta_{\rm core} r_{\rm core}^2$ i.e., that the circulation of a typical vortex scales with the eddy diffusivity.

To test (II.11) through (II.14) we need $r_{\rm core}$. The most precise way to obtain the typical vortex radius $r_{\rm core}$ is to identify individual vortices and measure each $r_{\rm core}$ according to some objective definition. A faster and more convenient alternative is to again use vortex-scaling theory and estimate $\langle \zeta^2 \rangle$ as ζ^2 integrated over a single vortex core, that is $\zeta_{\rm core}^2 r_{\rm core}^2$, multiplied by the number of vortices in the domain, $L^2/\ell_{\rm mix}^2$, and finally divided by L^2 to form the average. This gives $\langle \zeta^2 \rangle \sim (\zeta_{\rm core} r_{\rm core}/\ell_{\rm mix})^2$. Using (II.12) and (II.13) this implies that $r_{\rm core} \sim V/\sqrt{\langle \zeta^2 \rangle}$. These considerations motivate the definition of a new length ℓ_ζ as

$$\ell_\zeta \equiv \sqrt{\frac{V^2}{\langle \zeta^2 \rangle}}\,, \tag{II.15}$$

and the scaling hypothesis

$$r_{\rm core} \sim \ell_\zeta\,. \tag{II.16}$$

ℓ_ζ is simply an easily diagnosed surrogate for $r_{\rm core}$.

Invoking (II.16) we can replace $r_{\rm core}$ by ℓ_ζ in (II.11) through (II.14). In particular from (II.13) the vortex-scaling theory predicts that the ratio

$$\varkappa_1 \equiv \frac{V\lambda^2}{U\ell_{\rm mix}\ell_\zeta} = \frac{\lambda^2\sqrt{\langle \zeta^2 \rangle}}{\sqrt{\langle \tau^2 \rangle}}\,, \tag{II.17}$$

is constant. We see in Figure II.8(a) that this ratio is indeed remarkably constant although there is variation in the value of $\varkappa_1$ due to resolution differences (for further discussion see section II.8). These variations do not have a large effect on our estimates for D in the following sections, and for the purposes of making quantitative estimates we will take $\varkappa_1$ to be approximately 0.60 (the $L/\lambda = 25$ and 50 series). Another indication of the vortex gas scaling is that the ratio

$$\varkappa_2 \equiv -\frac{\langle \tau\zeta \rangle}{\sqrt{\langle \tau^2 \rangle \langle \zeta^2 \rangle}}\,, \tag{II.18}$$

is also roughly constant and equal to 0.53, independent of resolution effects — see Figure II.8(b).

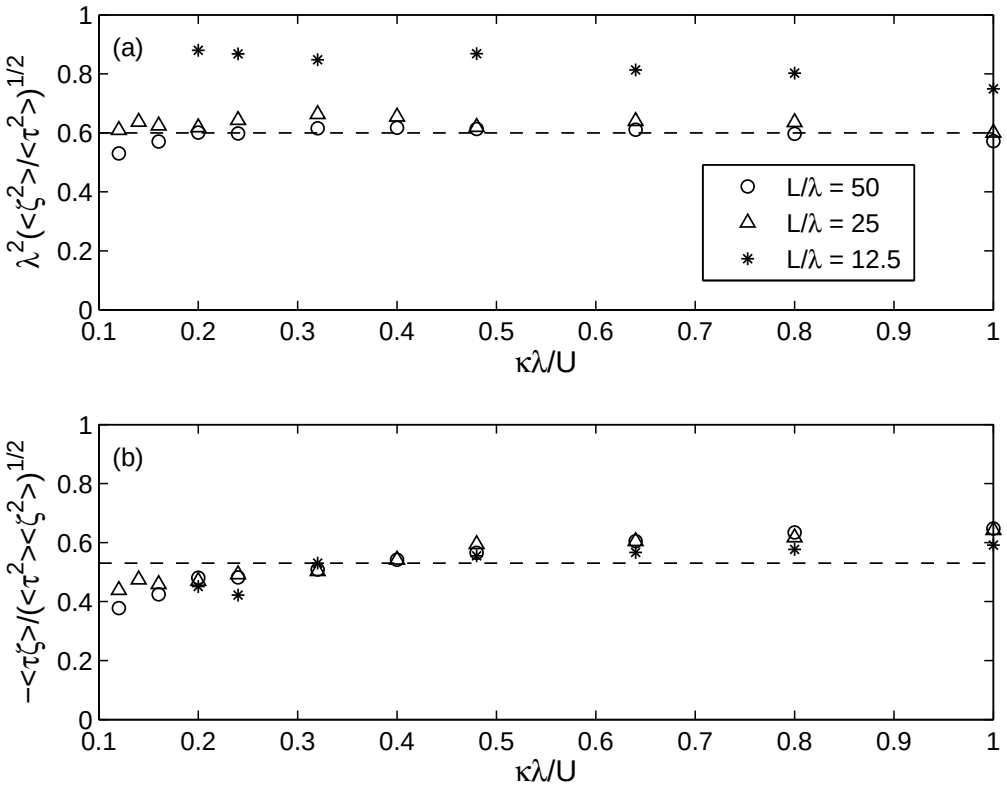

Figure II.8: A survey of the two constant ratios (a) $\varkappa_1 \equiv \lambda^2\sqrt{\langle\zeta^2\rangle}/\sqrt{\langle\tau^2\rangle}$ and (b) $\varkappa_2 \equiv \langle\tau\zeta\rangle\,/\sqrt{\langle\tau^2\rangle\,\langle\zeta^2\rangle}$. $\varkappa_1$ varies slightly due to resolution differences between L/λ series (see section II.8). The dashed lines indicate $\varkappa_1 \approx 0.60$ and $\varkappa_2 \approx 0.53$. The data shown here focuses on the local mixing regime. Results from some simulations are unavailable because $\langle\zeta^2\rangle$ was not collected in the original suite of simulations.

To further verify our vortex-scaling theory, we use an automated "vortex census" to quantify vortex statistics in simulations at seven different values of $\kappa\lambda/U$. In Figure II.9 we provide confirmation of the two relationships prominently involving the length scales $\ell_{\rm mix}$ and $r_{\rm core}$. In Figure II.9(a), we plot the mean number of vortices, N, for each value of $\kappa\lambda/U$. N is determined from 50 snapshots of the barotropic vorticity field in its equilibrated turbulent state. Vortex theory predicts $\ell_{\rm mix} \sim N^{-1/2}$ and our vortex census shows that $\ell_{\rm mix} \sim N^{-0.57\pm0.05}$. The variation in the exponent is due to changes in the vortex census parameters. These parameters and the vortex census algorithm are described in Appendix B. Figure II.9(b) plots the ratio $l_\zeta/r_{\rm core}$, where $r_{\rm core}$ is determined from the vortex census. The ratio is constant to within $\pm10\%$ although the observed $l_\zeta/r_{\rm core}$ does systematically increase as $\kappa\lambda/U$ decreases. The core radius is difficult to quantify because typical vortices only span 3-6 grid spaces for these large domain simulations. Still, the results in Figure II.8 and Figure II.9 give us confidence that the assumptions made at the outset of this section are indeed true: in the local mixing regime there is a self-similar population of vortices.

To conclude this section we notice that (II.17) can be rearranged as

$$\frac{V\lambda}{U\ell_{\rm mix}} \approx 0.60 \times \frac{\ell_\zeta}{\lambda}\,. \tag{II.19}$$

The dual-cascade scenario argues that direct and inverse cascade rates are equal and thus predicts the ratio $V\lambda/U\ell_{\rm mix}$ is constant. Equivalently, the large scale eddy turnover time, $\ell_{\rm mix}/V$ is equal to the linear baroclinic instability growth rate λ/U. However, we show in the next section that the right hand side of (II.19) is actually a non-constant function of $\kappa\lambda/U$ — see (II.26). Diagnosis of the simulations confirms both (II.19) and (II.26).

II.5 The energy balance

In the previous sections we introduced six unknown quantities $r_{\rm core}$ (or equivalently ℓ_ζ), $\tau_{\rm core}$, $\zeta_{\rm core}$, D, V and $\ell_{\rm mix}$. We regard the first and last as the most

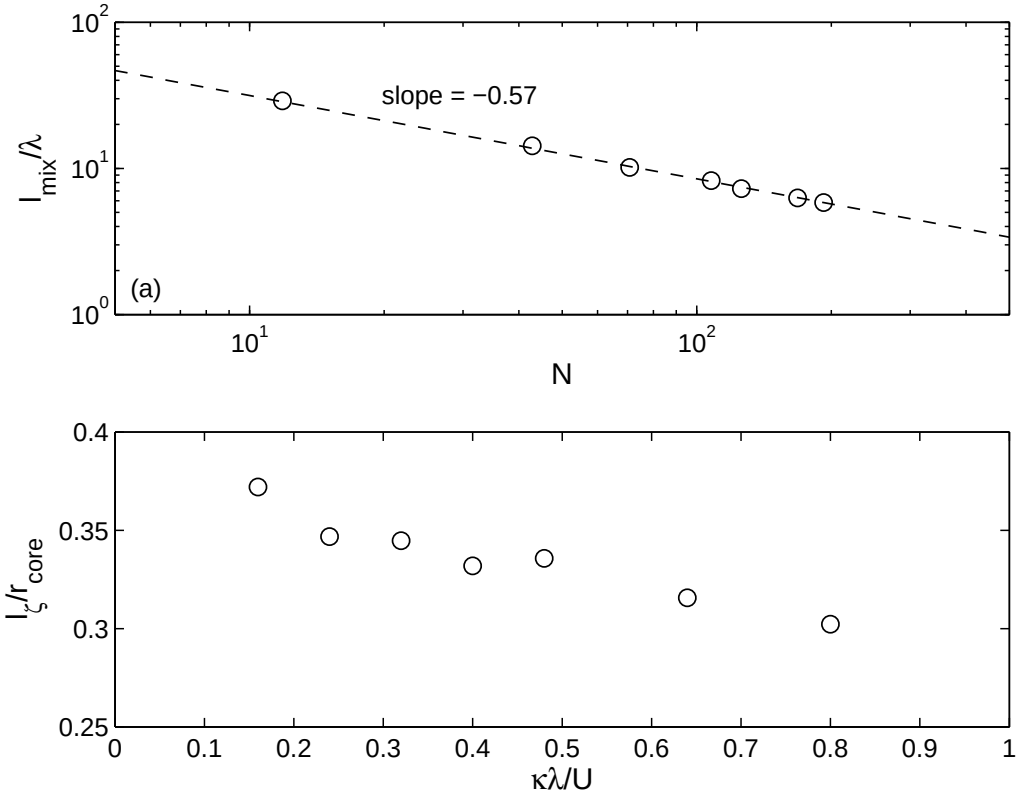

Figure II.9: (a) The number of vortices in the equilibrated turbulent state for seven different values of $\kappa\lambda/U$ as determined from an automated vortex census. Smaller values of $\kappa\lambda/U$ correspond to fewer vortices and a larger mixing length; vortex theory predicts $l_{mix} \sim N^{-1/2}$. (b) l_ζ divided by $r_{\rm core}$, as determined by the vortex census, at the same seven values of $\kappa\lambda/U$. The ratio is constant to within $\pm 10\%$. A description of the vortex census algorithm is given in Appendix B.

basic quantities and in (II.11) through (II.14) we have expressed the middle four in terms of these. A final relationship that we have yet to exploit is the statistically steady energy balance in (III.2). This provides a fifth relation between the six unknowns r_{core}, τ_{core}, ζ_{core}, D, V and ℓ_{mix}.

Neglecting hyperviscosity, we can expand the energy balance in (III.2) to write

$$U\lambda^{-2}\left\langle \psi_x \tau \right\rangle \approx \kappa \left(\left\langle |\nabla\psi|^2 \right\rangle - 2\sqrt{2}\left\langle \nabla\psi \cdot \nabla\tau \right\rangle + 2\left\langle |\nabla\tau|^2 \right\rangle \right) . \tag{II.20}$$

Diagnostics show that within the local regime the three terms on the right hand side of (II.20) are comparable[3].

The definitions in (II.1) and (III.12) and the fact that the flow is largely isotropic allows us to first re-write the energy balance as

$$\frac{U^2}{\lambda^2} D \approx \kappa \left(2V^2 - 2\sqrt{2}\left\langle \nabla\psi \cdot \nabla\tau \right\rangle + 2\left\langle |\nabla\tau|^2 \right\rangle \right) . \tag{II.21}$$

Using integration by parts, the quantity $\langle \nabla\psi \cdot \nabla\tau \rangle$, which we will refer to as the cross-invariant, can be re-written as $-\langle \tau\zeta \rangle$. Both temperature and barotropic vorticity are dominated by values in the vortex cores, therefore the product $\tau\zeta$ is strongly dominated by core values. Thus returning to our vortex core relations from section II.4, and specifically using (II.18) with the definitions of ℓ_{mix} and ℓ_ζ in (II.7) and (II.15), we can write

$$-\left\langle \tau\zeta \right\rangle = \varkappa_2 UV \frac{\ell_{\text{mix}}}{\ell_\zeta} , \tag{II.22}$$

where $\varkappa_2 \approx 0.53$. Note that the negative sign is necessary on the left hand side of (II.22) because τ and ζ are negatively correlated. This strong anti-correlation between τ and ζ is important because the cross-term makes a significant contribution to the dissipation in (II.20).

The final term on the right hand side of (II.20) involves $\langle |\nabla\tau|^2 \rangle$. Unfortunately, $\langle |\nabla\tau|^2 \rangle$ cannot be directly related to the vortex core properties because

[3]The global mixing regime is much simpler because the Ekman dissipation is dominated by the barotropic mode, $\varepsilon_{Ekman} \approx \kappa \left\langle |\nabla\psi|^2 \right\rangle$.

the domain-average of the temperature *gradient* fluctuations is not dominated by vortex cores. Instead, equal contributions to this average come from the vortex cores and the surrounding filamentary sea. In the sea between the vortices τ suffers a cascade to small scales and $|\nabla\tau|$ can become comparable to typical core values. The non-vortex contribution to $\langle|\nabla\tau|^2\rangle$ is further enhanced because the filamentary sea accounts for a much larger percentage of the domain than do the vortices.

The first hope then is that $\langle|\nabla\tau|^2\rangle$ is small relative to the other terms in (II.20). But diagnosis shows that this is not the case in the local mixing regime. Not only does $\langle|\nabla\tau|^2\rangle$ make an important contribution, but a surprisingly good approximation in the local mixing regime is that

$$\sqrt{2}\left\langle|\nabla\tau|^2\right\rangle \approx \langle\nabla\psi\cdot\nabla\tau\rangle \ . \tag{II.23}$$

That is, $\langle|\nabla\tau|^2\rangle$ cancels almost exactly half the cross-term, so that the total dissipation on the right hand side of (II.20) can be approximated by $\kappa(\langle|\nabla\psi|^2\rangle - \sqrt{2}\langle\nabla\psi\cdot\nabla\tau\rangle)$. Figure II.10($a$) shows the ratio of this truncated dissipation ε_{trunc} to the total dissipation due to Ekman friction ε_{Ekman} for 60 simulations. For most of parameter space, the truncated dissipation is accurate to within $\pm 5\%$ of the total Ekman dissipation. To understand why the approximation in (II.23) is so accurate, we must consider the large-scale limit of the governing equations and conservation of the cross-invariant in section II.6.

Returning to the energy balance in (II.21), and applying the approximations in (II.22) and (II.23) we have

$$\frac{U^2}{\lambda^2}D \approx \kappa\left(2V^2 - \sqrt{2}\varkappa_2 UV\frac{\ell_{\rm mix}}{\ell_\zeta}\right) . \tag{II.24}$$

If we first replace D with $cV\ell_{\rm mix}$ and then multiply (II.24) by a factor of $\lambda^3/U^3\ell_{\rm mix}^2$, we find that each of the three terms is proportional to some power of $V\lambda/U\ell_{\rm mix}$. From (II.17) this ratio is equivalent to $\varkappa_1\ell_\zeta/\lambda$. These steps reduce (II.24) to the

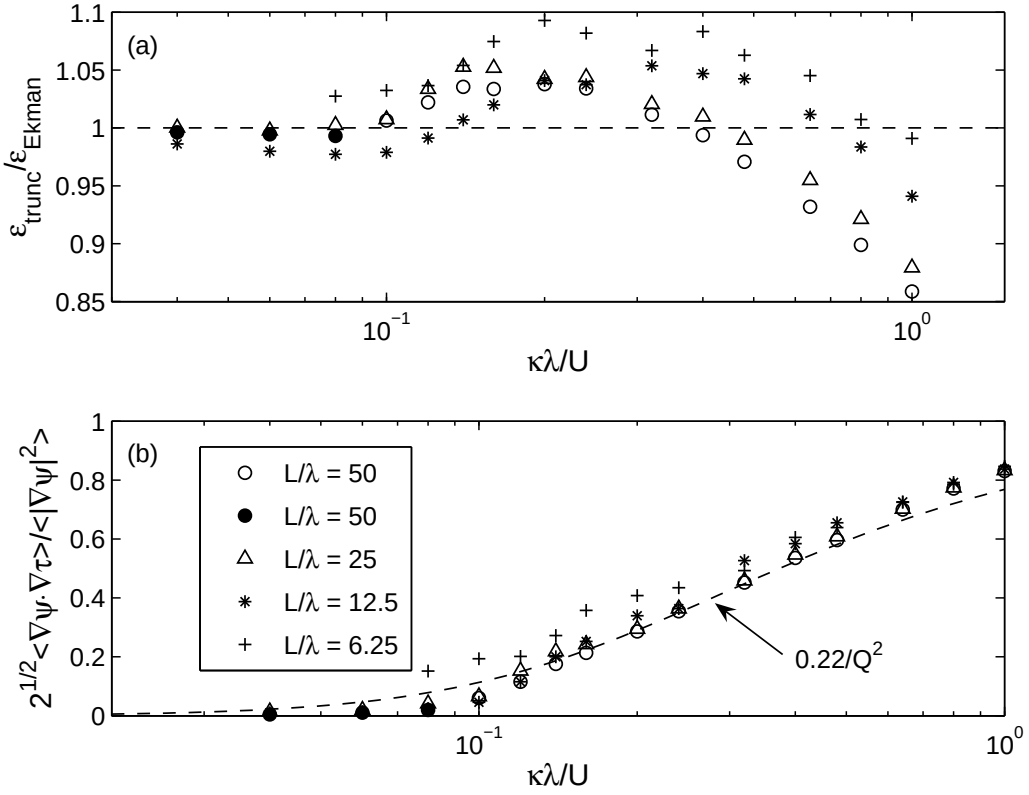

Figure II.10: (a) The ratio of the truncated dissipation $\varepsilon_{trunc} = \kappa\left(\langle|\nabla\psi|^2\rangle - \sqrt{2}\,\langle\nabla\psi\cdot\nabla\tau\rangle\right)$ to the total Ekman dissipation $\varepsilon_{Ekman} = \kappa\left(\langle|\nabla\psi - \sqrt{2}\nabla\tau|^2\rangle\right)$. (b) The ratio of the two terms comprising ε_{trunc}. One can show from (II.17), (II.22) and (II.26) that vortex-scaling theory predicts this ratio to be approximately $\sqrt{2}\varkappa_1\varkappa_2/2\mathcal{Q}^2$, where $\mathcal{Q}(\kappa_*)$ is defined in (II.27). The dashed line shows that there is good agreement between theory and the simulations. In the global mixing regime $\varepsilon_{trunc} \approx \langle|\nabla\psi|^2\rangle$.

quadratic equation

$$2\kappa_* \left(\varkappa_1 \frac{\ell_\zeta}{\lambda}\right)^2 - c\left(\varkappa_1 \frac{\ell_\zeta}{\lambda}\right) - \sqrt{2}\kappa_* \varkappa_1 \varkappa_2 \approx 0\,, \tag{II.25}$$

where $\kappa_* = \kappa\lambda/U$, the non-dimensional bottom friction. Solving (II.25) and choosing the positive root gives

$$\varkappa_1 \frac{\ell_\zeta}{\lambda} \approx \mathcal{Q}(\kappa_*)\,, \tag{II.26}$$

where

$$\begin{aligned}\mathcal{Q}(\kappa_*) &\equiv \frac{1}{2}\left[\frac{c}{2\kappa_*} + \sqrt{\frac{c^2}{4\kappa_*^2} + 2\sqrt{2}\varkappa_1\varkappa_2}\right]\,, \\ &= \frac{1}{2}\left[\frac{1}{8\kappa_*} + \sqrt{\frac{1}{64\kappa_*^2} + 0.9}\right]\,. \end{aligned} \tag{II.27}$$

In the second expression the numerical values are obtained using $c = 0.25$, $\varkappa_1 = 0.60$ and $\varkappa_2 = 0.53$.

The goal is to find a scaling for D, so we return to $D = cV\ell_{\rm mix}$, and express V in terms of ℓ_ζ and $\ell_{\rm mix}$ using (II.17). With $c = 1/4$ this leads to

$$D \approx \frac{U\ell_{\rm mix}^2}{4\lambda} \times \left(\varkappa_1 \frac{\ell_\zeta}{\lambda}\right)\,, \tag{II.28}$$

or using (II.26)

$$D \approx \frac{U\ell_{\rm mix}^2}{8\lambda}\left[\frac{1}{8\kappa_*} + \sqrt{\frac{1}{64\kappa_*^2} + 0.9}\right]\,. \tag{II.29}$$

A complete expression for D solely in terms of external parameters requires another relation connecting $\ell_{\rm mix}$ and to known quantities. Unfortunately we have not found a physical argument for this relationship. Instead in section II.7 we propose an empirical fit for $\ell_{\rm mix}$. The main result obtained from those empirical considerations is that in the local regime

$$\ell_{\rm mix}^{\rm loc} \approx 4\lambda \exp\left(\frac{3U}{10\kappa\lambda}\right)\,, \tag{II.30}$$

(see (II.38) and the surrounding discussion). Eliminating $\ell_{\rm mix}$ from (II.29) using (II.30) gives the energy-balance scaling, $D \approx D_{\rm EB}^{\rm loc}$, where

$$D_{\rm EB}^{\rm loc} \equiv 2\exp\left(\frac{3}{5\kappa_*}\right)\left[\frac{1}{8\kappa_*} + \sqrt{\frac{1}{64\kappa_*^2} + 0.9}\right] U\lambda\,. \tag{II.31}$$

This equation is the smooth curve in Figure II.1. Furthermore, panel (a) of Figure II.5 shows the ratio of the simulated D to $D_{\rm EB}$ within the local mixing regime. For data within the global mixing regime, $\ell_{\rm mix}$ is set equal to πL in (II.29). The ratio is close to unity in the local mixing regime, and even does reasonably well in the global mixing regime where c, $\varkappa_1$ and $\varkappa_2$ are variable. Further discussion of the transition from local to global mixing appears in section II.7.

II.6 The large-scale limit and the cross-invariant

Our analysis of the energy balance equation in section II.5 relies crucially on the approximation (II.23) which enables us to relate $\langle|\nabla\tau|^2\rangle$ to vortex properties. To understand this approximation we consider the large-scale, slow-time limit of the equations of motion i.e., the dynamics on length scales much greater than λ. To extract this limit we first non-dimensionalize length with λ and time with λ/U. Then if $\epsilon \equiv \lambda/\ell_{\rm mix} \ll 1$, one obtains the large-scale limit with $\partial_x \to \epsilon\partial_x$ and $\partial_t \to \epsilon\partial_t$. In order to retain the proper balance of terms, the amplitudes of ψ and τ are boosted by a factor of $1/\epsilon$. The result of this maneuver is the scaled evolution equations:

$$\nabla^2\psi_t + J\left(\psi,\nabla^2\psi\right) + J\left(\tau,\nabla^2\tau\right) + \nabla^2\tau_x = -\frac{\kappa_*}{\epsilon}\nabla^2\left(\psi - \sqrt{2}\tau\right) + O(\epsilon^2)\,, \quad \text{(II.32)}$$

$$\tau_t + J\left(\psi,\tau\right) - \psi_x = -\sqrt{2}\epsilon\kappa_*\nabla^2\left(\sqrt{2}\tau - \psi\right) + O(\epsilon^2)\,, \quad \text{(II.33)}$$

where $\kappa_* = \kappa\lambda/U$. The left of (II.32) and (II.33) is familiar from earlier studies of large-scale quasi-geostrophic turbulence (Salmon 1980, LH95). The right hand sides of (II.32) and (II.33) reveal the large-scale effects of bottom friction. In (II.32) the $O(\epsilon^{-1}\kappa_*)$ dissipative terms on the right are significant, if not dominant, depending on the size of κ_*. Notice also that the largest coupling of ψ into (II.33) is due to bottom friction, rather than the $O(\epsilon^2)$ non-linear terms.

If $\kappa_* = O(1)$, we must have $\psi - \sqrt{2}\tau = O(\epsilon)$ to control the ϵ^{-1} term on the right of (II.32). This is Arbic and Flierl's (2004a) equivalent barotropic

flow, where the lower layer is almost spun down[4]. Roughly speaking $\psi - \sqrt{2}\tau = O(\epsilon)$ is characteristic of most of the local regime. We resisted this conclusion and attempted to control the ϵ^{-1} term on the right of (II.32) by making κ_* sufficiently small. But this victory is pyrrhic because once $\kappa_*/\epsilon = O(1)$ the system is in the global regime. Thus in the local regime, where the concept of an eddy diffusivity is relevant, the bottom friction is always painful in the large-scale barotropic vorticity equation (II.32). This is a fundamental reason for the failure of the dual-cascade theory.

The non-linear terms in (II.32) and (II.33) conserve the cross-invariant

$$\langle \nabla\psi \cdot \nabla\tau \rangle = -\langle \tau\zeta \rangle \ . \tag{II.34}$$

The strong anti-correlation between τ and ζ within the vortex cores motivates this analysis of the cross-invariant. To obtain the cross-invariant conservation law, multiply (II.32) by τ and (II.33) by ζ and add the results. Averaging over space, one finds that to leading order

$$\frac{\partial}{\partial t}\langle \tau\zeta \rangle = \frac{\kappa_*}{\epsilon}\left(\langle \nabla\psi \cdot \nabla\tau \rangle - \sqrt{2}\left\langle |\nabla\tau|^2 \right\rangle \right) \ . \tag{II.35}$$

We emphasize that (II.35) is a new conservation law of the large-scale dynamics — there is no clear relation between (II.35) and the energy and enstrophy conservation laws of the full system. Now in statistical steady state there can be no net production of the cross-invariant $\langle \tau\zeta \rangle$. This requires that the right hand side of (II.35) is zero (or take a time average). This prediction is well verified in the simulations, and crucial in simplifying the energy balance equation in section II.5 (see (II.23) and subsequent discussion).

II.7 Empirical expressions for the mixing length

To eliminate the mixing length from (II.29) we need to express $\ell_{\rm mix}$ in terms of external parameters. We are unable to find a satisfactory physical ar-

[4]Notice that if ψ is precisely proportional to τ then the energy production $\langle \psi_x \tau \rangle$ also precisely vanishes. Thus the residual $\psi - \sqrt{2}\tau$ is certainly non-zero and very important.

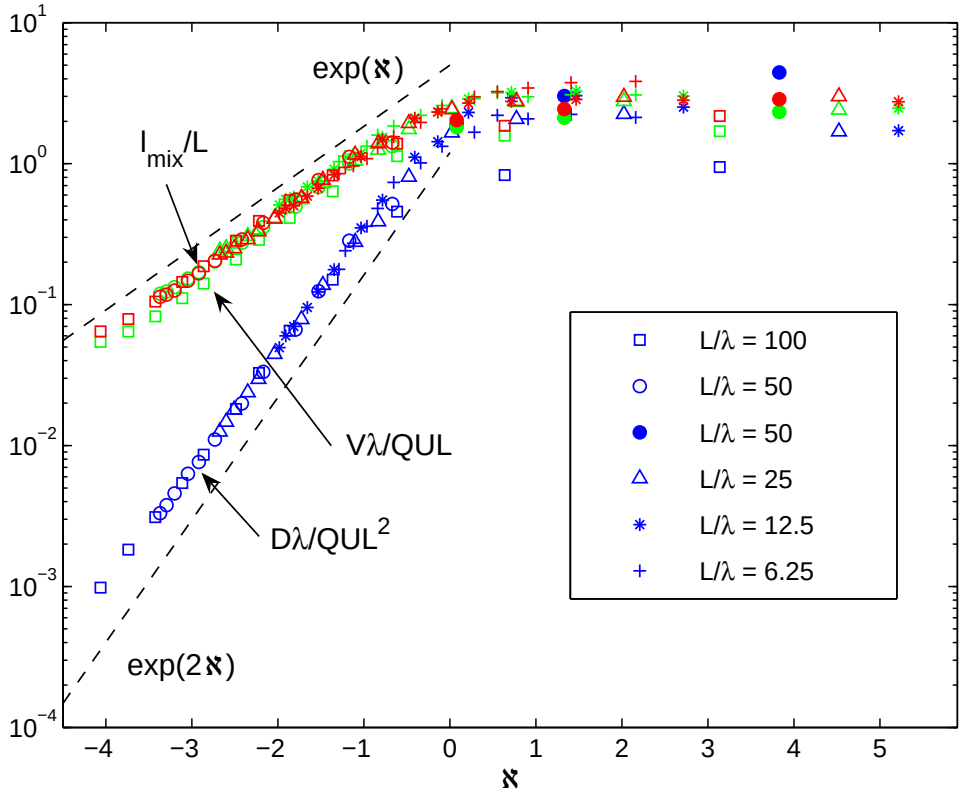

Figure II.11: According to the energy-balance relation and vortex-gas scaling, the local-mixing regime is characterized by $V\lambda/\mathcal{Q}UL \approx \ell_{\rm mix}/L \propto \exp(\aleph)$ and $(D\lambda/\mathcal{Q}UL^2) \propto \exp(2\aleph)$. These predictions are confirmed above by the collapse of the data to straight lines in the local regime where $\aleph < 0$. $\aleph$ also collapses the data in global regime where $\aleph > 0$. The variable $\aleph$ is defined in (II.36), and the function $\mathcal{Q}(\kappa_*)$ in (II.27).

gument and instead we indulge in some curve fitting. In Figure II.6(b), $\ell_{\rm mix}$ has an independent dependence on two dimensionless parameters, L/λ and $\kappa\lambda/U$. We found empirically that the introduction of the combination $\aleph$, defined by

$$\aleph \equiv \frac{3}{10}\frac{U}{\kappa\lambda} - \ln\left(\frac{\pi L}{4\lambda}\right) , \tag{II.36}$$

collapses the data in both the local and global regimes (see Figure II.11).

The definition (II.36) is constructed so that $\aleph = 0$ is roughly the border between local and global mixing. The factor 3/10 is a simple fraction which best collapses the $\ell_{\rm mix}$ data in the local mixing regime. The combination $\aleph$ accounts

for the observation that for increasing L/λ, the global-local transition occurs at smaller and smaller values of $\kappa\lambda/U$. However the dependence is very weak, and this motivates the logarithm of L/λ in (II.36).

Using $\aleph$, we propose the empirical formula

$$\ell_{\rm mix} \approx \pi L \frac{e^{\aleph}}{\sqrt{1+e^{2\aleph}}} \equiv \pi L \mathcal{F}(\aleph)\,. \tag{II.37}$$

Panel (c) of Figure II.6 shows that (II.37) collapses the $\ell_{\rm mix}$ data. Formula (II.37) is constructed so that

$$\ell_{\rm mix} \approx \begin{cases} \pi L\,, & \text{in the global regime, } e^{2\aleph} \gg 1\,, \\ \pi L \exp(\aleph) = 4\,\lambda \exp(3U/10\kappa\lambda)\,, & \text{in the local regime, } e^{2\aleph} \ll 1\,. \end{cases} \tag{II.38}$$

In the global mixing regime $\ell_{\rm mix}$ saturates at πL, or roughly half the domain size. In the local regime $\ell_{\rm mix}$ is independent of L and exponentially sensitive to $\kappa\lambda/U$.

It is our consistent experience that this exponential dependence of $\ell_{\rm mix}$ on $U/\kappa\lambda$ is more convincing than a power law in the local regime. For example, the $\ell_{\rm mix}/L$ points in Figure II.11 fall cleanly on the straight line corresponding to $e^{\aleph}$. This observation is the most compelling motivation for the introduction of $e^{\aleph}$ in (II.37) and (II.38).

In the local mixing regime the vortex-scaling theory in (II.13) and (II.14) predicts that $V \propto r_{\rm core}\ell_{\rm mix}$ and $D \propto r_{\rm core}\ell_{\rm mix}^2$. Since $r_{\rm core} \sim \ell_\zeta \propto \mathcal{Q}(\kappa_*)$ we can eliminate the dependence on $r_{\rm core}$ by considering $V/\mathcal{Q}$ and $D/\mathcal{Q}$, where $\mathcal{Q}(\kappa_*)$ is defined in (II.27). Thus in the local mixing regime vortex scaling predicts that

$$\frac{V}{\mathcal{Q}} \propto \ell_{\rm mix} \propto e^{\aleph}\,. \tag{II.39}$$

and

$$\frac{D}{\mathcal{Q}} \propto \ell_{\rm mix}^2 \propto e^{2\aleph}\,. \tag{II.40}$$

Figure II.11 shows the ratios above plotted against $\aleph$. The straight lines in the local regime ($\aleph < 0$) further confirm vortex-scaling. Figure II.11 also shows that

all the major properties of this dilute vortex gas are exponentially sensitive to the bottom drag.

II.8 Resolution and hyperviscosity

To prevent build-up of enstrophy at small scales, it is necessary to include a dissipative term acting selectively on high wavenumbers. Arbic and Flierl (2003, 2004b) have shown that geostrophic turbulence simulations do not depend strongly on the form of this small-scale dissipation, e.g. hyperviscosity or wavenumber filter. Regardless of form, though, the dissipation of energy due to this term should be relatively small.

In our simulations we follow LH95 and use a hyperviscous term of the form ∇^8 (see Appendix A). The rationale for this high-order operator is that it limits dissipation to the very largest wavenumbers, and leaves as much spectral room as possible for the direct enstrophy cascade. In order to compare our results with those reported in LH95 we repeated their main experiment, namely experiment I, which has the following parameters:

$$\frac{L}{\lambda} = 50, \quad \frac{\kappa\lambda}{U} = 0.08, \quad \frac{\nu}{UL^7} = 1.024 \times 10^{-13}, \quad nn = 256^2 \,.$$

Above, nn is the number of grid points.

In this simulation 22.2% of the total energy extracted from the mean flow in the statistically steady state was balanced by the hyperviscous term $hyp\nu$ in (A.16) and (A.17). In LH95 hyperviscosity contributed to 19.9% of the dissipation; this discrepancy is most likely due to differences in the Ekman dissipation term in the layer and modal formulations. However, in a simulation where L/λ was reduced to a value of 25, with $\kappa\lambda/U$, ν/UL^7 and nn remaining fixed, the hyperviscous dissipation dropped to 7.13%.

This latter simulation has a finer resolution per deformation radius. In other words, given the same number of grid points, the flow is better resolved for

Table II.1: Overview of small-scale dissipation parameters in all of the simulations. The symbols corresponding to each group of simulations are the same in all figures. The number of grid points per deformation radius was determined by taking the number of grid points on one side of the domain and dividing by $2\pi L/\lambda$.

Symbol	L/λ	ν/UL^7	Grid points	Grid points/λ
$+$	6.25	2.048×10^{-13}	128^2	3.26
$*$	12.5	2.048×10^{-13}	128^2	1.63
$\times$	12.5	6.55×10^{-12}	128^2	1.63
$\triangle$	25.0	1.024×10^{-13}	256^2	1.63
$\circ$	50.0	1.024×10^{-13}	512^2	1.63
$\bullet$	50.0	1.024×10^{-13}	256^2	0.815
$\square$	100.0	1.60×10^{-15}	512^2	0.815

smaller values of L/λ. We found that the resolution is at least as important as the actual coefficient of hyperviscosity, ν, in determining $hyp\nu$. Table II.1 gives an overview of the various small-scale dissipative parameters used in this study, and Figure II.12(a) shows Ekman dissipation ε_{Ekman} divided by total dissipation ε_{total} (Ekman and hyperviscous) for all the simulations. It is reassuring to see that as the resolution increases the hyperviscous contribution decreases.

In our earliest large-domain simulations (i.e. $L/\lambda = 100$ with $nn = 512^2$ and $L/\lambda = 50$ with $nn = 256^2$), the hyperviscous energy dissipation was roughly 20% to 30% of the total. We regard this as an uncomfortably large contribution from the hyperviscosity. Thus we performed a second series at $L/\lambda = 50$, doubling the resolution to $nn = 512^2$. The hyperviscous parameter ν was also reduced as the resolution was increased as described in Table II.1. Within the global mixing regime, smaller times steps are necessary for stability and a longer averaging time is necessary to remove turbulent fluctuations. This computational burden prevented the four global-mixing runs from being completed at 512^2 and so the comparison is limited to the local mixing regime. Comparing the $\bullet$'s with the $\circ$'s in Figure II.12(a) shows that increasing the resolution to 512^2 drops the hyperviscous energy

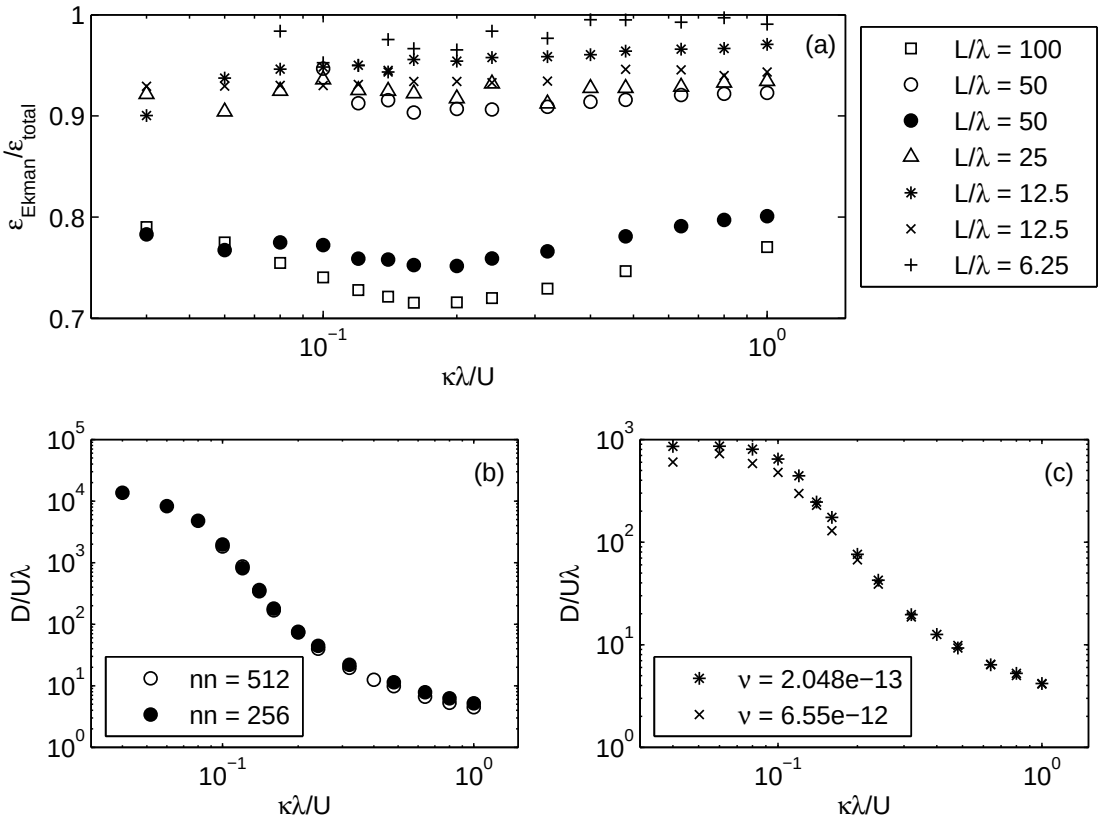

Figure II.12: (a) The ratio of the dissipation due to Ekman drag to the total dissipation (Ekman and hyperviscous). The two circle experiments ($L/\lambda = 50$) have different resolutions: 512^2 (open) and 256^2 (closed). Two series of simulations with $L/\lambda = 12.5$ were completed with different values of ν: 2.05e-13 (*) and 6.55e-12 ($\times$). (b) Values of D for runs with $L/\lambda = 50$. (c) Values of D with $L/\lambda = 12.5$.

dissipation considerably.

Other quantities are also sensitive to resolution. One example of this is the correlation coefficient c. Simulations with a fine resolution show that c is approximately constant and equal to $1/4$ in the local mixing regime. Values of c for the reduced resolution sequences with $L/\lambda = 100$ and 50 collapsed onto a single curve with values between 0.27 and 0.37 in the local regime (not shown). This systematic variation due to insufficient resolution was limited to data within the local mixing regime. This led us to omit data for simulations with $L/\lambda = 100$ for some plots. Also, in Figure II.8(a), $\langle \zeta^2 \rangle$ is shown to be sensitive to simulation resolution.

Considering the effect resolution has on $hyp\nu$, c, $\varkappa_1$ and other properties, it is somewhat surprising that varying resolution makes only a small change in D. Figure II.12(b) compares the values of D for the two series with $L/\lambda = 50$. All the simulations in the local mixing regime have been performed at both resolutions, and the values of D are so similar that it is difficult to distinguish the $\bullet$'s from the $\circ$'s in Figure II.12(b). This result gives us confidence in our $L/\lambda = 100$ results for D despite the large hyperviscous energy dissipation in this sequence (Figure II.12(a)).

As a further test, Figure II.12(c) shows that varying ν at fixed resolution has a small effect on D. Figure II.12(c) shows two sequences, $*$ and $\times$, with $L/\lambda = 12.5$ and $\nu_\times = 32\nu_*$, with $nn = 128^2$ in both cases. Again, the large change in ν has little impact on D, especially in the local mixing regime. In the global regime there is a systematic decrease in D for the simulations with increased hyperviscosity. This discrepancy may be due to the fact that the simulations with increased ν spin up faster, and are also less volatile.

II.9 Discussion and Conclusions

In this article we have shown that the main predictions of the dual-cascade theory of equilibrated baroclinic turbulence on an f-plane are inaccurate e.g., the ratios $Dk_0^2\lambda/U$ and $V\lambda/U\ell_{\rm mix}$ are not constant. We have identified the underlying physical reasons for the failure of this theory, e.g., the dominance of bottom drag in the large-scale barotropic vorticity equation (II.32), and the prominence of coherent vortices. We have proposed an alternative theory for baroclinic eddy fluxes based on vortex-gas scaling (Carnevale et al., 1991) and energy balance. Animations of equilibrated simulations show that vortices persist and travel across the domain. The baroclinic heat flux is evident in these animations as a systematic tendency for hot anti-cyclonic vortices to move northwards, and cold cyclonic vortices southwards. However a great difference from the barotropic problem studied by Carnevale et al. (1991) is that in the equilibrated state same-signed vortex-merger is rare.

An important feature of the vortex theory is that there are at least four relevant length scales. In the local regime these four adhere to the relationships

$$\lambda < r_{\rm core} \ll \ell_{\rm mix} \ll L\,. \tag{II.41}$$

Scale separation between L and $\ell_{\rm mix}$ is necessary for the validity of diffusive parameterizations, but there is also an important scale separation between $\ell_{\rm mix}$ and $r_{\rm core}$. In section II.4 we showed that the diffusivity D depends on both the mixing length and the core radius through

$$D \sim \frac{U\ell_{\rm mix}^2 r_{\rm core}}{\lambda^2}\,. \tag{II.42}$$

In section II.5 the mechanical energy equation (III.2) is used to express ℓ_ζ (and therefore $r_{\rm core}$) in terms of $\kappa\lambda/U$ e.g., see (II.26). And in section II.7 we proposed an empirical expression for $\ell_{\rm mix}$ in terms of $\kappa\lambda/U$ e.g., see (II.38). The exponential sensitivity of $\ell_{\rm mix}$ to $\kappa\lambda/U$ enters through this empirical relation. But a compelling

physical explanation for this exponential relation has eluded us. We believe that the answer is again related to the long-lived coherent vortices that dominate the flow. A full understanding of homogeneous quasi-geostrophic turbulence on an f-plane will require an analysis of how these coherent structures are created, how they work to halt the linear baroclinic instability, and how they interact in statistical equilibrium.

Of course, introduction of a planetary potential vorticity gradient, β, would make this model more applicable to the ocean and also provide a mechanism for halting, without damping, the inverse cascade and suppressing vortices. Held & Larichev (1996) and Lapeyre & Held (2003) have shown that β can indeed halt the inverse cascade, and they have presented scalings for the diffusive flux again applying the dual-cascade model. Danilov & Gurarie (2002) have presented barotropic simulations that include both bottom friction and β and have documented a transition between friction-dominated and β-dominated regimes. Still, an understanding of how these two mechanisms influence the eddy fluxes and the formation of coherent structures is incomplete. This will be one focus of a forthcoming study based on a new suite of simulations that include the effects of β and bottom friction. Preliminary results suggest that coherent structures can be prominent features even in simulations with moderate values of β. Thus the work presented here lays a foundation for understanding the role of coherent structures and eddy fluxes that will apply to more realistic models.

Acknowledgements

We thank Lien Hua and Patrice Klein for providing the spectral code used in this work. We have benefited from conversations with Paola Cessi, Stefan Llewellyn Smith, Rick Salmon and Geoff Vallis. Comments from K. Shafer Smith and an anonymous reviewer significantly improved the presentation.

This work was supported by the National Science Foundation under the

Collaborations in Mathematical Geosciences initiative (grant ATM0222109 and ATM0222104). AFT also gratefully acknowledges the support of an NDSEG Fellowship.

The text of this chapter, in full, is a reprint with minor modifications of the paper "Scaling baroclinic eddy fluxes: vortices and energy balance," *Journal of Physical Oceanography*, **36**, 720-738 (2006) (Copyright of the American Meteorological Society 2006). The dissertation author was the primary researcher and author of this paper. W. R. Young directed and supervised the research, which forms the basis of this chapter.

III

Assessment of a theory for eddy heat fluxes

III.1 Abstract

The eddy heat flux generated by the statistically equilibrated baroclinic instability of a uniform, horizontal temperature gradient is studied using a two-mode β-plane quasigeostrophic model. A summary of the dependence of the eddy diffusivity of temperature D_τ on β, bottom friction κ, the deformation radius λ and the vertical shear of the large-scale flow $2U$ is provided by numerical simulations at 110 different values of the non-dimensional parameter space $\beta_* = \beta\lambda^2/U$ and $\kappa_* = \kappa\lambda/U$. The diffusivity D_τ has a complicated dependence on both β_* and κ_*, highlighted by the fact that reducing κ_* leads to increases (decreases) in D_τ if β is less than (greater than) $\beta_*^{\rm piv} = 11/16$. Previous parameterizations of D_τ, based on Kolmogorovian cascade theories and dependent only on β_*, are shown to be unreliable.

A strong correlation between the barotropic vorticity ζ and the baroclinic mode (or temperature) τ, which exceeds 0.9 in the zonal mean flow, provides a source of energy to the barotropic mode at scales larger than the λ-scale forcing associated with baroclinic instability. The baroclinic mode also plays an active role in energizing the zonal mean flow through non-zero Reynolds stress correlations caused by eddy shearing along the jet flanks. Local inhomogeneity generated by

the spontaneous formation of zonal jets leads to limitations on the traditional use of turbulent diffusivities to describe domain-averaged eddy fluxes.

III.2 Introduction

Rhines (1977) and Salmon (1980) characterize energy transfers in baroclinic turbulence as a direct cascade of the baroclinic mode and a simultaneous inverse cascade of the barotropic mode. This dual cascade scenario serves as an interpretive framework for recent parameterizations of meridional eddy heat and potential vorticity fluxes (Larichev & Held 1995, Held & Larichev 1996, Lapeyre & Held 2003). In these theories the barotropic inverse cascade proceeds to small wavenumbers till the cascade halts at a wavenumber k_0. The length k_0^{-1} characterizes the largest barotropic eddies and k_0^{-1} is also the mixing length of heat and potential vorticity. There are two mechanisms which might determine k_0 by slowing or halting the inverse cascade: the planetary potential vorticity (PV) gradient, β, and bottom friction.

Because the β-effect does not dissipate energy, β alone cannot halt the inverse cascade and determine k_0. Thus bottom drag plays an essential role at the terminus of the inverse cascade by dissipating the kinetic energy continually supplied by release of available potential energy. In other words, truly halting the inverse cascade requires dissipation at large scales, and only bottom drag can accomplish this. An extreme case which makes this point is the problem of statistically steady baroclinic turbulence with $\beta = 0$. At this $\beta = 0$ end-point, the eddy heat flux is exponentially sensitive to the strength of the bottom drag coefficient (Thompson & Young 2006).

In view of the importance of bottom drag, it is dismaying that the bottom drag coefficient does not play an explicit role in the heat-flux parametrizations proposed by Held & Larichev (1996) and Lapeyre & Held (2003, LH03 hereafter). A defense of these dragless heat-flux parametrizations is that β directs energy into

zonal flows (Rhines 1975, Williams 1979, Panetta 1993, Vallis & Maltrud 1993, Lee 1997), which do not contribute to meridional eddy diffusion. In this view the strong zonal flows spontaneously generated by baroclinic turbulence, see Figure III.1 and Figure III.2, serve as a non-diffusive reservoir of barotropic kinetic energy and, through bottom friction, as the energy sink at the terminal wavenumber of the inverse cascade (Smith *et al.* 2002). Thus it is possible to maintain, following LH03, that with $\beta \neq 0$ the amplitude of eddy heat fluxes is insensitive to the bottom drag coefficient.

This seems too good to be true, and it is: a main goal in this computational study of baroclinic instability is to document the importance of bottom drag in limiting baroclinic eddy heat fluxes. We consider the combined effects of β and bottom friction on meridional eddy heat fluxes and report results based on a suite of 110 statistically equilibrated simulations of baroclinic turbulence. These simulations significantly extend and augment the parameter regimes of previous studies. Although the dependence on bottom drag is not nearly as strong as the exponential relation found by Thompson & Young (2006) in the $\beta = 0$ limit, the new simulations show that even with substantial β, bottom drag remains an important control parameter.

In section III.3 we introduce the energy balance integral and define the eddy diffusivities that are used to summarize the suite of simulations. In section III.4 we review and assess the LH03 theory of baroclinic eddy fluxes. Section III.5 provides two specific examples of how the barotropic inverse cascade is modified in the baroclinic system. In section III.6 we confirm that eddy diffusivities and the heat fluxes are insensitive to the domain scale L, and to the the hyperdiffusivity. Our conclusions are presented in section III.7. The equations of motion are summarized in Appendix A.

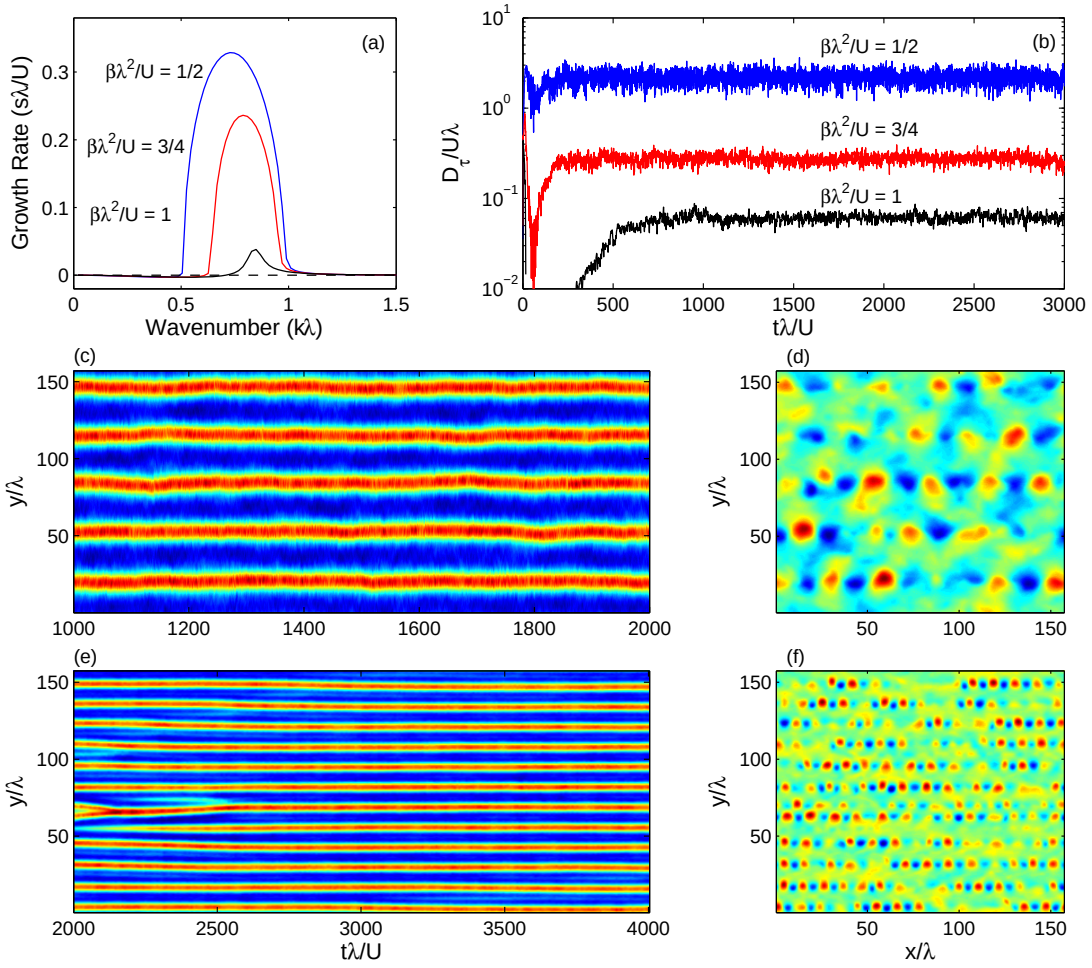

Figure III.1: Overview of the baroclinically unstable β-plane simulations. (a) Growth rates of the linear baroclinic instability for three values of $\beta_* \equiv \beta\lambda/U$ all with $\kappa_* \equiv \kappa\lambda/U = 0.02$; bottom friction produces instability at the frictionless critical value $\beta_* = 1$. (b) Three time series of the eddy diffusivity $D_\tau/U\lambda$ all at $\kappa_* = 0.02$. The "instantaneous" diffusivity is defined by taking $\langle\rangle$ in (III.1) only as an (x, y) average. (c) Hovmoller diagram of the zonally averaged barotropic velocity $-\bar{\psi}_y$ with $\beta_* = 1/2$, $\kappa_* = 0.02$. (d) Snapshot of the eddy streamfunction $\psi' = \psi - \bar{\psi}$ for the simulation in panel (c); ψ' is dominated by isotropic eddies with the same scale as the zonal jets in panel (c). Panels (e) and (f) are the same as (c) and (d) but for a simulation with $\beta_* = 1$ and $\kappa_* = 0.02$.

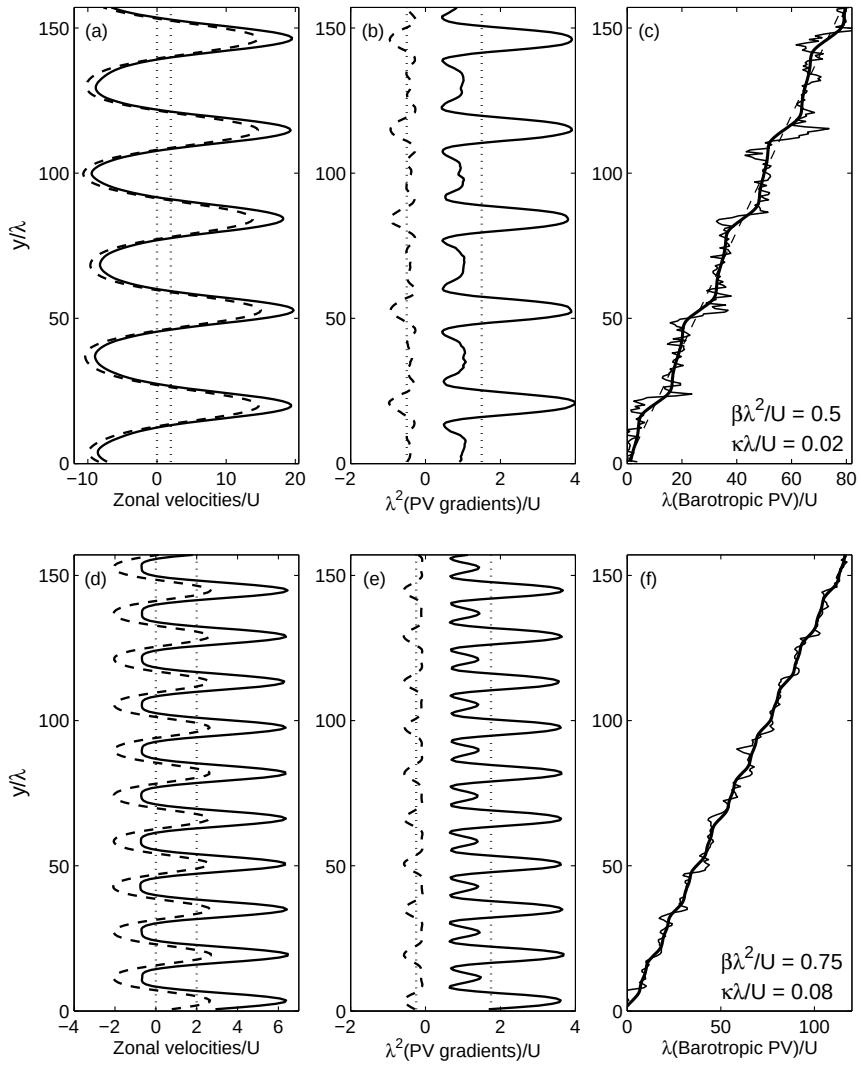

Figure III.2: Zonal mean fields at the parameter values indicated in panels (c) and (f). Panels (a) and (d) show the velocities, $\mathcal{U}_n = U_n - \bar{\psi}_{ny}$ in the upper (solid) and lower (dashed) layers. The basic-state velocity jump between the layers, $2U$, is indicated by the dotted lines. Panels (b) and (e) show the PV gradients in the upper and lower layers. The basic state gradients, $1+\beta_*$ and $1-\beta_*$, are indicated by dotted lines. In panels (c) and (f) the thick solid curve is the barotropic PV, $\beta y + \bar{\psi}_{yy}$; the thin jagged curve is an instantaneous section of barotropic PV, $\beta y + \nabla^2\psi$, along the line $x = 0$.

III.3 Eddy fluxes and diffusivities

To summarize the results of our simulations, we calculate an eddy diffusivity of temperature, D_τ, and obtain the dependence of D_τ on external parameters such as the domain size L, the bottom drag coefficient κ, the Rossby deformation radius λ, the imposed velocity jump $2U$ and β. Our notation is introduced systematically in Appendix A and is largely the same as that of Larichev & Held (1995): $\tau(x,y,t)$ and $\psi(x,y,t)$ are the disturbance stream functions of the baroclinic and barotropic modes respectively. The baroclinic stream function τ plays the role of an interface displacement or a thermal field. The large scale gradient of the baroclinic mode is $-U$, and thus a precise definition of the eddy diffusivity of temperature, D_τ, is

$$D_\tau \equiv U^{-1} \langle \psi_x \tau \rangle \ . \tag{III.1}$$

Here $\langle\rangle$ denotes both a horizontal average over the square $2\pi L \times 2\pi L$ domain, and an additional time average to remove residual turbulent fluctuations. An important point is that D_τ is useful only if it is insensitive to the domain size L (Haidvogel & Held 1980). In this case one can hope that D_τ inferred from a spatially homogeneous calculation can be employed in a more realistic flow with scale separation between a slowly varying mean and baroclinic eddies (Pavan & Held 1996).

The quantity $\langle \psi_x \tau \rangle$ in (III.1) is the product of the barotropic meridional velocity, ψ_x, and the thermal field τ i.e., the meridional heat flux is proportional to $\langle \psi_x \tau \rangle$. Moreover, the mechanical energy balance in a statistically steady state (see Appendix A) is

$$U\lambda^{-2} \langle \psi_x \tau \rangle = \kappa \left\langle |\nabla\psi - \sqrt{2}\nabla\tau|^2 \right\rangle + hyp\nu \,, \tag{III.2}$$

where "$hyp\nu$" indicates the hyperviscous dissipation of energy. The first term on the right hand side of (III.2) is the mechanical energy dissipation (Watts per

kilogram) by bottom drag, κ. We will refer to dissipation by bottom friction as

$$\varepsilon \equiv \kappa \left\langle |\nabla\psi - \sqrt{2}\nabla\tau|^2 \right\rangle , \tag{III.3}$$

which neglects the hyperviscous contribution in (III.2). The left hand side of (III.2) is the energy extracted from the unstable horizontal temperature gradient by baroclinic instability. Enstrophy budgets also identify $\langle \psi_x \tau \rangle$ as the large-scale source balancing the hyperviscous enstrophy sink at high wavenumbers.

As an alternative to the baroclinic-barotropic decomposition, the system can be represented in terms of two layers; the layerwise velocities and potential vorticities are defined in terms of ψ and τ in Appendix A. The domain-averaged PV fluxes in the upper and lower layers are linearly related to the eddy heat flux by the Taylor-Bretherton relationship

$$-\langle v_1 q_1 \rangle = \langle v_2 q_2 \rangle = \lambda^{-2} \langle \psi_x \tau \rangle . \tag{III.4}$$

The basic state gradients of upper and lower layer PV are $\beta + U/\lambda^2$ and $\beta - U/\lambda^2$ respectively. Thus the upper ($n = 1$) and lower ($n = 2$) layer PV diffusivities are related to D_τ by

$$D_\tau = D_1 \left(1 + \frac{\beta\lambda^2}{U} \right), \tag{III.5}$$

$$D_\tau = D_2 \left(1 - \frac{\beta\lambda^2}{U} \right). \tag{III.6}$$

Thus a single quantity, conveniently defined as D_τ in (III.1), summarizes all of the important quadratic power integrals and fluxes in homogeneous baroclinic turbulence.

Dimensional considerations (Haidvogel & Held 1980) show that

$$D_\tau = U\lambda \times D_{\tau *} \left(\frac{L}{\lambda}, \frac{\kappa\lambda}{U}, \frac{\beta\lambda^2}{U}, \frac{\nu}{UL^7} \right) , \tag{III.7}$$

where $D_{\tau *}$ is a dimensionless function. The final argument of $D_{\tau *}$, involving the hyperviscosity ν, is relatively small (see section III.6). For brevity we suppress

reference to this hyperviscous parameter. We also focus on a single value $L/\lambda = 25$, however, we check for dependence on L as described in section III.6.

Figure III.3(a) summarizes a suite of 110 numerical simulations revealing the main features of the function $D_{\tau *}(25, \beta_*, \kappa_*)$, where $\beta_* \equiv \beta\lambda^2/U$ and $\kappa_* \equiv \kappa\lambda/U$. $D_{\tau *}$ varies over five orders of magnitude in response to much smaller changes in β_* and κ_*. Some trends in Figure III.3 are clear: $D_{\tau *}$ decreases monotonically with increasing β_*. However, other trends are more complicated, particularly the role of bottom friction. Close to the special "pivot" value $\beta_* = \beta_*^{\rm piv} \approx 11/16$, $D_{\tau *}$ has a weak dependence on bottom friction. For $\beta_* < \beta_*^{\rm piv}$, increasing bottom friction reduces $D_{\tau *}$, whereas for $\beta_* > \beta_*^{\rm piv}$, increasing bottom friction increases $D_{\tau *}$. This behavior is shown in Figure III.3(b) where five values of β_* illustrate the bottom friction dependence. The same trend is seen in Figure 14 of Panetta (1993).

III.4 Assessment of LH03

The energy balance in (III.2) provides one relationship between the dissipation ε and the energy production, or equivalently, the eddy diffusivity D_τ. Specifically, using the definitions of D_τ and ε in (III.1) and (III.3), and neglecting the hyperviscous dissipation, we obtain

$$\frac{U^2}{\lambda^2} D_\tau \approx \varepsilon \,. \tag{III.8}$$

Figure III.4(a) shows that (III.8) is an excellent approximation; the small deviation of the ratio $\varepsilon\lambda^2/U^2 D_\tau$ from 1 is due to the $hyp\nu$ contribution to the dissipation. The hyperviscous dissipation is never more than 12% and can be reduced further by increasing the resolution (see section III.6).

Held & Larichev (1996) propose a closure obtained from cascade arguments in which β halts the barotropic inverse cascade by directing energy into zonal modes. Forming a diffusivity from β and the inverse cascade rate (which

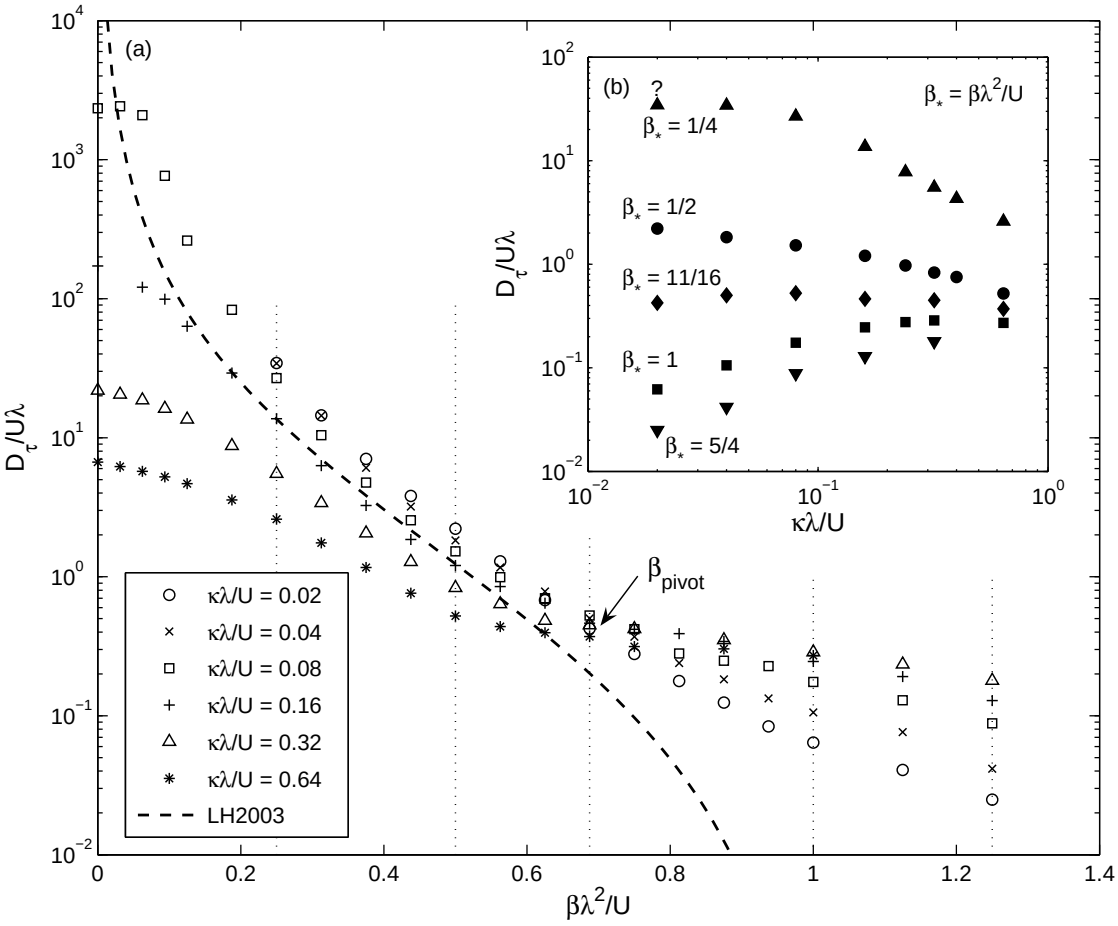

Figure III.3: (a) Survey of the non-dimensional meridional eddy heat flux $D_\tau/U\lambda$ at 110 different values of the parameters $\beta_* = \beta\lambda^2/U$ and $\kappa_* = \kappa\lambda/U$. The dashed curve indicates the D_τ parameterization proposed by Lapeyre & Held (2003) given by (III.10) (with $c = 1.25$). At $\beta_* = \beta_{\rm pivot} = 0.72$, there is weak dependence on κ_*. For $\beta_* < \beta_{\rm pivot}$, increasing κ_* decreases D_τ, while for $\beta_* > \beta_{\rm pivot}$, increasing κ_* increases D_τ. Data at five values of β_* (indicated by the dotted lines) are expanded in panel (b) to illustrate the weaker but still significant dependence on κ_*. The point at $\beta_* = 1/4$ and $\kappa_* = 0.02$ is flagged with a "?" to indicate possible dependence on domain size (see section III.6).

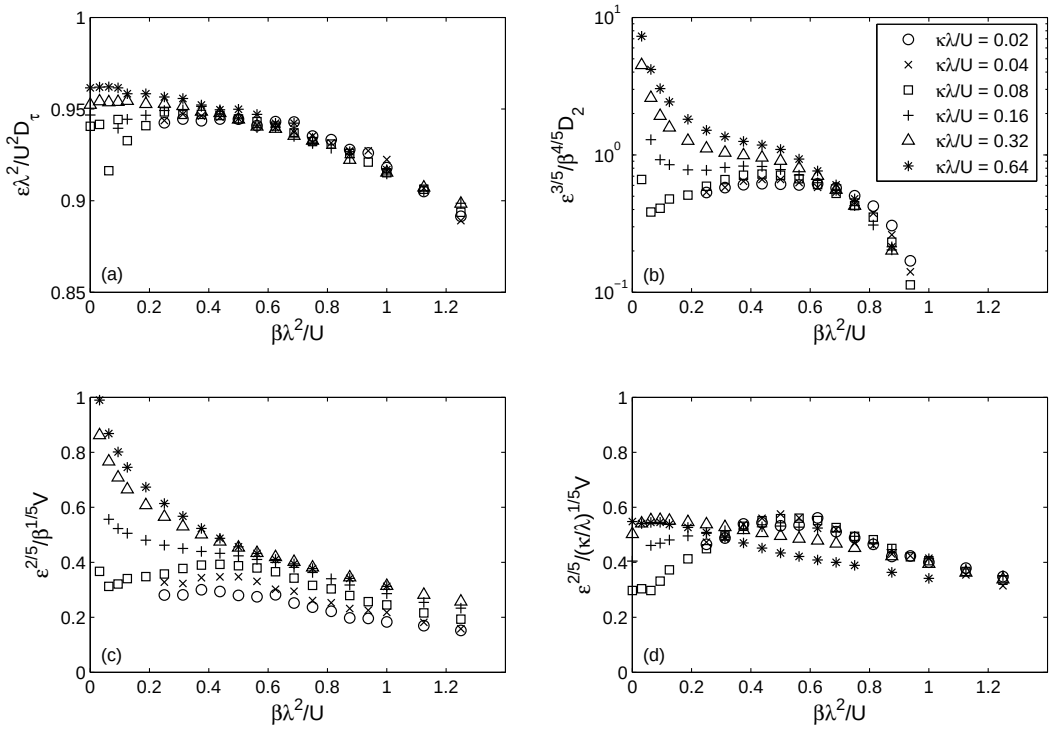

Figure III.4: (a) Ratio of terms in the energy balance approximation $U^2 D_\tau/\lambda^2 \approx \varepsilon$. The systematic departure from 1 is because the hyperviscous dissipation is not included in definition of ε in (III.3). (b) The ratio $D_2 \propto \varepsilon^{3/5}\beta^{-4/5}$. ($c$) The ratio $\varepsilon^{2/5}/V\beta^{1/5}$. ($d$) The ratio $\varepsilon^{2/5}\lambda^{1/5}/V\kappa^{1/5}$. The collapse in panel (d) is better than the LH03 proposal in panel (c).

is assumed to be equivalent to ε in a steady state), dimensional analysis gives $D_\tau = c\varepsilon^{3/5}\beta^{-4/5}$, where c is a dimensionless constant. This relation between D, ε and β is supported by the arguments and numerical simulations of Smith *et al.* (2002), which employ a barotropic model. Combining $D_\tau = c\varepsilon^{3/5}\beta^{-4/5}$ with (III.8) gives the Held & Larichev (1996) result, namely $D_\tau = c^{5/2}U^3/(\lambda^3\beta^2)$.

One immediate problem with Held & Larichev's argument is that there are three diffusivities: in addition to D_τ we have the PV diffusivities D_1 and D_2 in (III.5) and (III.6). If one argues that one of these three diffusivities involves only ε and β, then the other two will have additional dependence on other parameters. Thus the association of the dimensional combination $c\varepsilon^{3/5}\beta^{-4/5}$ with D_τ, as opposed to D_1 or D_2, is a significant hypothesis. Indeed LH03 updated the theory of Held & Larichev by identifying the eddy diffusivity $c\varepsilon^{3/5}\beta^{-4/5}$ with the lower layer PV diffusivity D_2, rather than D_τ:

$$D_2 \approx c\varepsilon^{3/5}\beta^{-4/5}\,. \tag{III.9}$$

The motivation for (III.9) is that the weaker PV gradient in the lower layer allows larger meridional particle excursions so that lower layer PV behaves more like a passive tracer. The ratio $\beta^{-4/5}\epsilon^{3/5}D_2^{-1}$ is shown in Figure III.4(b): there is strong dependence on both β and κ indicating that c in (III.9) is not constant.

Using (III.6) and (III.8), D_2 and ε are eliminated from (III.9), which yields the prediction

$$D_\tau/U\lambda \approx c^{5/2}\beta_*^{-2}\,(1-\beta_*)^{5/2}\,, \tag{III.10}$$

where $\beta_* \equiv \beta\lambda^2/U$. The relation above is the dotted curve in Figure III.3 with $c = 5/4$ [1]. Given the quantitative problems with (III.9), it is not surprising that (III.10) fails to condense the simulations.

The absence of κ_* in (III.10) leads to poor agreement at both small values of β_*, and also when β_* is close to 1. Thompson & Young (2006) discuss the case

[1] LH03 tested (III.9) with simulations only at $\kappa_* = 0.16$. At this particular value of κ_* our results agree with theirs.

$\beta_* = 0$ in detail. Their conclusion is that a well-defined D_τ — independent of domain size — exists provided that κ_* is not too small[2]. When β_* is close to 1, (III.10) does not account for the fact that bottom friction destabilizes the system beyond the frictionless critical value $\beta_* = 1$ (Holopainen 1961; Pedlosky 1987; Arbic & Flierl 2004). Equation (III.10) predicts $D_\tau \to 0$ as β_* approaches 1 from below, whereas statistically steady, small non-zero values of D_τ are achievable out to at least $\beta_* \approx 1.5$. Finally, if $\beta_* < \beta_*^{\rm piv}$ then D_τ decreases with increasing κ_*. But if $\beta_* > \beta_*^{\rm piv}$ then D_τ increases with increasing κ_*. Thus the simple remedy of making c in (III.10) a function of κ_* cannot collapse the data.

A consequence of the dimensional arguments leading to (III.9) is that other important descriptors of the flow also remain independent of bottom friction. Thus another prediction of LH03 is

$$V = c_V \varepsilon^{2/5} \beta^{-1/5} \,, \tag{III.11}$$

where

$$V \equiv \sqrt{\langle \psi_x^2 \rangle} \,, \tag{III.12}$$

is the RMS meridional velocity of the barotropic mode. However, when we plot the ratio $\varepsilon^{2/5}/(\beta^{1/5} V)$ in Figure III.4(c), we find that the result is not independent of κ_*. An empirical scaling obtained by replacing $\beta^{-1/5}$ with $(\kappa/\lambda)^{-1/5}$ in (III.11) results in a much better collapse of the data, shown in Figure III.4(d).

We conclude that the major predictions of LH03, (III.10) and (III.11), are not quantitatively reliable, and that the theory has no skill at predicting eddy transports.

As a standard against which future heat-flux parameterizations might be judged it is useful to have a compact formula for $D_{\tau *}$ in terms of β_* and κ_*. Thus we advocate the empirical expression

$$D_{\tau *} \approx \beta_*^{-4} \left[1.7 + (3 - 4\beta_*)\, \kappa_* \right]^{-4} \,, \quad \text{provided } 0.25 \le \beta_* \le 1.25 \,. \tag{III.13}$$

[2]The $\beta_* = 0$ points in Figure III.3 satisfy this condition and are in Thompson & Young's local mixing regime.

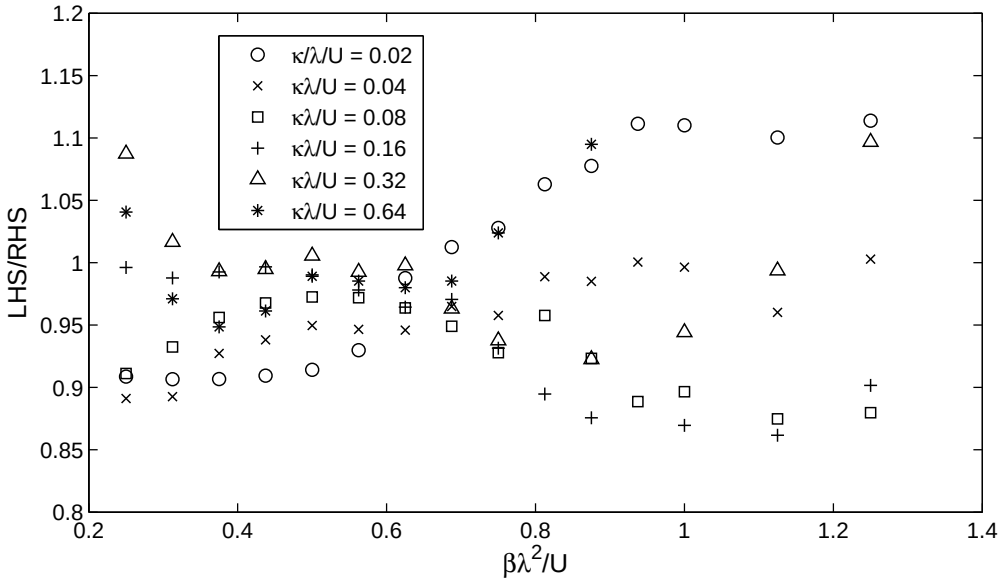

Figure III.5: The ratio of the LHS of (III.13) to the RHS.

Equation (III.13) is constructed using $\beta_*^{\rm piv} = 3/4$ and this fits $D_{\tau *}$ to within $\pm 10\%$ over a broad range of β_* and κ_* values (see Figure III.5). The fit (III.13) still has the problem that $D_{\tau *}$ grows to infinity as $\beta_* \to 0$. At small values of β_* a different expression, tending towards the exponential dependence on κ_* observed by Thompson & Young (2006), is required.

III.5 The barotropic cascade rate

A main assumption in the LH03 heat-flux closure is that the inverse cascade rate of the *barotropic* mode,

$$\varepsilon_\psi \equiv \kappa \left\langle |\nabla \psi|^2 \right\rangle \ , \tag{III.14}$$

is nearly equal to (or proportional to) the total cascade rate ε defined in (III.3). This assumption is used to construct (III.9) and is motivated by the results of Smith *et al.* (2002). These authors conducted a series of forced-dissipative barotropic simulations showing that in the β-dominated regime of barotropic turbulence, the meridional eddy diffusivity is proportional to $\varepsilon_\psi^{3/5} \beta^{-4/5}$.

A logical application of the results of Smith *et al.* to the baroclinic problem begins by writing the barotropic mode equation (A.6) in the form

$$\zeta_t + J(\psi, \zeta) + \beta\psi_x = f_\psi - \kappa\zeta - \nu\nabla^8\zeta\,, \tag{III.15}$$

where $\zeta \equiv \nabla^2\psi$, and the forcing of the barotropic mode by the baroclinic mode is

$$f_\psi \equiv \sqrt{2}\kappa\nabla^2\tau - U\nabla^2\tau_x - J(\tau, \nabla^2\tau)\,. \tag{III.16}$$

The barotropic energy equation is formed by multiplying (III.15) by ψ and averaging. Thus we find that the energy supplied to the barotropic inverse cascade is $\langle\psi f_\psi\rangle$ and that the dissipation of barotropic energy is ε_ψ in (III.14) (neglecting hyperviscous contributions). The assumption is that the theory and simulations of Smith *et al.* (2002) identify a universal scaling regime of barotropic turbulence in which all important physical quantities are determined by dimensional analysis based on only β and the cascade rate $\varepsilon_\psi \approx \langle\psi f_\psi\rangle$. All other details of the forcing function f_ψ are supposedly irrelevant. Thus in applying the results of Smith *et al.* (2002) to the baroclinic problem one should use ε_ψ, rather than ε, in scaling relations such as (III.9).

Figure III.6(a) shows that the ratio $\varepsilon_\psi/\varepsilon$ is not constant. It is striking that throughout much of the parameter space $\varepsilon_\psi/\varepsilon$ in Figure III.6(a) is significantly larger than one. This is expected because bottom drag retards the lower-layer flow so that estimates of the dissipation using the barotropic velocity are too large (Arbic & Flierl 2004). However the sensitivity of $\varepsilon_\psi/\varepsilon$ is notable, and one can further explain this by expanding ε in (III.3) as

$$\varepsilon = \varepsilon_\psi + \kappa\left(-2\sqrt{2}\,\langle\nabla\psi\cdot\nabla\tau\rangle + 2\,\langle|\nabla\tau|^2\rangle\right)\,. \tag{III.17}$$

The second term on the right hand side of (III.17) is negative because there is a strong anti-correlation between τ and $\zeta \equiv \nabla^2\psi$:

$$-2\sqrt{2}\,\langle\nabla\psi\cdot\nabla\tau\rangle = 2\sqrt{2}\,\langle\zeta\tau\rangle < 0\,, \tag{III.18}$$

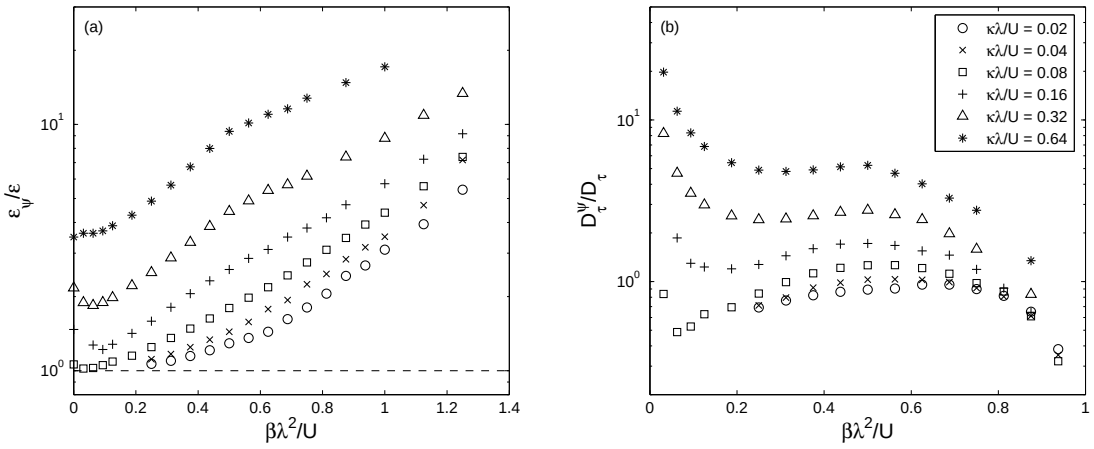

Figure III.6: (a) Ratio of the dissipation by the barotropic mode ε_ψ defined in (III.14) to the total dissipation ε defined in (III.3). (b) Ratio of the predicted diffusivity D_τ^ψ in (III.20) to the observed diffusivity D_τ. The constant c in (III.20) is taken to be 1.25.

(see Figure III.7). This anti-correlation means that ε is significantly less than the barotropic cascade rate ε_ψ.

Although Figure III.6(a) shows that there is not a simple relation between ε and ε_ψ, one can still attempt to use Smith *et al.*'s scaling by modifying (III.9) to

$$D_2 \approx c\varepsilon_\psi^{3/5}\beta^{-4/5}\,. \tag{III.19}$$

Combining (III.6) with (III.19), one then arrives at a modified version of (III.10):

$$D_\tau/U\lambda = c\beta_*^{-4/5}(1-\beta_*)\left(\varepsilon_\psi\lambda/U^3\right)^{3/5}\,. \tag{III.20}$$

We test (III.20) diagnostically in Figure III.6(b) with disappointing results. Thus this attempt to resuscitate LH03 is unsuccessful and we conclude that the barotropic diffusion regime identified by Smith *et al.* (2002) does not apply to the baroclinic problem.

The spontaneous formation of strong zonal-mean flows is a prominent feature of both the baroclinic problem and the barotropic problem. Therefore, it is tempting to think that the zonal mean dynamics of the baroclinic problem are dominated by the barotropic mode, especially since the zonal jets are almost

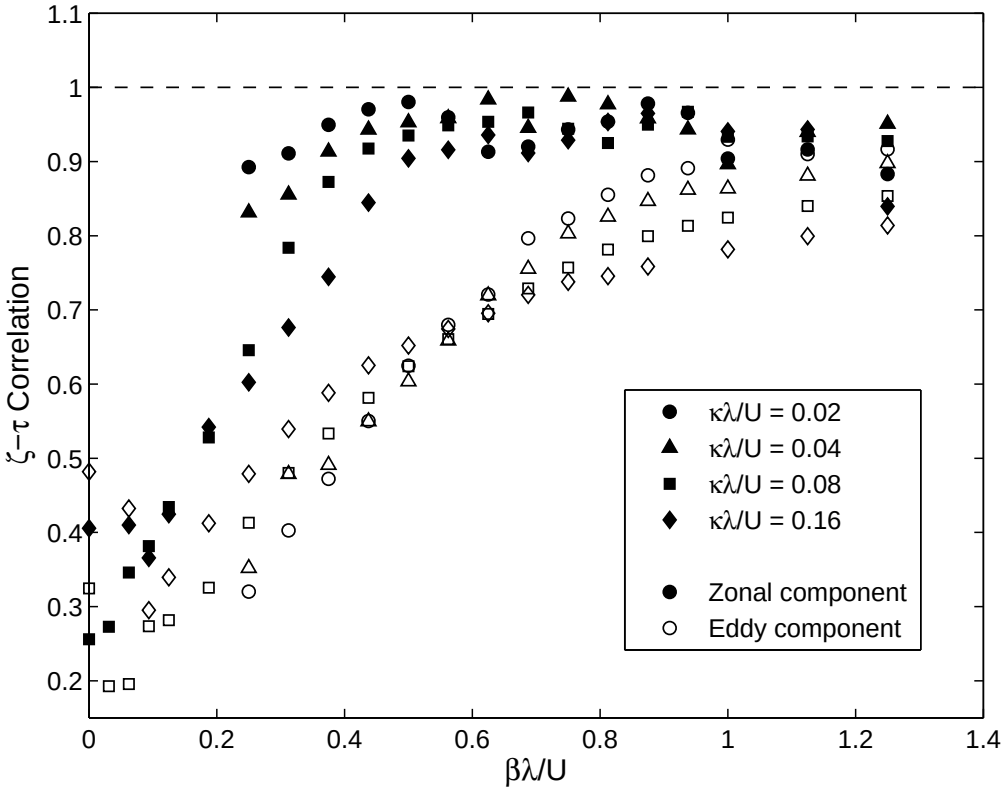

Figure III.7: Anti-correlation $-\langle\zeta\tau\rangle / \sqrt{\langle\zeta^2\rangle \langle\tau^2\rangle}$ between the barotropic vorticity ζ and the temperature τ for both zonally-averaged (solid symbols) and eddy (open symbols) components of the flow.

barotropic. However the zonal mean energy balance reveals some problems with this view. We obtain the zonal energy balance, in layer form, by multiplying the upper and lower layer PV equations (A.10) and (A.11) by $\bar{\psi}_1$ and $\bar{\psi}_2$ respectively, and averaging over both space and time. This yields

$$\begin{aligned} \mathcal{Z}_t &= \left\langle \bar{u}_{1y}\left(\overline{u_1'v_1'}\right) + \bar{u}_{2y}\left(\overline{u_2'v_2'}\right) + \tfrac{1}{2}\left(\bar{u}_2 - \bar{u}_1\right)\left(\overline{\psi_1'\psi_{2x}'}\right)\right\rangle \\ &- \frac{\kappa}{2}\left\langle \left|\left(\sqrt{2}-1\right)\bar{\psi}_{1y} - \left(\sqrt{2}+1\right)\bar{\psi}_{2y}\right|^2\right\rangle , \end{aligned} \tag{III.21}$$

where $\mathcal{Z}$ is the zonal energy

$$\mathcal{Z} \equiv \tfrac{1}{2}\left\langle \bar{\psi}_{1y}^2 + \bar{\psi}_{2y}^2 + \tfrac{1}{2}\lambda^{-2}\left(\bar{\psi}_1 - \bar{\psi}_2\right)^2\right\rangle . \tag{III.22}$$

The first three terms on the RHS of (III.21) are exchanges of energy between zonal and eddy components. The first two are sources of zonal energy due to non-zero Reynolds stress correlations caused by eddy tilting on the jet flanks. This process has been described as a type of negative viscosity (McIntyre 1970; Manfroi & Young 1999; Dritschel *et al.* 2006) responsible for the remarkable persistence and stability of zonal jets. The third term is a sink of zonal-mean energy representing extraction of potential energy stored in the mean temperature gradient through baroclinic instability. The final terms are dissipation of $\mathcal{Z}$ by bottom friction.

Figure III.8(a), which shows the upper and lower layer energy transfer terms for the simulation with $\beta_* = 3/4$ and $\kappa_* = 0.08$, illustrates the motivation for writing (III.21) in terms of layers. Nearly all energy transfer from the eddies into the zonal modes occurs in the upper layer. This behavior is characteristic of all simulations in which steady zonal jets form. Figure III.8(a) also confirms that the regions where upper layer energy transfer is largest are located on both flanks of the eastwards jets. Here the meridional shear is greatest and the eddies are sheared. The scaled barotropic zonal velocity $-\bar{\psi}_y$ is given by the dotted line for reference.

Figure III.8(a) implies that baroclinic and barotropic eddies make equal contributions to the energy in zonal modes. The lower layer transfer term has a

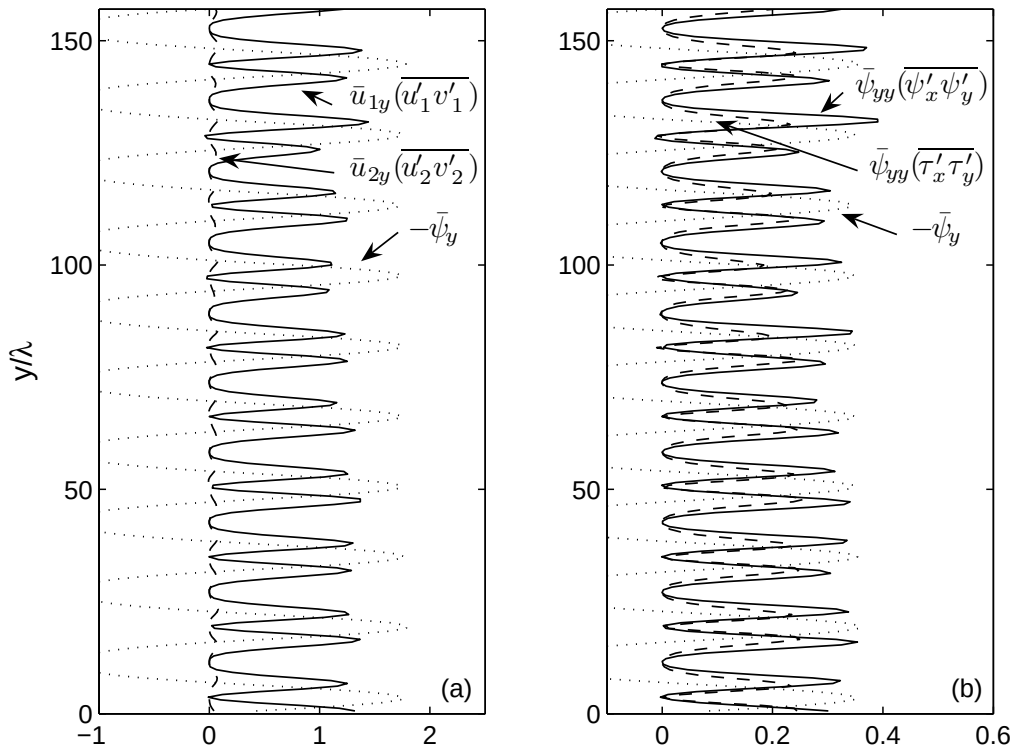

Figure III.8: (a) Zonal and time averages of the energy transfer terms in upper (solid line) and lower (dashed line) layers for the simulation with $\beta_* = 3/4$ and $\kappa_* = 0.08$. The barotropic zonal velocity divided by a factor of 2 is given by the dotted line. (b) Zonal and time averages of the transfer of energy into the barotropic zonal modes by the barotropic eddies (solid line) and the baroclinic eddies (dashed line) for the same simulation as panel (a). The barotropic zonal velocity divided by a factor of 10 is given by the dotted line.

complicated expansion in terms of modes:

$$\bar{u}_{2y}\left(\overline{u_2'v_2'}\right) = \left(\bar{\psi}-\bar{\tau}\right)_{yy}\left(-\psi_x'\psi_y' + \psi_x'\tau_y' + \psi_y'\tau_x' - \tau_x'\tau_y'\right) . \tag{III.23}$$

This term vanishes if $\bar{\psi}-\bar{\tau} \approx 0$, but our simulations show that $\bar{\psi} > \bar{\tau}$, i.e. the zonal flow is largely barotropic (see Figure III.2). Since the terms on the RHS of (III.23) must cancel, we conclude that both barotropic and baroclinic eddy components make important contributions to forcing the zonal mean component. This is confirmed by comparing, for example, the terms $\bar{\psi}_{yy}\left(\psi_x'\psi_y'\right)$ and $\bar{\tau}_{yy}\left(\tau_x'\tau_y'\right)$, which represent forcing of the barotropic zonal flow by barotopic and baroclinic eddies respectively. Figure III.8(b) shows that energy transfer by these two terms is roughly the same.

From Figure III.8 we conclude that the dual cascade view, where transfer between ψ and τ only occurs near λ, is incorrect. Instead, a substantial amount of energy can "jump" directly from baroclinic eddies into zonal modes at scales much larger than λ, thus bypassing the barotropic inverse cascade.

III.6 Domain size, resolution and hyperviscosity

To this point we have suppressed reference to the non-dimensional parameter L/λ. However, a diffusive parameterization is well-founded only if D_τ is independent of domain size and of the hyperviscosity and resolution (Haidvogel & Held 1980). Thus before one trusts the data in Figure III.3 one must show that large changes in the domain size L make only small changes in D_τ.

Some results of this sensitivity study are summarized in Figure III.9 which shows the barotropic jet velocity $u_J(y) \equiv -\bar{\psi}_y$ and D_τ for six simulations at $\beta_* = 1/2$ and $\kappa_* = 0.02$. In each case the time averaging was completed for at least $1000\lambda/U$. The length of the u_J-profile indicates the size of the domain, which varies between $2\pi\times(12.5\lambda)$ and $2\pi\times(50\lambda)$. The curves have been translated so that the dotted lines mark the zero crossings of $u_J(y)$. Run XI, which is the

simulation in Figure III.3, has five stable jets. The other five u_J-profiles show some indication of vacillation in n_J. Since run XI is stable with five jets, it is perhaps not surprising that runs XII and XIII, which halve the domain size, have between two and three jets. Still, the magnitude of the zonal flow is similar in each simulation and the indicated values of $D_{\tau *}$ in Figure III.9 are within 10% of the $D_\tau^{XI} = 2.217$. Motivated by these results we have adopted the policy of trusting a data point in Figure III.3 if the variation in D_τ resulting from halving and doubling the domain size is $\pm 10\%$. Thus according to this criterion run XI is trustworthy.

Runs with the smallest values of bottom friction in Figure III.3, namely $\kappa_* = 0.02$ and 0.04, fail the $\pm 10\%$ criterion if β is also sufficiently small. Thus in Figure III.3 we have not extended our survey of D_τ to $\beta_* < 1/4$ *and* $\kappa_* \leq 0.04$. Indeed with $\kappa \leq 0.04$ and $\beta = 0$ we are firmly in the global mixing regime described by Thompson & Young (2006). In this regime there are only a few vortices in the domain and statistical descriptions based on an eddy diffusivity are meaningless because there is no scale separation between L and the mixing length. The data points in Figure III.3(a) that extend to values of $\beta_* < 1/4$ all have largish values of κ_* so that these simulations are within Thompson & Young's local mixing regime even at $\beta_* = 0$.

To further probe sensitivity to domain size, resolution and hyperviscosity, we conducted the suite of 24 simulations summarized in Table III.1; the main simulations appearing in Figure III.3 are shown Table III.1 in boldface type. In 22 of these simulations we take $\kappa_* = 0.02$ and we obtain at least five runs at each of $\beta_* = 1/4$, 1/2, 3/4 and 1. This study tests different combinations of domain size L, numerical resolution, and hyperviscosity ν. For example, at $\beta_* = 1/2$, runs VIII, XI and XIII have the same resolution, whereas runs IX, X and XII have double resolution.

Table III.1 lists domain-averaged statistics for a number of key quantities. With the exception of the run at $\beta_* = 1/4$ and $\kappa_* = 0.02$, domain-averaged statistics are constant to within roughly $\pm 10\%$ and for simulations with $\beta_* \geq$

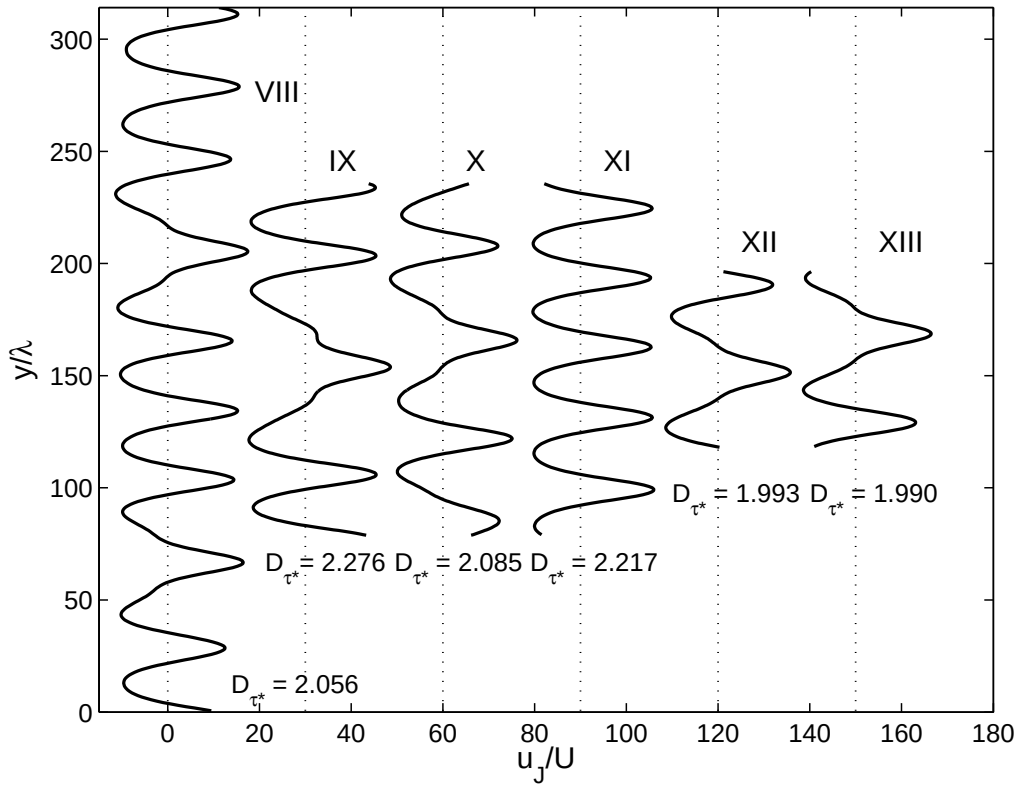

Figure III.9: Zonal and time-averaged barotropic velocities $u_J(y) \equiv -\bar{\psi}_y$ for sensitivity studies (VIII-XIII) listed in Table III.1 with $\beta_* = 1/2$. For clarity the curves have been translated horizontally; intersections with the dotted lines indicate zero crossings u_J. The five runs correspond to varying domain sizes and resolutions. Most runs suffer from quantization problems that may be related to differences in the hyperviscosity parameter. Run XI is stable and has an odd number of jets, therefore a quantization problem may be expected when halving the domain size (Runs XII and XIII). The domain-averaged heat flux is indicated for each simulation; domain-averaged statistics are within $\pm 5\%$ for all runs with $\beta_* > 1/4$ (see Table III.1).

Table III.1: Eddy statistics for sensitivity study simulations. All runs have $\kappa\lambda/U = 0.02$ except for two runs in italics which have $\kappa\lambda/U = 0.04$. The bold entries indicate the main simulations shown in Figure III.3.

	$\beta\lambda^2/U$	L/λ	ν/UL^7	Grid points	$D_\tau/U\lambda$	V/U	u_J/U	$\varepsilon_\nu/\varepsilon_{\text{tot.}}$
I	1/4	50	10^{-17}	512^2	39.48	19.42	35.38	0.0493
II	1/4	25	10^{-15}	512^2	36.50	20.53	33.13	0.0443
III	**1/4**	**25**	$\mathbf{10^{-15}}$	$\mathbf{256^2}$	**34.43**	**18.89**	**33.20**	**0.0575**
IV	1/4	12.5	10^{-13}	256^2	34.72	20.75	34.28	0.0285
V	1/4	12.5	10^{-13}	128^2	31.39	18.26	31.32	0.109
VI	*1/4*	*50*	10^{-17}	512^2	*35.68*	*17.35*	*18.65*	*0.0538*
VII	*1/4*	*25*	10^{-15}	256^2	*34.00*	*16.04*	*20.72*	*0.0557*
VIII	1/2	50	10^{-17}	512^2	2.056	5.092	8.848	0.0562
IX	1/2	25	10^{-17}	512^2	2.276	5.478	9.398	0.0148
X	1/2	25	10^{-15}	512^2	2.085	5.170	8.911	0.0395
XI	**1/2**	**25**	$\mathbf{10^{-15}}$	$\mathbf{256^2}$	**2.217**	**5.534**	**9.182**	**0.0562**
XII	1/2	12.5	10^{-13}	256^2	1.933	5.143	8.540	0.0380
XIII	1/2	12.5	10^{-13}	128^2	1.990	5.176	8.635	0.0563
XIV	3/4	50	10^{-17}	512^2	0.268	2.567	3.536	0.0575
XV	3/4	25	10^{-15}	512^2	0.269	2.608	3.539	0.0480
XVI	3/4	25	10^{-14}	256^2	0.251	2.577	3.422	0.0927
XVII	**3/4**	**25**	$\mathbf{10^{-15}}$	$\mathbf{256^2}$	**0.277**	**2.590**	**3.591**	**0.0601**
XVIII	3/4	12.5	10^{-13}	256^2	0.287	2.825	3.593	0.0456
XIX	3/4	12.5	10^{-13}	128^2	0.274	2.610	3.600	0.0588
XX	1	50	10^{-17}	512^2	0.0659	1.756	2.202	0.0772
XXI	1	25	10^{-15}	512^2	0.0640	1.713	2.178	0.0581
XXII	**1**	**25**	$\mathbf{10^{-15}}$	$\mathbf{256^2}$	**0.0620**	**1.681**	**2.132**	**0.0821**
XXIII	1	12.5	10^{-13}	256^2	0.0671	1.884	2.192	0.0673
XXIV	1	12.5	10^{-13}	128^2	0.0622	1.668	2.167	0.1121

1/2, all quantities are constant to within ±5%. Deviation between the different simulations are most likely related to differences in the hyperviscous contribution to the dissipation which is listed in the final column of Table III.1. Naturally the higher resolution runs have a smaller ratio of hyperviscous dissipation to total dissipation (although the coefficient ν is adjusted for domain size). It is satisfying that if the domain size is fixed and ν is varied by an order of magnitude, eddy statistics change only a little.

The exceptional run in Table III.1 is at $\beta_* = 1/4$ and $\kappa_* = 0.02$. In this case doubling L increases D_τ by 20%. This is the most sensitive data point in Figure III.3(a)[3] and accordingly we have flagged this data point Figure III.3(b) with a question mark. To confirm that a well defined eddy diffusivity exists at $\beta_* = 1/4$, we tested the data point with $\kappa_* = 0.04$ by doubling the domain size (see the two italic rows in table 1). This results in a 5% increase in D_τ and supports the view that the run at $\beta_* = 1/4$ and $\kappa_* = 0.04$ is trustworthy.

To summarize, based on the results in Table III.1 we conclude that the eddy diffusivity D_τ is independent of domain size to within ±10% for simulations with $\beta_* > 1/4$ or $\kappa_* > 0.02$.

III.7 Conclusions

In this computational study we have shown that D_τ depends on both β_* and κ_* over a broad region of parameter space. Although D_τ has a greater sensitivity to changes in β_* than in κ_*, especially in simulations where steady zonal jets form, scalings based on energy cascade arguments are inaccurate: see Figure III.4(b) and (c). While increases in β_* result in a monotonic decrease in the eddy heat flux, the κ_* dependence is more complicated with D_τ increasing (decreasing) in response to increasing κ_* at β_* greater than (less than) $\beta_*^{\rm piv}$.

[3]The fact that $D_\tau/U\lambda$ is larger in the large-domain simulation (run I in Table III.1) suggests that the leveling off of the slope at $\kappa_* = 0.02$ in the $\beta_* = 1/4$ series of Figure III.3(b) is the first indication of domain dependence.

Perhaps the most novel result presented here is the importance of the baroclinic mode in determining the eddy heat flux and other important descriptors of the equilibrated flow. In simulations in which β leads to the spontaneous generation of zonal jets, it is inappropriate to view the baroclinic mode as simply an innocuous deformation-scale mechanism for energizing the inverse cascade of the barotropic mode. This view fails in at least two important respects:

(a) total dissipation ε cannot be easily related to the barotropic dissipation ε_ψ;

(b) barotropic and baroclinic eddies make equal contributions to forcing the zonal flow.

With respect to point (a), we show in section III.5 that there is a strong correlation between the barotropic vorticity ζ and the baroclinic streamfunction τ. Thus the cross-term in ε, which is equal to $2\sqrt{2}\kappa\,\langle\zeta\tau\rangle$, is an energy source for the barotropic mode. Regarding point (b), previous theories (Vallis & Maltrud 1993; Lapeyre & Held 2003) assume that all energy in the zonal modes results from transfers out of the *barotropic* eddies at a wavenumber k_β determined by the strength of β. However, results from our simulations summarized in Figure III.8 show that *upper layer* Reynolds stress correlations are responsible for almost all of the energy transfer into the zonal mean component. If one expresses this upper-layer transfer in terms of modes then it projects in a complicated fashion on both the barotropic and baroclinic modes. Thus it is misleading to view the excitation of zonal mean flows as a purely barotropic process.

The importance of the baroclinic mode is in some ways not too surprising since differences in PV transport between upper and lower layers have been reported prior to this study (Lee & Held 1993). The upper layer is more wavelike and zonal jets are more efficient barriers to transport at upper levels (Greenslade & Haynes 2006). The lower layer, on the other hand, appears more turbulent and allows larger excursions across the jet paths. This behavior led Lapeyre & Held

(2003) to make the sensible choice of applying a turbulent diffusivity to the lower layer flow.

While the lower layer is more turbulent and perhaps more amenable to a diffusive parameterization, the results of our simulations also highlight important limitations in applying turbulent diffusivities in β-plane turbulence. Haidvogel & Held (1980) stressed the importance of scale separation between mean-flow variations and eddies in defining a physically meaningful, horizontally-homogeneous problem. To illustrate this point, Haidvogel & Held contrast quasigeostrophic turbulence with Bénard convection as shown in their Figure 1 (and reproduced in panels (a) and (c) of Figure III.10). Haidvogel & Held argue that quasigeostrophic turbulence is a homogeneous problem because (1) a steady state exists and (2) eddy statistics remain insensitive to changes in domain size. Bénard convection does not satisfy criterion (2) and is therefore not a homogeneous turbulence problem.

Under the influence of β, though, zonal jets develop spontaneously leading to local inhomogeneity. In this case, the diagram shown in panel (b) of Figure III.10, following Haidvogel & Held (1980), is a more relevant picture of β-plane quasigeostrophic dynamics. The sketch in panel (b) is also analogous to Dritschel *et al.*'s (2006) comparison of β-plane turbulence to layering in a weakly-mixed stratified fluid, or what they refer to as the Phillips effect. In panel (b), the mean flow can be identified in one of two ways. If the mean flow includes both the basic state gradient (solid line) and the gradient arising from the zonal jets, then the assumption of scale separation between mean and eddy quantities is not satisfied. In this case the dominant eddies are the storms embedded within the jets, and these eddies have scales comparable to the jet width. The alternative, then, is to view the mean as the basic state and include the jets as part of the eddy field. There are two striking examples as to why this description of the flow may be misleading.

If we consider the zonally-averaged upper layer PV equation (A.10) in

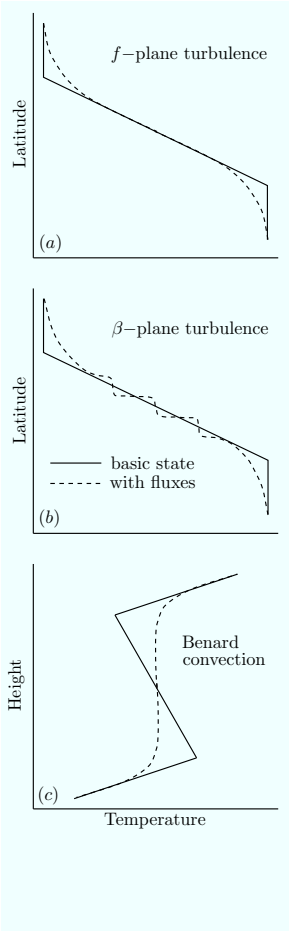

Figure III.10: Diagrammic sketch of homogeneous and inhomogeneous turbulence examples based on Haidvogel & Held's (1980) Figure 1. (a) In quasigeostrophic turbulence where $\beta = 0$ or is weak, there is sufficient scale separation between the mean temperature gradient and the eddies so that far from boundaries, the system tends towards homogeneity. (b) Under the influence of β, zonal jets are spontaneously generated leading to local inhomogeneity. The spacing between the jets is insensitive to changes in domain size. (c) Bénard convection is a classical example of inhomogeneous turbulence in which the size of the system is always important.

the limit where all dissipation is in the lower layer[4], we find

$$\left(\overline{v_1' q_1'}\right)_y = 0\,. \tag{III.24}$$

The upper layer PV flux is independent of meridional position; the PV flux is also proportional to D_τ through the relationship $-\langle v_1 q_1\rangle = \lambda^{-2}\langle v\tau\rangle$ given in (III.4). Traditional diffusivities, such as D_τ reported in Figure III.3, represent full domain averages, but we can also consider y-dependent diffusivities with respect to the zonally averaged PV flux. For example, in the upper layer

$$\overline{v_1' q_1'} \equiv -\mathcal{D}_1\left(\beta + U\lambda^{-2} + \bar{q}_{1y}\right)\,. \tag{III.25}$$

Because of the zonal jets, $\bar{q}_{1y}$ varies significantly in the meridional direction. Since $\overline{v_1' q_1'} = \langle v_1' q_1'\rangle$ at every point, $\mathcal{D}_1$ must also depend on the meridional direction. Furthermore, $\overline{v_1' q_1'} = \langle v_1' q_1'\rangle$ allows us to relate the domain-averaged diffusivity D_1, given in (III.5), to $\mathcal{D}_1$ by

$$D_1 = \mathcal{D}_1\left(1 + \frac{\bar{q}_{1y}}{\beta + U\lambda^{-2}}\right)\,. \tag{III.26}$$

In the upper layer $\bar{q}_{1y}$ is comparable to $\beta + U\lambda^{-2}$, which produces the bumpy ramps seen in Figure III.2(c) and (e). The diffusivity D_1 is well posed, but only provides a gross view of transport processes in the upper layer—for example it does not capture the importance of zonal jets as barriers of transport.

In the lower layer, we can describe the zonally-averaged PV flux in terms of $\mathcal{D}_2$, where

$$\overline{v_2 q_2} \equiv -\mathcal{D}_2\left(\beta - U\lambda^{-2} + \bar{q}_{2y}\right)\,. \tag{III.27}$$

Although in the lower layer $\overline{v_2' q_2'} \neq \langle v_2 q_2\rangle$, the hope is that $\bar{q}_{2y} \ll \beta - U\lambda^{-2}$ so that $D_2 = \langle \mathcal{D}_2\rangle$. While $\bar{q}_{2y} \ll \bar{q}_{1y}$, the vanishing PV gradient in the lower layer means that $\bar{q}_{2y}$ can not be neglected in most cases (see Figure III.2(e)). The limiting case is when $\beta = U\lambda^{-2}$. If $\mathcal{D}_2$ were simply a constant, integration of

[4]This corresponds to the case where $\varkappa = 1$ as described in Appendix A. In our simulations $\varkappa = \sqrt{2}$, which projects a small amount of dissipation into the upper layer.

(III.27) with respect to y would imply that $\langle v_2 q_2 \rangle$ disappears in this special case. However, because $-\langle v_1 q_1 \rangle = \langle v_2 q_2 \rangle = \lambda^{-2} \langle v\tau \rangle$, Figure III.3 confirms that $\langle v_2 q_2 \rangle$ has a statistically steady non-zero value at $\beta_* = 1$. Thus especially in the lower layer, retaining the meridional dependence of the eddy diffusivity is essential for accurately describing the eddy fluxes.

The strong local gradients associated with zonal jets in β-plane turbulence may mean that turbulent diffusivity parameterizations, which have long been a important descriptor of quasigeostrophic turbulence, are ultimately insufficient to describe the complex dependence of meridional eddy fluxes on external parameters such as bottom friction and β. Furthermore, the failure of barotropic cascade theories to adapt to the baroclinic system suggests that new models of energy transfer in baroclinic turbulence are needed. The simulations described here suggest that coherent structures, such as zonal jets and barotropic eddies, are a necessary ingredient in any complete model of baroclinic turbulence. This is the focus of ongoing work.

Acknowledgements

We thank Lien Hua and Patrice Klein for providing the spectral code used in this work. We have benefitted from conversations with Paola Cessi, Rick Salmon, Isaac Held, Guillaume Lapeyre, Geoff Vallis, Shaffer Smith and Boris Galperin

This work was supported by the National Science Foundation grant OCE-0220362. AFT also gratefully acknowledges the support of an NDSEG Fellowship.

The text of this chapter, in full, is a reprint with minor modifications of the paper "Assessment of a theory for eddy heat fluxes," submitted for publication to the *Journal of Atmospheric Sciences*. The dissertation author was the primary researcher and author of this paper. W. R. Young directed and supervised the research, which forms the basis of this chapter.

IV

Towards a theory of β-plane baroclinic turbulence: zonal jets, storm tracks and eddy fluxes

IV.1 Introduction

Two-dimensional and quasi-geostrophic (QG) turbulence are dominated by coherent structures. Spin-down simulations of two-dimensional or f-plane barotropic turbulence is governed by successive vortex merger (McWilliams 1984), whereas in forced-dissipative systems, vortices can persist for many hundreds of eddy turnover times (Provenzale 1999). In both cases, the flow is largely determined by the summation of the velocity fields created by individual vortices. Coherent vortices are also prevalant in baroclinic QG turbulence (Larichev & Held 1995) and were shown by Thompson and Young (2006) to have a strong baroclinic character similar to hetons (Hogg & Stommel 1985).

With the addition of a planetary potential vorticity gradient, or β-effect, the dominant coherent structures become zonal bands of alternating eastward and westward flow. Axisymmetric vortices persist, however, and tend to align within the eastward flowing jets, similar to storm tracks in the atmosphere (Chang *et al.* 2002). Zonal flows have been documented in a number of numerical studies (Williams 1979, Panetta 1993, Vallis & Maltrud 1993, Cho & Polvani 1996, Nozawa

& Yoden 1997, Lee 1997, Lee 2005) and have direct applications to observations of zonal flows in the large planetary atmospheres (Vasavada & Showman 2005). Furthermore, recent evidence provided from satellite altimeter data suggests that with sufficient averaging, the Earth's ocean and marginal seas are replete with zonal jets (Maximenko *et al.* 2005), with mesoscale eddies possibly providing the oceanic equivalent of atmospheric storms. Despite the ubiquity of these flows, the relationship between zonal jets and domain-averaged descriptors such as the energy production, potential vorticity fluxes and total energy content is still poorly understood.

Both the formation and maintenance of zonal jets in QG baroclinic turbulence are dependent on coherent structures that link small-scale eddies to the large-scale background flow. The dynamics of this process are summarized in Figure IV.1. The fastest growing mode of the linear baroclinic instability problem is independent of the meridional direction (see Figure I.2) and gives rise to what is termed the "elevator mode"—alternating meridional bands of warm fluid moving poleward and cold fluid moving equatorward. These bands are shown in Figure IV.1, where they are also perturbed by a large-scale zonal flow described by the sinusoidal curve at left. As the meridional bands are tilted by the background flow, non-zero Reynolds stresses are generated on both flanks of the jet. On the northern flank, the meridional shear, which is characterized by $\bar{u}_y < 0$, tilts the elevator mode such that $\overline{u'v'} < 0$, where bars represent zonal averages. On the southern flank, shear of sign $\bar{u}_y > 0$ creates a tilt that leads to $\overline{u'v'} > 0$. If we apply a standard diffusive parameterization to describe the Reynolds stresses, $\overline{u'v'} = -D\overline{u}_y$, we find that D must be negative on both flanks of the jet. This negative viscosity (McIntyre 1970) provides the zonal mean flow with a source of momentum that strengthens the jets.

Eddy tilting is also responsible for the remarkable persistence of zonal jets, both in numerical simulations and geophysical flows. As the magnitude of the jet velocities grows, the meridional shear becomes stronger. The shear continues

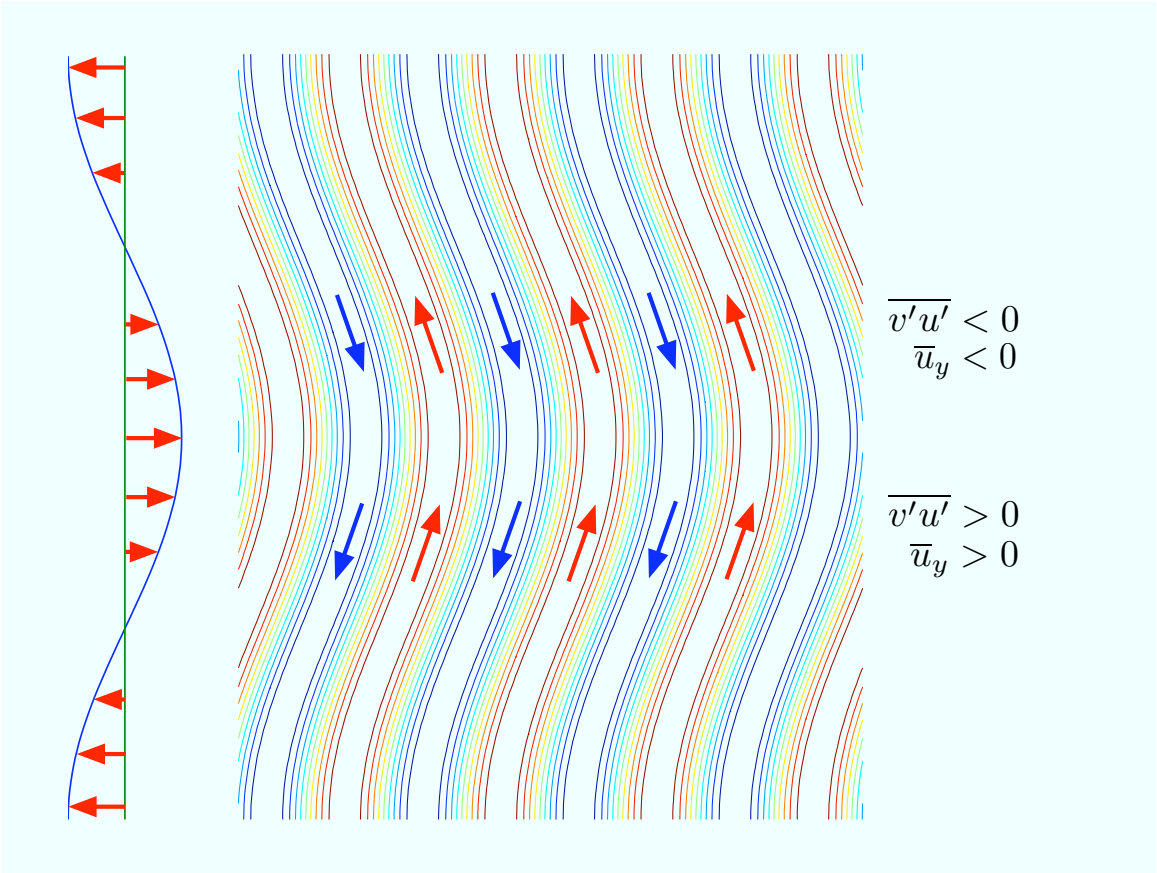

Figure IV.1: Diagram of the Reynolds stress correlations, which give rise to jet formation and persistence. The thin contours represent the fastest-growing (elevator) mode of the linear baroclinic instability with warm fluid moving northward and cold fluid moving southward. The system is perturbed by a large-scale zonal flow given by the sinusoidal curve to the left. The subsequent tilting of the meridional bands gives rise to non-zero Reynolds stress terms that have the same sign as the background shear. This in turn creates a negative viscosity that feeds energy back into the jets and generates a positive feedback loop whereby the jet strengthens and the magnitude of both the Reynolds stresses and the shear increases. The growth of the jet can eventually be balanced by large-scale friction.

to stretch eddies in a manner that provides a source of energy to the zonal mean component of the flow. The growth of the jets will eventually equilibrate if a dissipation mechanism such as large-scale friction is included to saturate the negative viscosity effects.

Figure IV.2 shows three snapshots of the barotropic streamfunction from a two-mode β-plane QG model forced with a uniform, horizontal temperature gradient (a description of the two-mode model appears in Appendix A). Accompanying each snapshot is the zonally-averaged zonal barotropic velocity $u_J \equiv -\bar{\psi}_y$, which is non-dimensionalized by U, where $2U$ is the vertical shear arising from the basic state temperature gradient. The panels each show a zonal strip of the doubly periodic $2\pi \times 25\lambda$ square domain, where λ is the Rossby deformation radius. The snapshots occur at the initiation of turbulence just as the linear instability breaks down. In panels (a) the linear instability and corresponding elevator mode is still evident, and the zonal flow is weak, although there is some small departure of the zonal flow away from zero. In panels (b) the meridional bands have begun to tilt, which leads to rapid growth of the zonal mean flow. Finally, in panels (c) the dominant variation in the streamfunction contours is now in the meridional direction, orthogonal to the linear instability mode. The zonal flow has also increased by approximately an order of magnitude over a period of only 4 to 5 λ/U, where U/λ is roughly the linear growth rate. Thus there is a rapid exchange of energy in wavenumber space between modes $k \neq 0, l = 0$ and $k = 0, l \neq 0$.

In Chapter II (also Thompson & Young 2006), the dominant contribution to the meridional heat flux in the two-mode QG model with $\beta = 0$ was shown to come from coherent vortices. The heat flux arises from a systematic northward (southward) migration of anti-cyclonic (cyclonic) eddies with warm (cold) fluid trapped in the cores. Scalings for the heat flux were derived that relied heavily on observations of a strong correlation between the barotropic vorticity ζ and temperature (baroclinic streamfunction) τ fields. The barotropic vorticity–temperature correlation of the zonal mean flow is discussed in section IV.2.

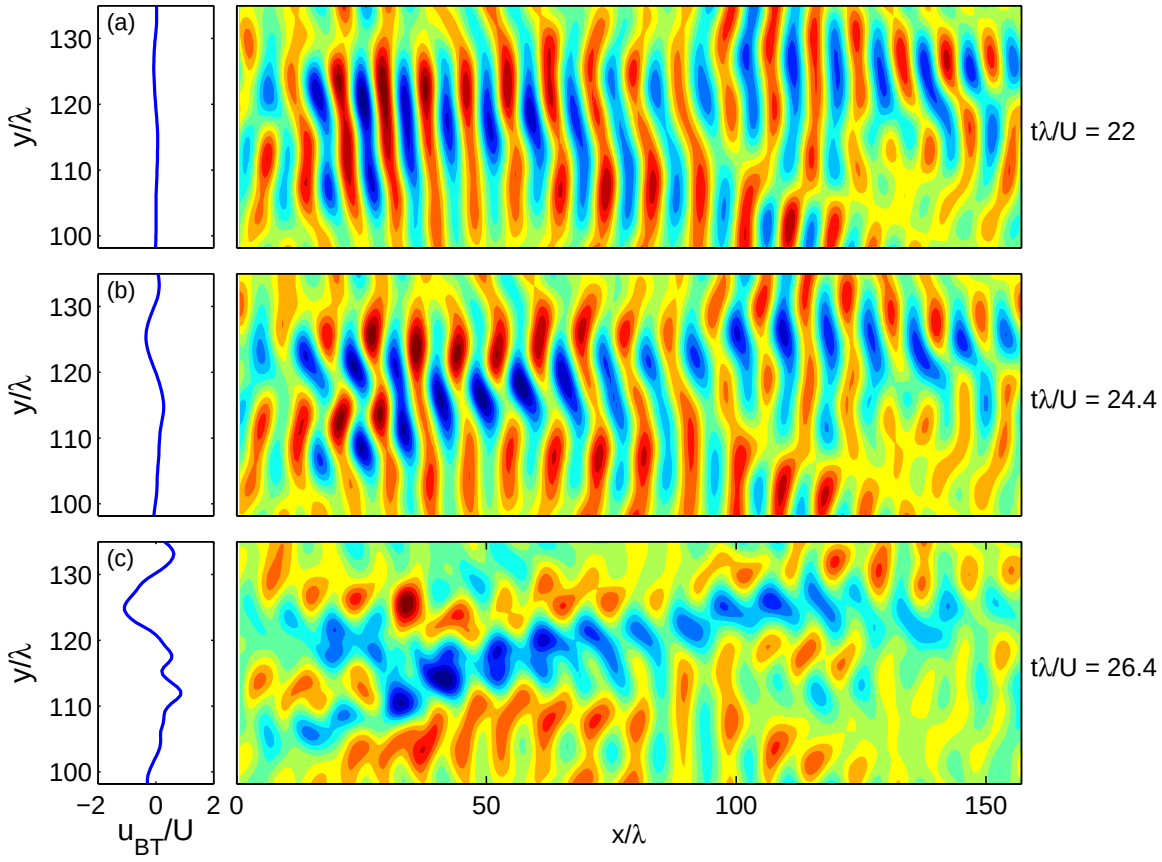

Figure IV.2: Zonally-averaged zonal barotropic velocity $u_J \equiv -\bar{\psi}_y$ (left) and snapshots of the barotropic streamfunction ψ (right), illustrating the initiation of a zonal jet. (a) The system is initially dominated by the fastest-growing mode of the linear instability and the zonal flow is weak. (b) The weak flow is sufficient to tilt the meridional bands, which in turn strengthens the jet (see discussion in section IV.1). (c) The strength of the zonal flow continues to increase leading to further tilting of the remaining eddies. After a period of only $4\lambda/U$ the jet is well estabilished. For this simulation $\beta\lambda^2/U = 1/2$ and $\kappa\lambda/U = 0.02$.

On the β-plane, the equilibrated temperature field is characterized by zonal bands comprised of alternating patches of warm and cold fluid. These patches of fluid represent "storms" in the storm-track view of zonal jets. The boundary between these storms meanders to accommodate the size of the temperature anomalies, which have a meridional scale much larger than λ (indeed they are shown to be comparable to the jet spacing in section IV.3). Between the strong eastward jets, in the region of westward flow, warm anomalies that are sheared away from the storms are preferentially entrained into the bounding jet to the north, while cold anomalies are preferentially entrained into the bounding jet to the south. Figure IV.3 shows an example of one of these events in a series of snapshots detailing the northward transport of a warm patch of fluid from one jet to another.

Events similar to the one depicted in Figure IV.3 occur frequently for both warm and cold fluid patches and may be the primary contribution to the domain-averaged heat flux of the system. If we accept that these heat transport events, as well as the mechanism of negative viscosity, are important processes in the life cycle of a zonal jet, then one must conclude that traditional approaches to describing β-plane turbulence, which focus only on zonally-averaged properties of the flow or neglect coherent structures altogether, are incomplete.

In this chapter we re-visit the numerical simulations of Panetta (1993), who performed the first thorough study of zonal jet properties in a baroclinic QG system. Panetta (1993) documented in great detail the stability and meridional structure of the zonal jets that spontaneously form on the β-plane; however, details of the relationship between the eddy and zonal mean components of the flow were not discussed. The results of this chapter are obtained using a numerical model similar to the one used by Panetta (1993) (see Appendix A for details), where we have significantly increased the resolution and domain size, as well as expanded the parameter space explored. In section IV.2 we provide further information about the zonal jets. In particular we show that the version of Rhines scaling proposed

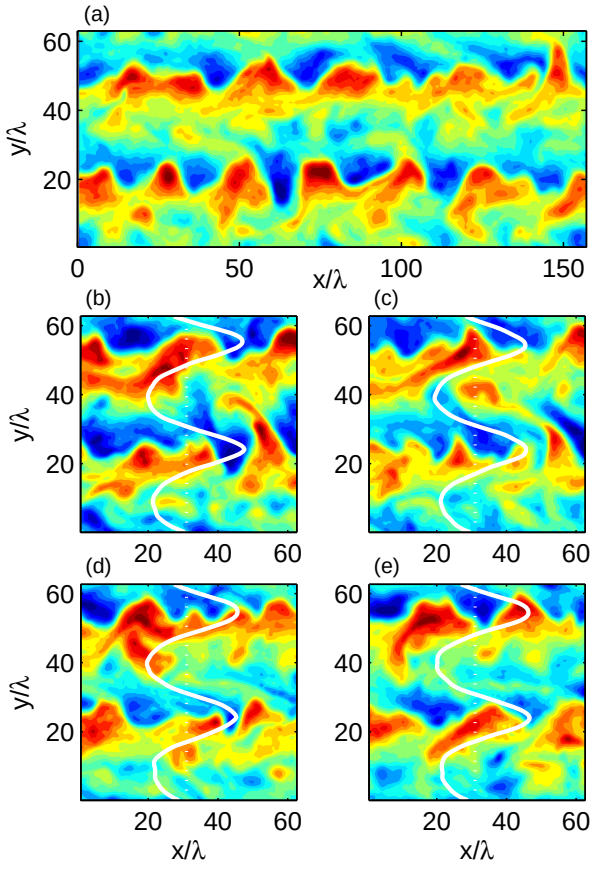

Figure IV.3: Snapshots of the temperature (baroclinic streamfunction) field τ illustrating β-plane heat transport. Panel (a) shows how warm and cold patches of fluid align along the jet paths similar to storms along a storm track in the atmosphere, while panels (b) - (e) show the migration of a warm patch of fluid northward from one jet to another. The white curves show the zonally-averaged zonal barotropic velocity at each time step. (b) The upper portion of the warm eddy on the right hand side of the domain centered at $y/\lambda = 30$ is sheared by the barotropic flow. (c) This causes an eddy of warm fluid to be released into the westward flow, (d) where it is advected downstream and eventually entrained by the large warm eddy in the upper jet (e). This process is an important mechanism for heat transport in the system. Each snapshot is separated by a period λ/U; $\beta\lambda^2/U = 1/2$ and $\kappa\lambda/U = 0.02$ in this simulation.

by Panetta (1993) successfully relates the jet spacing to the RMS eddy velocity and β. In section IV.3 we consider the large eddies that develop along the jet paths and examine their contribution to the eddy heat flux. Section IV.4 presents conclusions and suggestions for future work.

IV.2 Zonal jets in baroclinic turbulence

Panetta (1993) showed that persistent, quasi-steady, almost barotropic, zonal jets appear spontaneously in a baroclinically unstable doubly periodic flow. Zonal jets in baroclinic systems have also been studied in channel flows (Lee 1997) and on a sphere (Lee 2005). These jets are asymmetric in that mass transport in the strong, narrow eastward jets is balanced by a weaker and broader flow in the westward flowing regions. We re-visit Panetta's jets with the ability to significantly improve the size of the domain and the horizontal resolution of the simulations. The majority of Panetta's simulations had a domain size of $2\pi L \times 2\pi L$ with $L = 15\lambda$ and a grid resolution of 64^2. At this resolution, there is less than one grid point per deformation radius. Our main simulations have size $2\pi L \times 2\pi L$ with $L = 25\lambda$ and a grid resolution of 256^2. Discussion of a few larger-domain and higher-resolution simulations appears in section III.6. Since the domain is doubly periodic, the simulation must select an integer number of jets. Thus extending the domain size is an important check on a number of the features described in Panetta (1993).

Figure III.2 confirms some of the important qualitative observations of Panetta (1993). First, the jets are largely barotropic, but increases in either $\beta_* \equiv \beta\lambda^2/U$ or $\kappa_* \equiv \kappa\lambda/U$, while holding the other parameter fixed, results in an increase in the baroclinicity of the zonal flow. Also, the velocity jump between the upper and lower layers is largest in the eastward flowing jets. Panels (b) and (e) of Figure III.2 show that the PV gradients in either layer are always non-zero, indicating that the mixing is insufficient to completely homogenize the PV between

the jets. Still, a rough PV staircase (or a bumpy ramp) is evident in the barotropic mode (panels (c) and (f) in Figure III.2); the PV is well-mixed in the westward -flowing regions, while a sharp PV gradient occurs in the eastward jets.

Since the jets are quasi-barotropic, we refer to the zonally-averaged barotropic velocity as the "jet velocity," and we use the notation

$$u_J(y,t) \equiv -\bar{\psi}_y \,, \tag{IV.1}$$

where $\bar{\psi}$ is the zonal average of the barotropic stream function. We estimate a jet spacing and wavenumber k_J by counting the number of jets, n_J, in the domain. In some cases n_J is unambiguous (e.g., five jets in Figure III.2(a) and ten in panel (d)). In other cases n_J is not clearly defined and in those cases we use a half integer (e.g., we judge that the profile with $\kappa_* = 0.04$ in Figure IV.4(a) has $n_J = 5.5$). Since the domain is $2\pi L \times 2\pi L$ square, the jet wavenumber is then given by

$$k_J \equiv \frac{n_J}{L} \,. \tag{IV.2}$$

Figure IV.4(a) shows u_J at four different values of κ_*, all with $\beta_* = 1/2$. In addition to the zonal average, the curves represent time-averages over $\Delta t = 1000\lambda/U$ to remove small pulsations in the jet amplitude. The two simulations shown as bold curves have a steady number of jets, whereas the other two simulations show some fluctuations in jet number due to quantization problems. Figure IV.4(b) plots the increase in n_J with increasing bottom friction κ_*.

Figure IV.5(a) and (b) illustrates that increasing β_* with fixed bottom friction increases n_J. The u_J-profiles in Figure IV.5(a) are again averages over a period of $1000\lambda/U$. At small values of β_*, the jets are less steady and there is significant meridional meandering. Consequently, the time-averaged zonal velocity in these cases is much smaller than the instantaneous velocity. The profile with $\beta_* = 1/4$ in Figure IV.5(a) suffers from this time averaging.

Figure IV.4(b) shows that at $\beta_* = 1/2$, n_J increases roughly like $\kappa_*^{1/4}$, while Figure IV.5(b) shows that at $\kappa_* = 0.08$, n_J grows linearly with β_*. The reader

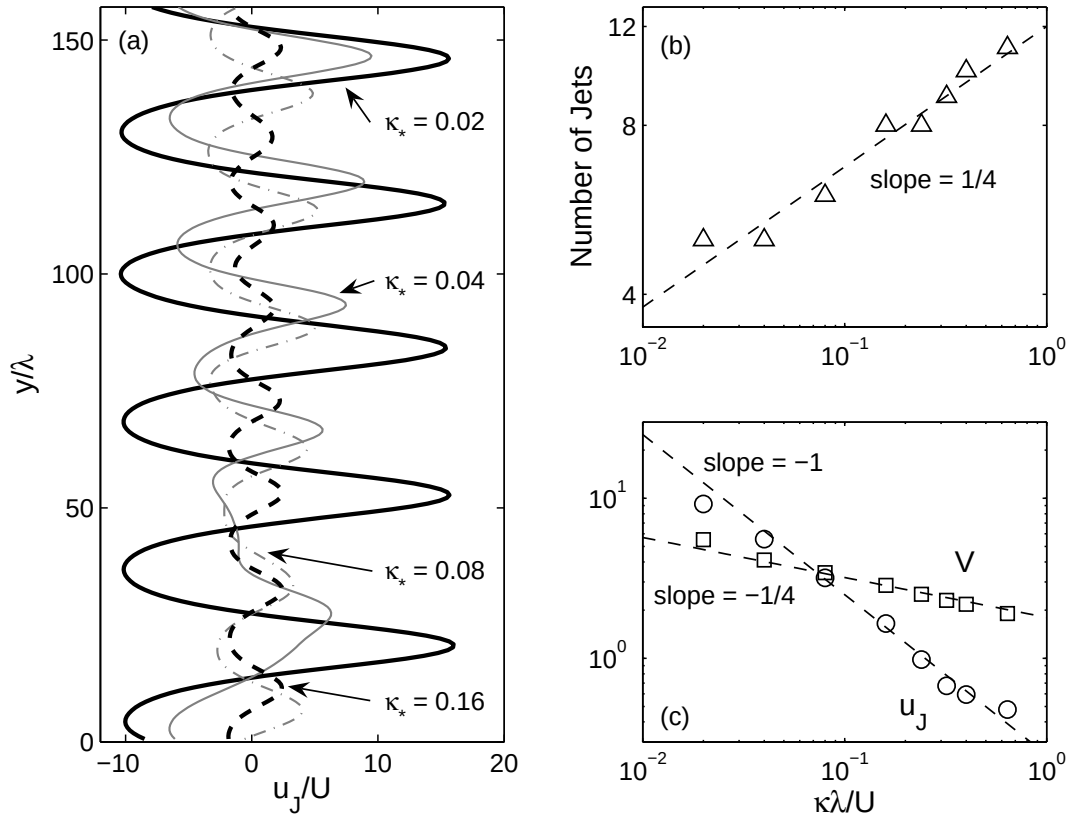

Figure IV.4: (a) The zonal mean barotropic "jet" velocity $u_J(y,t) \equiv -\bar{\psi}_y$ at four values of $\kappa_* \equiv \kappa\lambda/U$, with $\beta_* = 1/2$. (b) As κ_* is reduced the number of jets, n_J, decreases and the jet spacing $\ell_J \equiv 2\pi L/n_J$ increases; $n_J \propto \kappa_*^{1/4}$ is not inconsistent with the data. (c) Both u_J and the RMS meridional velocity V increase as bottom friction is reduced, but with different dependence on κ_*.

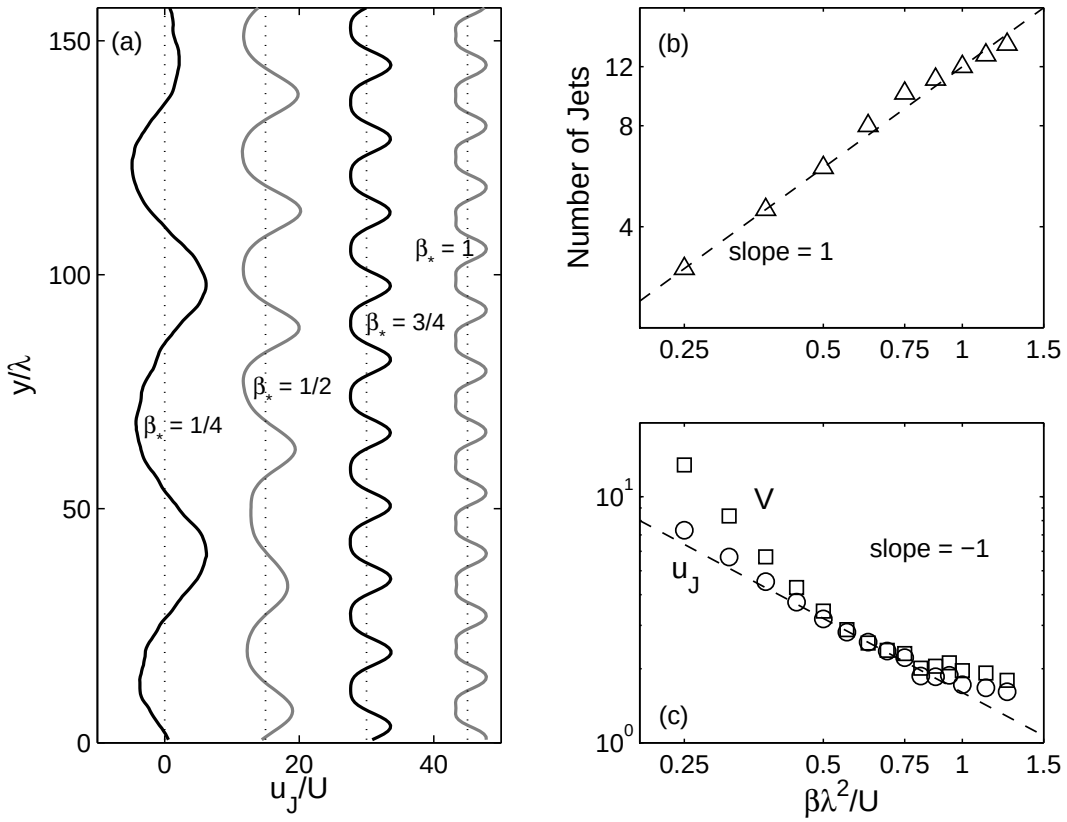

Figure IV.5: (a) The zonal mean barotropic "jet" velocity $u_J(y,t) \equiv -\bar{\psi}_y$ at four values of $\beta_* = \beta\lambda^2/U$, with $\kappa_* = 0.08$. (b) As β_* increases the number of jets, n_J also increases and the jet spacing $\ell_J \equiv 2\pi L/n_J$ decreases; $n_J \propto \beta_*$ is not inconsistent with the data. (c) At $\kappa_* = 0.08$, u_J and the barotropic meridional velocity V are comparable over a broad range of β_* values. This is not true for all simulations, see Figure IV.4(c).

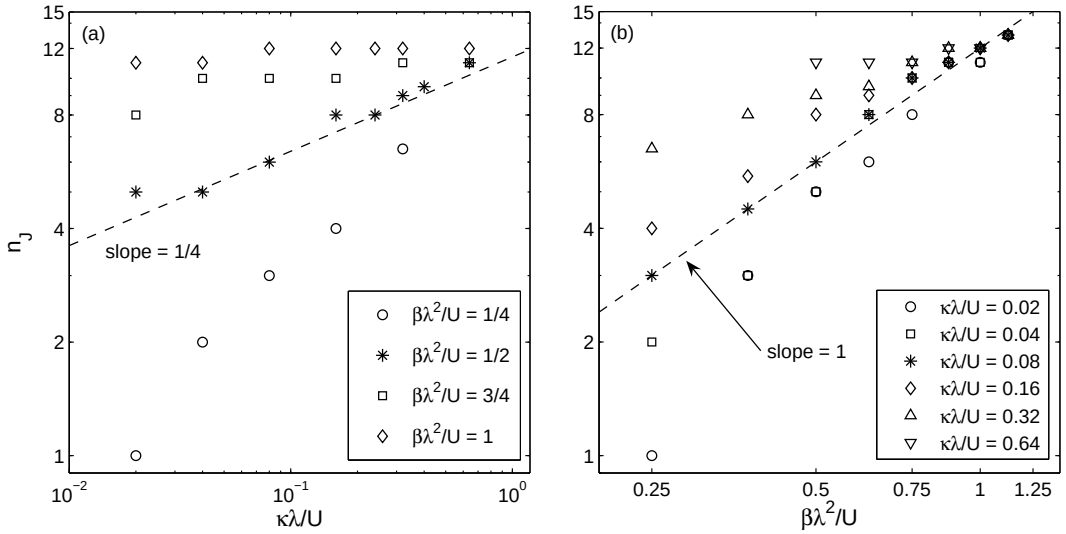

Figure IV.6: Survey of the number of jets n_J as a function of (a) bottom friction and (b) β. The $*$'s in panel (a) correspond to data in Figure IV.4(b), while the $*$'s in panel (b) correspond to data in Figure IV.5(b). The value n_J is defined by counting the number of jets in equilibrated simulations.

might be tempted to conclude that $n_J \sim \beta_* \kappa_*^{1/4}$. However the simple scaling laws in Figure IV.4(b) and Figure IV.5(b) are special and do not apply except along those particular slices through the parameter space. Figure IV.6 provides a more complete survey of the equilibrated value of n_J and shows that the dependence of n_J on κ_* and β_* is not a simple power law such as $\beta_* \kappa_*^{1/4}$.

IV.2.i Panetta's version of Rhines' scaling

Although n_J in Figure IV.6 is too complicated to be described by a simple power law involving the external parameters β_* and κ_*, the hope is that n_J can be simply related to other equilibrated statistics of the flow. For example, Figure IV.4(b) shows that the number of jets n_J scales roughly as $\kappa_*^{1/4}$ and therefore k_J in (IV.2) also varies as $\kappa_*^{1/4}$. Rhines' scaling would then suggest $u_J \sim \beta k_J^{-2} \sim \kappa^{-1/2}$. However this version of Rhines' scaling is not successful: Figure IV.4(c) shows that u_J depends more strongly on κ_*, with a proportionality closer to κ_*^{-1} at this value

of β_*. Using the meridional velocity V, defined in (III.12), as the velocity scale in Rhines' formula is also unsuccessful as the slope is too shallow, $V \sim \kappa_*^{-1/4}$.

Panetta (1993) suggests a different version of Rhines' scaling by taking the velocity scale to be the square root of the total eddy kinetic energy. Thus Panetta defines

$$k_\beta \equiv \sqrt{\frac{\beta}{2V_E}}\,, \tag{IV.3}$$

where

$$V_E = \sqrt{\langle |\nabla\psi'|^2 + |\nabla\tau'|^2 \rangle}\,. \tag{IV.4}$$

The primes indicate that the zonal mean has been removed, i.e. $\nabla\psi = \nabla\psi' - u_J$. At small values of bottom friction, Panetta (1993) found good correlation between k_J and k_β (see his Figure 4). As further confirmation, in Figure IV.7 we show contours of the ratio k_J/k_β over a range of κ_* and β_* values (locations where we have data points are indicated by the $\times$'s).

There is particularly good agreement between k_β and k_J when the jets are strong and quasisteady, which corresponds to small κ_* and large β_*. The agreement between k_β and k_J breaks down as the jets become weaker, specifically in simulations with small β_* and large κ_*. In simulations where both β_* and κ_* are weak, as few as two jets occupy the domain. Quantization is likely responsible for the poorer agreement between k_J and k_β in this corner of parameter space.

The main conclusion of this subsection is that Panetta's version of Rhines' scaling, namely $k_J/k_\beta \approx 1$, is successful at condensing the results. The best value of the ratio k_J/k_β is actually slightly greater than one, say roughly 1.1. But this is remarkably good given the complex dependence of n_J on κ_* and β_* summarized in Figure IV.6.

IV.2.ii The $\bar{\zeta} - \bar{\tau}$ anti-correlation

In Chapter III, Figure III.7 indicates that there is a significant anti-correlation between the barotropic vorticity $\zeta \equiv \nabla^2\psi$ and the temperature field τ.

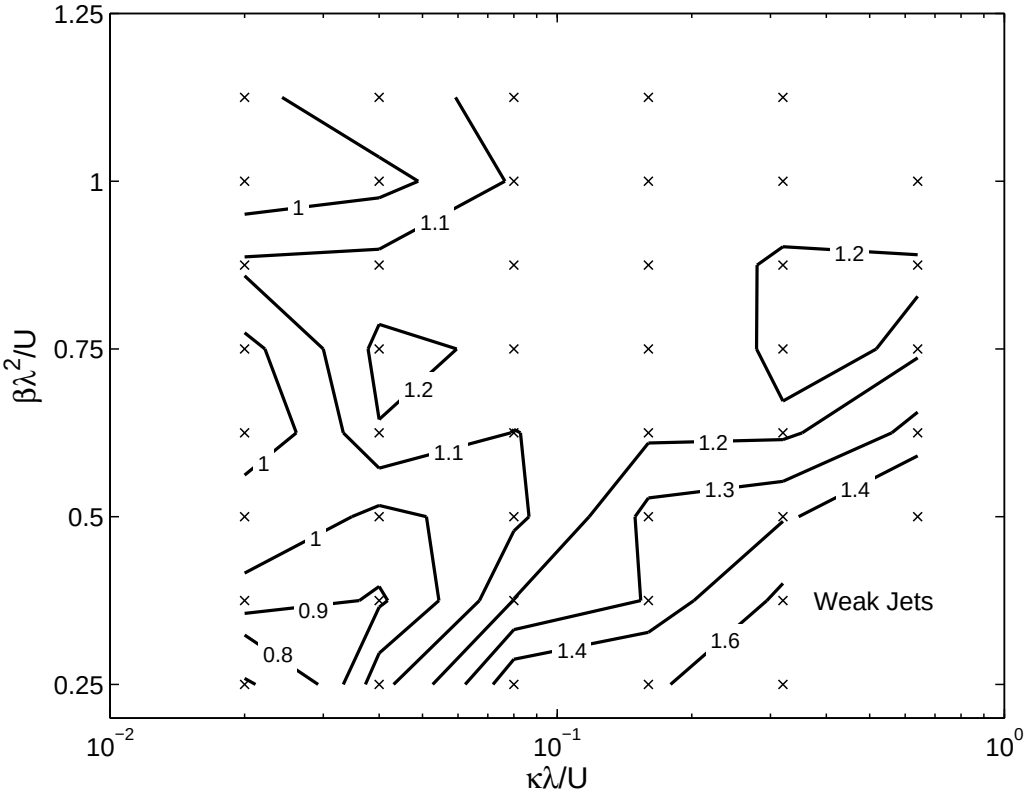

Figure IV.7: Contours of the ratio k_J/k_β. The wavenumber $k_J = n_J/L$ is calculated from the observed number of jets, while k_β is the Rhines scale as defined by Panetta (1993), $k_\beta = \sqrt{\beta/2V_E}$, where V_E is the square root of the total eddy energy as defined in (IV.4).

Figure III.7 also indicates that this correlation is stronger in the zonal-mean component than in the eddy component. This correlation means that the cross-term $\langle\zeta\tau\rangle$ implicit in (III.3) makes an important contribution to the total dissipation by bottom friction.

An examination of the upper and lower layer PV equations provides one explanation for the observed anti-correlation between ζ and τ. We first assume that the effects of bottom friction and advection by the basic state zonal flow are small, and that the flow is largely barotropic. With these approximations, the layer PV equations (A.10) and (A.11) become

$$\frac{Dq_1}{Dt} \approx -G_1\psi_x\,, \tag{IV.5}$$

$$\frac{Dq_2}{Dt} \approx -G_2\psi_x\,, \tag{IV.6}$$

where $D/Dt = \partial t + J\left(\psi,\ \right)$ and $G_1 = \beta + U\lambda^{-2}$, $G_2 = \beta - U\lambda^{-2}$ are the upper and lower layer basic state PV gradients. The prediction of (IV.5) and (IV.6) is that the upper and lower layer PV behave like passive tracers forced by a mean PV gradient that differs in the two layers. Multiplying (IV.6) by $-G_1/G_2$ and summing the two equations gives the result

$$\frac{D}{Dt}\left(q_1 - \frac{G_1}{G_2}q_2\right) \approx 0\,, \tag{IV.7}$$

or

$$\frac{q_1}{G_1} \approx \frac{q_2}{G_2}\,. \tag{IV.8}$$

Using the relationships $q_1 = \zeta + \nabla^2\tau - \lambda^{-2}\tau$ and $q_2 = \zeta - \nabla^2\tau + \lambda^{-2}\tau$, we find that (IV.8) predicts

$$U\lambda^{-2}\zeta \approx -\beta\left(\lambda^{-2}\tau - \nabla^2\tau\right)\,. \tag{IV.9}$$

Note that ζ and $\nabla^2\tau - \lambda^{-2}\tau$ are the barotropic and baroclinic PVs respectively.

Figure IV.8 plots profiles of $\bar{\zeta}\lambda/U$ and $\beta_*\left(\bar{\tau}_{yy} - \lambda^{-2}\bar{\tau}\right)\lambda/U$ for six different simulations. Both fields have the same meridional structure explaining the strong anti-correlation between $\bar{\zeta}$ and $\bar{\tau}$. Since $k_J^{-1} \gg \lambda$, then $\lambda^{-2}\bar{\tau} \gg \bar{\tau}_{yy}$. The prediction

of (IV.9) is supported well not only by the meridional structure of the two fields, but also by their amplitudes in panels (*a, b, d* and *e*). Inclusion of the $\bar{\tau}_{yy}$ term also introduces some of the large-wavenumber curvature observed in the $\bar{\zeta}$ profile in regions between the eastward jets.

The agreement is somewhat weaker in the $\beta_* = 1$ simulations, which is primarily due to the $\bar{\tau}_{yy}$ term. We find that at $\beta_* = 1$, $\lambda^2\bar{\zeta} \approx -\bar{\tau}$ is a much better approximation. Note that simulations at $\beta_* = 1$ represent a special case since here $G_2 = 0$. In this case it is most likely a poor assumption to neglect the bottom friction term on the RHS of (IV.6).

A weaker, but still significant, anti-correlation occurs in the eddy field. The correlation $c_{\zeta'\tau'}$ is defined as

$$c_{\zeta'\tau'} = \frac{\langle \zeta'\tau' \rangle}{\sqrt{\langle \zeta'^2 \rangle \langle \tau'^2 \rangle}}, \tag{IV.10}$$

and is shown in Figure III.7 (open symbols). From (IV.9) we also expect $\zeta'\lambda/U \approx \beta_* \left(\nabla^2\tau' - \lambda^{-2}\tau'\right)\lambda/U$. However, this result is difficult to verify since the correlation of the two eddy fields has a strong dependence on β_*, with $c_{\zeta'\tau'}$ increasing in response to increases in β. The $\zeta - \tau$ correlation at large values of β is larger than the $\zeta - \tau$ correlation observed in the f-plane simulations of Thompson & Young (2006), where $c_{\zeta\tau}$ was approximately a constant equal to 0.53.

The dependence of $c_{\zeta'\tau'}$ on β_* has prevented application of the "cross-invariant" analysis in Chapter II. Still, just as in the f-plane case, the correlation between ζ' and τ' arises through the prevalence of coherent isotropic eddies. As on the f-plane, these eddies have an important baroclinic component[1]. In β-plane simulations the large-scale eddies align along the jet paths and are the dominant features after removal of the zonal mean. We discuss these eddies further in the following section.

[1]The stronger correlation between the zonal averages of ζ and τ is most likely because the assumption that the flow is predominantly barotropic is a better approximation in the zonal mean flow.

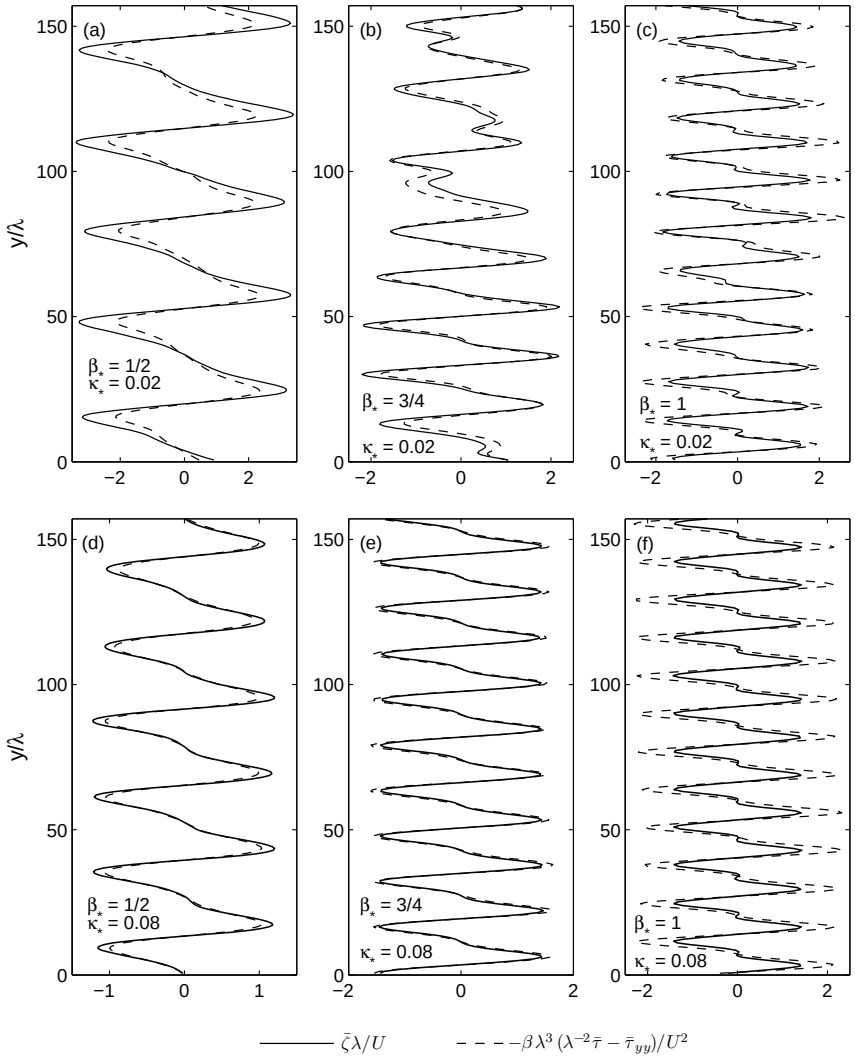

Figure IV.8: Zonally-averaged profiles of barotropic vorticity $\bar{\zeta}\lambda/U$ (solid lines) and $-\beta_*\left(\lambda^{-2}\bar{\tau}-\bar{\tau}_{yy}\right)\lambda/U$ (dashed lines).

IV.3 Jet-scale eddies in baroclinic turbulence

Embedded within the eastward-flowing zonal jets are a series of large eddies, similar to atmospheric storms in a storm track. These eddies are isotropic and tend to have roughly the same scale as the jets, i.e. $k_e \approx k_J$, where k_e is the peak wavenumber of the eddies. This agreement in length scale occurs because each eddy in a positive-negative vortex pair is comparable to the size of the eastward jet (the strong eastward flow is observed to meander around these eddies). A more pronounced asymmetry between the eastward and westward flowing regions would most likely lead to a larger difference between k_J and k_e. Figure IV.9(a) shows a snapshot of the barotropic eddy streamfunction $\psi' = \psi - \bar{\psi}$ for the simulation $\beta_* = 1/2$, $\kappa_* = 0.02$; the time and zonal mean $\bar{\psi}$ is given by the solid line for comparison.

These jet-scale eddies also have an important baroclinic component as indicated by the snapshot of the eddy baroclinic streamfunction $\tau' = \tau - \bar{\tau}$ in Figure IV.9(b). The eddies in the τ' field tend to be less isotropic than their ψ' counterparts. This is most likely a reflection of the eddy tilting by the meridional shear, which gives rise to non-zero Reynolds stresses and a negative viscosity that forces the zonal mean flow (Robinson 2006, Dritschel *et al.* 2006 and discussion in section IV.1). Figure IV.9(c) shows a snapshot of the upper layer Reynolds stresses $u_1'v_1'$ with the upper layer zonally-averaged zonal velocity $-\bar{\psi}_{1y}$ overlaid. Lower layer Reynolds stresses are found to be negligible in the baroclinic system as discussed in Chapter III. The Reynolds stresses have large amplitudes along the flanks of the eastward jets and the many tilted structures suggest the importance of the negative eddy viscosity.

Figure IV.10(a) and (c) show two-dimensional spectra of the eddy temperature field τ' from two different simulations. Each spectrum represents an average of at least 300 realizations of physical fields spanning a period $1000\lambda/U$. A circle of radius $k_J\lambda$ marked by the bold dashed curve indicates that eddy energy

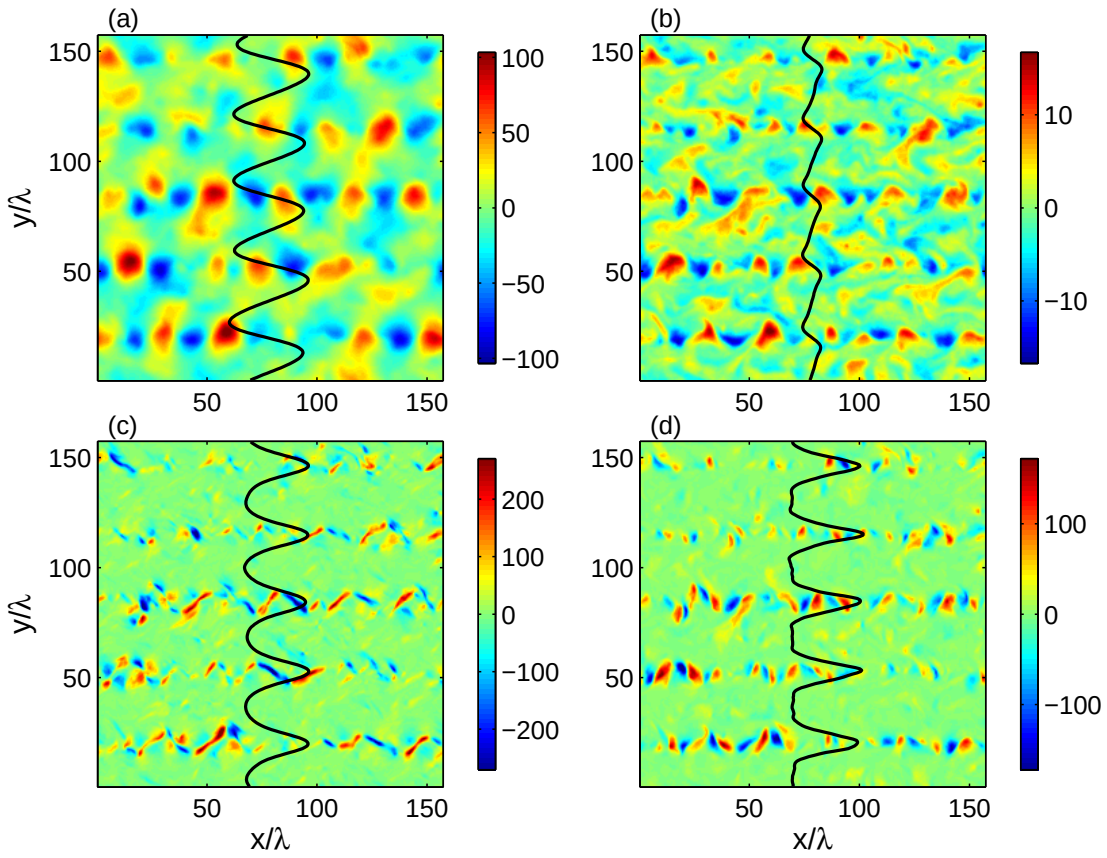

Figure IV.9: Snapshots of the non-dimensionalized eddy fields from the simulations with $\beta_* = 1/2$ and $\kappa_* = 0.02$. The panels show the (a) barotropic streamfuntion $\psi'/U\lambda$, (b) baroclinic streamfunction $\tau'/U\lambda$, (c) upper layer Reynolds stresses $v_1'u_1'/U^2$ and (d) eddy heat flux $\psi_x'\tau'/U^2\lambda$. The solid curves indicate time and zonal averages of the (a) barotropic streamfunction (divided by a factor of 4), (b) baroclinic streamfunction, (c) upper layer velocity and (d) eddy heat flux (multiplied by a factor of 25).

is indeed peaked near the jet scale. Also in these panels, the thin white curves are contours of the linear instability growth rate and the small white dots are the resolved wavenumbers in the spectral code. The spectrum of the eddy barotropic streamfunction ψ' is peaked at the same scales as τ'.

In the traditional view of baroclinic turbulence, the baroclinic mode energizes the barotropic inverse cascade at scales comparable to the deformation radius λ through baroclinic instability. However, here we find that most of the energy in the τ' field occurs at scales much larger than λ. Figure IV.10(a) and (c) also show that the jet-scale eddies appear in a region of wavenumber space that is predicted to be linearly stable. The low wavenumber cutoff can be reduced by replacing the basic state vertical shear, $2U$, with the maximum vertical shear in the eastward jets. The maximum shear is greater than the basic state, and thus reduces the effective β_*. Even this modification, though, is unable to move the peak wavenumber into a linearly unstable region[2]. Thus, the jet-scale eddies may in part result from an inverse cascade, although a significant portion of energy remains in the baroclinic component of the flow.

In Figure IV.11 we show that the dominant contribution to the eddy heat flux comes from the jet-scale eddies. Beginning with 300 snapshots of ψ' and τ', truncated fields, $\tilde{\psi}$ and $\tilde{\tau}$ are formed by setting the Fourier coefficients for all wavenumbers within a given wavenumber radius R (with units of $k\lambda$) equal to zero. The eddy heat flux calculated from an ensemble average of the 300 snapshots of the truncated fields,

$$\tilde{D}_\tau \equiv U^{-1} \left\langle \tilde{\psi}_x \tilde{\tau} \right\rangle , \tag{IV.11}$$

is plotted in Figure IV.11 as a function of R for two different simulations. For wavenumbers less than $k_J\lambda$, indicated by the dotted lines, $\tilde{D}_\tau \approx D_\tau$, i.e. eddies larger than k_J^{-1} do not contribute to the heat flux. Between k_J and $2k_J$, $\tilde{D}_\tau$ drops

[2]Because of the large meridional shear in the zonal flow, the true low wavenumber cutoff most likely falls between the limits determined by using the basic state vertical shear $2U$ and the maximum vertical shear in the eastward jets.

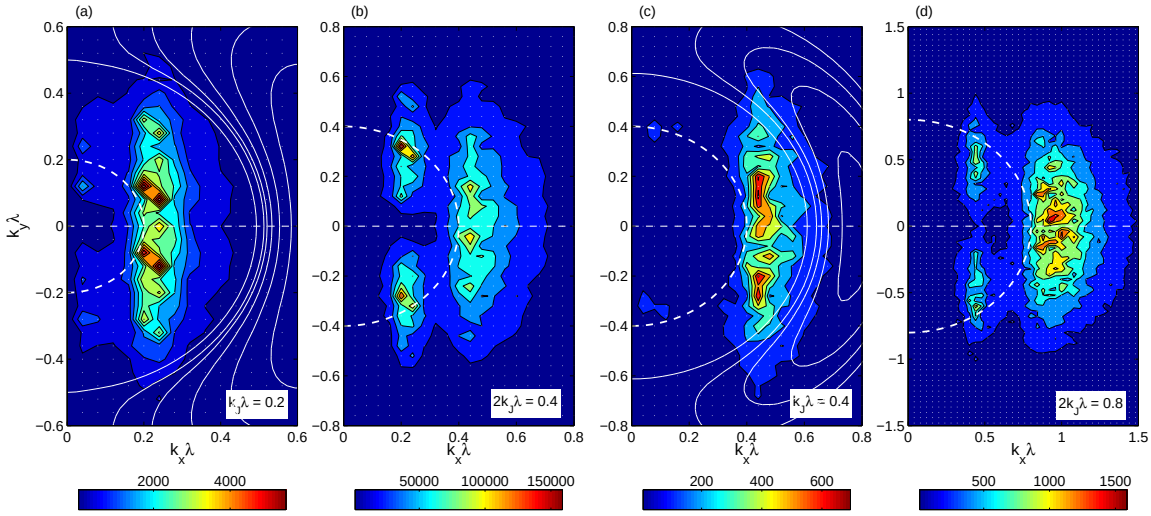

Figure IV.10: (a) Two-dimensional spectrum of the eddy baroclinic streamfunction τ' for the simulation with $\beta_* = 1/2$ and $\kappa_* = 0.02$. The bold dashed curve marks a circle of radius $k_J\lambda = 0.2$. The thin contours mark the region of linear instability and the dots indicate resolved wavenumbers in the spectral code. The energy peak in τ' occurs at scales slightly greater than k_J, but at wavenumbers less than the low wavenumber cutoff of the linear instability. (b) Two-dimensional spectrum of the eddy heat flux $\psi'_x\tau'$ for the simulation with $\beta_* = 1/2$ and $\kappa_* = 0.02$. The peak in energy occurs near twice the jet wavenumber $2k_J = 0.4$. Panels (c) and (d) show the same information as panels (a) and (b) but for the simulation $\beta_* = 0.75$ and $\kappa_* = 0.08$. The jet wavenumber for this simulation is $k_J\lambda = 0.4$. Each spectrum represents an average of at least 300 realizations of physical fields spanning a period $1000\lambda/U$.

quickly to roughly 30% of D_τ suggesting that jet-scale eddies are responsible for nearly all the heat flux in the equilibrated flow. A further confirmation of this is given in Figure IV.10(b) and (d), which show two-dimensional spectra of the total eddy heat flux. Here the peaks occur at roughly $2k_J$. The heat flux peak is expected at twice k_J if ψ' is in phase with τ' (see Figure IV.9), since ψ'_x would then be a quarter cycle out of phase with τ'.

A snapshot of the eddy heat flux ${\psi'}_x\tau'$ is provided in Figure IV.9(d). Since regions of strong positive (northward) and negative (southward) fluxes align on the jet path, the zonally averaged flux (given by the solid curve) is much smaller than the local amplitudes. This can be seen since the contour plot spans a range of nearly $400U\lambda$, while the zonally-averaged heat flux given by the solid line in Figure IV.9(d) has a maximum and minimum of roughly $3U\lambda$ and $2U\lambda$ respectively.

Another remarkable aspect of the large eddies within the eastward flowing jets is that these features appear to be quasi-stationary. Figure IV.12 presents Hovmoller diagrams of the eddy potential vorticity in the upper and lower layers at two fixed meridional positions. In panels (a) and (b) the time series is recorded along $y/\lambda = 20.2$ in Figure IV.9, which is within the core of an eastward jet. The time series in panels (c) and (d) are taken along $y/\lambda = 36.8$ in Figure IV.9, within a westward flowing region.

Anomalies within the eastward flowing jets are generally stationary although these periods of stasis are interspersed with sharp changes in the slope indicating a rapid movement to the east. The dashed line in panel (a) marks one of these events. The slope of the dashed line is equal to the time-averaged zonal velocity along $y/\lambda = 20.2$. The stability of these eddies may arise from a balance between eastward advection by the zonal flow and westward Rossby wave propagation. This suggests that within the eastward jets the underlying eddy fields may be a quasi-stationary lattice of eddies that periodically undergo rapid shifts in their structure before re-establishing a steady state. The behavior of the upper and lower layer PVs is qualitatively similar, although the eddy field of the upper layer

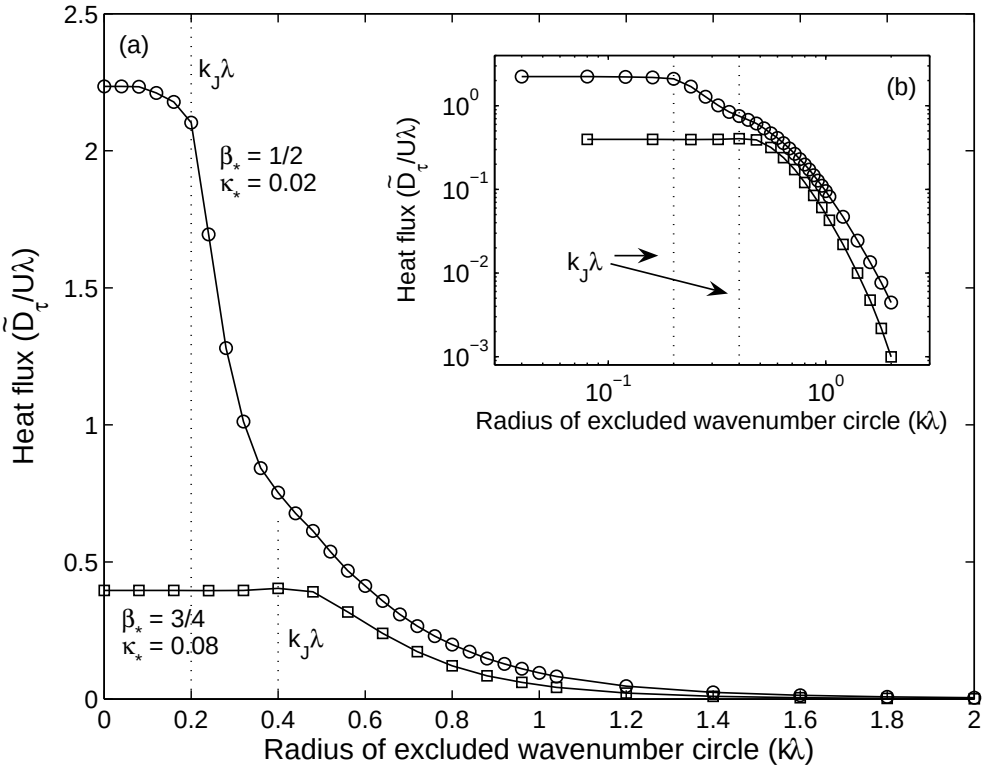

Figure IV.11: (a) The truncated eddy heat flux $\tilde{D}_\tau/U\lambda$ as a function of the radius of the excluded wavenumber circle R for two simulations. Truncated fields $\tilde{\psi}$ and $\tilde{\tau}$ are formed by setting Fourier coefficients for wavenumbers less than R equal to zero. The time and spatial average $\left\langle \tilde{\psi}_x \tilde{\tau} \right\rangle$ is $U^2\lambda^{-2}\tilde{D}_\tau$. The jet wavenumber $k_J\lambda$ for each simulation is given by the dotted lines. (b) The same data as in panel (a) shown on log-log axes.

has a larger magnitude within the eastward jets. Thus, although these eddies have an important baroclinic character, they are influenced primarily by a barotropic flow.

In the region where the flow is westward, the Hovmoller diagrams shows that smaller eddies are advected by the zonal mean flow. The slope of the anomalies in panels (c) and (d) are consistent with velocity of the westward jets (indicated by the dashed line in panel (c)). This behavior can be observed in animations of the flow: small coherent features are sheared off the large eddies on the jet flanks and carried along in the westward flow until they become entrained into another jet at a different latitude. This is essentially the mechanism for transporting heat as discussed in section IV.1 and Figure IV.3. It is interesting that the large difference in amplitude between the upper and lower layer observed in the eastward jets does not occur within the westward jets. The greater baroclinicity of the eastward jets indicates that the growth of eddies due to baroclinic instability will be largest in the eastward jet cores.

The results of this section suggest that a discrete set of eddies, with scales comparable to the jet spacing, are responsible for the equilibrated meridional heat flux. These eddies have an important baroclinic component, which may transfer energy directly into the zonal mean flow (see discussion in section III.5). An understanding of the quasi-stationary nature of these eddies would be an important element of a complete model of β-plane baroclinic turbulence.

IV.4 Conclusions and future work

The results presented in this chapter have been mainly descriptive in an attempt to characterize the major components of baroclinic β-plane turbulence. The two dominant features are the large-scale (i.e. much greater than the deformation radius λ) zonal jets and the jet-scale eddies. While the zonal jets are almost barotropic, especially at small values of bottom friction, the eddies always retain

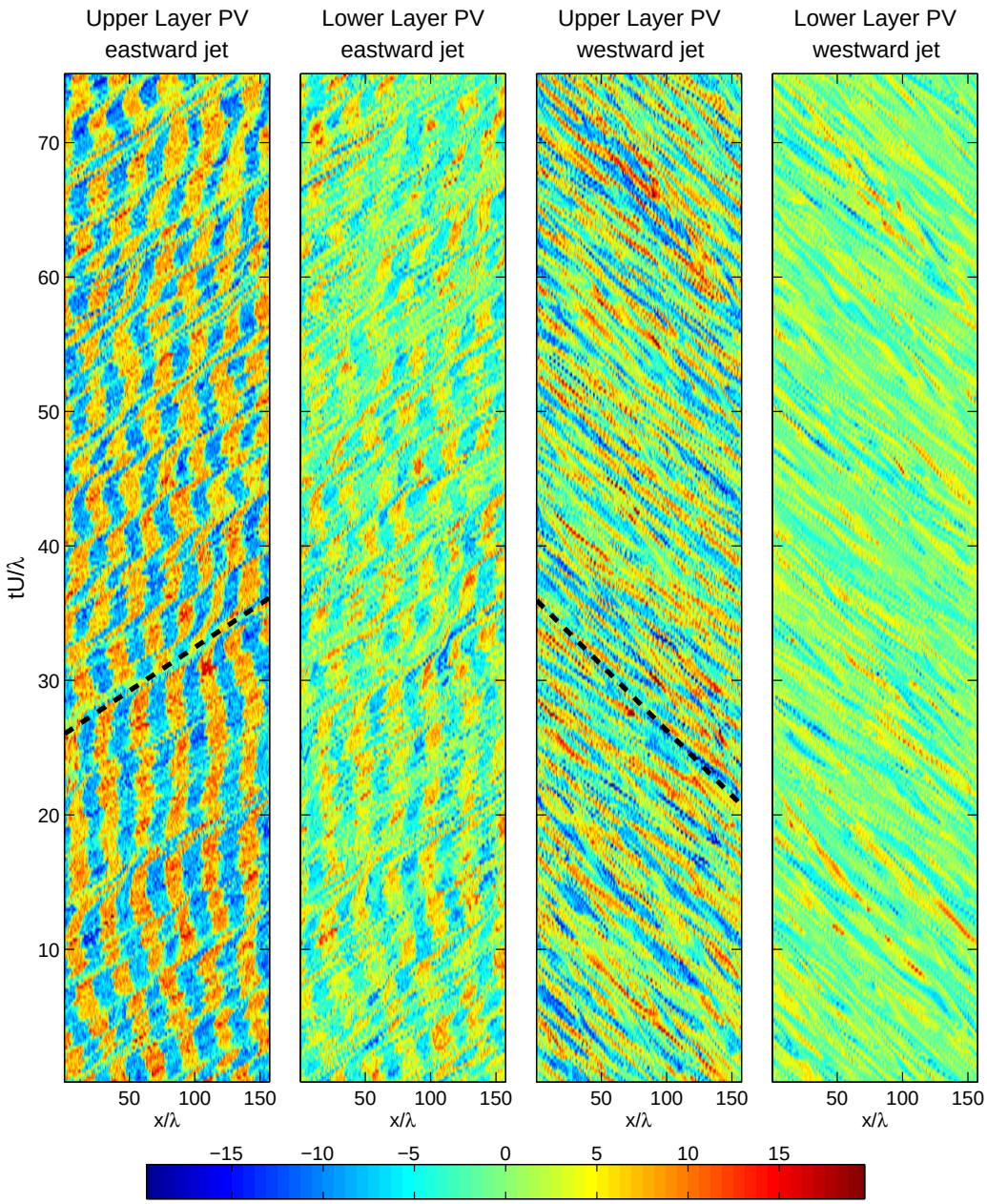

Figure IV.12: Hovmoller diagram of the eddy potential vorticity in the (a), (c) upper layer $q_1\lambda/U$ and (b), (d) lower layer $q_2\lambda/U$. The upper layer potential vorticity in panel (a) is divided by a factor of two. Panels (a) and (b) are taken along the line $y/\lambda = 20.2$ in Figure IV.9, within the jet core. Panels (c) and (d) are taken along the line $y/\lambda = 36.8$ in Figure IV.9, within the region of westward flow. The dashed lines in panels (a) and (c) have slopes equal to the time-averaged jet speed in the eastward and westward jet cores respectively.

an important baroclinic component. The baroclinicity of the eddy field is exemplified by the difference in Reynolds stress correlations between the upper layer, where this mechanism is the primary forcing of the zonal mean flow, and the lower layer, where the correlation is negligible (see discussion in III.5). The eddy and zonal mean components are also linked through Panetta's (1993) scaling in (IV.3), which relates the jet scale to the eddy kinetic energy.

While persistent zonal jets in β-plane turbulence is a feature that has been observed since the work of Rhines (1975) and Williams (1978), a complete theory of how the eddy field interacts with the zonal mean component is still lacking. At first glance, the observation that the zonal jets have an "almost barotropic" character (Panetta 1993) suggests that the baroclinic eddies simply act as a small-scale forcing on the barotropic mode. This view has found support through the β-plane study of Vallis & Maltrud (1993) and the barotropic simulations on a sphere by Huang & Robinson (1998). An important observation made by Huang & Robinson (1998) is that eddies comparable to the forcing scale transfer energy directly into the large-scale zonal flow. In this case there is no inverse cascade of energy.

While a type of negative viscosity suggested by Figure III.8 indicates that non-local spectral transfers are also important in β-plane baroclinic turbulence, adapting the analysis of Huang & Robinson to the baroclinic system is somewhat problematic because the forcing scale is no longer specified. Indeed, the discussion in section III.5 indicates that a significant amount of energy in the zonal mean component comes directly from the baroclinic mode, bypassing the barotropic inverse cascade.

Thus the anisotropic nature of β-plane turbulence, brought about by the spontaneous generation of zonal jets and the resulting inhomogeneities across a single jet, imply that a full model of baroclinic turbulence must account for meridional variations in the eddy fluxes and other descriptors of the flow. Figure

IV.13 shows the y-dependent (a) diffusivity

$$\mathcal{D}_i \equiv \frac{\overline{v_i' q_i'}}{G_i + \bar{q}_{iy}}\,, \tag{IV.12}$$

(b) mixing length

$$\ell_i \equiv \frac{\sqrt{\overline{q_i'^2}}}{G_i + \bar{q}_{iy}}\,, \tag{IV.13}$$

(c) meridional velocity

$$V_i \equiv \sqrt{\overline{\psi_{ix}'^2}}\,, \tag{IV.14}$$

and (d) correlation coefficient

$$c_i \equiv \frac{\overline{v_i' q_i'}}{\sqrt{\overline{\psi_{ix}'^2}\,\overline{q_i'^2}}}\,, \tag{IV.15}$$

for a simulation with $\beta_* = 3/4$ and $\kappa_* = 0.08$. The upper layer quantities ($i = 1$) are given by the solid curves and the lower layer quantities ($i = 2$) are given by the dashed curves; $G_1 = \beta + U\lambda^{-2}$ and $G_2 = \beta - U/\lambda^{-2}$ are the upper and lower layer basic state PV gradients.

The most striking feature of Figure IV.13 is the strong meridional variations in all the major descriptors of the flow. In panel (a) the upper and lower layer diffusivities even have significant structure across a single jet. Specifically, the diffusivities are elevated along the jet flanks, which correspond to regions of strong meridional shear and a large mixing length (panel (b)). The meridional velocity is correlated with the jet velocity in this simulation as shown in panel (c) although there is a significant baroclinic signature. Finally, in panel (d) the correlation coefficient gives further evidence of the different behavior in the upper and lower layers. The correlation is larger in the lower layer where a weaker PV gradient allows larger meridional excursions and the flow is more turbulent in nature. In the upper layer, where the correlation coefficient is smaller, the zonal jets act as more efficient barriers to transport and the flow is more wavelike in character.

Results such as those in Figure IV.13 and the evidence of a negative viscosity in the simulations of Huang & Robinson (1998) and others have led Dritschel

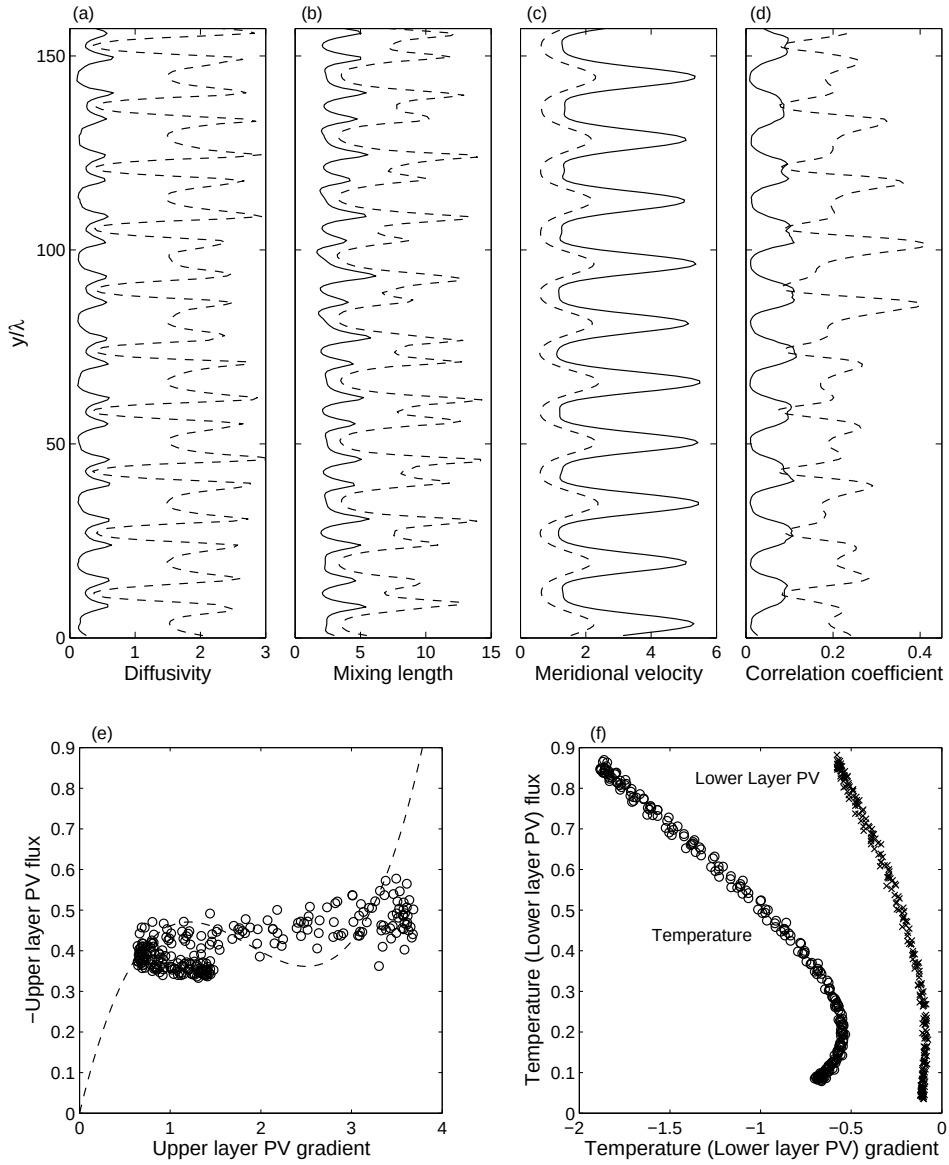

Figure IV.13: Meridional profiles of (a) turbulent diffusivity $\mathcal{D}_i$, (b) mixing length ℓ_i, (c) V_i and (d) correlation coefficient c_i, as defined in (IV.12) - (IV.15), for upper (solid line) and lower (dashed line) layers in a simulation with $\beta_* = 3/4$ and $\kappa_* = 0.08$. (e) Scatter plot of the absolute value of the zonally-averaged upper layer PV flux against the zonally-averaged upper layer PV gradient $\bar{q}_{1y}$. (f) Scatter plot of the zonally-averaged temperature (lower layer PV) flux against the zonally-averaged temperature (lower layer PV) gradient given by the $\circ$'s ($\times$'s). Both panels (e) and (f) represent time averages as well as zonal averages. The dashed line in panel (e) sketches the non-monotonic flux–gradient relationship described by Phillips (1972) and Balmforth *et al.* (1998).

et al. (2006) to compare the formation of zonal jets in β-plane turbulence to the layering phenomena observed in a stratified, weakly mixed fluid (Linden 1979, Park *et al.* 1994). Dritschel *et al.* (2006) refer to jet formation and maintenance as the Phillips effect since the jets (or layers in the stratified case) are due to a non-monotonic relationship between the potential vorticity (buoyancy) gradient and the potential vorticity (buoyancy) flux. The importance of this non-monotonic flux was first discussed by Phillips (1972) and was elaborated on by Balmforth *et al.* (1998) and is shown schematically by the dashed line in Figure IV.13(e).

This model seems especially promising in the upper layer, where the potential vorticity flux is constant despite strong gradients in the zonally-averaged potential vorticity (Figure IV.13(e)). We have attempted to formulate a "phenomenological" model of the zonal jets based on these observations, but to date this approach has been unsuccessful. One of the more peculiar and ultimately frustrating aspects of the eddy fluxes, is that both the eddy flux of temperature and the lower layer flux of potential vorticity are not only non-monotonic functions of their respective gradients, but as shown in Figure IV.13(f), they are not even single-valued functions of the gradients. This approach warrants further study, but at the moment there are a number of open questions. For example, to construct a model similar to Balmforth *et al.* (1998), a physically-based relationship between the eddy kinetic energy and the mixing length is needed. Not only is this relationship uncertain, but even our ability to relate the total eddy energy to the eddy kinetic energy in a simple way from our simulations has proved difficult.

A final remarkable result of the equilibrated zonal flow is its similarity to the zonal velocities obtained by Manfroi & Young (1999) in their barotropic study of β-plane turbulence. Manfroi & Young performed a pertubation expansion about the critical Reynolds number for a sinusiodal meridional flow on a β-plane. The amplitude equation obtained from this expansion predicts that the most unstable disturbance is a zonal flow with a much larger length scale than that of the basic state. Prediction of the jet wavenumber requires analysis of the Cahn-Hilliard

equation given in Manfroi & Young's equation (4.1)

$$u_t = -\alpha_1 u - \alpha_2 u_{yy} - \alpha_3 u_{yyyy} - \alpha_4 \left(u^2\right)_y + \alpha_5 \left(u_y^3\right)_y \,, \tag{IV.16}$$

where the coefficients α_1 through α_5 are determined from the perturbation expansion.

Figure IV.14 shows the barotropic zonal velocity u_J and its second derivative from (a) our baroclinic quasigeostrophic model and (b) from the solution of the Cahn-Hilliard equation in (IV.16). The coefficients in (IV.16) have been adjusted to improve the agreement with the baroclinic model, but despite this, the agreement between the two profiles is exceptional. The suggestion is that perhaps baroclinic instability, the fastest growing mode of which is a meridional sinusoid, provides a similar type of forcing as in Manfroi & Young (1999). An important point, however, is that the barotropic zonal flows obtained from the baroclinic quasigeostrophic model only resembles the Cahn-Hilliard solution in its "large-friction" regime (their Figure 8). Manfroi & Young show that within the weakly non-linear analysis that generates the amplitude equations, near-sinusiodal solutions are obtained when the amplitude equations are weakly unstable, i.e. the critical wavenumber k_c in Manfroi & Young's Figure 1 is only slight greater than 0. The difficulty in adapting the Cahn-Hilliard theory to the results of our numerical simulations is that it is unclear how the coefficients in (IV.16) are determined for the baroclinic system. This is the focus of ongoing work.

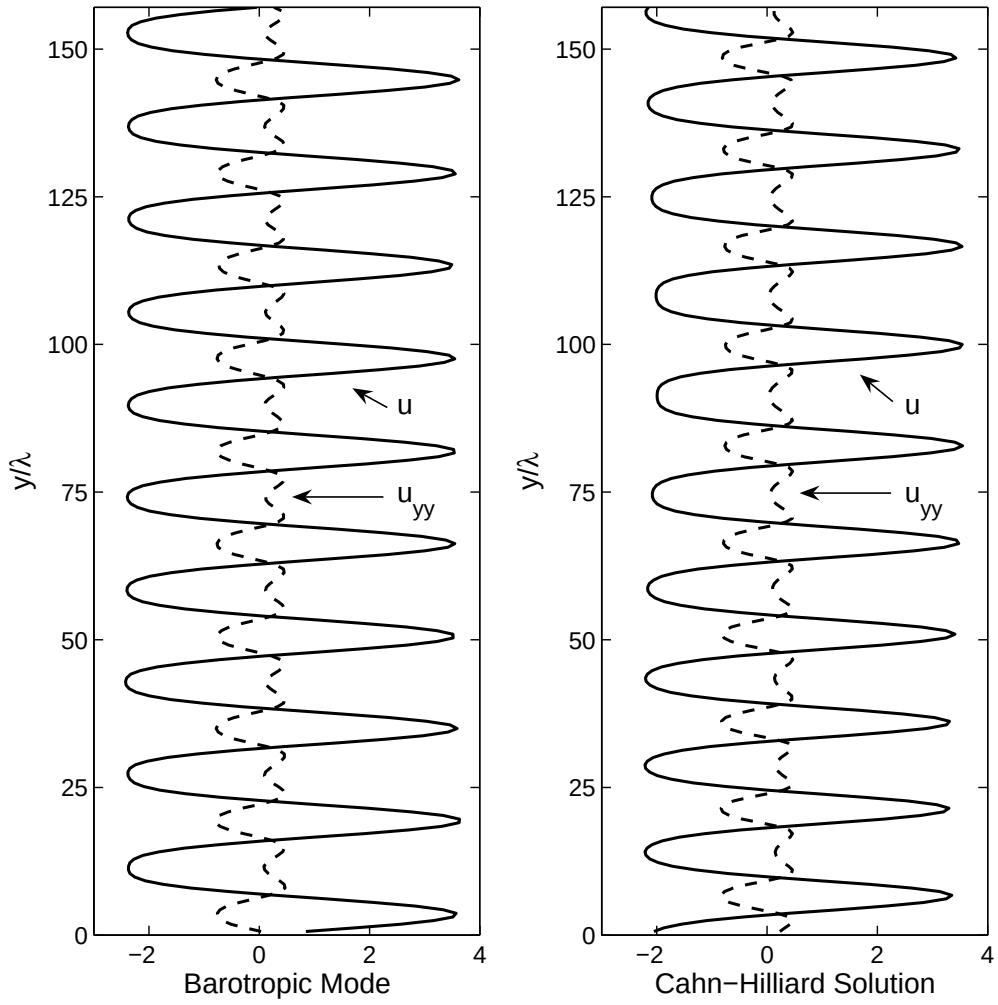

Figure IV.14: (*a*) Time and zonally averaged barotropic zonal velocity $u_J \equiv -\bar{\psi}_y$ and its second derivative from the two-mode quasigeostrophic simulations described in this chapter. (*b*) Solution of the Cahn-Hilliard equation given in (IV.16) and its second derivative.

V

Spatial and temporal patterns of small-scale mixing in Drake Passage

V.1 Abstract

Temperature and salinity profiles obtained with XCTD (expendable conductivity, temperature and depth) probes throughout Drake Passage, Southern Ocean between February 2002 and July 2005 are analyzed to estimate turbulent diapycnal eddy diffusivities to a depth of 1000 m. Diffusivity values are inferred from density/temperature inversions and internal-wave vertical strain. Both methods reveal the same pattern of spatial variability across Drake Passage; diffusivity estimates from inversions exceed those from vertical strain by a factor of three over most of Drake Passage.

The Polar Front (PF) separates two dynamically different regions. Strong thermohaline intrusions characterize profiles obtained north of the PF. South of the PF, stratification is determined largely by salinity, and temperature is typically unstably stratified between 100- and 600-m depth. In the upper 400 m, turbulent diapycnal diffusivities are $\mathcal{O}(10^{-3}$ m^2 s$^{-1})$ north of the PF, but decrease to $\mathcal{O}(10^{-4}$ m^2 s$^{-1})$ or smaller south of the PF. Below 400 m diffusivities typically exceed 10^{-4} m^2 s^{-1}. Diffusivities decay weakly with depth north of the PF, whereas diffusivities

increase with depth and peak near the local temperature maximum south of the PF. The meridional pattern in near-surface mixing corresponds to local maxima and minima of both wind stress and wind stress variance. Near-surface diffusivities are also found to be larger during winter months north of the PF. Wind-driven near-inertial waves, strong mesoscale eddy activity and double-diffusive convection are suggested as possible factors contributing to observed mixing patterns.

V.2 Introduction

Observations in the Southern Ocean suggest that mixing is intense and widespread, even well above rough topography. Naveira Garabato *et al.* (2004) analyze velocity fluctuations caused by the internal wave field in Drake Passage and the Scotia Sea to show that turbulent diapycnal eddy diffusivities κ_ρ can exceed background values by up to three orders of magnitude. They further find that values of κ_ρ greater than 10^{-3} m^2 s^{-1} extend more than 2000 m above the bottom. From analysis of strain variance in the WOCE hydrographic profiles of the Southern Hemisphere, Sloyan (2005) shows that enhanced mixing above topography occurs throughout the Southern Ocean. Also, unlike mid-latitude ocean basins, where diffusivities return to background levels within 1000 m of the bottom, elevated diffusivities are found up to depths of at least 1500 m (Sloyan 2005). The detection of elevated mixing rates in the Southern Ocean suggests that diapycnal mixing significantly influences local dynamics.

However, the pathways through which mixing influences Southern Ocean dynamics are not well understood, mainly because the Southern Ocean has many features that differentiate it from other ocean basins. The Southern Ocean is subject to wind forcing and mesoscale eddy activity that are well above mid- and low-latitude levels (Rintoul *et al.* 2001, Sprintall 2003). Zonal velocities are also significantly larger in the Southern Ocean because of the strong Antarctic Circumpolar Current (ACC). Furthermore, within the ACC, isopycnals slope upward

toward the surface and can outcrop, allowing deep and intermediate waters to be affected by wind and buoyancy forcing. Speer *et al.* (2000) describe how surface fluxes convert upwelled water into Intermediate Water and Subantarctic Mode Water, which are then advected away from the outcropping site. Thus the Southern Ocean is subject to a number of unique forcings, and it is unclear whether mixing descriptions (e.g., subgridscale parameterizations in large-scale climate models) based upon mid- and low-latitude physics are appropriate at higher southern latitudes.

This uncertainty about the relative importance of mixing in Southern Ocean dynamics has led to a disparity in how diapycnal mixing is incorporated in models of the Southern Ocean's meridional circulation. Historically, it is thought that a balance between wind-driven Ekman flow and mesoscale eddies determines the meridional circulation (Johnson & Bryden 1989, Speer *et al.* 2000). In the studies of Karsten *et al.* (2002) and Bryden & Cunningham (2003), diapycnal mixing has little effect on Southern Ocean dynamics. Instead, sub-surface mixing occurs primarily along isopycnals and all diapycnal exchanges are limited to surface processes. However, Cessi & Fantini (2004) suggest that diapycnal mixing plays a prominent role in determining the deep stratification of the Southern Ocean. Cessi & Fantini (2004) also find that the depth of the thermocline can depend on the magnitude of κ_ρ. A more complete understanding of diapycnal mixing processes in this region is necessary to assess the validity of the various proposed circulation models.

Additionally, a better understanding of diapycnal mixing processes in the Southern Ocean may offer a solution to the long-standing global "missing mixing" problem. Munk's (1966) estimate of a uniform diapycnal eddy diffusivity, $\kappa_\rho = 10^{-4}\ \mathrm{m^2\,s^{-1}}$, assumes that nearly all North Atlantic Deep Water (NADW) upwells at low latitudes. The discrepancy between this predicted value and observed open-ocean values, which are an order of magnitude smaller (Gregg 1987, Toole *et al.* 1994, Kunze & Sanford 1996), is partially explained by the patchiness of low-

latitude turbulence–i.e., turbulence is elevated over rough topography (Polzin *et al.* 1997). As an alternative solution, Toggweiler & Samuels (1995) propose that conversion of NADW into new water masses through upwelling and mixing in the Southern Ocean may effectively short circuit the low latitude diapycnal mixing described by Munk (1966). Conversion of NADW depends on both the magnitude and distribution of diapycnal mixing and the rate at which upwelled water is exported to other ocean basins via the meridional circulation. Significant NADW upwelling in the Southern Ocean would reduce the low-latitude value of κ_ρ needed for mass conservation.

Unfortunately, mixing rates in the Southern Ocean remain poorly constrained, primarily because few direct observations exist in the region. The remoteness and harsh conditions of the Southern Ocean have so far prevented extensive microstructure measurements that can explicitly resolve small-scale diapycnal mixing. Although this leaves some uncertainty in the quantitative description of mixing rates, the results of previous Southern-Ocean-based studies (Polzin & Firing 1997, Naveira Garabato *et al.* 2003, Sloyan 2005) clearly show that mixing processes in this region are characterized by strong spatial intermittency.

Kunze (2003), Naveira Garabato *et al.* (2004) and Sloyan (2005) all focus on abyssal mixing processes and offer little information about the temporal variability of the mixing events. In fact, few studies have addressed the temporal variability of mixing events in the open ocean. Gregg (1977) and Finnegan *et al.* (2002) present open-ocean mixing measurements repeated at the same location during different seasons. Gregg (1977) provides some evidence of seasonal dependence, while numerical studies (Nagasawa *et al.* 2000) have confirmed that the intensity of internal waves can vary in response to seasonal changes in the wind stress. Finnegan *et al.* (2002), who focus on topographic effects, do not comment on any temporal variability.

With the importance of both spatial and temporal variability in mind, we analyze a unique data set collected in Drake Passage over the past five years as part

of Scripps Institution of Oceanography's (SIO) High Resolution XBT/XCTD Network. This study departs from previous studies in Drake Passage by concentrating on mixing events in the upper 1000 m of the water column. Small-scale mixing rates are inferred from finescale observations using the Thorpe scale method (Dillon 1982), which requires detecting turbulent overturns in an otherwise stable density profile. We also analyze vertical strain spectra as an independent measure of turbulent diffusivities. Our results focus primarily upon the observed spatial mixing patterns with a view towards understanding what processes dominate upper-ocean mixing in the Southern Ocean.

To our knowledge, this is the first study that determines small-scale mixing rates from XCTD data. While XCTDs have slightly higher noise than traditional CTDs, this is compensated by the fact that XCTDs do not suffer the same error associated with ship roll. We show that, with sufficient coverage, XCTDs (and possibly XBTs in regions where density is largely independent of salinity) provide a relatively inexpensive method for estimating the magnitude and spatial variability of mixing rates. However, XCTDs do not offer the accuracy or physical insight afforded by more costly microstructure measurements.

We discuss both the Thorpe scale and the vertical strain spectral methods in section V.3. A description of the data set and our processing techniques appears in section V.4, which also includes a comparison with other Thorpe scale studies. We discuss our results in section V.5 with emphasis on spatial and seasonal variations in mixing intensity. Thorpe scale estimates are also compared to estimates obtained from the strain spectral analysis. We suggest possible mechanisms for the observed spatial and temporal patterns in section V.6, and our conclusions appear in section V.7.

V.3 Background

V.3.i Thorpe scales

Because of the expensive nature of collecting ocean data at microscale resolution, many theories have been proposed that allow small-scale mixing rates to be estimated from coarser-resolution data. A basic goal is to determine the kinetic energy dissipation rate ε, which is related to the stratification and a turbulent mixing length, the Ozmidov scale L_O (Ozmidov 1965), by

$$\varepsilon = L_O^2 N^3, \tag{V.1}$$

where $N^2 = -g\rho_0^{-1}\,(\mathrm{d}\rho/\mathrm{d}z)$ is the squared buoyancy frequency. Ferron *et al.* (1998) offer the physical explanation that L_O corresponds to the vertical distance l that a particle of fluid moves if all its kinetic energy is converted to potential energy (assuming that $\varepsilon \sim w^3/l$, where w is a vertical velocity scale). Therefore L_O is a measure of the maximum size of an overturn in a stratified fluid. It is difficult to obtain an estimate for L_O independently since ε can only be resolved with centimeter-scale microstructure measurements.

The Thorpe scale L_T (Thorpe 1977, Dillon 1982) provides a length associated with the size of density overturns in an otherwise stably stratified fluid. The method involves re-ordering a potential density profile that may contain inversions into a stable monotonic profile. Anywhere in the initial profile where a gravitational instability exists, the displacement from the original position to the re-ordered position, known as the Thorpe displacement d', is non-zero. The root mean square of the Thorpe displacements associated with a single overturn region gives the Thorpe scale L_T for that turbulent event, or

$$L_T \equiv \sqrt{\langle d'^2 \rangle}, \tag{V.2}$$

where $\langle\rangle$ indicates an average over a single overturn. Although overturns are not one-dimensional, the Thorpe scale gives a good estimate of an overturn size as long

as the mean horizontal gradient is much smaller than the vertical gradient, which is satisfied in the Southern Ocean.

Since L_O and L_T are two different estimates of overturning lengths, it is reasonable to expect that a linear relationship exists between the two, although spatial and temporal variability in the turbulent field means that any relation is only valid in a statistical sense. Dillon (1982) studies the relationship between L_O and L_T and finds that $L_O = (0.79 \pm 0.4)L_T$. A number of other studies followed, including Crawford (1986) who proposes a smaller coefficient $L_O = (0.66 \pm 0.27)L_T$ for an oceanic thermocline and Ferron *et al.* (1998) who propose a larger coefficient $L_O = (0.95 \pm 0.6)L_T$ for an abyssal region. The errors of both these studies overlap Dillon's (1982) original results, which we will apply in our present analysis. This then implies that the turbulent dissipation of an individual overturn can be calculated directly from the buoyancy frequency and the Thorpe scale. Using (V.1) gives

$$\varepsilon_i = 0.64 L_{Ti}^2 \langle N \rangle_i^3 , \tag{V.3}$$

where subscript i refers to the ith overturn.

Turbulent dissipation is often converted to a diapycnal eddy diffusivity κ_ρ using the model given in Osborn (1980), where

$$\kappa_\rho = \Gamma \varepsilon N^{-2}. \tag{V.4}$$

The mixing efficiency Γ has been shown to vary depending on the origin of the turbulence (Caldwell & Moum 1995), although most studies assume Γ is a constant equal to 0.2. We will follow this convention as well.

There is an important distinction between the two values of N used in the calculation of ε and κ_ρ. In determining the dissipation of a single overturn, the buoyancy frequency in (V.3) should be the mean value of N in the reordered region of the overturn, or $\langle N \rangle_i$, since overturns occur preferentially in regions of low stratification (Alford & Pinkel, 2000). The calculation of κ_ρ in (V.4) requires that the background buoyancy frequency N be applied since (V.4) arises from

a representation of κ_ρ as a turbulent diffusion acting on the background density gradient (see discussion in Ferron *et al.* 1998).

From (V.3) and (V.4) we can see that, outside of overturning regions, both ε and κ_ρ are zero. Calculation of a depth-averaged quantity includes both overturning and quiet regions. An example is given by

$$\overline{\varepsilon} = \frac{\sum_i \varepsilon_i L_{zi}}{H}, \tag{V.5}$$

where L_{zi} is the size of the ith overturn and H is the depth over which we choose to average. It is important to note that $\overline{\varepsilon}$ can be smaller than the minimum resolvable turbulent dissipation of an individual overturn. To ease notation we will not use overbars, and unless otherwise stated, all symbols refer to depth-averaged quantities for the remainder of the paper.

There remains some uncertainly about the validity of the relationships $L_O = 0.8 L_T$ and $\Gamma = 0.2$. Furthermore, the theory surrounding Thorpe scales assumes that the system is in steady state, which is a difficult condition to verify in a region as energetic as the ACC. Therefore we view with some caution the magnitude of the results presented here and focus primarily on the spatial and temporal patterns that appear to be a robust feature of mixing in Drake Passage.

V.3.ii Strain spectral analysis

An independent method of inferring dissipation rates comes from evidence that ocean mixing is related to the energy density of the internal gravity wave field. Nonlinear wave-wave interactions transfer energy and momentum to increasingly smaller-scale waves, which are more likely to break down into turbulence. McComas & Müller (1981) and Henyey *et al.* (1986) suggest formulas to estimate turbulent dissipation rates by comparing the shape of energy spectra, which are influenced by wave-wave interactions, to the energy spectrum of a canonical internal wave field proposed by Garrett & Munk (1975) and referred to here as GM. Gregg (1989) verifies that a correlation exists between the internal wave shear and

mixing rates in the open ocean at vertical scales greater than 10 m. Wijesekera *et al.* (1993) test the various internal wave–dissipation models and find that under certain conditions, scalings comparing the strain rates of the internal wave field to the GM spectrum provide better agreement with observational data than the internal wave shear. Wijesekera *et al.* (1993) also show that reasonable dissipation estimates are obtained even when the wave field varies significantly from the GM form, which is likely the case in Drake Passage.

Vertical strain can be obtained from vertical derivatives of properties such as potential density and temperature (a discussion of our methods appears in section V.5.iv), and Fourier transforming gives the spectral representation of vertical strain, ϕ_λ. Following Kunze (2003) strain variance levels $\langle \xi_z^2 \rangle$ are determined by integrating ϕ_λ from a minimum vertical wavenumber $k_{\text{min.}}$ out to a maximum wavenumber $k_{\text{max.}}$ such that

$$\left\langle \xi_z^2 \right\rangle = \int_{k_{\text{min.}}}^{k_{\text{max.}}} \phi_\lambda \mathrm{d}k = 0.2. \tag{V.6}$$

The constant 0.2 in (V.6) is somewhat arbitrary. We find that varying this constant has a small effect on mixing amplitudes, and does not affect the spatial pattern we describe in section V.5.iv. The GM strain variance level is computed over the same wavenumber band so that

$$\left\langle \xi_z^2 \right\rangle_{GM} = \frac{\pi E_0 b j_*}{2} \int_{k_{\text{min.}}}^{k_{\text{max.}}} \frac{k^2}{(k + k_*)^2} \mathrm{d}k, \tag{V.7}$$

where $E_0 = 6.3 \times 10^{-5}$ is the dimensionless energy level, $b = 1300$ m the scale depth of the thermocline, $j_* = 3$ the reference mode number and $2\pi k_* = \beta_* = 0.0073\,(N/N_0)$ the reference wavenumber with $N_0 = 0.00524\,\mathrm{s}^{-1}$. These parameters are given in Gregg and Kunze (1991). Note that the GM strain spectrum given in (V.7) is flat for $k \gg k_*$. In oceanic data a k^{-1} rolloff is observed at high wavenumbers, which has led to a modification of the GM spectrum by including a factor of k^{-1} to the empirical formula beyond $k = 0.1$ cpm (Winkel 1998). In our study, the integrations in (V.6) and (V.7) occur over the flat part of the GM spectrum.

Once the strain variance levels have been determined, we follow the results of Gregg *et al.* (2003) and calculate the turbulent diffusivity from the formula

$$\kappa_\rho^\phi = \kappa_0 \frac{\langle \xi_z^2 \rangle^2}{\langle \xi_z^2 \rangle_{GM}^2} \mathcal{H}(R_\omega)\, \mathcal{J}(f, N), \tag{V.8}$$

where $\kappa_0 = 0.05 \times 10^{-4}$ m^2 s^{-1}. The two functions $\mathcal{H}$ and $\mathcal{J}$ are empirical results that account for changes in the frequency content of the GM wave field and changes in latitude respectively. Henyey (1991) shows that frequency content is related to the shear-strain ratio $R_\omega = \langle V_z^2 \rangle / (N^2 \langle \xi_z^2 \rangle)$, where V_z is the vertical derivative of horizontal velocity. We do not have velocity data to accompany our profiles; therefore we rely on shear-strain ratio estimates from previous studies. Naveira Garabato *et al.* (2004) report a consistent mean value of R_ω between 8 and 12, independent of location. Kunze (personal communication) also finds values of R_ω between 10 and 20 at high latitudes. Taking $R_\omega = 10$ with

$$\mathcal{H}(R_\omega) = \frac{3R_\omega (R_\omega + 1)}{4\left(R_{\omega GM}^2\right)} \sqrt{\frac{2}{R_\omega - 1}} \tag{V.9}$$

and $R_{\omega GM} = 3$, we find that the turbulent diffusivity is enhanced by nearly a factor of 5 above regions with typical GM wave fields. Over the range $8 < R_\omega < 20$, $\mathcal{H}$ varies by a factor of 3.5. The formula given in (V.9) is equivalent to equation (4) of Gregg *et al.* (2003) multiplied by $(R_\omega / R_{\omega GM})^2$ to convert from shear-variance ratios to strain-variance ratios.

The latitude dependence also tends to enhance mixing at high latitudes, although we find that the effect is less influential than the shear-ratio dependence. The function $\mathcal{J}$ is given by

$$\mathcal{J}(f, N) = \frac{f \cosh^{-1}(N/f)}{f_{30} \cosh^{-1}(N_0/f_{30})}, \tag{V.10}$$

where N_0 is defined above and $f_{30} = f(30^\circ) = 7.29 \times 10^{-5}$ s^{-1}. Applying characteristic Drake Passage values to (V.10), $N = 2.5 \times 10^{-3}$ s^{-1} and $f_{58} = 1.2 \times 10^{-4}$ s^{-1}, we find the amplification is small with $\mathcal{J} \approx 1.25$. The factor $\mathcal{J}$ has a stronger effect at low latitudes and has been used by Gregg *et al.* (2003) to explain the observation of reduced mixing near the equator.

V.4 Measurements

V.4.i Measurement location

Since 1996 the High Resolution XBT/XCTD Network maintained by SIO has collected temperature and salinity data in Drake Passage along WOCE-designated transect AX22, between Tierra del Fuego and the Antarctic Penninsula (Figure V.1). Starting in February of 2002 the Sippican Digital XCTD was introduced, which has an improved vertical resolution of approximately 0.13 meters. During each subsequent cruise, six XCTDs were released at the following latitudes: $56.0^o, 57.0^o, 57.5^o, 58.0^o, 59.0^o$ and 60.5^o S.[1] Since 2002, 22 transects have been completed with XCTD data. After discarding erroneous profiles, we analyze no less than 19 individual profiles at each of the six latitude locations. These profiles are roughly evenly divided between summer and winter months. Figure V.1 indicates the position of each of these casts. While the latitudes of the casts are consistent, the longitude can vary due to the particular scientific mission of the cruise or inclement weather. Most casts fall along the middle of three typical routes across Drake Passage (Sprintall 2003) indicated by the dashed line in Figure V.1. Profiles of temperature and salinity from casts that deviate from this middle route do not show significant variations from the other casts.

Figure V.1 also shows the bathymetry of Drake Passage. XCTDs only sample the upper 1000 m of the water column and therefore our measurements are well above the sill depth of the major topographical features. The most significant of these features close to our measurement sites is the Shackleton Fracture Zone, which lies to the east of the southernmost casts. Strong internal waves and eddy activity may be generated in this region (Cunningham *et al.* 2003), but it is unclear if the effects propagate back towards our study area because of the strong eastward ACC. Naveira Garabato *et al.* (2004) have also found elevated mixing

[1]The XBTs, which only measure temperature, have a finer horizontal resolution of 15-20 km. We only analyze XCTDs since salinity makes an important contribution to the density throughout Drake Passage.

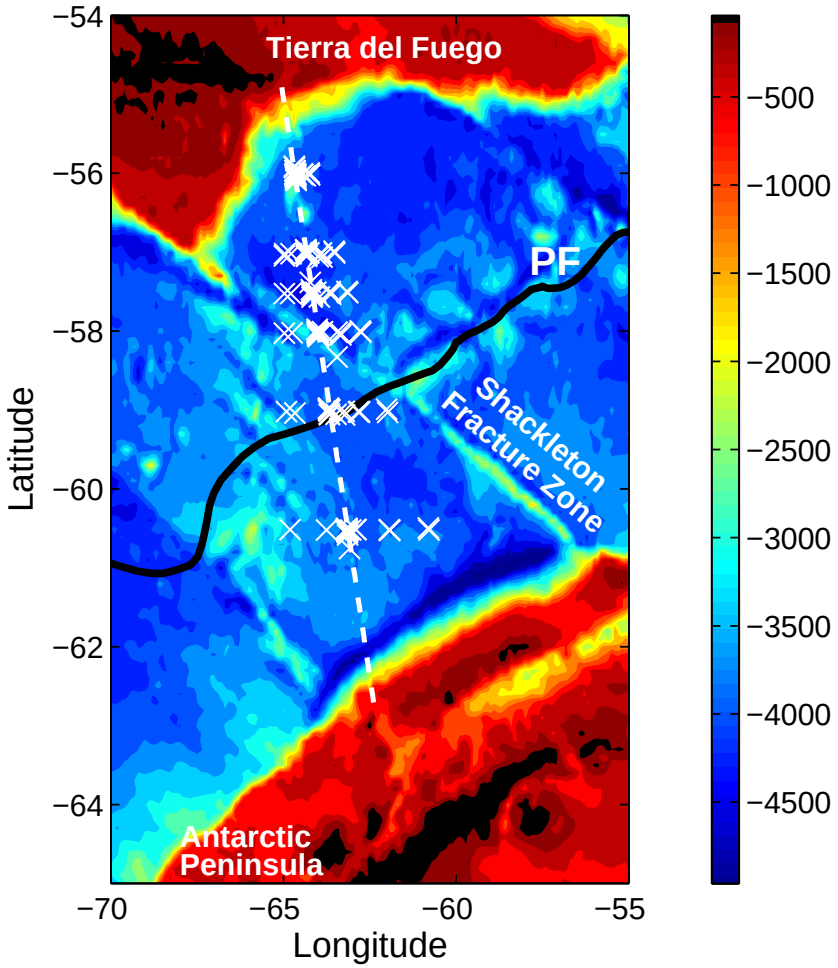

Figure V.1: The position (×) of each XCTD cast used in the current study. A majority of the casts occur along a single cruise track illustrated by the dashed line. No less than 19 casts were available for analysis at each of six different latitudes. The mean position of the Polar Front (PF) from Orsi *et al.* (1995) is given by the solid line, and the contoured bathymetry (m) is from Smith and Sandwell (1997).

over topography located roughly 500 km to the west of our current study site and north of the Sub-Antarctic Front. It is possible that internal waves generated in this region could radiate towards our measurement sites.

V.4.ii Data acquisition and processing

Data were collected using a Sippican Digital XCTD profiler with a known fall rate. As an XCTD falls through the water column, thermistor resistance and conductivity are relayed back to the ship through a copper wire to the Sippican MK12 data acquisition software. The expendable profilers employ a dual spooling mechanism that decouples the effects of ship roll that affect typical CTDs. The dual spooling mechanism allows XCTDs to be viable tools for observing finescale structure in Drake Passage.

The XCTDs sample to a depth of 1100 m, although the lower 100 m are prone to error due to wire stretch. The upper 100 m are also noisy due to weak stratification within the mixed layer. Therefore we present our results for the region between 100 and 1000 m.

We first formed spectra of the raw temperature and salinity profiles and determined a noise floor for each quantity. The salinity was found to be considerably noisier than the temperature profiles due to a mismatch between temperature and conductivity sensors. To eliminate this problem we smoothed the temperature and salinity profiles with triangular filters that had a vertical scale of 1 m for the temperature profiles and 4 m for the salinity profiles.[2] The smoothed temperature and salinity profiles were used to form the potential density profile with density referenced to the surface.

Over much of Drake Passage, only the potential density profiles can be used to determine overturns because of compensated thermohaline intrusions or an unstable temperature stratification. However, south of the Polar Front there

[2]We worried about the effects of smoothing temperature and salinity over different scales, especially because of observed thermohaline intrusions, but our results were essentially unchanged when temperature was smoothed out to the same scale as salinity.

is a persistent temperature maximum between 400 and 600 m, below which temperature steadily decreases. In this region stratification is weak, and noise in the salinity profiles can produce large spurious overturns. Therefore below the temperature maximum we followed Peters *et al.* (1995) and analyzed both density and temperature profiles, only accepting overturns if they are detected in both properties (see discussion below). Visual inspection of the profiles indicates that this is an efficient way to eliminate spurious overturns in weakly stratified regions.

After profiles are re-ordered to be gravitationally stable, overturns are defined to be regions over which the integral of Thorpe displacements is equal to zero (Dillon 1982). The limiting factor in overturn detection is the noise level of the potential density profiles. After detrending and analyzing a number of different sections, the average noise in the XCTDs was determined to be $\delta\rho = 0.001$ kg m^{-3}. Following Galbraith and Kelley (1996) the minimum thickness of a resolvable overturn is given by

$$L_{\rho_{\text{min.}}} \approx 2\frac{g}{N^2}\frac{\delta\rho}{\rho_0}, \tag{V.11}$$

where ρ_0 is the mean density. Since N^2 can vary by an order of magnitude over Drake Passage, the resolution size depends strongly on both latitude and depth. In Figure V.2 we show (a) N and (b) $L_{\rho_{\text{min.}}}$ throughout Drake Passage averaged over all casts. In our detection algorithm, each possible overturn must be thicker than $L_{\rho_{\text{min.}}}$ (with a minimum size of 4 m, the salinity smoothing scale), and the difference between its maximum and minimum density must be $2\delta\rho$ before it is accepted as a valid overturn. Over most of Drake Passage, $L_{\rho_{\text{min.}}}$ is only slightly greater than 4 m, but south of the Polar Front at depths close to 1000 m, stratification is weak and $L_{\rho_{\text{min.}}}$ approaches 20 m. Although Stansfield *et al.* (2001) show that the largest overturns make the most important contribution to the turbulent dissipation, we may underestimate mixing in very weakly stratified regions if many smaller overturns are discarded.

Galbraith & Kelley (1996) propose two tests, the run-length test and the

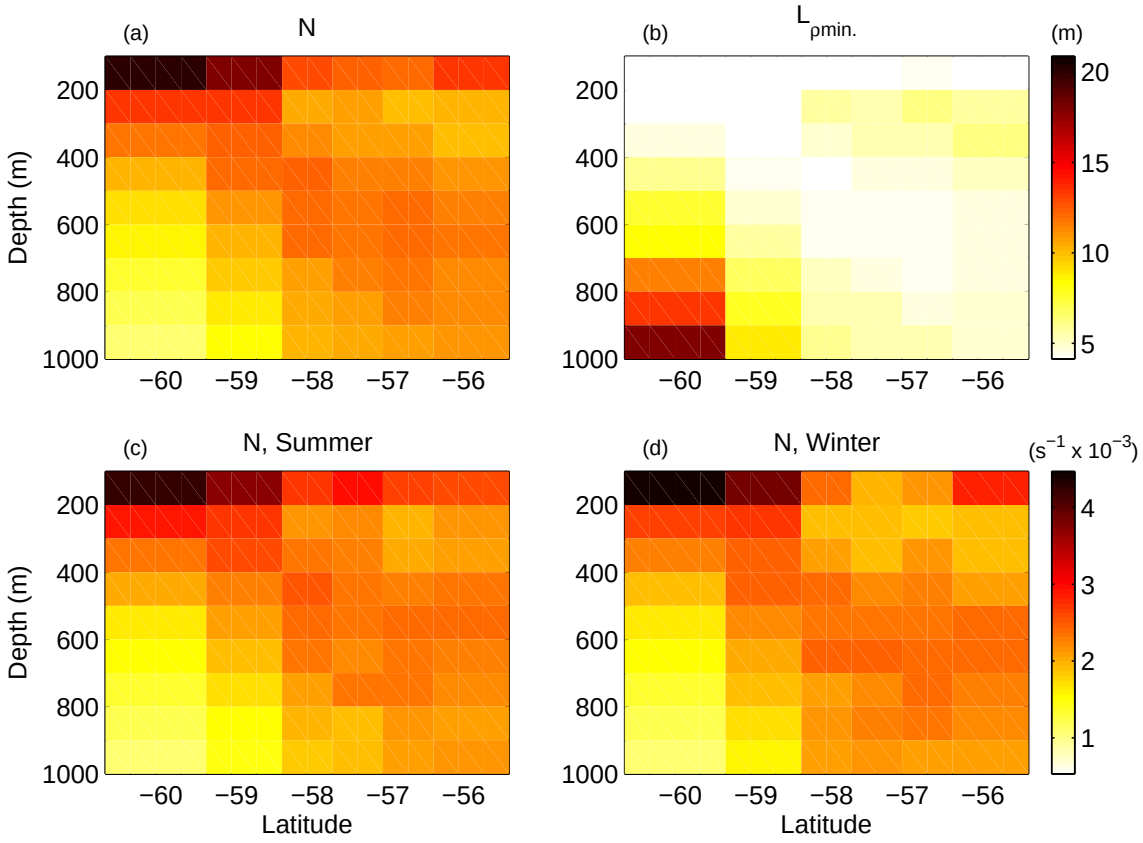

Figure V.2: (a) Buoyancy frequency N divided into 100 m bins and averaged over all casts at each latitude. (b) Minimum resolvable overturn size $L_{\rho_{\text{min.}}}$ in each 100 m bin based on (V.11) using the mean buoyancy frequency in (a) and $\delta\rho = 0.001$ kg m^{-3}. No overturns smaller than 4 m are accepted due to our data processing. Buoyancy frequency divided into (c) summer and (d) winter months show little seasonal signal. The scale is the same in panels (a), (c) and (d).

water-mass test, to eliminate spurious overturns. Johnson & Garrett (2004) have since shown that the run-length test is often unreliable for distinguishing between real overturns and noise, and they suggest that Thorpe scale estimates provide an upper bound on mixing rates when the run-length test is not applied. The water-mass test is designed to eliminate spurious overturns due to T/S mismatch as occurs with XCTDs. Most T/S mismatch is eliminated by our smoothing procedures. However, we find that most of our overturns are close to or just below the critical value for acceptance proposed by Galbraith & Kelley (1996). Visual inspection of these overturn regions on a T-S diagram do not show the looping structure that is characteristic of T/S mismatch (Galbraith & Kelley 1996). Following Martin & Rudnick (2005) we use a water-mass-test criteria less strict than Galbraith & Kelley (1996) by a factor of 2. Most overturns that fail our water-mass test are found at depth, south of the Polar Front, and are also typically eliminated on the basis of overturns not appearing in both temperature and potential density profiles.

Figure V.3 shows examples of typical profiles in the northern (upper panels) and southern (lower panels) regions of Drake Passage. The use of temperature profiles to detect overturns is shown at both sites for comparison, but in general this method only modifies mixing rates below the temperature maximum south of the Polar Front. The red curves in panels (a), (b), (f) and (g) are the reordered profiles, while the Thorpe displacements due to potential density (black) and temperature (red) are shown in panels (d) and (i). The large overturn in density at the bottom of panel (i) is a common feature of southern Drake Passage profiles and is caused by noise in the salinity profile. The resulting values of L_T for each accepted overturn are shown in panels (e) and (j). An expanded view of one of the larger overturns in our data set is shown in panels (f-h).

Initially 5686 possible overturns are detected, and after all tests are applied, 1301 overturns are accepted as real. For each overturn, values for L_T, N and ε are computed (not depth-averaged quantities). Profiles of L_T and ε are con-

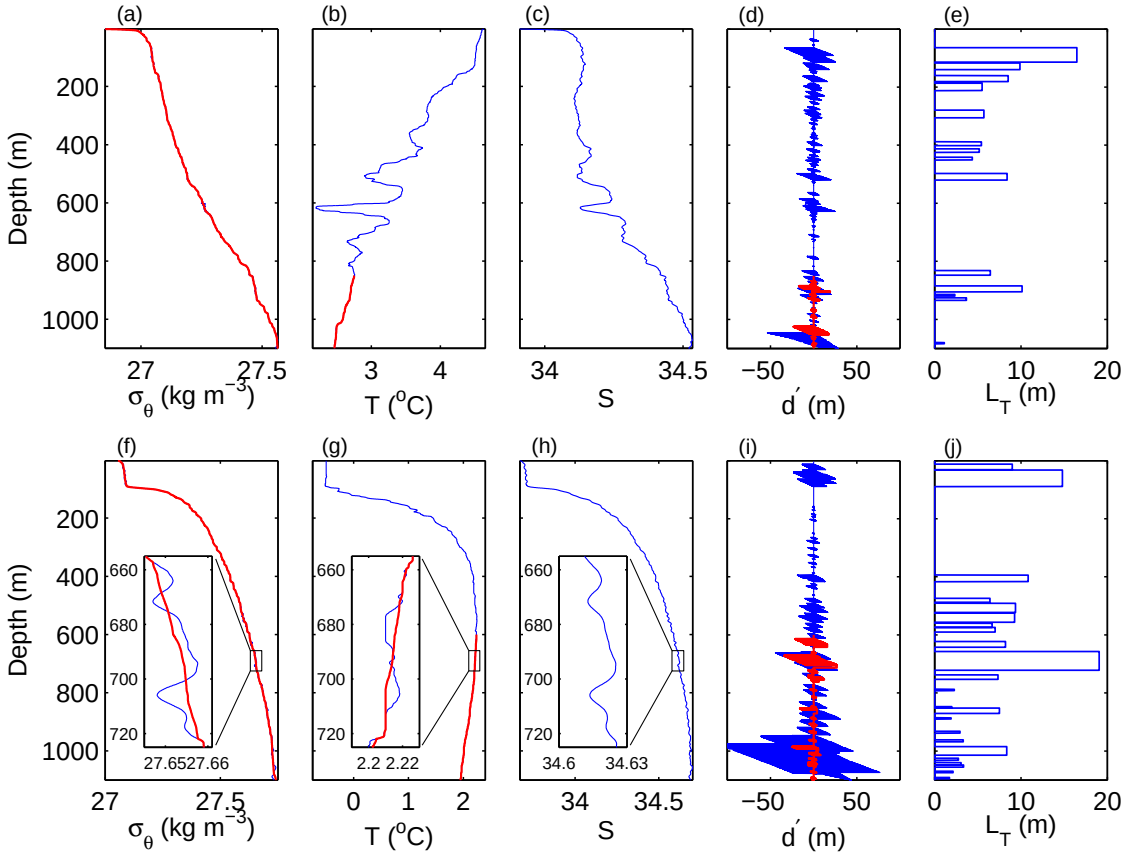

Figure V.3: (a), (f) Potential density, (b), (g) temperature and (c), (h) salinity profiles at typical profiles north and south of the Polar Front respectively. The cast shown in the upper panels was collected at 56° S in November of 2004 while the cast in the lower panels was collected at 60.5° S in June of 2003. In the potential density and temperature panels the red thick curve indicates the re-ordered profile. Temperature is only re-ordered outside of regions where double-diffusive convection may be important. Panels (d) and (i) show the Thorpe displacements for both the re-ordered density (black curve) and re-ordered temperature (red curve). In panels (e) and (j), each block represents a turbulent overturn whose vertical thickness and horizontal length represents the individual overturn's vertical size and Thorpe scale respectively. Panels $(f\text{-}g)$ show expanded views of one of the largest overturns in our data set.

structed that are zero outside of overturns and nonzero within. Profiles of κ_ρ are computed from (V.4) using ε and the background buoyancy frequency calculated over 100 m bins. Depth averaged quantities of L_T, ε and κ_ρ are computed over the same 100 m bins following (V.5), and each bin is averaged over many casts.

V.4.iii XCTD noise effects

Johnson & Garrett introduce the non-dimensional parameters Q and n to describe the two limiting factors of overturn detection: density resolution and vertical resolution. Using values from our study given in Table V.1, Q, the amplitude of the noise scaled by the density change over the section, is

$$Q = \frac{\delta\rho}{(\mathrm{d}\rho/\mathrm{d}z)\,H} = 0.01 - 0.1, \tag{V.12}$$

and n is given by

$$n = \frac{H}{h} \approx 800, \tag{V.13}$$

where $\delta\rho$ is the instrument noise, $\mathrm{d}\rho/\mathrm{d}z$ the stratification, H the section length and h the vertical sampling interval. For $nQ > 1$, density resolution limits overturn detection (as in our study), while for $nQ < 1$, vertical resolution limits overturn detection (Stansfield *et al.* 2001).

In Table V.1 we present values for dimensional and non-dimensional noise parameters of different Thorpe scale studies. The studies listed, with the exception of Timmermans *et al.* (2003), include near-surface measurements similar to ours. Timmermans *et al.* (2003) consider thermohaline staircase structures in the deep Canada Basin and analyze temperature profiles as opposed to density so that $\delta\rho$ and $\mathrm{d}\rho/\mathrm{d}z$ are replaced by δT and $\mathrm{d}T/\mathrm{d}z$ in Table V.1. Figure V.4 illustrates the location of these studies in parameter space. Overturn detection improves as Q decreases and n increases. Johnson & Garrett (2004) find that studies in the upper left region of Figure V.4 are reliable, whereas true overturns are indistinguishable from noise in the study of Timmermans *et al.* (2003). The weak stratification of Drake Passage pushes the limits of XCTD overturn detection, which is reflected in

Table V.1: Noise parameters for various Thorpe scale studies, where $\delta\rho$ is the instrument noise, $\mathrm{d}\rho/\mathrm{d}z$ the stratification, H the depth of the section analyzed and h the distance between measurements. Timmermans *et al.* (2003) (Timm. 03) used only temperature profiles for overturns so that $\delta\rho$ and $\mathrm{d}\rho/\mathrm{d}z$ are replaced by δT and $\mathrm{d}T/\mathrm{d}z$. Noise parameters of XCTD temperature profiles in the Pacific are given for comparison. The two GK96 entries are separate data sets analyzed by Galbraith & Kelley (1996) and the two values of $\delta\rho$ from Stansfield *et al.* (2001) (Stans. 01) represent two different types of CTDs that were utilized. The study of Finnegan *et al.* (2002) is given by Finn. 02. The non-dimensional parameters Q and n are defined in (V.12) and (V.13) and discussed in section V.4.iii.

Study	$\delta\rho$ (kg m^{-3})	$\mathrm{d}\rho/\mathrm{d}z$ (kg m^{-4})	H (m)	h (m)	Q	n
GK96 (SLE)	0.001	0.09	50	0.02	0.0002	2500
GK96 (EUBEX)	0.001	0.0009	1000	0.25	0.001	4000
Stans. 01	0.0006/0.004	0.01	100	0.01	0.0006/0.004	1000
Finn. 02	0.0005	0.005–0.0001	300	0.40	0.0003–0.017	750
XCTDs (Drake P.)	0.001	0.001–0.0001	100	0.13	0.01–0.1	800
	δT (° C)	$\mathrm{d}T/\mathrm{d}z$ (° C m^{-1})				
Timm. 03	0.00013	0.001	5	0.03	0.02–0.3	20–200
XCTDs (Pacific)	0.005	0.01	100	0.13	0.005	800

our comparatively large values of $L_{\rho_{\text{min.}}}$ (cf. Finnegan *et al.* (2002) where $L_{\rho_{\text{min.}}}$ varies between 0.2 and 10 m). However, as discussed below, we find good agreement between spatial patterns in the Thorpe scale and strain spectral methods. This latter method depends on scales larger than 15 m that should be unaffected by noise and gives us confidence in our results.

Figure V.5 (*a*) presents the cumulative density function of the total dissipation based on the size of all accepted overturns. The solid vertical line represents the minimum value of $L_{\rho_{\text{min.}}}$ (4 m), the dotted line is the mean value of $L_{\rho_{\text{min.}}}$ over Drake Passage (6.5 m) and the dashed line is the maximum value of $L_{\rho_{\text{min.}}}$ (19.5 m). Figure V.5 (*b*) shows that the probability density function of overturn size is lognormally distributed as described by Ferron *et al.* (1998) and Stansfield *et al.* (2001). The peak in the distribution occurs between 10 and 12 m. Therefore if $L_{\rho_{\text{min.}}} > 12$ m we might expect a significant portion of the overturns to be indistinguishable from noise. Note that $L_{\rho_{\text{min.}}}$ exceeds 12 m in only a small region of our domain (Figure V.2 (*b*)).

As a final test we analyzed both density and temperature profiles from 20 XCTD casts in the mid-latitude South Pacific and found κ_ρ values of $\mathcal{O}(10^{-5}$ - 10^{-4} m^2 s^{-1}), comparable to open-ocean levels acquired from microstructure measurements. The parameters for the temperature profiles of these Pacific XCTDs are included in Table V.1 and Figure V.4 for comparison.

V.5 Results

V.5.i Drake Passage and the Polar Front

While the focus of this study is primarily on mixing, the XCTD data set offers one of the few multi-year surveys of hydrography available in the Southern Ocean. For this reason we briefly comment upon some of the temperature and salinity properties of Drake Passage before discussing our mixing results.

The most striking feature of the XCTD data is that profiles in northern

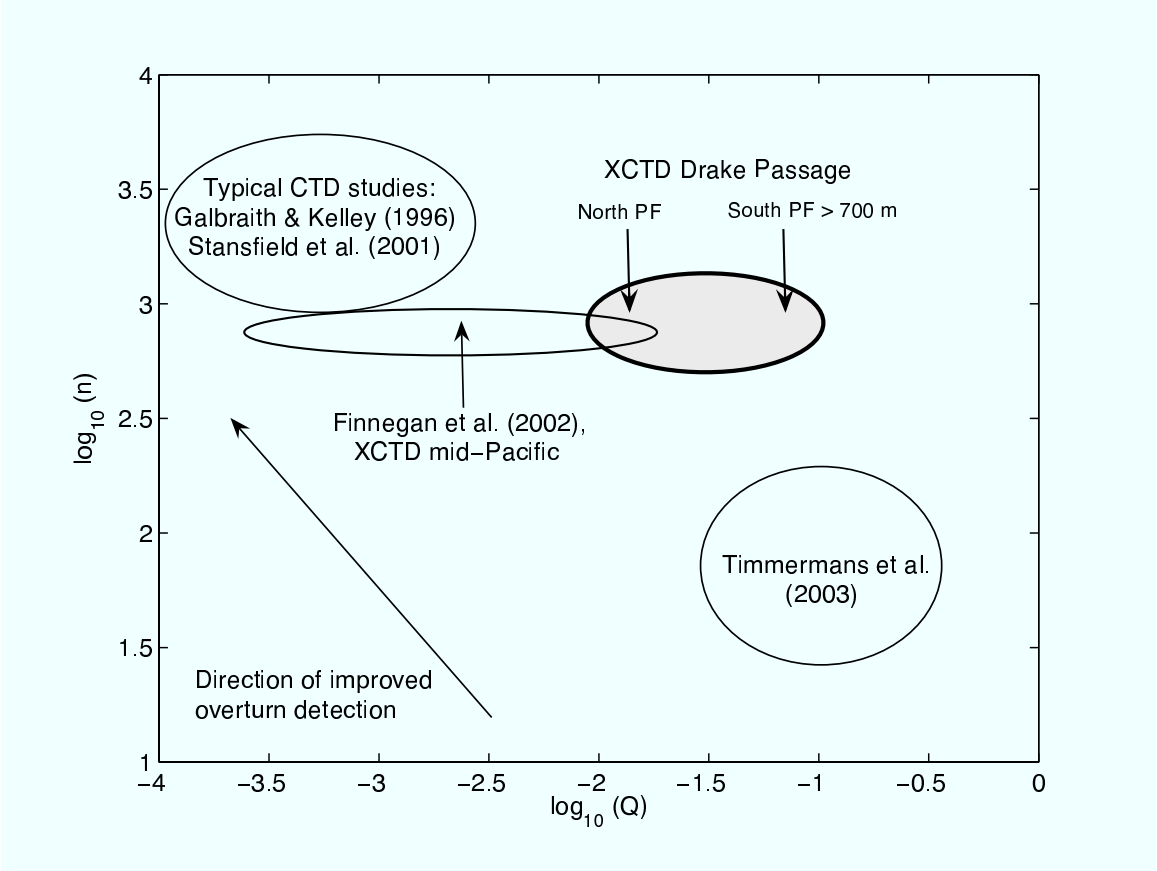

Figure V.4: Diagram of Thorpe scale studies and their associated noise parameters based on Johnson and Garrett's (2004) Figure 3. The definitions of Q and n are given in (V.12) and (V.13). The various studies labeled here are described in Table V.1. Overturn resolution improves as n increases and as Q decreases. The current study is given by the shaded oval, with noise parameters north of the Polar Front having smaller values of Q and south of the Polar Front below 700 m having larger values of Q. The Thorpe scale method could not distinguish overturns from noise in Timmermans *et al.* (2003); we find that overturn detection is marginal below 700 m south of the Polar Front.

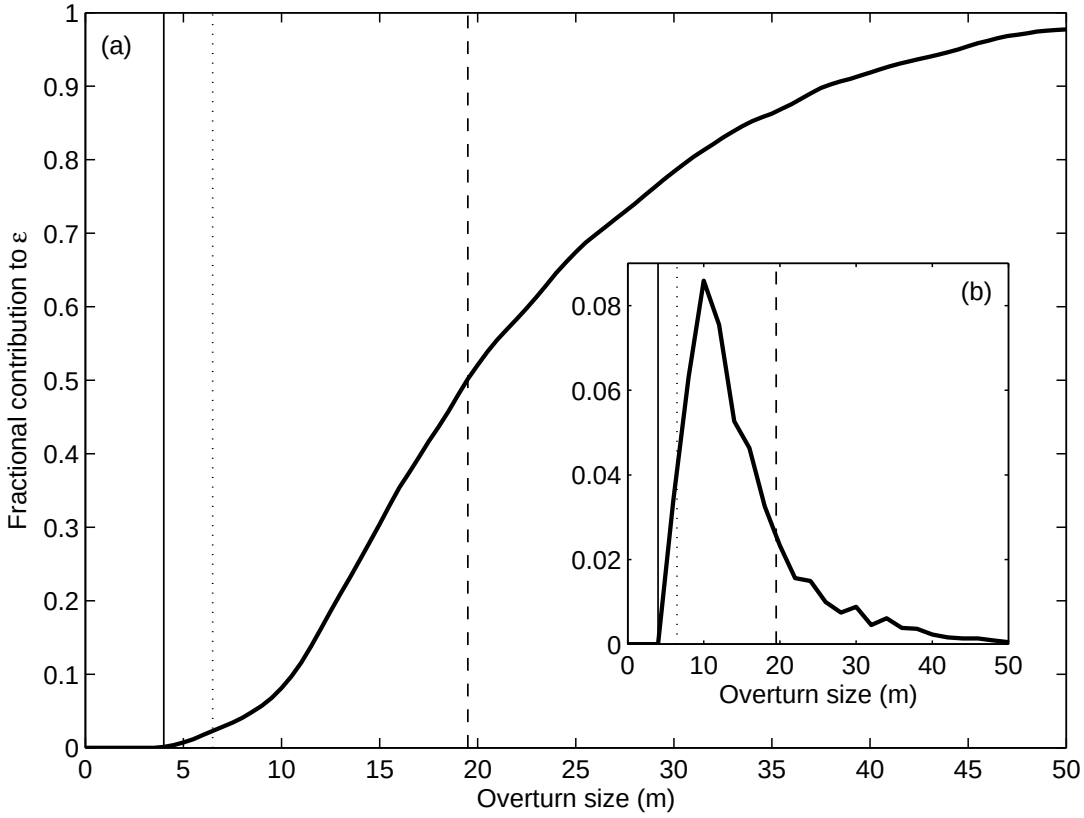

Figure V.5: (a) Cumulative density function of total dissipation ε based on overturn size and (b) probability density function of overturn size for all accepted overturns. Originally 5686 inversions were detected, and 1301 of these were accepted as true overturns. The solid vertical lines mark the minimum value of $L_{\rho_{\text{min.}}}$, the dotted lines mark the mean value of $L_{\rho_{\text{min.}}}$ and the dashed lines mark the maximum value of $L_{\rho_{\text{min.}}}$ in our study (Figure V.2).

and southern Drake Passage exhibit distinct differences, with the transition between the two regions occurring at the Polar Front (PF). The average position of the PF, taken as the northernmost extent of the 2° C isotherm at 200 m (Orsi *et al.* 1995) and shown in Figure V.1, passes our measurement sites at 58.4° S, but the instantaneous position of the PF can vary by hundreds of kilometers. Figure V.6 (a) shows the position of the PF as determined by the closely-spaced XBTs during each cruise used in our study. The horizontal lines indicate the measurement latitudes of the XCTDs. To emphasize the importance of the PF transition, we show σ_θ, T and S profiles from two casts taken at the same latitude (59° S) and separated by only three months, but taken on different sides of the PF. These two casts show markedly different characteristics despite temporal and spatial proximity.

North of the PF, profiles are characterized by rapid, compensating inversions in temperature and salinity that have a thickness of 20 to 50 m (Figure V.3 (b) & (c) and Figure V.6 (f) & (g)). Mesoscale eddy energy is significantly larger north of the PF (Sprintall 2003, Lenn *et al.* 2005). These eddies give rise to thermohaline intrusions that are persistent features of northern Drake Passage (Joyce *et al.* 1978, Toole 1981) and give the region its T/S interleaving signature. South of the PF eddy energy is much lower and there is little deviation between profiles. Temperature in the upper 100 m varies seasonally, but a sharp minimum consistently occurs near 100 m (Figure V.6 (c)). Temperature then increases weakly until it reaches a maximum between 400 and 600 m. Below this depth temperature steadily decreases. Although temperature is unstably stratified between the two extrema, the density profile remains stably stratified due to the salinity field. The unstable temperature and the stable salinity gradients suggest that the water column could be prone to double diffusive convection, which we discuss further in section V.6.ii.

Figure V.2 shows buoyancy frequency values averaged over (a) all casts and also divided into (c) winter (April to September) and (d) summer (October to March) months. The stratification between 100 and 1000 m of Drake Passage

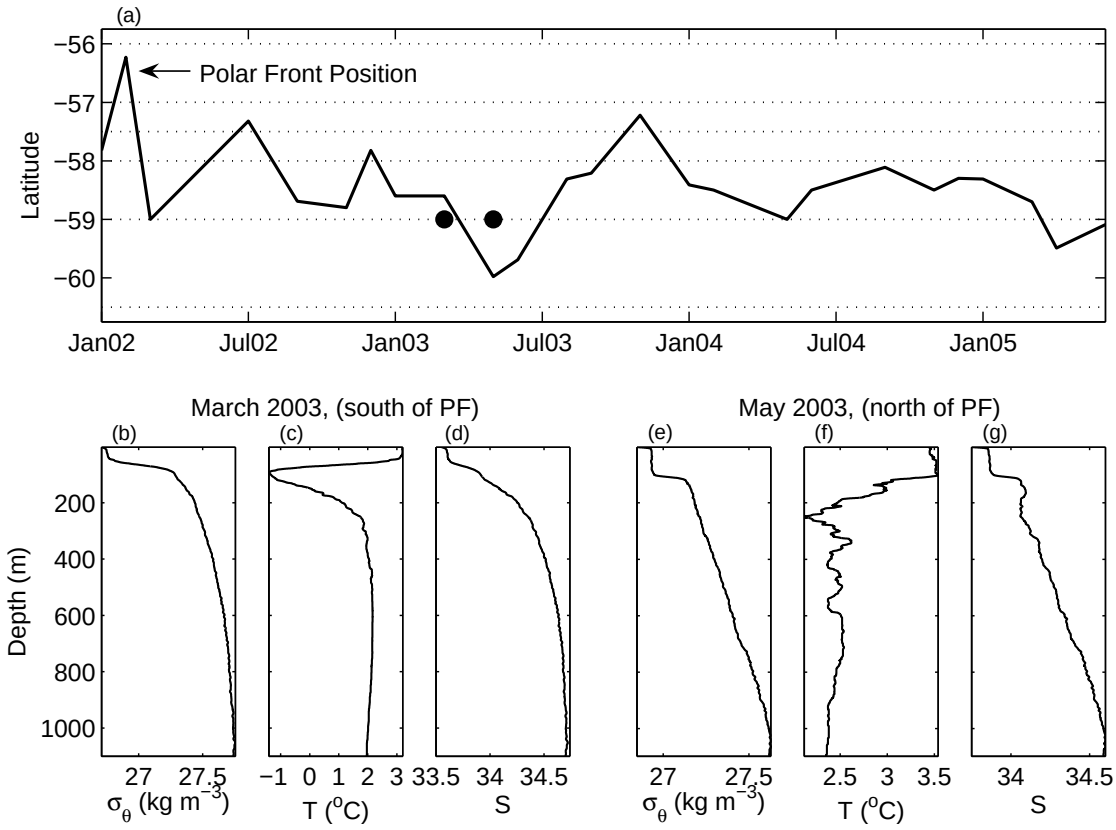

Figure V.6: (a) Position of the Polar Front at 200 m depth as determined from each Drake Passage cruise from 2002-2005. Dotted lines indicate the lattitudes of XCTD casts. Panels $(b$-$d)$ and $(e$-$g)$ show σ_θ, T and S at 59° S at times when the cast was south and north of the Polar Front respectively. The cruise dates of the bottom panels are marked by dots in panel (a).

varies little between winter and summer. Despite the rapid changes in temperature and salinity north of the PF, the buoyancy frequency is roughly constant with $N \approx 2.5 \times 10^{-3}$ s^{-1}, although at depths between 200 and 400 m N is slightly smaller. In contrast, stratification south of the PF decreases monotonically with increasing depth. Over the upper 1000 m, N typically drops by a factor of 5.

The sharp change in properties across the PF suggests that different physical processes may govern mixing in these two regions.

V.5.ii Thorpe scales

Along with buoyancy frequency, the Thorpe scale L_T is the fundamental quantity from which ε and in turn κ_ρ are inferred. The depth-averaged value of ε depends on the number and size of overturns (that pass the criteria in section V.4.ii) as well as the magnitude of L_T associated with each overturn.

Figure V.7 (a) shows 100 m depth-averaged L_T for all casts. In northern Drake Passage, elevated values of L_T up to 5 m are found in the upper 100 to 400 m and decay away from the surface. The surface-intensified values extend as far south as 58^o S and are largest near 57^o S. Below 500 m L_T is approximately 2 m. In southern Drake Passage, surface values are considerably smaller with $L_T \approx 1$ m. Rather than decaying with depth, L_T increases to a maximum value of roughly 2.5 m near a depth of 500 m. Below this peak, L_T decreases with depth. In Figure V.7 and Figure V.8 the cross-hatched area indicates a region where $L_{\rho_{\text{min.}}} > 12$ m (Figure V.2 (b)) and overturn detection is marginal. Overall, our L_T estimates are comparable to previous Thorpe scale studies that encountered regions of weak stratification, such as Ferron *et al.* (1998) and Finnegan *et al.* (2002).

Figure V.8 shows that there is a strong seasonal variation in L_T. The surface-intensified L_T values observed in Figure V.7 (a) are largely due to winter mixing events. The dominant spatial pattern is also clearer in winter months (Figure V.8 (a)), when a relatively quiet region with L_T less than 2 m stretches from the surface in southern Drake Passage to a depth of almost 1000 m in northern

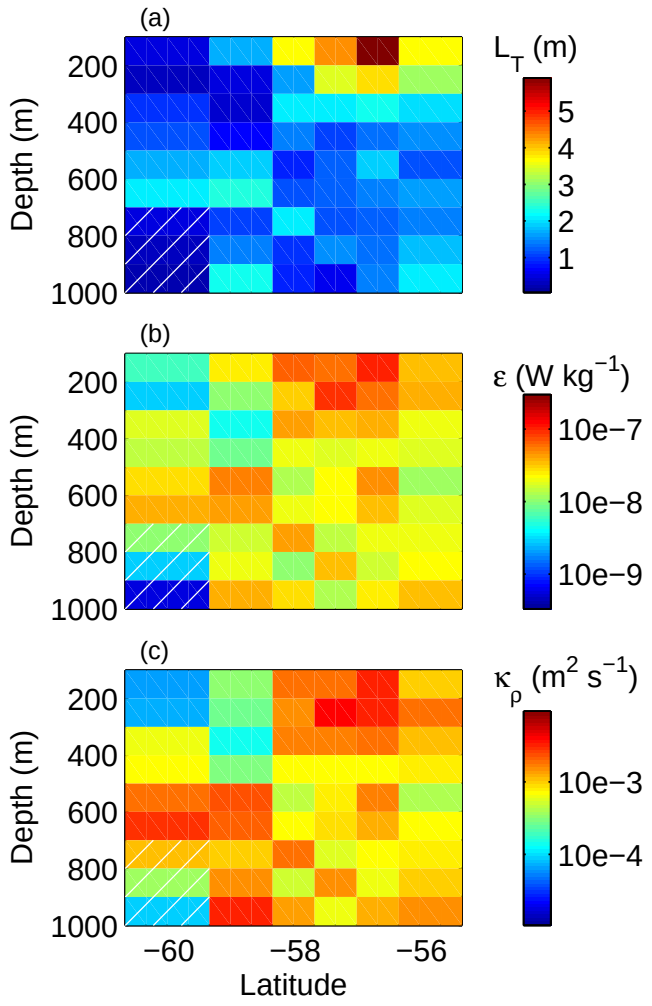

Figure V.7: (a) Thorpe scale L_T, (b) turbulent dissipation rate ε and (c) turbulent diffusivity κ_ρ averaged over 100 m bins for all the casts at each latitude. The cross-hatched area indicates regions where stratification is weak and overturn detection is marginal (see section V.4.iii).

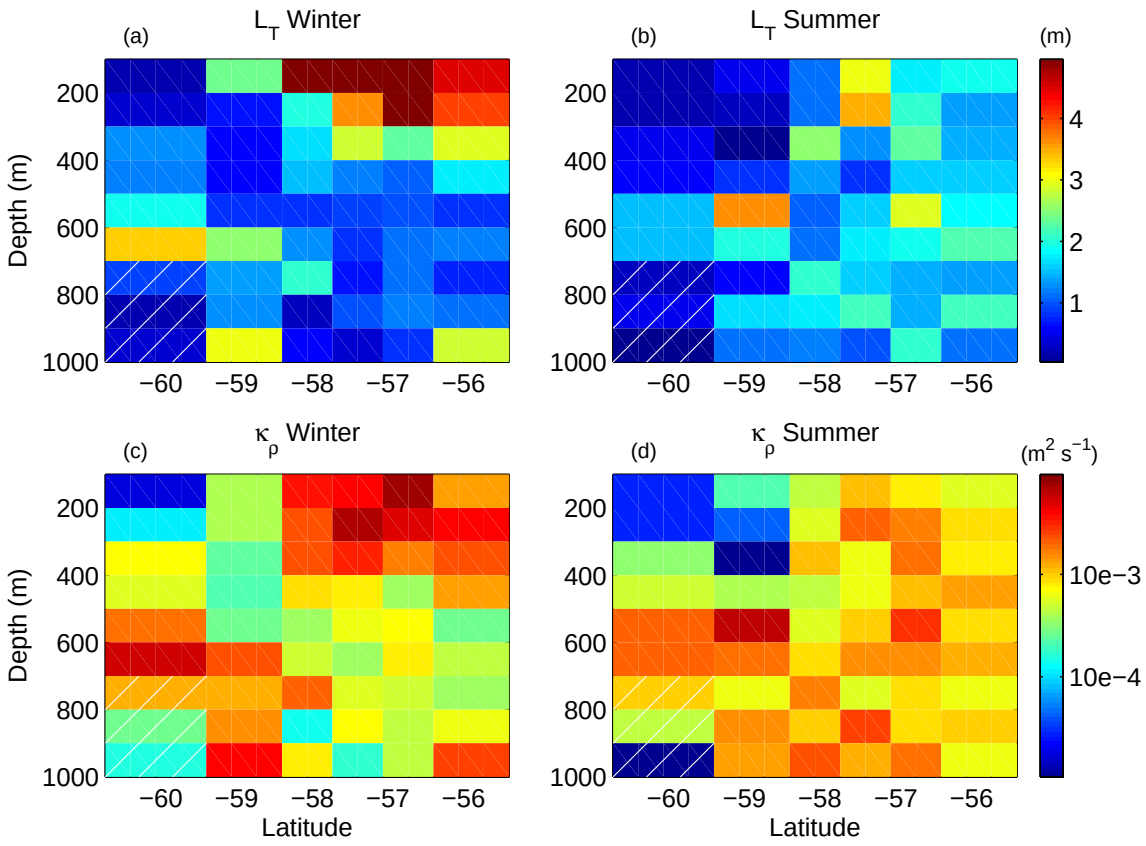

Figure V.8: Upper panels show 100 m depth-averaged Thorpe scales L_T for casts taken during (a) winter (April-September) and (b) summer (October-March) months. The lower panels show 100 m depth-averaged turbulent diffusivity κ_ρ divided in (c) winter and (d) summer months. The cross-hatched area indicates regions where stratification is weak and overturn detection is marginal (see section V.4.iii).

Drake Passage. During summer months (Figure V.8 (b)), Thorpe scale values are more vertically uniform although L_T generally remains larger in northern Drake Passage. The mid-depth maximum in L_T in southern Drake Passage is observed in both summer and winter months with a maximum value $L_T \approx 3.5$ m occurring at 59° S in the summer and shifting to 60.5° S in the winter.

V.5.iii Thorpe scale estimates of ε and κ_ρ

Figure V.7 (b) presents 100 m depth-averaged values of ε for all casts. Again the dominant spatial pattern indicates enhanced dissipation at the surface in northern Drake Passage and a mid-depth maximum at latitudes of 59° and 60.5° S. Dissipation values span approximately two orders of magnitude ranging from 10^{-7} to 10^{-9} W kg^{-1}. The spatial pattern in ε is clearer during winter months (not shown). During summer months ε has a nearly uniform value of 10^{-8} W kg^{-1} across the Passage with the exception of the 100-200 m bins north of the PF where ε is slightly larger and the 800-1000 m bins at 60.5° S where ε is slightly smaller.

Figure V.7 (c) shows 100 m depth-averaged κ_ρ for all casts; values are determined from ε and N according to (V.4). In general κ_ρ follows the same spatial pattern as ε although the pattern here is more distinct. Near the surface in northern Drake Passage, κ_ρ exceeds 10^{-3} m^2 s^{-1} and then decays with depth to a background level of about 4×10^{-4} m^2 s^{-1}. In southern Drake Passage the diffusivities are smaller with minimum rates of 2×10^{-5} m^2 s^{-1} at 60.5° S near the surface and peaking at 2×10^{-3} m^2 s^{-1} at 500 to 700 m depth.

Figure V.8 (c) and (d) show κ_ρ divided into winter and summer months. Again the dominant spatial pattern in κ_ρ is clearer during winter months. North of the PF, near-surface values of κ_ρ decrease significantly from winter to summer months while at depths greater than 400 m, the summer values of κ_ρ are as large or larger than winter values. The net result is a smoothing of the dominant spatial pattern in the summer.

In Figure V.9 we present 100 m depth-averaged values (bold lines) of ε

and κ_ρ for all casts collected (a & c) south of the PF and (b & d) north of the PF. As described above, a pattern of surface-elevated mixing north of the PF is clearly shown, as is the trend of increasing mixing with depth to 600 m south of the PF. Again, the PF appears to delineate regions of differing mixing patterns. In each 100 m bin the outer vertical lines represent statistical uncertainty based on the bootstrap method (Efron & Gong 1983).[3]

The values of ε and κ_ρ shown in Figure V.7 through Figure V.9 are larger than typically observed open-ocean sub-thermocline background levels, although they remain smaller than elevated mixing rates observed above rough topography (as in Drake Passage, Naveira Garabato *et al.* 2004) and over sills (as in the Romanche Fracture Zone, Ferron *et al.* 1998). However, open-ocean comparisons may be inadequate because of the unique characteristics of Drake Passage, such as strong zonal flow and strong mesoscale eddy activity (Lenn *et al.* 2005). The dynamic pathways between eddies and turbulent dissipation are not well understood, but it has been suggested that eddies may enhance mixing (Polzin, personal communication). Further discussion appears in section V.6.ii. In the following section we present an alternative method of inferring κ_ρ to help verify these results.

V.5.iv Strain rate estimates of κ_ρ

Kunze (2003) calculates strain spectra from profiles of buoyancy frequency and the vertical derivative of potential temperature. While the buoyancy frequency estimate can be sensitive to salinity variations where stratification is weak, temperature-inferred strain is not expected to work well in regions where finestructure water-mass variability, such as thermohaline intrusions and interleaving, is strong. Since interleaving is a distinctive feature of Drake Passage, it is not surprising that temperature-inferred strain produce κ_ρ estimates signifi-

[3]Values of ε and κ_ρ were binned into 100 m intervals. These binned profiles were subsampled and averaged 100 times using one-half of the available data in each bin. The error bars in Figure V.9 represent the 3rd and 97th percentile of the resulting distribution. We use 75 casts collected north of the PF, and 39 casts collected south of the PF.

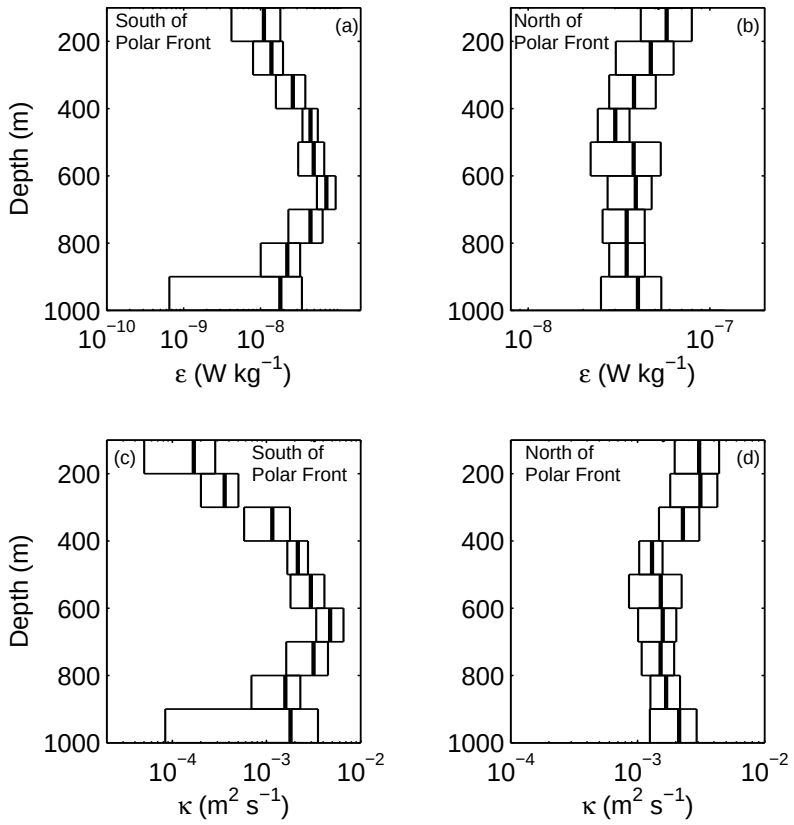

Figure V.9: Turbulent dissipation rate ε averaged over 100 m bins for all casts (a) south of the Polar Front and (b) north of the Polar Front. The lower panels show 100 m depth-averaged turbulent diffusivity κ_ρ for all casts (c) south of the Polar Front and (d) north of the Polar Front. In each 100 m bin the width determined by the two outer vertical lines represents statistical uncertainty as determined by a bootstrap technique (Efron and Gong 1983, see section V.5.iii).

cantly larger than the buoyancy frequency estimates. As an alternative, Finnegan *et al.* (2002) analyze strain spectra initially formed from displacement profiles of potential density. We find that both the buoyancy frequency profiles and the displacement profiles give spectra with the same amplitude to within 15%, and more importantly, they show the same spatial distribution of mixing across Drake Passage.[4]

We divide the data into 200 m segments so that there are no large changes in buoyancy frequency within each bin. The uppermost segment is taken to start at 150 m in order to exclude the mixed layer, which can give anomalously large strain variances. All other segments begin at multiples of 100 m so they are half-overlapping. To determine strain we first remove a linear trend, then normalize the result by the mean buoyancy frequency over each segment. Spectra at each latitude and from each depth are averaged over all casts.

Figure V.10 shows spectra from two different latitudes and at various depths. Our vertical wave number spectra for strain agree well with the GM model (bold curve) with a flat region at intermediate wavenumbers that rolls off to a slightly red spectra at the highest resolved wavenumbers. The left hand panels show spectra from casts taken exclusively north of the PF at 56° S, while the right hand panels are from 60.5° S, exclusively south of the PF. The strain variance ratios are determined by integrating both the measured spectra and the GM spectra from $k_{\text{min.}} = 0.01$ out to $k_{\text{max.}}$ as described in (V.6). The value of $k_{\text{max.}}$ is given in each panel by the dashed vertical line. Figure V.10 shows that the amplitude of the strain spectra decreases with depth at locations north of the PF, while the amplitude increases with depth at locations south of the PF. The vertical eddy diffusivity based on the strain spectral analysis κ_ρ^ϕ is computed using the formula in (V.8) where we have taken $\mathcal{H}(R_\omega)\mathcal{J}(f,N) = 5$ based on the

[4]The spectra plotted in Figure V.10 are based on the buoyancy frequency profiles. These were chosen because there is less noise at high wavenumbers, although we note that this does not affect our mixing rate estimates which depend on strain variances at low wavenumbers.

discussion in section V.3.ii. The corresponding value of κ_ρ^ϕ is given in each panel.

Figure V.11 (a) shows a representation of κ_ρ^ϕ for all casts. The spatial pattern found using the Thorpe scale method remains the dominant feature. Mixing rates are elevated near the surface north of the PF, whereas mixing rates tend to be larger away from the surface south of the PF. Although still present, the mid-depth maximum in mixing south of the PF is not as clearly defined in the strain rate estimate primarily because κ_ρ^ϕ does not decrease rapidly below the temperature maximum as κ_ρ does in the Thorpe scale analysis. Also, κ_ρ^ϕ spans a smaller range of values than κ_ρ (Figure V.7 (c)).

Figure V.11 (b) gives the ratio of κ_ρ to κ_ρ^ϕ. Throughout Drake Passage the Thorpe scale estimate is generally larger than the strain estimate. This suggests that the Thorpe scale estimate may provide an upper bound on mixing rates (see discussion in section V.4.ii). Over most regions of Drake Passage the ratio of the two estimates is roughly 2-3 and only exceeds 5 in one bin at 59^o S. Because of the assumptions that go into both the Thorpe scale and strain spectral methods, specifically the reliance on numerical constants R_ω and L_T/L_O, there appears to be relatively good agreement between the two methods. The fact that both methods exhibit the same spatial pattern suggests that the dominant contribution to overturning is internal wave breaking.

V.6 Discussion

The results of the previous section provide evidence that mixing events north and south of the PF are distinctly different. Mixing estimates from both Thorpe scale and strain rate methods most likely reflect internal wave breaking. However, the spatial and seasonal mixing patterns are also correlated with distinct patterns in winds, thermohaline intrusions and mesoscale eddy activity across Drake Passage. In this section we discuss the implications of these different processes.

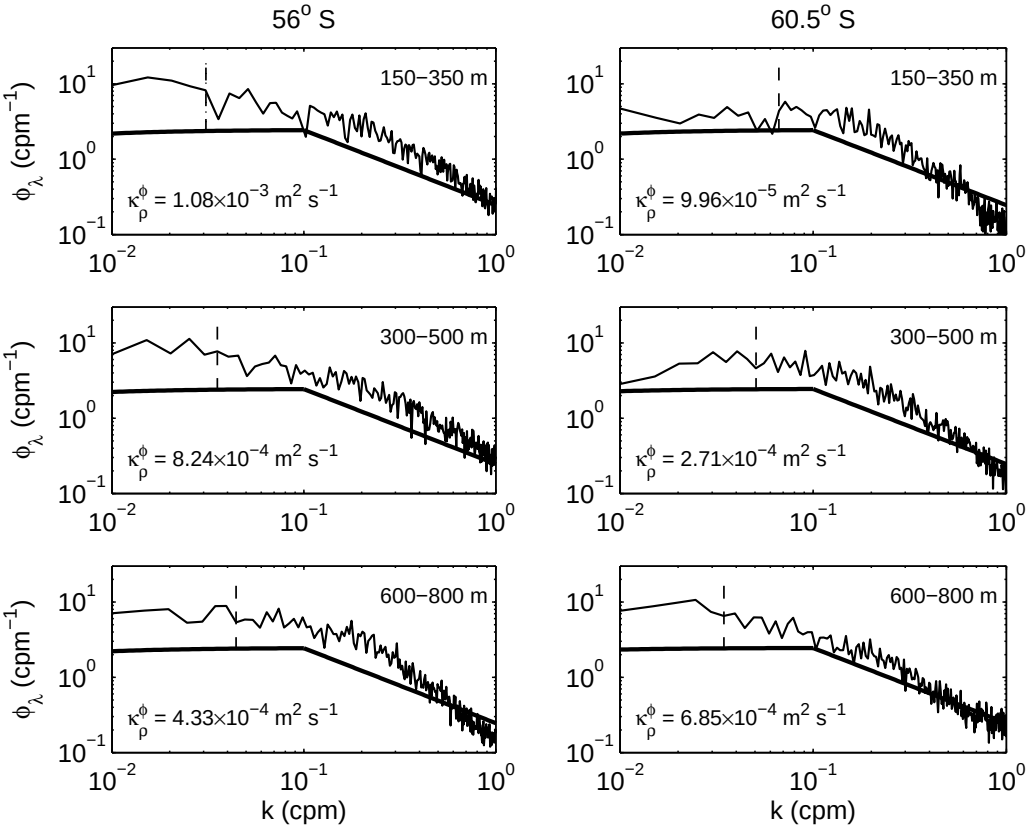

Figure V.10: Vertical strain spectra formed from the buoyancy frequency over 200 m bins as compared to the Garrett-Munk model spectra (bold line). The spectra represent averages over all casts at a given latitude and bin. The left hand panels are from casts at 56° S, which were always north of the Polar Front, while right hand panels are from casts at 60.5° S, which were always south of the Polar Front. The vertical dashed line represents the value of $k_{\text{max.}}$ as described in (V.6) with $k_{\text{min.}} = 0.01$. The accompanying value of κ_ρ^ϕ, the turbulent diffusivity as calculated from (V.8), appears in each panel.

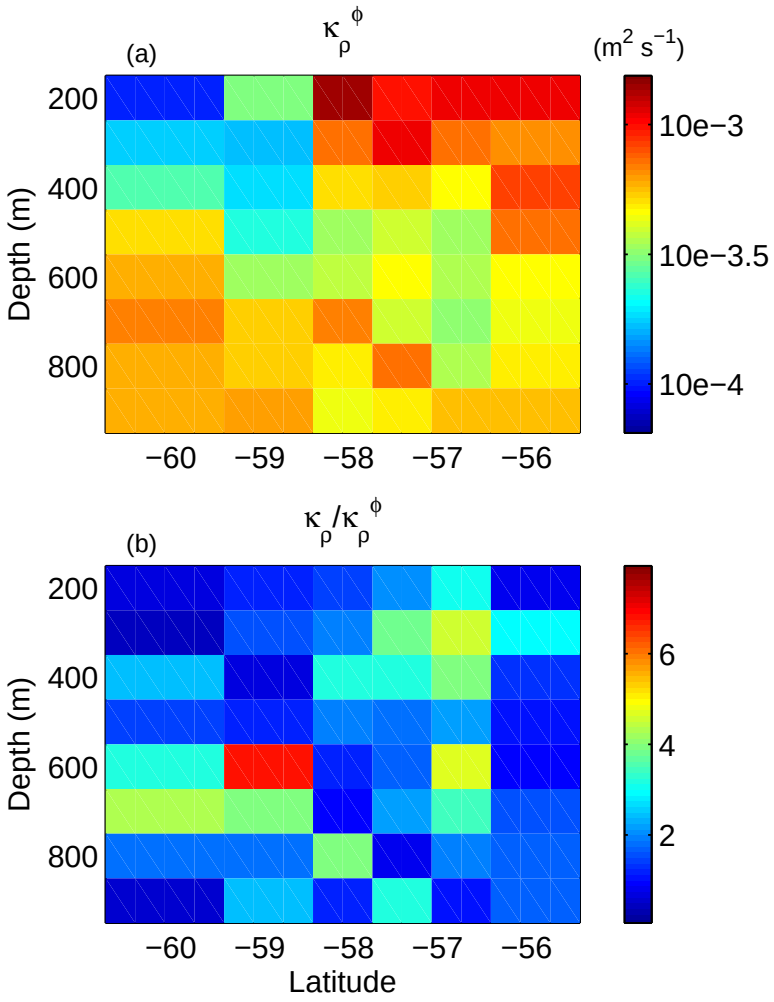

Figure V.11: (a) Turbulent diffusivity as calculated from the vertical strain rate κ_ρ^ϕ following the discussion in section V.3.ii. The data are divided into 200 m half-overlapping bins and represent an average over all casts at each latitude. (b) Ratio of κ_ρ as derived from the Thorpe scale method to κ_ρ^ϕ calculated from the vertical strain rate.

V.6.i Winds

Large diffusivity values near the surface in northern Drake Passage suggest that winds may influence mixing in this region. In a steady state ocean (which may not be a particularly accurate model for the Southern Ocean), the rate of energy input by wind must be equal to the turbulent dissipation. Wunsch's (1998) study of the wind work on the general ocean circulation shows that the total energy input is dominated by Southern Ocean winds. Local dissipation of this energy would help support the high mixing rates we observe in Drake Passage. While Wunsch (1998) considers the role of low-frequency wind work on the general circulation, Alford (2001) describes how higher-frequency fluctuations in the winds can generate inertial motions in the mixed layer that propagate downward as near-inertial internal waves and eventually break causing small-scale mixing. This second process is more likely to explain the spatial patterns and the seasonality of the upper-ocean mixing signal. Alford (2003) notes that his turbulent dissipation values for the Southern Ocean are likely under-estimated because data-poor high-southern-latitude NCEP winds are unreliable.

To study the wind's influence on mixing in Drake Passage, we analyze QuikScat mean wind fields obtained from CERSAT at IFREMER[5]. The winds are computed from the NASA SeaWinds scatterometer and are provided as monthly averages on a global $0.5^{o} \times 0.5^{o}$ resolution geographical grid. Over our study period, both wind speed and wind stress exhibit the same spatial and seasonal patterns. We present the wind stress data here because the energy flux input by wind is proportional to $\tau \cdot \mathbf{u}$, where τ is the wind stress and $\mathbf{u}$ is the current velocity.

Figure V.12 (a) shows the average wind stress in Drake Passage for all months between January 2002 and July 2005. Strong winds give rise to a large wind stress west of the southern tip of South America. The strong eastward flow of the ACC may advect near-inertial waves formed in this region towards our study

[5]http://ifremer.fr/cersat

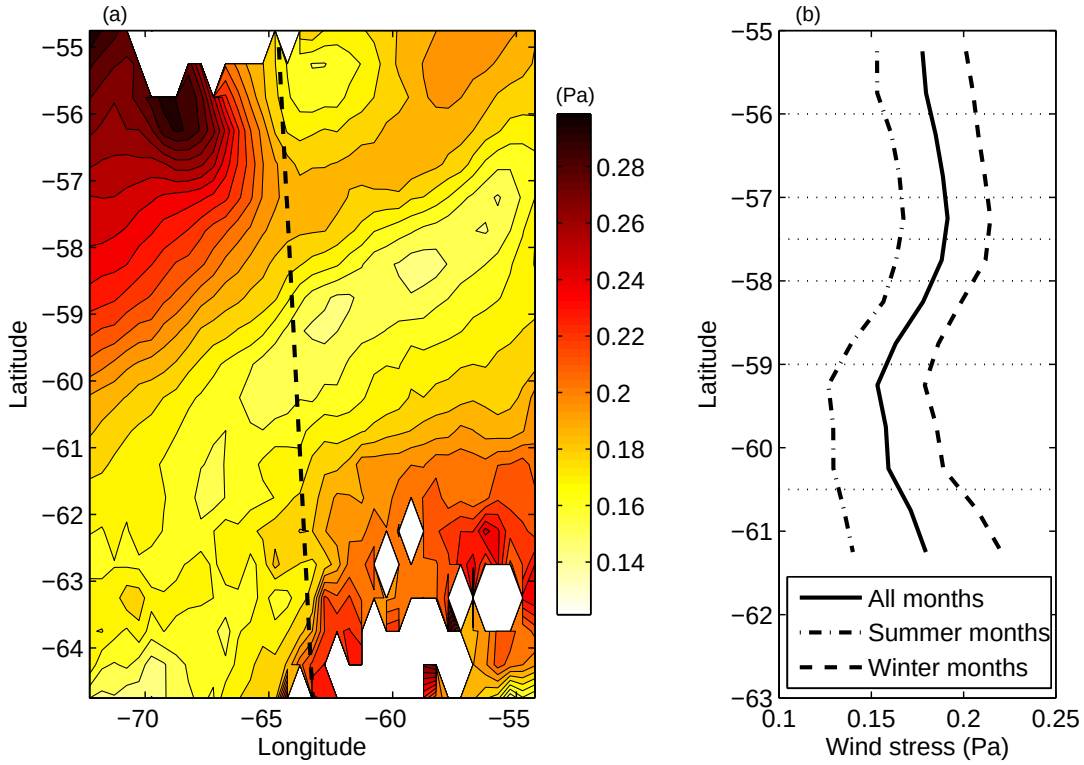

Figure V.12: (a) Average wind stress from QuikScat data for all months between January 2002 and July 2005. The dashed line gives the position of the mean cruise track. (b) Average wind stress along the mean cruise track for all months (solid line) and also divided into summer (dash-dot line) and winter (dashed line) months. The dotted lines give the mean latitudes of the measurement sites.

site. Wind stress decays moving eastward into our study site. Figure V.12 (b) presents wind stress data along the mean cruise track (given by the dashed line in panel (a)) averaged over all months as well as winter (April-Sept.) and summer (Oct.-March) months. Along the cruise track, wind stress peaks just south of 57^o S and has a minimum near 59.5^o S. The locations of the wind stress extrema correspond well with the locations of extrema in our surface values of κ_ρ (Figure V.7 (c)). These results complement the hydrography by providing further evidence that the region north of the PF is more energetic than south of the PF.

The seasonal change in wind stress amplitude is roughly uniform across

Drake Passage despite our observations of a seasonal mixing signal north of the PF (Figure V.8). We expect that storms produce the greatest energy flux into the surface layer, therefore wind stress variance may provide a better indicator of the wind's influence on mixing. Figure V.13 plots wind stress variance along the mean cruise track using 12-hour QuikScat winds from summer and winter months between January 2002 and July 2005. In agreement with Gille (2005), we find that the magnitude of the wind stress variance increases significantly during winter months throughout Drake Passage. During summer, wind stress variance is nearly uniform across Drake Passage, whereas during winter months there is a clear peak in variance at the northern measurement sites (indicated by the dotted lines). This provides a possible explanation for the seasonal signal in κ_ρ north of the PF.

V.6.ii Other Possible Mixing Mechanisms

North of the PF

Observations of compensating interleaving in temperature (T) and salinity (S) (Figure V.3 (b) & (c) and Figure V.6 (f) & (g)) suggest that thermohaline intrusions play an important role in the dynamics of Drake Passage. Toole (1981) points out that in Drake Passage, intrusions are typically confined to the upper 1000 m. Therefore our XCTD casts capture the region of strongest thermohaline variability. Thermohaline intrusions are associated with double diffusive convection, which may represent an alternative source of mixing. While thermohaline intrusions can be driven by both fingering (Ruddick & Turner, 1979) and diffusive (Thompson & Veronis, 2005) interfaces, fingering convection tends to be more vigorous.

Focusing on casts north of the PF, we analyze 60 prominent cases of T/S interleaving and determine the density ratio for each of these possible intrusions. We select the region of the intrusion where the T/S profiles are susceptible to fingering (i.e. T is the stabilizing component), in which case the density ratio is defined by $R_\rho \equiv \alpha\Delta T/\beta\Delta S$. Here ΔT and ΔS are the T and S differences over

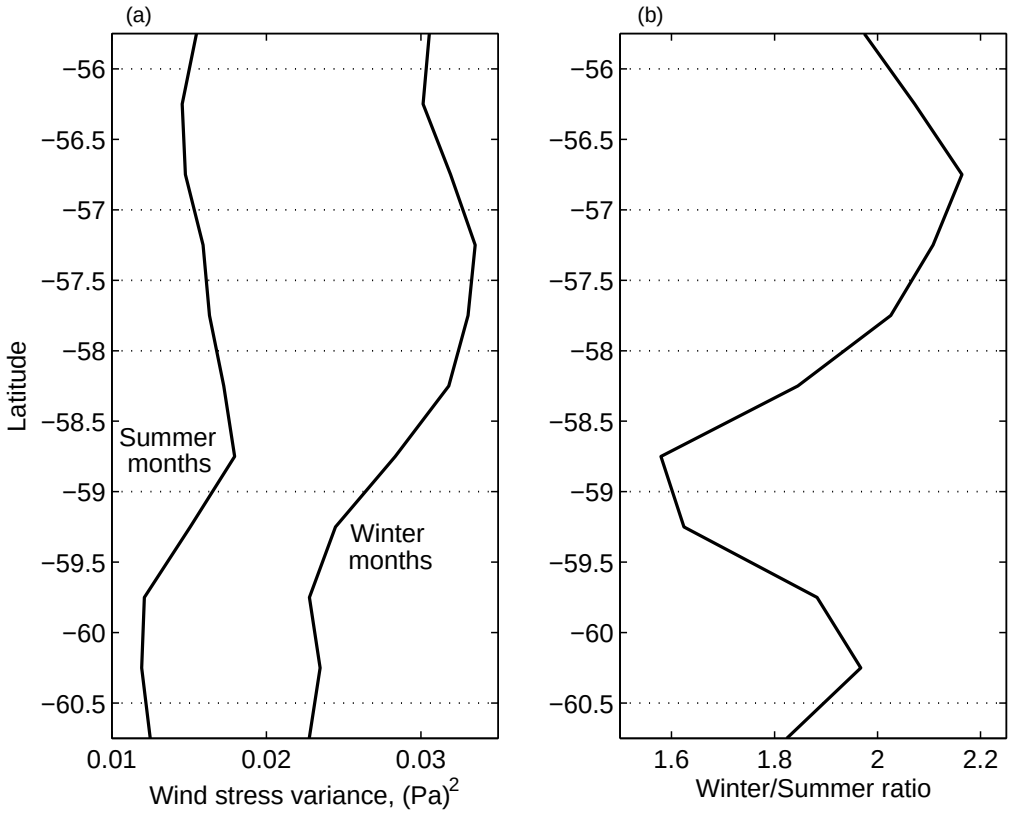

Figure V.13: (a) Wind stress variance from twice-daily QuikScat data along the mean cruise track divided into winter (April-Sept.) and summer (Oct.-March) months. (b) Ratio of the wind stress variance during winter and summer months which shows a clear peak near 57^o S. The dotted lines give the mean latitudes of the measurement sites.

the region where S is unstably stratified, and α and β are local coefficients of expansion for T and S respectively. Mean values of α and β for each intrusion are calculated using the 1980 equation of state for seawater (UNESCO 1981). Over these 60 interleaving regions we find that R_ρ has a mean value of 1.46 with a standard deviation of 0.29. The mean thickness of the regions we analyze is 23.5 m, and the maximum thickness is 50 m.

Fingering convection becomes stronger as R_ρ approaches 1. Our values for R_ρ suggest that thermohaline intrusions in this region may, in places, exhibit strong fingering and could be a source of diapycnal mixing. However, strong zonal flow, eddies and internal waves may act to disrupt finger structures making it difficult to calculate vertical fluxes. Walsh & Ruddick (2000) show that turbulence significantly alters the growth and formation of intrusions as well as the associated fluxes of heat and salt. Larson & Gregg (1983) hypothesize that near-inertial waves aid in intrusion formation, which may also point to strong internal wave activity north of the PF.

There is no observational evidence that eddies enhance diapycnal mixing; still, they have a large influence on Drake Passage dynamics north of the PF. The ability of Drake Passage eddies to stir large-scale T/S gradients and form thermohaline intrusions is discussed by Garrett (1982). The intrusions are assumed to generate fingering convection from which Garrett (1982) calculates a diapycnal diffusivity. This primitive model predicts κ_ρ to be an order of magnitude smaller than those inferred from the internal wave field. Ferrari & Polzin (2005) consider similar dynamics in the North Atlantic and suggest that a better understanding of the processes that arrest interleaving could determine whether mesoscale eddies enhance mixing.

While the possibility exists that thermohaline intrusions, mesoscale eddies and internal waves interact in complicated ways to enhance mixing, these dynamics are poorly understood. Still, all these processes indicate that the region north of the PF is more energetic than south of the PF. The complete lack of interleaving

south of the PF indicates that physical processes governing mixing in this region are potentially very different.

South of the PF

South of the PF, T and S stratification in the upper 500 m of the water column is susceptible to the diffusive regime of double diffusive convection (lower panels of Figure V.3). The T/S profiles in this area are similar to profiles collected in eastern and central Weddell Sea where thermohaline staircases form (Muench *et al.* 1990). Staircase structures, however, are not apparent in the Drake Passage data set. It is possible that the resolution of the XCTDs is unable to capture this behavior, although it is more likely that conditions, such as the region's proximity to large topographic features, strong currents and frontal systems, are unfavorable for staircase formation.

We calculate $R_\rho \equiv \beta\Delta S/\alpha\Delta T$, which by convention is the inverse of the fingering case so that R_ρ is always ≥ 1. ΔT is the difference between the T minimum near the surface and the mid-depth T maximum; ΔS is the S change over the same depth. Averaging over all casts with similar profiles, we find that $R_\rho = 2.66$ with a standard deviation of 0.50. This value is larger than those reported in the Weddell Sea, where $R_\rho = 1.52$ and 1.36 in regions of stronger and weaker temperature gradients respectively (Muench *et al.* 1990). Mixing is enhanced as $R_\rho \to 1$, so that our value suggests that double diffusive convection is generally weak. When R_ρ exceeds 3, thermohaline staircases are unlikely to form (Muench *et al.* 1990).

Howard *et al.* (2004) suggest a method for determining diapycnal diffusivities in the absence of staircases, however the fluxes derived from this technique are swamped by the turbulent mixing inferred from the Thorpe scale and strain rate. However, it is intriguing that Muench *et al.* (1990) observe a sharp increase in eddy diffusivity near the local T maximum, with κ_T exceeding 10^{-3} $\mathrm{m^2\,s^{-1}}$. Both our Thorpe scale and strain spectral methods predict an increase in κ_ρ near

the T maximum south of the PF. The fact that double diffusion alone can not describe mixing south of the PF is, perhaps, not surprising since wind forcing and eddy activity, while smaller south of the PF, are still elevated above levels in mid-latitude oceans.

V.7 Summary and open questions

In this paper we use two independent techniques to calculate turbulent mixing rates in the upper 1000 m of Drake Passage from expendable CTD (XCTD) probes. Uncertainty in the magnitude of our dissipation ε and diffusivity κ_ρ estimates may arise from our choice of certain numerical constants (see section V.3). Furthermore, the theoretical basis for both the Thorpe scale and internal wave-vertical strain techniques is subject to a number of assumptions that are not well-tested in energetic regions like Drake Passsage. Therefore, our main conclusions focus on the identification of robust mixing patterns that appear in the two analyses.

The Polar Front (PF) delineates two regions governed by different physical processes. Profiles collected north of the PF are dominated by compensated interleaving, whereas strong interleaving is absent from all profiles collected south of the PF. The clearest spatial signal we observe is an order of magnitude decrease in surface (upper 400 m) mixing rates moving from north to south across the PF. The clearest seasonal signal occurs in surface values north of the PF with mixing rates larger in the winter. Mixing rates decay weakly with depth north of the PF. South of the PF mixing increases steadily with depth and peaks near the local temperature maximum. Mixing rates below the temperature maximum are not well constrained because overturn detection becomes marginal. Where overturns are well-resolved, our Thorpe scale estimates are consistently larger by a factor of 2-3 than those obtained from the strain spectral method. Strain spectral estimates, which parameterize mixing caused by internal wave breaking, could underestimate

mixing rates if other processes, such as salt fingering, make a similar contribution to the dissipation. However, we suspect that the dominant contribution to mixing is internal wave breaking, and Thorpe scale estimates provide an upper bound on mixing rates (see discussion in section V.4.ii).

Figure V.14 summarizes some possible mechanisms that may influence the spatial and temporal mixing patterns that we observe. Wunsch (1998) indicates that the largest energy input to the oceans due to low-frequency wind work occurs in the Southern Ocean, which may lead to large turbulent dissipation rates. Energy input from high-frequency winds can form near-inertial internal waves that eventually transfer their energy to small scales when they break. In our study, elevated mixing rates near the surface are found at latitudes corresponding to peaks in both wind stress and wind stress variance. Also, seasonal variations in wind stress variance and diapycnal diffusivities are largest north of the PF. Double diffusive processes may also contribute to mixing in Drake Passage. The strong interleaving found north of the PF suggests that thermohaline intrusions, which give rise to salt fingering, are prevalent. Weaker mixing may occur due to the diffusive regime of double diffusive convection in regions where temperature is unstably stratified south of the PF. Perhaps the most distinguishing feature of Drake Passage is the persistent influence of mesoscale eddies, but their role in small-scale mixing is not well understood.

There is insufficient information in the XCTD data set to definitively determine which of the mechanisms listed above, if any, are responsible for the mixing patterns we observe. This question and questions surrounding the overall importance of mixing in Southern Ocean dynamics can only be answered by future studies. This will partly require development of theoretical models and numerical techniques to evaluate the types of mixing processes and dynamic pathways to turbulence that may be unique for the Southern Ocean. One of the more intriguing processes is the potential role of energetic eddies in enhancing mixing. Eddies may produce interleaving that leads to double diffusive convection (e.g.,

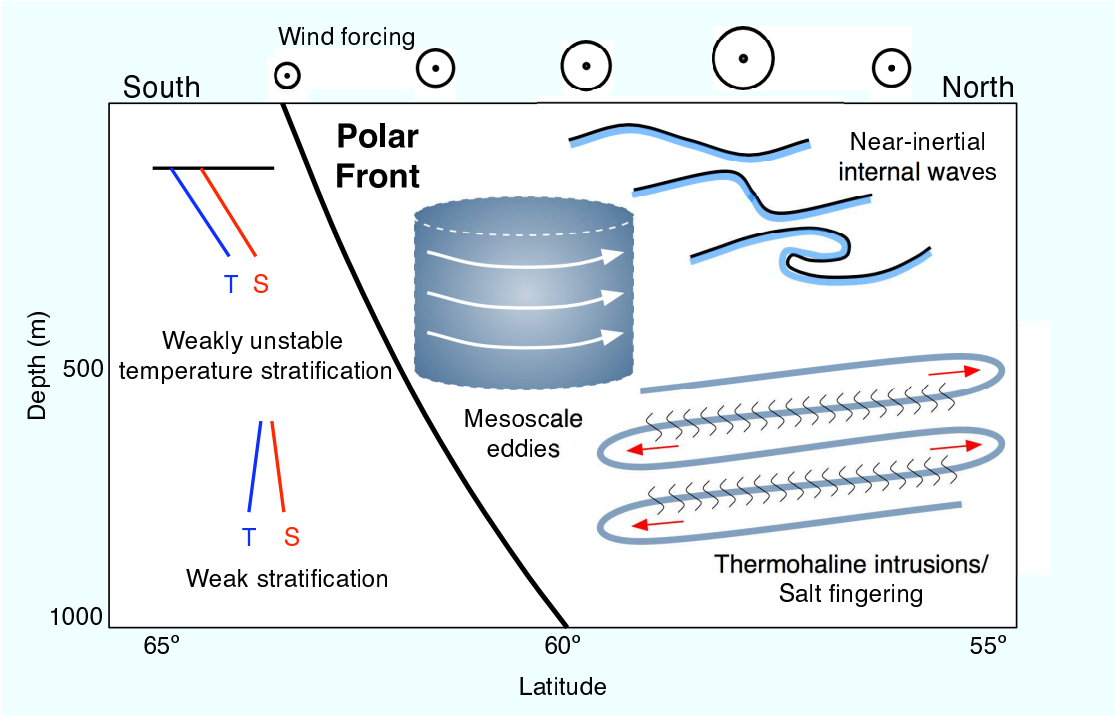

Figure V.14: Schematic of possible mixing processes in Drake Passage. The Polar Front (depicted schematically here) divides two very different regions. North of the Polar Front, strong wind forcing generates near-inertial internal waves that transfer energy to small scales. These waves can break causing small-scale mixing. Thermohaline intrusions are also prevalent north of the Polar Front and may enhance mixing through salt fingering. Mesoscale eddy activity is large north of the Polar Front, although the role of eddies in vertical mixing processes is not well understood. Near the surface south of the Polar Front, temperature and salinity profiles are susceptible to the diffusive regime of double diffusive convection and mixing is weak. South of the Front mixing increases to a depth of at least 600 m. Below this depth stratification is weak and our mixing estimates are poorly constrained.

Ferrari & Polzin 2005), and they may also interact non-linearly with the internal wave field to pump energy to small-scale motions (e.g., Zhai *et al.* 2005). An improved understanding of Southern Ocean mixing processes would also benefit from a dedicated field program in the region, especially one that includes microstructure measurements. Such measurements would help to verify evidence, presented here and in other studies (Naveira Garabato 2004, Sloyan 2005), that small-scale mixing is intense and widespread throughout the water column and likely influences both local Southern Ocean circulation and the global themohaline circulation.

Acknowledgments

XBT and XCTD sampling in Drake Passage is performed with the assistance of NSF-supported Raytheon Polar Services personnel and other cruise participants. Their support is appreciated and essential to the continued success of the sampling program. We thank Alberto Naveira Garabato both for conversations that led us to pursue this study and for sharing data from Drake Passage. We have also benefited from discussions with Jody Klymak, Eric Kunze and Kurt Polzin and from two anonymous reviews. We gratefully acknowledge the following awards that have supported this research: an NDSEG Fellowship (AFT), NSF OCE-0049066 (STG), NSF OPP-0337998 (JS).

The text of this chapter, in full, is a reprint with minor modifications of the paper "Spatial and temporal patterns of small-scale mixing in Drake Passage," accepted for publication in the *Journal of Physical Oceanography*. The dissertation author was the primary researcher and author of this paper. S. T. Gille, J. Sprintall and J. A. McKinnon directed and supervised the research, which forms the basis of this chapter; J. Sprintall supplied the XCTD data.

Appendix A

The two-mode equations of motion

The derivation of the modal equations used in our study is based on Flierl (1978), and also includes forcing terms that arise when there is a mean shear in the basic state as discussed in Hua & Haidvogel (1986). Our equations differ from Hua & Haidvogel only in the form of the hyperviscous term, which is used to absorb enstrophy cascading to the highest wavenumbers. The main difference between the modal decomposition used here and the method used by Larichev and Held (1995) appears in the coefficients of the bottom drag term as shown below.

The continuous quasigeostrophic equations are written as

$$\frac{\partial}{\partial t}Q + J(\Psi, Q) = -\nu\nabla^8 Q\,. \tag{A.1}$$

Here J represents the Jacobian, $J(a,b) \equiv a_x b_y - a_y b_x$, Ψ is the stream function such that $u = -\Psi_y$ and $v = \Psi_x$, and

$$Q = \nabla^2\Psi + (f/N)^2\,\Psi_{zz}\,, \tag{A.2}$$

is the potential vorticity. We consider dynamics on a β-plane, and take the Brunt-Vaisala frequency N to be constant. The coefficient of hyperviscosity is given by ν and H is the depth of the ocean. The Rossby deformation radius is $\lambda = NH/\pi$.

Using a truncated modal expansion in the vertical, we consider the baro-

tropic and first baroclinic modes with a mean shear. We write this as

$$\Psi(x,y,z,t) = \psi(x,y,t) + [-Uy + \tau(x,y,t)]\,\sqrt{2}\cos\left(\frac{\pi z}{H}\right)\,, \tag{A.3}$$

where ψ and τ are the perturbation stream functions of the barotropic and baroclinic modes respectively. The factor of $\sqrt{2}$ arises from normalization of the modes (Flierl 1978). The corresponding potential vorticity is

$$Q = \nabla^2\psi + \left(\nabla^2\tau - \lambda^{-2}\tau + U\lambda^{-2}y\right)\sqrt{2}\cos\left(\frac{\pi z}{H}\right)\,. \tag{A.4}$$

We now apply the modal decomposition of Ψ to the the quasigeostrophic equation and project in the barotropic and baroclinic modes. The frictional, or Ekman drag, terms arise from the bottom boundary condition,

$$w(x,y,-H,t) = \delta_E\nabla^2\Psi(x,y,-H,t)\,, \tag{A.5}$$

where δ_E is the Ekman layer depth. In our model the Ekman drag coefficient is defined by $\kappa = f\delta_E/H$.

The resulting modal equations are:

$$\nabla^2\psi_t + J(\psi,\nabla^2\psi) + J(\tau,\nabla^2\tau) + U\nabla^2\tau_x + \beta\psi_x = -\kappa\nabla^2(\psi - \varkappa\tau) - \nu\nabla^8(\nabla^2\psi)\,, \tag{A.6}$$

and

$$\begin{aligned}\left(\nabla^2 - \lambda^{-2}\right)\tau_t \;&+\; J(\psi,(\nabla^2-\lambda^{-2})\tau) + J(\tau,\nabla^2\psi) + U\left(\nabla^2+\lambda^{-2}\right)\psi_x + \beta\tau_x \\ &=\; \varkappa\kappa\nabla^2(\psi - \varkappa\tau) - \nu\nabla^8(\nabla^2-\lambda^{-2})\tau\,.\end{aligned} \tag{A.7}$$

The variable $\varkappa$ above controls the projection of the bottom drag onto the layers. The modal projection in (A.3) and (A.4) results in $\varkappa = \sqrt{2}$. To limit the effect of bottom drag to the lower layer, set $\varkappa = 1$ (as in Larichev & Held 1995).

To make a comparison with LH03 we introduce equivalent layer variables

$$\psi_1 = \psi + \tau\,, \qquad\qquad \psi_2 = \psi - \tau\,, \tag{A.8}$$

and the corresponding potential vorticities

$$\begin{aligned} q_1 &= \nabla^2\psi_1 + \tfrac{1}{2}\lambda^{-2}(\psi_2 - \psi_1) = \nabla^2\psi + (\nabla^2\tau - \lambda^{-2}\tau)\,, \\ q_2 &= \nabla^2\psi_2 + \tfrac{1}{2}\lambda^{-2}(\psi_1 - \psi_2) = \nabla^2\psi - (\nabla^2\tau - \lambda^{-2}\tau)\,. \end{aligned} \tag{A.9}$$

The layer equations are obtained by adding and subtracting (A.6) and (A.7):

$$q_{1t} + Uq_{1x} + G_1\psi_{1x} + J(\psi_1, q_1) = Diss_1\,, \tag{A.10}$$

$$q_{2t} - Uq_{2x} + G_2\psi_{2x} + J(\psi_2, q_2) = Diss_2\,. \tag{A.11}$$

Above, the PV gradients are

$$G_1 = \beta + \lambda^{-2}U\,, \qquad G_2 = \beta - \lambda^{-2}U\,, \tag{A.12}$$

and the dissipative terms are

$$Diss_1 \equiv (\varkappa - 1)\kappa\nabla^2\psi_\varkappa - \nu\nabla^8 q_1\,, \tag{A.13}$$

$$Diss_2 \equiv -(\varkappa + 1)\kappa\nabla^2\psi_\varkappa - \nu\nabla^8 q_2\,, \tag{A.14}$$

with

$$\psi_\varkappa \equiv \psi - \varkappa\tau = \frac{\varkappa + 1}{2}\psi_2 - \frac{\varkappa - 1}{2}\psi_1\,. \tag{A.15}$$

Notice that the velocity jump between the two layers is $2U$.

The energy balance is obtained in the standard manner by multiplying the barotropic and baroclinic modal equations by ψ and τ respectively and averaging over space. In a statistically steady state the energy balance requires

$$U\lambda^{-2}\left\langle\psi_x\tau\right\rangle = \kappa\left\langle|\nabla\psi_\varkappa|^2\right\rangle + hyp\nu\,, \tag{A.16}$$

where $\psi_\varkappa \equiv \psi - \varkappa\tau$. The hyperviscous term in (A.16) is

$$hyp\nu = \nu\left\langle|\nabla\nabla^4\psi|^2\right\rangle + \nu\left\langle|\nabla\nabla^4\tau|^2\right\rangle + \nu\lambda^{-2}\left\langle\left(\nabla^4\tau\right)^2\right\rangle\,. \tag{A.17}$$

Setting $\varkappa = \sqrt{2}$ we obtain (III.2).

We record some well known identities which are easily obtained using the layer variables. First and foremost, the three different fluxes are all related by:

$$\lambda^{-2}\left\langle \psi_x \tau \right\rangle = \tfrac{1}{2}\lambda^{-2}\left\langle \psi_{2x}\psi_1 \right\rangle = \left\langle v_2 q_2 \right\rangle = -\left\langle v_1 q_1 \right\rangle \,. \tag{A.18}$$

The corresponding eddy diffusivities are defined by

$$\left\langle v_1 q_1 \right\rangle = -D_1 G_1 \quad \text{(definition of } D_1\text{)}\,, \tag{A.19}$$

$$\left\langle v_2 q_2 \right\rangle = -D_2 G_2 \quad \text{(definition of } D_2\text{)}\,, \tag{A.20}$$

$$\left\langle \psi_x \tau \right\rangle = -D_\tau U \quad \text{(definition of } D_\tau\text{)}\,. \tag{A.21}$$

Using (A.18), the three diffusivities are related by

$$D_\tau = (1+\beta_*)D_1 = (1-\beta_*)D_2\,, \tag{A.22}$$

where $\beta_* \equiv \beta\lambda^2/U$. There are some problems with these diffusivities e.g., when $\beta_* = 1$ the instability is still active and so the three fluxes are nonzero and related by (A.18). This forces the conclusion that $D_2 = \infty$, not $D_2 = 0$ as suggested in Lapeyre & Held (2003). For this reason we prefer to deal exclusively with D_τ.

Another quantity of interest is the action $\mathcal{A}$, where

$$\mathcal{A} \equiv \frac{1}{2}\left(\frac{q_1^2}{G_1} + \frac{q_2^2}{G_2}\right)\,. \tag{A.23}$$

The action arises from the enstrophy balance, which is obtained by multiplying (A.10) and (A.11) by q_1 and q_2 respectively and performing a purely spatial average over the domain. This yields

$$\frac{1}{2}\left\langle q_1^2 \right\rangle_t + G_1\left\langle v_1 q_1 \right\rangle = \left\langle q_1 Diss_1 \right\rangle\,, \tag{A.24}$$

$$\frac{1}{2}\left\langle q_2^2 \right\rangle_t + G_2\left\langle v_2 q_2 \right\rangle = \left\langle q_2 Diss_2 \right\rangle\,. \tag{A.25}$$

The terms involving the potential vorticity fluxes can be eliminated by dividing (A.24) and (A.25) by G_1 and G_2 and using the relationship $-\left\langle v_1 q_1 \right\rangle = \left\langle v_2 q_2 \right\rangle$ from

(A.18). Finally we can expand the dissipation term on the right using (A.13) and (A.14), which gives the time evolution of the action

$$\begin{aligned}
\mathcal{A}_t &= -\frac{\kappa}{2}\left[\frac{(\varkappa-1)^2}{G_1}\left\langle\left(\nabla^2\psi_1\right)^2\right\rangle + \frac{(\varkappa+1)^2}{G_2}\left\langle\left(\nabla^2\psi_2\right)^2\right\rangle\right] \\
&- \frac{\kappa}{4}\left[\left(\frac{\varkappa-1}{G_1}+\frac{\varkappa+1}{G_2}\right)\left((\varkappa-1)\left\langle|\nabla\psi_1|^2\right\rangle + (\varkappa+1)\left\langle|\nabla\psi_2|^2\right\rangle\right)\right] \\
&- \nu\left[\frac{1}{G_1}\left\langle\left(\nabla^4 q_1\right)^2\right\rangle + \frac{1}{G_2}\left\langle\left(\nabla^4 q_2\right)^2\right\rangle\right] \\
&+ \frac{\kappa}{2}\left[(\varkappa-1)(\varkappa+1)\left(\frac{1}{G_1}+\frac{1}{G_2}\right)\left\langle\nabla^2\psi_1\nabla^2\psi_2\right\rangle\right] \\
&+ \frac{\kappa}{2}\left[\varkappa\left(\frac{\varkappa-1}{G_1}+\frac{\varkappa+1}{G_2}\right)\left\langle\nabla\psi_1\cdot\nabla\psi_2\right\rangle\right]. \qquad \text{(A.26)}
\end{aligned}$$

If $\varkappa = 1$, (A.26) simplifies greatly to become

$$\begin{aligned}
\mathcal{A}_t = &- \kappa\left[\frac{2}{G_2}\left\langle\left(\nabla^2\psi_2\right)^2\right\rangle + \frac{1}{G_2}\left\langle|\nabla\psi_2|^2\right\rangle\right] \\
&+ \kappa\left[\frac{1}{G_2}\left\langle\nabla\psi_1\cdot\nabla\psi_2\right\rangle\right] - \nu\left[\frac{1}{G_1}\left\langle\left(\nabla^4 q_1\right)^2\right\rangle + \frac{1}{G_2}\left\langle\left(\nabla^4 q_2\right)^2\right\rangle\right] \qquad \text{(A.27)}
\end{aligned}$$

The cross-invariant analysis of Chapter II is a large-scale analog of the action equation given in (A.26).

Appendix B

Vortex census algorithm

The automated vortex census algorithm primarily follows the method outlined in McWilliams (1990) to identify vortices in a two-dimensional gridded vorticity field at a given time. The method begins by identifying all points above a vorticity threshold value ζ_{min}. Following McWilliams (1990) this value is taken to be 5% of the maximum vorticity magnitude in the field. The vortices are also required to have a vorticity extrema at their centers. Thus any point whose magnitude is smaller than one or more of its surrounding points is also excluded. Because we are interested in counting axisymmetric structures, we added a further constraint based on the Okubo-Weiss parameter (Okubo 1970, Weiss 1991), which measures the relative importance of vorticity versus strain. The Okubo-Weiss parameter is

$$OW = s_n^2 + s_s^2 - \zeta^2 = 4\left(u_x^2 + u_y v_x\right), \tag{B.1}$$

where $s_n = u_x - v_y$ is the normal component of strain and $s_s = u_y + v_x$ is the shear component of strain. The Okubo-Weiss parameter is negative when rotation dominates and positive when strain dominates. Therefore we require that the Okubo-Weiss parameter at the center of each of our vorticies be negative and have a magnitude larger than a threshold OW_{min}. Similar to the vorticity we take OW_{min} to be 5% of the maximum OW magnitude in the field (the value of OW at the point of maximum magnitude is always negative).

The boundary of each vortex is determined following the method in

McWilliams (1990), which traces a counterclockwise path around the boundary based on a vorticity threshold. Using the boundary to measure r_{core} proved to be difficult since not all vortices are perfectly axisymmetric and many vortices only have a core radius of 3-4 grid points. We found that a more effective method for determining an average vortex radius was to count all the points that had a negative value of OW and a magnitude greater than OW_{min}. Considering the physical fields, these points were found to lie almost exclusively inside the vortex cores. Dividing the number of points that satisfy the OW threshold by the number of vortices in that particular snapshot provides an estimate of the area of an average vortex (this is not the true area since we are only counting points). From observations of the physical fields, the square root of this number was found to agree well with a typical core radius and was taken as the value for r_{core} in Figure II.9(b).

Simulations with $L/\lambda = 25$ and $\kappa\lambda/U = [0.16, 0.24, 0.32, 0.48, 0.64, 0.80]$ were run for a time $tU/\lambda = 125$ in the equilibrated state during which 50 snapshots of barotropic vorticity and the Okubo-Weiss parameter of the barotropic mode were saved. The vortex census was completed for each snapshot and the values for N and r_{core} plotted in Figure II.9 are the mean of these 50 realizations. The values for ζ_{min} and OW_{min} were varied systematically. These changes alter the resulting values of N and r_{core}, but the relationship between different values of bottom drag does not change significantly. For example, changes in threshold values cause the slope in Figure II.9(a) to vary between -0.52 and -0.62.

Appendix C

Two-layer invariants with quadratic bottom friction

Grianik *et al.* (2004) and Arbic (2006) consider a quadratic bottom friction in place of the tradiational linear bottom friction to model Ekman bottom drag in numerical simulations of quasigeostrophic turbulence. An analysis of the effects of quadratic bottom drag on the formation and persistence of both the vortices and jets observed in the simulations described in Chapters II-IV was beyond the scope of this disserations. However, some of the important quadratic invariants, especially those used in deriving the eddy heat flux parameterization of Chapter II, can be applied to the case with quadratic bottom friction. This Appendix summarizes these relationships specifically for the case of f-plane turbulence where the cross-invariant described in section II.6 is crucial.

Limiting dissipation to the lower layer, the two-layer quasigeostrophic equations on an f-plane are given by

$$Q_1 + J(\Psi_1, Q_1) = 0, \tag{C.1}$$

$$Q_2 + J(\Psi_2, Q_2) = D, \tag{C.2}$$

where

$$\Psi_1 = -Uy + \psi_1, \tag{C.3}$$

$$\Psi_2 = \psi_2, \tag{C.4}$$

$$Q_1 = \nabla^2\Psi_1 + \frac{1}{2\lambda^2}\left(\Psi_2 - \Psi_1\right) = \frac{Uy}{2\lambda^2} + q_1, \tag{C.5}$$

$$Q_2 = \nabla^2\Psi_2 + \frac{1}{2\lambda^2}\left(\Psi_1 - \Psi_2\right) = -\frac{Uy}{2\lambda^2} + q_2, \tag{C.6}$$

and D is drag due to bottom friction.

We can re-write (C.1) and (C.2) using (C.3) through (C.6), which yields

$$q_{1t} + \frac{U}{2\lambda^2}\psi_{1x} + Uq_{1x} + J\left(\psi_1, q_1\right) = 0, \tag{C.7}$$

$$q_{2t} - \frac{U}{2\lambda^2}\psi_{2x} + J\left(\psi_2, q_2\right) = D. \tag{C.8}$$

The definition of the bottom quadratic drag (Grianik *et al.* 2004) is then given by

$$D = -C_D\hat{\mathbf{k}}\cdot\left(\nabla\times|\mathbf{u_2}|\mathbf{u_2}\right) = -C_D\left[\frac{\partial}{\partial x}\left(|\mathbf{u_2}|v_2\right) - \frac{\partial}{\partial y}\left(|\mathbf{u_2}|u_2\right)\right]. \tag{C.9}$$

The first step is to form the energy balance which is accomplished by multiplying (C.7) and (C.8) by ψ_1 and ψ_2 respectively and then integrating over the domain. Assuming the domain is doubly periodic, in steady state the energy balance gives

$$\frac{U}{2\lambda^2}\left\langle\psi_1\psi_{2_x}\right\rangle = \left\langle\psi_2 D\right\rangle. \tag{C.10}$$

Note that terms like $\left\langle\psi_i\psi_{i_x}\right\rangle = 0$ and $\left\langle\psi_i\psi_{j_x}\right\rangle = -\left\langle\psi_j\psi_{i_x}\right\rangle$ because of the doubly periodic boundary conditions. We can switch back and forth between layers and modes using the following formulas:

$$\psi = \frac{\psi_1+\psi_2}{2}, \quad \tau = \frac{\psi_1+\psi_2}{2}, \quad \psi_1 = \psi+\tau, \quad \psi_2 = \psi-\tau. \tag{C.11}$$

As a check, re-writing the LHS of (C.10) in terms of modes produces

$$\frac{U}{2\lambda^2}\left\langle\psi\psi_x - \psi\tau_x + \tau\psi_x - \tau\tau_x\right\rangle = \frac{U}{\lambda^2}\left\langle\tau\psi_x\right\rangle, \tag{C.12}$$

which is the energy production of the modal equations. The RHS of (C.12) can be viewed as $\langle v'T' \rangle$ where v is the barotropic meridional velocity and the baroclinic streamfunction τ is proportional to the temperature field.

With a few simple steps the quadratic bottom friction can be reduced to a more manageable form:

$$\begin{aligned} \langle \psi_2 D \rangle &= -C_D \left[\left\langle \psi_2 \frac{\partial}{\partial x} \left(|\nabla \psi_2| \psi_{2x} \right) \right\rangle + \left\langle \psi_2 \frac{\partial}{\partial y} \left(|\nabla \psi_2| \psi_{2y} \right) \right\rangle \right], & \text{(C.13)} \\ &= C_D \left(\left\langle |\nabla \psi_2| \psi_{2x}^2 \right\rangle + \left\langle |\nabla \psi_2| \psi_{2y}^2 \right\rangle \right), & \text{(C.14)} \\ &= C_D \left\langle |\nabla \psi_2|^3 \right\rangle. & \text{(C.15)} \end{aligned}$$

The projection of bottom friction into the modal equations is more complicated and takes the form

$$C_D \left\langle |\nabla \psi_2|^3 \right\rangle = C_D \left\langle |\nabla \psi - \nabla \tau|^3 \right\rangle = C_D \left[\left(\left\langle |\nabla \psi|^2 \right\rangle - 2 \left\langle \nabla \psi \cdot \nabla \tau \right\rangle + \left\langle |\nabla \tau|^2 \right\rangle \right)^{3/2} \right]. \tag{C.16}$$

If the vortex scaling theory described in Chapter II also applies for a system with quadratic bottom friction, the first two terms on the RHS of (C.16) can be written in terms of vortex properties such as the core radius, etc. The final term, $\langle |\nabla \tau|^2 \rangle$, is more problematic because its magnitude depends on the entire domain (not just the vortices). This term may also make a significant contribution to the dissipation (at least in the linear bottom friction case). In the f-plane analysis of Chapter II, $\langle |\nabla \tau|^2 \rangle$ was determined by considering another quadratic invariant, referred to as the "cross-invariant". The cross-invariant is formed by multiplying the barotropic vorticity equation by τ and the baroclinic vorticity equation by $\lambda^2 \nabla^2 \psi$. After averaging over the domain, terms of $O(\lambda^2)$ in the baroclinic vorticity equation are neglected. These $O(\lambda^2)$ terms were shown to be small in the f-plane case.

In the following I obtain the analogous cross-invariant for quadratic bottom friction. First, it is useful to determine what the cross term becomes in the

layer case. It is simply,

$$\langle \nabla\psi \cdot \nabla\tau \rangle = \left\langle \frac{\nabla\psi_1 + \nabla\psi_2}{2} \cdot \frac{\nabla\psi_1 - \nabla\psi_2}{2} \right\rangle = \frac{1}{4}\left(\left\langle |\nabla\psi_1|^2 \right\rangle - \left\langle |\nabla\psi_2|^2 \right\rangle \right). \quad \text{(C.17)}$$

The equivalent of multiplying the baroclinic streamfunction to the barotropic vorticity equation is to multiply $(\psi_1 - \psi_2)$ by both the upper and lower PV equations and sum the resulting equations. Integration by parts eliminates a number of terms and what remains yields

$$\begin{aligned} &\left\langle \psi_1 \nabla^2\psi_{1_t} \right\rangle + \left\langle \psi_1 \nabla^2\psi_{2_t} \right\rangle - \left\langle \psi_2 \nabla^2\psi_{1_t} \right\rangle - \left\langle \psi_2 \nabla^2\psi_{2_t} \right\rangle - U \left\langle \psi_2 \nabla^2\psi_{1_x} \right\rangle \\ &\qquad + \left\langle \psi_1 J\left(\psi_2 \nabla^2\psi_2\right) \right\rangle - \left\langle \psi_2 J\left(\psi_1, \nabla^2\psi_1\right) \right\rangle = \langle \psi_1 D \rangle - \langle \psi_2 D \rangle . \quad \text{(C.18)} \end{aligned}$$

In Chapter II the non-linear terms are eliminated by multiplying the barotropic vorticity by the baroclinic vorticity equation. Note that only the $O\left(\lambda^{-2}\right)$ terms in the baroclinic vorticity equation are retained since the cross invariant only holds for large scales. At $O\left(\lambda^{-2}\right)$ the upper and lower layer vorticity equations are the same, so there are two independent equations which are

$$\begin{aligned} \left\langle \nabla^2\psi_1\psi_{2_t} \right\rangle - \left\langle \nabla^2\psi_1\psi_{1_t} \right\rangle + U \left\langle \nabla^2\psi_1\psi_{2_x} \right\rangle + \left\langle \nabla^2\psi_1 J\left(\psi_1, \psi_2\right) \right\rangle &= 0, \quad \text{(C.19)} \\ \left\langle \nabla^2\psi_2\psi_{2_t} \right\rangle - \left\langle \nabla^2\psi_2\psi_{1_t} \right\rangle + \left\langle \nabla^2\psi_2 J\left(\psi_1, \psi_2\right) \right\rangle &= 0. \quad \text{(C.20)} \end{aligned}$$

Finally, using (C.19) and (C.20) to eliminate the Jacobian terms in (C.18) we get

$$\frac{\partial}{\partial t}\left(\left\langle |\nabla\psi_1|^2 \right\rangle - \left\langle |\nabla\psi_2|^2 | \right\rangle \right) = \langle \psi_2 D \rangle - \langle \psi_1 D \rangle . \quad \text{(C.21)}$$

The LHS is proportional to the cross invariant and should be approximately constant in the steady state so that

$$\langle \psi_1 D \rangle - \langle \psi_2 D \rangle \approx 0. \quad \text{(C.22)}$$

The modal form of $\langle \psi_2 D \rangle$ is given (C.16) and $\langle \psi_1 D \rangle$ is equivalent to:

$$\begin{aligned} \langle \psi_1 D \rangle &= -C_D \left[\left\langle \psi_1 \frac{\partial}{\partial x}\left(|\nabla\psi_2| \psi_{2_x} \right) \right\rangle + \left\langle \psi_1 \frac{\partial}{\partial y}\left(|\nabla\psi_2| \psi_{2_y} \right) \right\rangle \right], \quad \text{(C.23)} \\ &= C_D \left(\left\langle |\nabla\psi_2| \psi_{2_x} \psi_{1_x} \right\rangle + \left\langle |\nabla\psi_2| \psi_{2_y} \psi_{1_y} \right\rangle \right), \quad \text{(C.24)} \\ &= C_D \left\langle |\nabla\psi_2| \nabla\psi_1 \cdot \nabla\psi_2 \right\rangle, \quad \text{(C.25)} \end{aligned}$$

with

$$C_D \langle |\nabla\psi_2|\nabla\psi_1 \cdot \nabla\psi_2\rangle = C_D \langle |\nabla\psi - \nabla\tau| (\nabla\psi + \nabla\tau) \cdot (\nabla\psi - \nabla\tau)\rangle \quad \text{(C.26)}$$

$$= C_D \left(\left\langle |\nabla\psi - \nabla\tau||\nabla\psi|^2 \right\rangle - \left\langle |\nabla\psi - \nabla\tau||\nabla\tau|^2 \right\rangle \right) \quad \text{(C.27)}$$

Recall that the goal is to eliminate $\langle|\nabla\tau|^2\rangle$ in the energy balance. Using (C.16), (C.22) and (C.27) we have

$$\left\langle |\nabla\psi - \nabla\tau| \left(|\nabla\psi|^2 - 2\nabla\psi \cdot \nabla\tau + |\nabla\tau|^2 \right) \right\rangle = \left\langle |\nabla\psi - \nabla\tau| \left(|\nabla\psi|^2 - |\nabla\tau|^2 \right) \right\rangle, \quad \text{(C.28)}$$

which leads to the conclusion that

$$\langle |\nabla\psi - \nabla\tau| \nabla\psi \cdot \nabla\tau \rangle = \left\langle |\nabla\psi - \nabla\tau| |\nabla\tau|^2 \right\rangle. \quad \text{(C.29)}$$

Unfortunately (C.29) does not imply that $\langle \nabla\psi \cdot \nabla\tau \rangle = \langle |\nabla\tau|^2 \rangle$. The energy balance can be written in its truncated form

$$\frac{U}{\lambda^2} \langle \tau\psi_x \rangle = C_D \left\langle |\nabla\psi - \nabla\tau| \left(|\nabla\psi|^2 - \nabla\psi \cdot \nabla\tau \right) \right\rangle, \quad \text{(C.30)}$$

but this still has the "painful" $|\nabla\tau|^2$ kicking around. Therefore it appears that we can not write the energy balance exclusively in terms of vortex properties.

However, diagnostics of numerical simulations (Arbic 2006) could verify if the cross-invariant is still valid with quadratic bottom friction. A nice check on the theory for the layered model would be to compare $\langle \psi_1 D \rangle$ to $\langle \psi_2 D \rangle$. These two terms should be approximately equal, as (C.22) suggests. The truncated dissipation in (C.30) could also be compared to to the total dissipation given in (C.16). Again these should be approximately equal if the theory described here is valid.

Appendix D

β-plane simulation data

The following is a summary of the results of the β-plane simulations. The data here can be used as a check against the calibration of future simulations. The quantities in the table are defined as:

$$D_\tau \equiv U^{-1} \langle \psi_x \tau \rangle \,, \tag{D.1}$$

$$V \equiv \sqrt{\langle \psi_x^2 \rangle}\,, \tag{D.2}$$

$$\ell_{\text{mix.}} \equiv U^{-1} \sqrt{\langle \tau^2 \rangle}\,, \tag{D.3}$$

$$u_J \equiv \sqrt{\langle \bar{\psi}_y^2 \rangle}\,, \tag{D.4}$$

$$\varepsilon \equiv \kappa \left\langle |\nabla\psi - \sqrt{2}\nabla\tau|^2 \right\rangle \,. \tag{D.5}$$

Table D.1: Summary of results from the β-plane simulations.

$\beta\lambda^2/U$	$\kappa\lambda/U$	$D_\tau/U\lambda$	V/U	$\ell_{\text{mix.}}/\lambda$	u_J/U	$\varepsilon\lambda/U^3$
1/4	0.02	34.428	18.894	13.208	33.198	32.449
5/16	0.02	14.490	12.762	9.320	21.420	13.687
3/8	0.02	7.045	8.646	6.998	15.681	6.648
7/16	0.02	3.813	6.707	5.518	11.843	3.601
1/2	0.02	2.215	5.514	4.532	9.211	2.091
9/16	0.02	1.292	4.416	3.665	7.022	1.216
5/8	0.02	0.679	3.258	2.842	5.233	0.640
11/16	0.02	0.424	2.963	2.488	4.280	0.400
3/4	0.02	0.279	2.609	2.200	3.592	0.260
13/16	0.02	0.178	2.291	1.944	3.015	0.166
7/8	0.02	0.124	2.189	1.839	2.650	0.115
15/16	0.02	0.0839	1.861	1.627	2.314	0.0777
1	0.02	0.0642	1.760	1.616	2.167	0.0589
9/8	0.02	0.0408	1.541	1.548	1.971	0.0369
5/4	0.02	0.0249	1.371	1.559	1.843	0.0222
1/4	0.04	34.240	16.151	12.422	20.710	32.313
5/16	0.04	14.405	11.121	8.082	12.745	13.645
3/8	0.04	6.082	7.128	6.242	9.076	5.755
7/16	0.04	3.200	5.295	4.822	6.964	3.026
1/2	0.04	1.824	4.111	3.835	5.558	1.723
9/16	0.04	1.166	3.520	3.260	4.651	1.098
5/8	0.04	0.783	3.215	2.865	3.989	0.735
11/16	0.04	0.501	2.703	2.445	3.273	0.470
3/4	0.04	0.371	2.657	2.285	2.931	0.347
13/16	0.04	0.240	2.265	1.953	2.426	0.223
7/8	0.04	0.182	2.176	1.884	2.221	0.169
15/16	0.04	0.133	1.945	1.748	2.025	0.124
1	0.04	0.106	1.808	1.708	1.914	0.0975
9/8	0.04	0.0763	1.847	1.739	1.808	0.0692
5/4	0.04	0.0416	1.618	1.648	1.722	0.0370

$\beta\lambda^2/U$	$\kappa\lambda/U$	$D_\tau/U\lambda$	V/U	$\ell_{\text{mix.}}/\lambda$	u_J/U	$\varepsilon\lambda/U^3$
0	0.08	2344.170	121.172	72.247	81.392	2204.958
1/32	0.08	2425.062	120.212	64.902	87.402	2283.561
1/16	0.08	2089.737	114.452	61.662	81.435	1914.972
3/32	0.08	764.755	69.540	43.342	43.513	722.160
1/8	0.08	261.773	40.104	27.430	23.990	244.169
3/16	0.08	83.145	22.974	17.215	12.644	78.232
1/4	0.08	26.835	13.463	11.090	7.306	25.451
5/16	0.08	10.425	8.355	7.597	5.684	9.874
3/8	0.08	4.752	5.698	5.502	4.514	4.501
7/16	0.08	2.550	4.273	4.270	3.730	2.413
1/2	0.08	1.524	3.430	3.462	3.184	1.439
9/16	0.08	0.993	2.880	2.915	2.814	0.937
5/8	0.08	0.700	2.541	2.545	2.563	0.659
11/16	0.08	0.526	2.373	2.321	2.357	0.493
3/4	0.08	0.420	2.302	2.233	2.215	0.391
13/16	0.08	0.280	2.008	1.950	1.866	0.261
7/8	0.08	0.249	2.046	1.946	1.855	0.231
15/16	0.08	0.2285	2.112	2.005	1.880	0.210
1	0.08	0.175	1.962	1.893	1.720	0.1602
9/8	0.08	0.129	1.919	1.903	1.672	0.117
5/4	0.08	0.0882	1.793	1.854	1.612	0.0788
0	0.16	172.090	27.356	29.090	9.092	162.926
1/16	0.16	120.967	21.573	21.332	7.677	124.880
1/8	0.16	63.345	15.400	14.760	5.565	59.824
3/8	0.16	29.190	10.971	10.990	2.850	27.632
1/4	0.16	13.700	7.963	8.247	2.563	13.004
5/16	0.16	6.297	5.727	6.140	1.861	5.980
3/8	0.16	3.252	4.351	4.748	1.480	3.095
7/16	0.16	1.854	3.416	3.780	1.564	1.757
1/2	0.16	1.205	2.858	3.160	1.649	1.139
9/16	0.16	0.849	2.498	2.760	1.631	0.798
5/8	0.16	0.6456	2.252	2.458	1.646	0.607
11/16	0.16	0.464	2.021	2.203	1.454	0.433
3/4	0.16	0.419	2.001	2.154	1.538	0.390
13/16	0.16	0.389	2.040	2.180	1.616	0.362
7/8	0.16	0.342	2.040	2.175	1.633	0.316
1	0.16	0.246	1.924	2.062	1.514	0.225
9/8	0.16	0.191	1.905	2.064	1.522	0.173
5/4	0.16	0.129	1.730	2.024	1.443	0.116

$\beta\lambda^2/U$	$\kappa\lambda/U$	$D_\tau/U\lambda$	V/U	$\ell_{\text{mix.}}/\lambda$	u_J/U	$\varepsilon\lambda/U^3$
0	0.32	21.890	8.419	10.980	2.004	20.847
1/32	0.32	20.500	7.620	9.702	1.904	19.562
1/16	0.32	18.645	7.179	9.045	1.819	17.782
3/32	0.32	16.222	6.777	8.512	1.709	15.475
1/8	0.32	13.570	6.346	7.950	1.637	12.952
3/16	0.32	8.748	5.368	6.745	1.358	8.334
1/4	0.32	5.523	4.534	5.698	1.114	5.262
5/16	0.32	3.395	3.802	4.790	0.937	3.231
3/8	0.32	2.060	3.173	3.993	0.771	1.954
7/16	0.32	1.282	2.682	3.372	0.662	1.215
1/2	0.32	0.833	2.301	2.888	0.674	0.786
9/16	0.32	0.637	2.106	2.605	0.842	0.599
5/8	0.32	0.483	1.912	2.365	0.897	0.454
11/16	0.32	0.449	1.897	2.289	1.043	0.420
3/4	0.32	0.422	1.913	2.285	1.145	0.394
7/8	0.32	0.351	1.896	2.257	1.255	0.324
1	0.32	0.287	1.864	2.244	1.290	0.262
9/8	0.32	0.235	1.867	2.285	1.367	0.213
5/4	0.32	0.179	1.791	2.203	1.350	0.161
0	0.64	6.682	4.197	6.310	0.884	6.426
1/32	0.64	6.20	4.128	6.023	0.876	5.964
1/16	0.64	5.735	3.971	5.805	0.8481	5.518
3/32	0.64	5.232	3.824	5.587	0.834	5.031
1/8	0.64	4.67	3.704	5.385	0.776	4.475
3/16	0.64	3.565	3.392	4.945	0.735	3.417
1/4	0.64	2.598	3.093	4.488	0.666	2.485
5/16	0.64	1.752	2.734	3.965	0.579	1.674
3/8	0.64	1.164	2.422	3.507	0.535	1.109
7/16	0.64	0.761	2.126	3.072	0.467	0.723
1/2	0.64	0.522	1.902	2.738	0.478	0.496
9/16	0.64	0.439	1.826	2.545	0.626	0.415
5/8	0.64	0.396	1.804	2.482	0.749	0.373
11/16	0.64	0.371	1.796	2.435	0.845	0.350
3/4	0.64	0.315	1.721	2.482	0.857	0.294
7/8	0.64	0.303	1.810	2.451	1.064	0.281
1	0.64	0.2715	1.835	2.471	1.1565	0.2489

References

Alford, M. H. & R. Pinkel, 2000: Observations of overturning in the thermocline: The context of ocean mixing. *J. Phys. Oceanogr.*, **30**, 805-832.

Alford, M. H., 2001: Internal swell generation: The spatial distribution of energy flux from the wind to mixed layer near-inertial motions. *J. Phys. Oceanogr.*, **31**, 2359-2368.

Alford, M. H., 2003: Improved global maps and 54-year history of wind-work on ocean inertial motions. *Geophys. Res. Lett.*, **30**, Art. No. 1424.

Arbic, B. K., 2006: On the dissipation of midocean eddies: Lessons from baroclinically unstable geostrophic turbulence damped by bottom quadratic drag. *J. Phys. Oceanogr.*, Submitted.

Arbic, B. K. & G. R. Flierl, 2003: Coherent vortices and kinetic energy ribbons in asymptotic, quasi two-dimensional f-plane turbulence. *Phys. Fluids*, **15**, 2177-2189.

Arbic, B. K. & G. R. Flierl, 2004a: Baroclinically unstable geostrophic turbulence in the limits of strong and weak bottom Ekman friction: Application to midocean eddies. *J. Phys. Oceanogr.*, **34**, 2257-2273.

Arbic, B. K. & G. R. Flierl, 2004b: Effects of mean flow direction on energy, isotropy, and coherence of baroclinically unstable beta-plane geostrophic turbulence. *J. Phys. Oceanogr.*, **34**, 77-93.

Banks, H. T., R. A. Wood, J. M. Gregory, T. C. Johns & G. S. Jones, 2000: Are observed decadal changes in intermediate water masses a signature of anthropogenic climate change? *Geophys. Res. Lett.*, **27**, 2961-2964.

Bryden, H. L. & S. A. Cunningham, 2003: How wind-forcing and air-sea heat exchange determine the meridional temperature gradient and stratification for the Antarctic Circumpolar Current. *J. Geophys. Res.*, **108**, Art. No. 3275.

Caldwell, D. R. & J. N. Moum, 1995: Turbulence and mixing in the ocean. *Rev. Geophys.*, **81**, (Suppl.), 1385-1394.

Carnevale, G. F., J. C. McWilliams, Y. Pomeau, J. B. Weiss, & W. R. Young, 1991: Evolution of vortex statistics in two-dimensional turbulence. *Phys. Rev. Lett.*, **66**, 2735-2737.

Cessi, P. & M. Fantini, 2004: The eddy-driven thermocline. *J. Phys. Oceanogr.*, **34**, 2642-2658.

Chang, E. K. M., S. Lee & K. L. Swanson, 2002: Storm track dynamics. *J. Climate*, **15**, 2163-2183.

Charney, J. G., 1947: The dynamics of long waves in a baroclinic westerly current. *J. Meteorol.*, **4**, 135-162.

Cho, J. Y. K. & L. M. Polvani, 1996: The emergence of jets and vortices in freely evolving, shallow-water turbulence on a sphere. *Phys. Fluids*, **8**, 1531-1552.

Crawford, W. R., 1986: A comparison of length scales and decay times of turbulence in stably stratified flows. *J. Phys. Oceanogr.*, **16**, 1847-1854.

Cunningham, S. A., S. G. Alderson, B. A. King & M. A. Brandon, 2003: Transport and variability of the Antarctic Circumpolar Current in Drake Passage. *J. Geophys. Res.*, **108**, Art. No. 8084.

Danilov, S. & D. Gurarie, 2002: Rhines scale and spectra of the β-plane turbulence with bottom drag. *Phys. Rev.*, **65E**, R067301.

Dillon, T. M., 1982: Vertical overturns: A comparison of Thorpe and Ozmidov scales. *J. Geophys. Res.*, **87**, 9601-9613.

Dritschel, D. G., P. H. Haynes, & M. E. McIntyre, 2006: Multiple jets as PV staircases: the Phillips effect and the resilience of eddy-transport barriers. Submitted to the Savannah Special Issue of *J. Atmos. Sci.*

Eady, E. T., 1949: Long waves and cyclone waves. *Tellus*, **1**, 33-52.

Efron, B. & G. Gong, 1983: A leisurely look at the bootstrap, the jackknife, and cross-validation. *Am. Stat.*, **37**, 36-48.

Egbert, G. D. & R. Ray, 2000: Significant dissipation of tidal energy in the deep ocean inferred from satellite altimeter data. *Nature*, **45**, 775-778.

Ferrari, R. & K. L. Polzin, 2005: Finescale structure of the T-S relation in the eastern North Atlantic. *J. Phys. Oceanogr.*, **35**, 1437-1454.

Ferron, B., H. Mercier, K. Speer, A. Gargett & K. Polzin, 1998: Mixing in the Romanche Fracture Zone. *J. Phys. Oceanogr.*, **28**, 1929-1945.

Finnegan, T. D., D. S. Luther & R. Lukas, 2002: Observations of enhanced diapycnal mixing near the Hawaiian Ridge. *J. Phys. Oceanogr.*, **32**, 2988-3002.

Flierl, G. R., 1978: Models of vertical structure and the calibration of two-layer models. *Dyn. Atmos. Oceans*, **2**, 342-381.

Galbraith, P. S. & D. E. Kelley, 1996: Identifying overturns in CTD profiles. *J. Atmos. Oceanic Technol.*, **13**, 688-702.

Garrett, C., 1982: On the parameterization of diapycnal fluxes due to double-diffusive intrusions. *J. Phys. Oceanogr.*, **12**, 952-959.

Garrett, C. & W. Munk, 1975: Space-time scales of internal waves - Progress report. *J. Geophys. Res.*, **80**, 291-297.

Gill, A. E., 1982: *Atmosphere-Ocean Dynamics*. Academic Press, 662pp.

Gille, S. T., 2002: Warming of the Southern Ocean since the 1950s. *Science*, **295**, 1275-1277.

Gille, S. T., 2005: Statistical characterization of zonal and meridional ocean wind stress. *J. Atmos. Ocean. Tech.*, *Accepted*.

Green, J. S. A., 1970: Transfer properties of the large-scale eddies and the general circulation of the atmosphere. *Quart. J. Roy. Meteor. Soc.*, **96**, 157-185.

Greenslade, M. D. & P. H. Haynes, 2006: Vertical transition in transport and mixing in baroclinic flows. Submitted to the Savannah Special Issue of *J. Atmos. Sci.*

Gregg, M. C., 1977: Variations in intensity of small-scale mixing in the main thermocline. *J. Phys. Oceanogr.*, **7**, 436-454.

Gregg, M. C., 1987: Diapycnal mixing in the thermocline: a review. *J. Geophys. Res.*, **92**, 5249-5286.

Gregg, M. C., 1989: Scaling turbulent dissipation in the thermocline. *J. Geophys. Res.*, **94**, 9686-9698.

Gregg, M. C. & E. Kunze, 1991: Internal wave shear and strain in Santa Monica basin. *J. Geophys. Res.*, **96**, 16709-16719.

Gregg, M. C., T. B. Sanford & D. P. Winkel, 2003: Reduced mixing from the breaking of internal waves in equatorial ocean waters. *Nature*, **422**, 513-515.

Grianik, N., I. M. Held, K. S. Smith & G. K. Vallis, 2004: The effects of quadratic drag on the inverse cascade of two-dimensional turbulence. *Phys. Fluids*, **16**, 73-78.

Haidvogel D. B. & I. M. Held, 1980 (HH80 in Chapter III): Homogeneous quasi-geostrophic turbulence driven by a uniform temperature gradient. *J. Atmos. Sci.*, **37**, 2644-2660.

Held, I. M. & V. D. Larichev, 1996: A scaling theory for horizontally homogeneous, baroclinically unstable flow on a beta plane. *J. Atmos. Sci.*, **53**, 946-952.

Henyey, F. S., 1991: Scaling of internal wave predictions for ε, in *Dynamics of Internal Gravity Waves in the Ocean: Proc. 'Aha Huliko'a Hawaiian Winter Workshop*, Honolulu, HI, U of Hawaii, P. Müller & D. Henderson, Eds., 233-236.

Henyey, F. S., J. Wright & S. M Flatté, 1986: Energy and action flow through the internal wave field: An eikonal approach. *J. Geophys. Res.*, **91**, 8487-8495.

Hogg, N. G. & H. M. Stommel, 1985. The heton, an elementary interaction between discrete baroclinic vortices, and its implications concerning eddy heat-flow *Proc. Royal soc. Lond. A* **397**, 1-20.

Hollowy, G. & M. Hendershott, 1977: Stochastic closure for nonlinear Rossby waves. *J. Fluid Mech.*, **82**, 747-765.

Holopainen, E. O., 1961: On the effect of friction in baroclinic waves. *Tellus*, **13**, 363-367.

Howard, S. L., J. Hyatt & L. Padman, 2004: Mixing in the pycnocline over the western Antarctic Peninsula shelf during Southern Ocean GLOBEC. *Deep-Sea Res. II*, **51**, 1965-1979.

Hua, B. L. & D. B. Haidvogel, 1986: Numerical simulations of the vertical structure of quasi-geostrophic turbulence. *J. Atmos. Sci.*, **43**, 2923-2936.

Huang, H.-P. & W. A. Robinson, , 1998: Two-dimensional turbulence and persistent zonal jets in a global barotropic model. *J. Atmos. Sci.*, **55**, 611-632.

Huppert, H. E., 1971: On the stability of a series of double diffusive layers. *Deep-Sea Res.*, **18**, 1005-1021.

Johnson, G. C. & H. L. Bryden, 1989: On the size of the Antarctic Circumpolar Current. *Deep-Sea Res.*, **36A**, 39-53.

Johnson, H. L. & C. Garrett, 2004: Effects of noise on Thorpe scales and run lengths. *J. Phys. Oceanogr.*, **34**, 2359-2372.

Joyce, T. M., W. Zenk & J. M. Toole, 1978: The anatomy of the Antarctic Polar Front in Drake Passage. *J. Geophys. Res.*, **83**, 6093-6114.

Karsten R., H. Jones & J. Marshall, 2002: The role of eddy transfer in setting the stratification and transport of a circumpolar current. *J. Phys. Oceanogr.*, **32**, 39-54.

Karsten, R. & J. Marshall, 2002: Constructing the residual circulation of the ACC from observations. *J. Phys. Oceanogr.*, **32**, 3315-3327.

Kelley, D., 1984: Effective diffusivities within thermohaline staircases. *J. Geophys. Res.*, **89**, 10484-10488.

Kelley, D., 1990: Fluxes through diffusive staircases: a new formulation. *J. Geophys. Res.*, **95**, 3365-3371.

Klymak, J. M., J. N. Moum, J. D. Nash, E. Kunze, J. B. Girton, G. S. Carter, C. M. Lee, T. B. Sanford & M. C. Gregg, 2006: An estimate of tidal energy lost to turbulence at the Hawaiian Ridge. *J. Phys. Oceanogr.*, **36**, 1148-1164.

Kunze, E., 2003: Yes, we have no abyssal mixing, in *Near-Boundary Processes and Their Parameterizations: Proc. 'Aha Huliko'a Hawaiian Winter Workshop*, Honolulu, HI, U of Hawaii, P. Müller & D. Henderson, Eds., 85-93.

Kunze, E. & T. B. Sanford, 1996: Abyssal mixing: Where it is not. *J. Phys. Oceanogr.*, **26**, 2286-2296.

Lapeyre, G. & I. M. Held, 2003 (LH03 in Chapter III): Diffusivity, kinetic energy dissipation, and closure theories for the poleward eddy heat flux. *J. Atmos. Sci.*, **60**, 2907-2916.

Larichev, V. & I. Held, 1995 (LH95 in Chapter II): Eddy amplitudes and fluxes in a homogeneous model of fully developed baroclinic instability. *J. Phys. Oceanogr.*, **25**, 2285-2297.

Larson, N. G. & M. C. Gregg, 1983: Turbulent dissipation and shear in thermohaline intrusions. *Nature*, **306**, 26-32.

Lee, S., 1997: Maintenance of multiple jets in a baroclinic flow. *J. Atmos. Sci.*, **54**, 1726-1738.

Lee, S., 2005: Baroclinic multiple zonal jets on the sphere. *J. Atmos. Sci.*, **62**, 2484-2498.

Lee, S., & I. M. Held, 1993: Baroclinic wave packets in models and observations. *J. Atmos. Sci.*, **50**, 1413-1428.

Lenn, Y. D., T. K. Chereskin, J. Sprintall & E. Firing, 2005: Mean jets, mesoscale variability and eddy momentum fluxes in the surface-layer of the Antarctic Circumpolar Current in Drake Passage. *J. Marine. Res.*, Submitted.

Linden, P. F., 1979: Mixing in stratified fluids. *Geophys. Astrophys. Fluid Dyn.*, **3**, 3-23.

Manfroi, A. J. & W. R. Young, 1999: Slow evolution of zonal jets on the beta plane. *J. Atmos. Sci.*, **56**, 784-800.

Marmorino, G. D. & D. R. Caldwell, 1976: Heat and salt transport through a diffusive thermohaline interface. *Deep-Sea Res.*, **23**, 59-67.

Martin, J. P. & D. L. Rudnick, 2005: Inferences and observations of turbulent dissipation and mixing in the upper ocean at the Hawaiian Ridge. *J. Phys. Oceanogr.*, Submitted.

Maximenko, N. A., B. Bang & H. Sasaki, 2005: Observational evidence of alternating zonal jets in the world ocean. *Geophys. Res. Lett.*, **32**, L12607.

McComas, C. H. & P. Müller, 1981: The dynamic balance of internal waves. *J. Phys. Oceanogr.*, **11**, 970-986.

McIntyre, M. E., 1970: On the non-separable baroclinic parallel flow instability problem. *J. Fluid Mech.*, **40**, 273-306.

McWilliams, J. C., 1984: The emergence of isolated coherent vortices in turbulent flow. *J. Fluid Mech.*, **146**, 21-43.

McWilliams, J. C., 1990: The vortices of two-dimensional turbulence. *J. Fluid Mech.*, **219**, 361-385.

Moum, J. N., 1990: The quest for K_ρ–Preliminary results from direct measurements of turbulent fluxes in the ocean. *J. Phys. Oceanogr.*, **12**, 256-271.

Muench, R. D., H. J. S. Fernando & G. R. Stegen, 1990: Temperature and salinity staircases in the Northwestern Weddell Sea. *J. Phys. Oceanogr.*, **20**, 295-306.

Munk, W. H., 1966: Abyssal recipes. *Deep-Sea Res.*, **13**, 207-230.

Munk, W. & C. Wunsch, 1998: Abyssal recipes II: energetics of tidal and wind mixing. *Deep-Sea Res.*, **45**, 1977-2010.

Nagasawa, M., Y. Niwa & T. Hibiya, 2000: Spatial and temporal distribution of the wind-induced internal wave energy available for deep water mixing in the North Pacific. *J. Geophys. Res.*, **105**, 13933-13943.

Naveira Garabato, A. C., K. L. Polzin, B. A. King, K. J. Heywood & M. Visbeck, 2004: Widespread intense turbulent mixing in the Southern Ocean. *Nature*, **303**, 210-213.

Nowlin, W. D., Jr., T. Whitworth & R. D. Pillsbury, 1977: Structure and transport of the Antarctic Circumpolar Current at Drake Passage from short-term measurements. *J. Phys. Oceanogr.*, **7**, 788-802.

Nozawa, T. & S. Yoden, 1997: Formation of zonal band structure in forced two-dimensional turbulence on a rotating sphere. *Phys. Fluids*, **9**, 2081-2093.

Okubo, A., 1970: Horizontal dispersion of floatable particles in the vicinity of velocity singularities such as convergences. *Deep Sea Res.*, **17**, 445-454.

Orsi, A. H., T. Whitworth & W. D. Nowlin, 1995: On the meridional extent and fronts of the Antarctic Circumpolar Current. *Deep-Sea Res. I*, **42**, 641-673.

Osborn, T. R., 1980: Estimates of the local rate of vertical diffusion from dissipation measurements. *J. Phys. Oceanogr.*, **10**, 83-89.

Osborn, T. R. & C. S. Cox, 1972: Oceanic fine structure. *Geophys. Fluid Dyn.*, **3**, 321-345.

Ozmidov, R. V., 1965: On the turbulent exchange in a stably stratified ocean. *Izv. Acad Sci. USSR, Atmos. Oceanic Phys.*, **1**, 861-871.

Panetta, L., 1993: Zonal jets in wide baroclinically unstable regions: persistence and scale selection. *J. Atmos. Sci.*, **50**, 2073-2106.

Park, Y.-G., J. A. Whitehead & A. Gnanadeskian, 1994: Turbulent mixing in stratified fluids: layer formation and energetics. *J. Fluid Mech.*, **279**, 279-311.

Pavan, V. & I. M. Held, 1996: The diffusive approximation for eddy fluxes in baroclinically unstable jets. *J. Atmos. Sci.*, **53**, 1262-1272.

Pedlosky, J., 1983: The growth and decay of finite-amplitude baroclinic waves. *J. Atmos. Sci.*, **40**, 1863-1876.

Pedlosky, J., 1987: *Geophysical Fluid Dynamics.* 2nd ed. Springer-Verlag, 710pp.

Peters, H., M. C. Gregg & T. B. Sanford, 1995: On the parameterization of equatorial turbulence: Effect of finescale variations below the range of the diurnal cycle. *J. Geophys. Res.*, **100**, 18333-18348.

Polzin, K. L., J. M. Toole, J. R. Ledwell & R. W. Schmitt, 1997: Spatial variability of turbulent mixing in the abyssal ocean. *Science*, **276**, 93-96.

Polzin, K. L., & E. Firing, 1997: Estimates of diapycnal mixing using LADCP and CTD data from I8S. *Int. WOCE Newsl.*, **29**, 39-42.

Provenzale, A., 1999: Transport by coherent barotropic vortices. *Ann. Rev. Fluid Mech.*, **31**, 55-93.

Rhines, P. B., 1975: Waves and turbulence on a beta-plane. *J. Fluid Mech.* **69**, 417-443.

Rhines, P. B., 1977: The dynamics of unsteady currents. *The Sea*, Vol. 6, E. A. Goldberg, I. N. McCane, J. J. O'Brien & J. H. Steele, Eds., Wiley, 189-318.

Richards, K. J., N. A. Maximenko, F. O. Bryan & H. Sasaki, 2006: Zonal jets in the Pacific Ocean. *Geophys. Res. Lett.*, **33**, L03605.

Rintoul, S., C. Hughes & D. Olbers, 2001: The Antarctic Circumpolar Current System. *Ocean Circulation and Climate*, G. Siedler et al., Eds., International Geophysics Series, Vol. 77, Academic Press, 271-302.

Riviere, P. & P. Klein, 1997: Effects of an asymmetric friction on the nonlinear equilibration of a baroclinic system. *J. Atmos. Sci.*, **54**, 1610-1627.

Riviere, P., A. M. Treguier & P. Klein, 2004: Effects of bottom friction on nonlinear equilibration of an oceanic baroclinic jet. *J. Phys. Oceanogr.*, **34**, 416-432.

Robinson, W. A., 2006: On the self-maintenance of midlatitude jets. *J. Atmos. Sci.*, **63**, 2109-2122.

Ruddick, B. R. & J. S. Turner, 1979: The vertical length scale of double-diffusive intrusions. *Deep-Sea Res.*, **26A**, 903-913.

Salmon, R., 1978: Two-layer quasigeostrophic turbulence in a simple special case. *Geophys. Astrophys. Fluid Dyn.*, **10**, 25-52.

Salmon, R., 1980: Baroclinic instability and geostrophic turbulence. *Geophys. Astrophys. Fluid Dyn.*, **15**, 167-211.

Sloyan, B. M., 2005: Spatial variability of mixing in the Southern Ocean. *Geophys. Res. Lett.*, **32**, Art. No. L18603.

Smith, K. S., G. Boccaletti, C. C. Henning, I. Marinov, C. Y. Tam, I. M. Held, & G. K. Vallis, 2002: Turbulent diffusion in the geostrophic inverse cascade. *J. Fluid Mech.,* **469**, 13-48.

Smith, K. S. & G. K. Vallis, 2002: The scales and equilibration of midocean eddies: forced-dissipative flow. *J. Phys. Oceanogr.*, **32**, 1699-1720.

Smith, W. F. & D. T. Sandwell, 1997: Global sea floor topography from satellite altimetry and ship depth soundings. *Science*, **277**, 1956-1962.

Speer, K., S. R. Rintoul & B. Sloyan, 2000: The diabatic deacon cell. *J. Phys. Oceanogr.*, **30**, 3212-3222.

Sprintall, J., 2003: Seasonal to interannual upper-ocean variability in the Drake Passage. *J. Mar. Res.*, **61**, 27-57.

Stansfield, K., C. Garrett & R. Dewey, 2001: The probability distribution of the Thorpe displacement within overturns in Juan de Fuca Strait. *J. Phys. Oceanogr.*, **31**, 3421-3434.

Starr, V. P., 1968: *Physics of Negative Viscosity Phenomena.* McGraw-Hill, 256pp.

Stone, P. H., 1972: A simplified radiative-dynamical model for the static stability of rotating atmospheres. *J. Atmos. Sci.*, **29**, 11-37.

Timmermans, M. L., C. Garrett & E. Carmack, 2003: The thermohaline structure and evolution of the deep waters in the Canada Basin, Arctic Ocean. *Deep-Sea Res.*, **50A**, 1305-1321.

Thompson, A. F. & G. Veronis, 2005: Diffusively-driven overturning of a stable density gradient. *J. Mar. Res.*, **63**, 291-313.

Thompson, A. F. & W. R. Young, 2006: Scaling baroclinic eddy fluxes: vortices and energy balance. *J. Phys. Oceanogr.*, **36**, 720-738.

Thorpe, S. A., 1977: Turbulence and mixing in a Scottish loch. *Philos. Trans. Roy. Soc. London*, **286A**, 125-181.

Toggweiler, J. R. & B. Samuels, 1995: Effect of Drake Passage on the global thermohaline circulation. *Deep-Sea Res. I*, **42**, 477-500.

Toggweiler, J. R. & B. Samuels, 1998: On the ocean's large-scale circulation near the limit of no vertical mixing. *J. Phys. Oceanogr.*, **28**, 1832-1852.

Toole, J. M., 1981: Intrusion characteristics in the Antarctic Polar Front. *J. Phys. Oceanogr.*, **11**, 780-793.

Toole, J. M., K. L. Polzin & R. W. Schmitt, 1994: Estimates of diapycnal mixing in the abyssal ocean. *Science*, **264**, 1120-1123.

UNESCO, 1981: Tenth report of the joint panel on oceanographic tables and standards. *UNESCO Tech. Papers in Mar. Sci.*, **36**, 24.

Vallis, G. K. & M. E. Maltrud, 1993: Generation of mean flow and jets on a beta plane and over topography. *J. Phys. Oceanogr.*, **23**, 1346-1362.

Vasavada, A. R. & A. P. Showman, 2005: Jovian atmospheric dynamics: an update after Galileo and Cassini. *Rep. Prog. Phys.*, **68**, 1935-1996.

Walsh, D. & B. Ruddick, 2000: Double-diffusive interleaving in the presence of turbulence: The effect of a nonconstant flux ration. *J. Phys. Oceanogr.*, **30**, 2231-2245.

Weiss, J., 1991: The dynamics of enstrophy transfer in two-dimensional hydrodynamics. *Physica D*, **48**, 273-294.

Wijesekera, H., L. Padman, T. Dillon, M. Levine, C. Paulson & R. Pinkel, 1993: The application of internal-wave dissipation models to a region of strong mixing. *J. Phys. Oceanogr.*, **23**, 269-286.

Williams, G. P., 1979: Planetary circulations: 2, The Jovian quasigeostrophic regime. *J. Atmos. Sci.*, **36**, 932-968.

Winkel, D. P., 1998: Influences of mean shear in the Florida Current on turbulent production by internal waves. Ph.D. dissertation, University of Washington.

Wunsch, C., 1998: The work done by the wind on the oceanic general circulation. *J. Phys. Oceanogr.*, **28**, 2332-2340.

Wunsch, C. & R. Ferrari, 2004: Vertical mixing, energy, and the general circulation of the oceans. *Ann. Rev. Fluid Mech.*, **36**, 281-314.

Zhai, X., R. J. Greatbatch & J. Zhao, 2005: Enhanced vertical propagation of storm-induced near-inertial energy in an eddying ocean channel model. *Geophys. Res. Lett.*, **32**, Art. No. L18602.